University of Southampton

ALL-OPTICAL NONLINEAR SIGNAL PROCESSING DEVICES AND THEIR APPLICATIONS WITHIN FIBRE-OPTIC COMMUNICATION SYSTEMS

by

Ju Han Lee

A thesis submitted for the degree of Doctor of Philosophy

FACULTY OF ENGINEERING AND APPLIED SCIENCE
OPTOELECTRONICS RESEARCH CENTRE
DEPARTMENT OF ELECTRONICS AND COMPUTER SCIENCE

January 2003

University of Southampton

ABSTRACT

FACULTY OF ENGINEERING AND APPLIED SCIENCE
OPTOELECTRONICS RESEARCH CENTRE
DEPARTMENT OF ELECTRONICS AND COMPUTER SCIENCE

Doctor of Philosophy

ALL-OPTICAL NONLINEAR SIGNAL PROCESSING DEVICES AND THEIR APPLICATIONS WITHIN FIBRE-OPTIC COMMUNICATION SYSTEMS

by Ju Han Lee

This thesis is concerned with research into the development of a range of all-optical fibre based nonlinear devices for optical communication applications. The research can be divided into two main themes. The first concerns the use of superstructured fibre Bragg grating technology together with fibre based nonlinear devices to improve the overall system performance in both OCDMA and OTDM systems. The second theme area concerns the use of highly nonlinear holey fibre within a range of nonlinear signal processing devices and an analysis of the performance of these devices from a system context.

Firstly, the benefits to be obtained from incorporating a nonlinear switch within a SSFBG based OCDMA system is demonstrated both numerically and experimentally. The fact that error-free and penalty-free operation has been achieved in two channel multiplexing experiments implies that the approach should give equivalent system benefits when used in OCDMA systems operating under multi-user operation. The use of a superstructured fibre Bragg grating to pre-shape optical pulses to obtain more-optimal operation of various nonlinear, all-optical switches is also presented. Specifically 2.5 ps soliton pulses are converted into 20 ps rectangular pulses at the input to both fibre and semiconductor optical amplifier based switches and it is shown that rectangular switching windows can be achieved. A 5-10-fold reduction in timing jitter sensitivity is demonstrated. Subsequently a dramatic performance improvement in an 80 Gbit/s OTDM demultiplexing system is demonstrated with 10 ps rectangular control pulses.

A range of nonlinear devices based on a holey fibre is demonstrated. Holey fibre has a nonlinearity around 10~100 times greater than conventional fibre. The use of a short (8.7 m), highly nonlinear holey fibre based optical switch is presented and shown to provide enhanced code recognition quality in a SSFBG based OCDMA system. The use of a short (75 m), highly nonlinear holey fibre to obtain strong L^+-band Raman amplification and SRS based signal modulation is also demonstrated. The use of HF within Brillouin based devices is next considered. Both stimulated and spontaneous Brillouin scattering effects are investigated. The observed high SBS lasing threshold is found to be mainly due to reduction in the effective gain coefficient caused by structural non-uniformity along the HF length. A 5.8 m length of HF is then used to achieve tuneable WDM wavelength conversion based on XPM and it is experimentally demonstrated that HF with normal GVD should be used for this sort of device in order to eliminate the coherence degradation related intensity noise observed in experiments employing anomalously dispersive HF. Finally, a FWM based wavelength converter using a 15 m, highly nonlinear HF with a high SBS threshold is presented. The high SBS threshold is achieved by applying structural variation to the HF along its length during the fabrication process.

TABLE OF CONTENTS

ACKNOWLEDGEMENTS

Firstly, I would like to thank my supervisor Prof. David J. Richardson for his patient guidance and support. I appreciate his decision to accept me as a PhD student was very hard to make given funding circumstances at ORC three years ago and it has turned out to be a great opportunity for me. Somewhere at the top of this list should be my parents who have always supported me in whatever I do. Special thanks must be given to my wife, Kyung Yi Kim who waited for me for two and a half years in the Republic of Korea, and who finally married me in October 2002.

I owe a great deal of debt of gratitude to my colleagues and friends; Dr. Peh Chiong Teh, Dr. Morten Ibsen, and Mr. Walter Belardi for their collaboration and for constructive discussions on many aspects of the work. I acknowledge that nothing could have been done without them. All of my colleagues and friends such as Mr. Ronaldus P. H. Haaksman, Mr. Paulo J. Almeida, Mr. Fabio Ghiringhelli, Dr. Carlos Alegria, Mrs. Anoma McCoy, Ms. Francesca Parmigiani, Mr. Jonathan Price, and Mr. Ian Musgrave should receive special mention for helping me enjoy work and my life as a student. Many thanks should be given to Dr. Kentaro Furusawa, Dr. Periklis Petropoulos, Dr. Tanya. M. Monro, and Mr. Zulfadzli Yusoff for their useful inputs of my work. I also would like to express my gratitude to Dr. Anders T. Clausen, Dr. Leif Oxenløwe, Mr. Kim S. Berg, and Prof. Palle Jeppsen for joyful collaboration in COM center, Technical University of Denmark. I am indebted to Mr. Sang-Young Lee, the Education Director of Embassy of the Republic of Korea for his constant support and patient encouragement during the 3-year course.

Many thanks should also be due to the IEEE Laser and Electro-Optic Society (LEOS) for awarding me with a prestigious 2002 IEEE/LEOS Graduate Student Fellowship.

Finally, I would also like to acknowledge that my three-year PhD course was fully funded and supported by the Overseas Study Scholarship Scheme by the Ministry of Education of the Government of Republic of Korea.

AUTHOR'S CONTRIBUTION

The work in this thesis has been mostly carried out in collaboration with other colleagues in the ORC although the author has played the key role in each of the particular experiments reported here.

In the optical CDMA system related work, both encoding/decoding grating design and construction of the corresponding system setups were performed by Dr. Peh Chiong Teh. Fabrication of the gratings was performed by Dr. Morten Ibsen.

In the square pulse switching technology experiments, Dr. P. Petropoulos designed and characterised the 20-ps wide square pulse grating whilst the author himself designed the 10-ps grating. Dr. Morten Ibsen fabricated both of these gratings. The 80 Gbit/s OTDM systems experiments were performed at the COM center, Technical University of Denmark, and the system test beds were built by Dr. Leif Oxenløwe, and Mr. Kim S. Berg.

In the range of experiments on holey fibre based nonlinear optical devices, Dr. Tanya M. Monro and Ms. Vittoria Finazzi designed the fibres, and Mr. Walter Belardi and Dr. Kentaro Furusawa fabricated the corresponding holey fibres.

LIST OF FIGURES

CHAPTER ONE

INTRODUCTION

CHAPTER TWO

CHAPTER EIGHT

A TUNEABLE WDM WAVELENGTH CONVERTER BASED ON CROSS PHASE MODULATION EFFECTS IN HOLEY FIBRE

CHAPTER NINE

FOUR-WAVE MIXING BASED, 10 GBIT/S TUNEABLE WAVELENGTH CONVERSION USING A HOLEY FIBRE WITH A HIGH STIMULATED

ABBREVIATIONS

AOM	Acousto-Optic Modulator
AOTF	Acousto-Optic Tuneable Filter
ASE	Amplified Spontaneous Emission
BER	Bit Error Rate
CW	Continuous Wave
C – band	1525nm ~ 1565nm
DSF	Dispersion Shifted Fibre
DS-OCDMA	Direct Sequence - Optical Code Division Multiple Access
EDFA	Erbium Doped Fibre Amplifier
EFRL	Erbium Fibre Ring Laser
FBG	Fibre Bragg Grating
FH – CDMA	Frequency Hopping - Code Division Multiple Access
FWHM	Full Width at Half Maximum
FWM	Four-Wave Mixing
GVD	Group Velocity Dispersion
HF	Holey Fibre
HNLF	Highly Nonlinear Fibre
HR	High Reflector
IP	Internet Protocol
LMA	Large Mode Area
L – band	1565 ~ 1625 nm
L^+ - band	1625 ~1665 nm
M – NOLM	All-optical Modulator Nonlinear Optical Loop Mirror
MOPA	Master Oscillator and Power Amplifier
MUX	Multiplexer
NOLM	Nonlinear Optical Loop Mirror
OCDMA	Optical Code Division Multiple Access
OSA	Optical Spectrum Analyser
OTDM	Optical Time Division Multiplexing
PC	Polarisation Controller

PM	Polarisation Maintaining
PMD	Polarisation Mode Dispersion
RF	Radio Frequency
RZ	Return-to-Zero
SBS	Stimulated Brillouin Scattering
S – band	1480 ~1525 nm
SEM	Scanning Electron Microscope
SHG	Second Harmonic Generation
SOA	Semiconductor Optical Amplifiers
SPM	Self-Phase Modulation
SRS	Stimulated Raman Scattering
SSFBG	Supersturctured Fibre Bragg Grating
TOAD	Tera-hertz Optical Asymmetric Demultiplexer
UNI	Ultrafast Nonlinear Interferometer
U – band	1625 ~1675 nm, similar to L^+ - band
UV	Ultraviolet
WC	Wavelength Converter
WC - NOLM	Wavelength Converter Nonlinear Optical Loop Mirror
WDM	Wavelength Division Multiplexing
XGM	Cross-Gain Modulation
XPM	Cross-phase modulation

CHAPTER ONE

INTRODUCTION

The huge demands for the expansion of data transmission capacity in fibre-optic telecommunication systems and related optical networks, means that the development of all-optical signal processing devices and technologies with which to tackle the performance limitations that otherwise result from the unavoidable conversion from the optical to electrical domains has become of great practical interest. In particular, signal processing approaches and devices based on the nonlinear properties of either optical fibres or semiconductor active devices have been studied and successfully applied to a variety of applications in telecommunication systems. This thesis reports works carried out in two distinct areas; namely, (i) the use of superstructured fibre Bragg gratings (SSFBG's) to reshape optical pulses to enhance the performance of various nonlinear devices (Chapters 2, 3, and 4), and (ii) the use of highly nonlinear holey fibres to reduce device length and power requirements for a range of nonlinear optical devices (Chapters 5, 6, 7, 8, and 9). Both of these subjects are aimed at broadening the technology base available for high-capacity fibre-optic communication systems. This Chapter provides the background knowledge for each area of study. This Chapter is organised as follows. In Section 1.1 a brief introduction to the main nonlinear optical effects in optical fibre is presented. In Section 1.2 an overview of superstructured fibre Bragg grating technology is presented. Section 1.3 is devoted to an overview of holey fibre technology.

1.1 Nonlinear Effects in Optical Fibres and Semiconductor Optical Amplifiers (SOA's)

A great number of signal processing approaches and devices based on the nonlinear properties of both optical fibres and semiconductor active devices have been studied and successfully applied to a variety of applications in telecommunication systems. Devices demonstrated to date include amongst others, wavelength converters [1.1, 1.2, 1.3], optical demultiplexers [1.4, 1.5], noise rejection filters [1.6, 1.7], amplifiers [1.8, 1.9], clock recovery subsystems [1.10], and data regenerators [1.11]. The two main forms of nonlinear effect used are (a) Kerr nonlinear effects and (b) inelastic nonlinear scattering effects (i.e. Raman and Brillouin scattering). Kerr nonlinear effects including self-phase modulation, cross-phase modulation, and four-wave mixing are due to the response of the bound electrons in a nonlinear optical medium to an intense optical field, whilst Raman and Brillouin scattering effects are caused by the presence of vibrational states of atoms (phonons) in the optical medium.

In this Section, the most significant nonlinear effects in optical fibre are reviewed. This review is carried out from a positive perspective focussing on device applications, however, it should be appreciated that these effects can be highly undesirable in other instances. For example, four-wave mixing induced crosstalk between WDM channels [1.12] and Raman effect induced signal power depletion [1.13] can significantly degrade the performance of DWDM communication systems. The nonlinear properties of semiconductor active devices are also briefly discussed. This Section is organised as follows. Section 1.1.1 introduces the wave equation and the concept of induced polarisation which are essential to understanding nonlinear properties in optical fibre. In Section 1.1.2 an overview of self-phase modulation (SPM) in optical fibre is presented. The cross-phase modulation (XPM) effect is discussed in Section 1.1.3. In Section 1.1.4 four-wave mixing as an independent effect is described. Raman scattering and Brillouin scattering are discussed in Section 1.1.5 and 1.1.6, respectively. Section 1.1.7 is devoted to a discussion of the nonlinear properties of semiconductor optical amplifiers (SOA's).

1.1.1 Nonlinearities in Optical Fibre

Optical fibre shows a nonlinear response to intense optical fields. The origin of this nonlinear response is related to anharmonic motion of bound electrons under the influence of an applied field. The induced polarisation $\vec{P}$ from the electric dipoles is thus not linear in the electric field, but is described by the more general relation

$$\vec{P} = \varepsilon_0 \left(\chi^{(1)} \cdot \vec{E} + \chi^{(2)} : \vec{E}\vec{E} + \chi^{(3)} \vdots \vec{E}\vec{E}\vec{E} + \cdots \right) \qquad (1.1)$$

where ε_0 is the vacuum permittivity and $\chi^{(j)} (j = 1,2,3,\cdots)$ is jth order susceptibility. To account for the light polarisation effects, $\chi^{(j)}$ is a tensor of rank $j+1$. The linear susceptibility $\chi^{(1)}$ is the dominant contribution to $\vec{P}$, the effects of which are included through the refractive index n and the attenuation coefficient α. The second-order susceptibility $\chi^{(2)}$ is responsible for nonlinear effects such as second-harmonic generation and sum-frequency generation. However, symmetric molecule such as SiO_2 has a zero value for $\chi^{(2)}$. As a result optical fibres do not generally exhibit second-order nonlinear effects. The lowest order nonlinear effects in optical fibre originate from the third-order susceptibility $\chi^{(3)}$ which is responsible for phenomena such as third-harmonic generation, four-wave mixing, and the intensity dependence of the refractive index (Kerr effect). In particular, the nonlinear processes which generate new frequency components, i.e. third-harmonic generation or four-wave mixing requires special efforts to achieve phase matching.

For a better understanding of the nonlinear phenomena in optical fibre, it is necessary to consider the theory of electromagnetic wave propagation in dispersive nonlinear media. Like all electromagnetic phenomena, the propagation of optical fields in optical fibre is governed by Maxwell's equations as follows.

$$\nabla \times \vec{E} = -\frac{\partial \vec{B}}{\partial t} \qquad (1.2)$$

$$\nabla \times \vec{H} = \vec{J} + \frac{\partial \vec{D}}{\partial t} \qquad (1.3)$$

$$\nabla \cdot \vec{D} = \rho \quad (1.4)$$

$$\nabla \cdot \vec{B} = 0 \quad (1.5)$$

where $\vec{E}$ and $\vec{H}$ are electric and magnetic field vectors, respectively, and $\vec{D}$ and $\vec{B}$ are the corresponding electric and magnetic flux densities. The current density vector $\vec{J}$ and the charge density ρ represent the sources for the electromagnetic field. In the absence of free charges in a medium such as optical fibre, $\vec{J} = 0$ and $\rho = 0$.

The flux densities $\vec{D}$ and $\vec{B}$ originate from the electric and magnetic fields ($\vec{E}$ and $\vec{H}$) propagating inside the medium and can be expressed through the constitutive relations given by

$$\vec{D} = \varepsilon_0 \vec{E} + \vec{P} \quad (1.6)$$

$$\vec{E} = \mu_0 \vec{H} + \vec{M} \quad (1.7)$$

where $\vec{M}$ is the induced magnetic polarisations. $\vec{M} = 0$ in optical fibre since it is a nonmagnetic medium. The above Maxwell's equations can be converted into the wave equation as below that describes light propagation in optical fibre by taking the curl of Eq. (1.2) and using Eqs. (1.3), (1.6), and (1.7).

$$\nabla \times \nabla \times \vec{E} = -\frac{1}{c^2}\frac{\partial^2 \vec{E}}{\partial t^2} - \mu_0 \frac{\partial^2 \vec{P}}{\partial t^2} \quad (1.8)$$

where c is the velocity of light in vacuum and the relation $\mu_0 \varepsilon_0 = 1/c^2$ was used. If only the third-order nonlinear effects governed by $\chi^{(3)}$ are included, then the induced polarisation can be divided into two components as follows [1.14].

$$\vec{P}(\vec{r},t) = \vec{P}_L(\vec{r},t) + \vec{P}_{NL}(\vec{r},t) \quad (1.9)$$

where the linear part $\vec{P}_L$ and the nonlinear part $\vec{P}_{NL}$ are related to the electric field by the general relations [1.14]

$$\vec{P}_L(\vec{r},t) = \varepsilon_0 \int_{-\infty}^{\infty} \chi^{(1)}(t-t') \cdot \vec{E}(\vec{r},t')dt' \quad (1.10)$$

$$\vec{P}_{NL}(\vec{r},t) = \varepsilon_0 \iiint_{-\infty}^{\infty} \chi^{(3)}(t-t_1,t-t_2,t-t_3) \vdots \vec{E}(\vec{r},t_1)\vec{E}(\vec{r},t_2)\vec{E}(\vec{r},t_3)dt_1 dt_2 dt_3 \quad (1.11)$$

These relations are valid in the electric-dipole approximation such that the medium response is local. The wave equation of Eq. (1.8) can be further simplified by using Eq. (1.9) and the relation $\nabla \times \nabla \times \vec{E} = \nabla(\nabla \cdot \vec{E}) - \nabla^2 \vec{E} = -\nabla^2 \vec{E}$ where $\nabla \cdot \vec{D} = \varepsilon \nabla \cdot \vec{E} = 0$ and ε represents the medium dielectric constant. The equation thus can be written in the following form.

$$\nabla^2 \vec{E} - \frac{1}{c^2}\frac{\partial^2 \vec{E}}{\partial t^2} = -\mu_0 \frac{\partial^2 \vec{P}_L}{\partial t^2} - \mu_0 \frac{\partial^2 \vec{P}_{NL}}{\partial t^2} \quad (1.12)$$

1.1.2 Self-Phase Modulation (SPM)

The most common effect of fibre nonlinearity is known as self-phase modulation. The nonlinear effect results from the intensity dependence of the refractive index. The nonlinear refractive index in optical fibre can be expressed as

$$n = n_0 + n_2 I \quad (1.13)$$

where linear refractive index n_0 is ~1.46 and n_2, the Kerr nonlinearity coefficient is ~3 x 10^{-20} m^2/W. I represents the optical intensity of the signal ($I = P_{optical}/A_{eff}$, $P_{optical}$: optical power, A_{eff} : effective mode area). Both n_0 and n_2 are functions of material composition and the waveguide structure of the optical fibre. As the signal peak power increases the refractive index of the fibre core also increases.

The main features of SPM can be theoretically understood during the course of solving the wave equation of Eq. (1.12). In order to solve Eq. (1.12), it is required to make several assumptions. First, $\vec{P}_{NL}$ is treated as a small perturbation to $\vec{P}_L$. Second, the optical field maintains its polarisation along the fibre length. Third, the optical field has a spectral width $\Delta\omega$ such that $\Delta\omega << \omega_0$ where ω_0 is the light frequency in vacuum. In the slowly varying envelope approximation, the electric field can be written in the form

$$\vec{E}(\vec{r},t) = \frac{1}{2}\hat{x}[E(\vec{r},t)\exp(-i\omega_0 t) + c.c.] \quad (1.14)$$

where c.c. stands for complex conjugate, $\hat{x}$ is the polarisation unit vector of the light (assumed to be linearly polarised along the x axis), and the amplitude $E(\vec{r},t)$ is a slowly varying function of time. The nonlinear polarisation component $\vec{P}_{NL}$ can also be expressed in a similar way

$$\vec{P}_L(\vec{r},t) = \frac{1}{2}\hat{x}[P_L(\vec{r},t)\exp(-i\omega_0 t) + c.c.] \quad (1.15)$$

$$\vec{P}_{NL}(\vec{r},t) = \frac{1}{2}\hat{x}[P_{NL}(\vec{r},t)\exp(-i\omega_0 t) + c.c.] \quad (1.16)$$

If the nonlinear response is assumed to be instantaneous, Eqs. (1.10) and (1.11) then reduce to

$$\vec{P}_L(\vec{r},t) = \varepsilon_0 \chi^{(1)} \cdot \vec{E}(\vec{r},t) \quad (1.17)$$

$$\vec{P}_{NL}(\vec{r},t) = \varepsilon_0 \chi^{(3)} \vdots \vec{E}(\vec{r},t)\vec{E}(\vec{r},t)\vec{E}(\vec{r},t) \quad (1.18)$$

The assumption of instantaneous nonlinear response is in effect equivalent to neglecting the contribution of molecular vibrations to $\chi^{(3)}$ (Raman effect).

When Eq. (1.14) is substituted in Eq. (1.18), $\vec{P}_{NL}(\vec{r},t)$ has a term at a frequency of ω_0 and another term at the third-harmonic frequency of $3\omega_0$. Since the latter term is generally negligible due to the difficulty in achieving momentum conservation in such a process, $\vec{P}_{NL}(\vec{r},t)$ can be expressed as follows using Eq. (1.16).

$$P_{NL}(\vec{r},t) = \varepsilon_0 \varepsilon_{NL} E(\vec{r},t) \quad (1.19)$$

where ε_{NL} is the nonlinear part of the dielectric constant defined by

$$\varepsilon_{NL} = \frac{3}{4}\chi^{3}_{xxxx}|E(\vec{r},t)|^2 \quad (1.20)$$

By substituting Eqs. (1.14), (1.15), and (1.16) in Eq. (1.12), the wave equation can be converted into the following form in the frequency domain.

$$\nabla^2 \tilde{E} + \varepsilon(\omega) k_0 \tilde{E} = 0 \quad (1.21)$$

where $k_0 = \omega / c$. The Fourier transform is defined by

$$\tilde{E}(\vec{r},\omega-\omega)=\int_{-\infty}^{\infty}E(\vec{r},t)\exp[i(\omega-\omega_0)t]dt \qquad (1.22)$$

and the frequency dependent dielectric constant is given by

$$\varepsilon(\omega)=1+\tilde{\chi}_{xx}^{(1)}(\omega)+\varepsilon_{NL} \qquad (1.23)$$

The dielectric constant can be used to define the refractive index n and the absorption coefficient α using the definition of $\varepsilon=(n+i\alpha/2k_0)^2$. Since n is found to be intensity dependent because of ε_{NL}, it is customary to introduce

$$n=n_0+n_2|E|^2 \qquad (1.24)$$

Using Eqs. (1.20) and (1.23), the nonlinear refractive index coefficient n_2 can thus be expressed in the form

$$n_2=\frac{3}{8n_0}\mathrm{Re}(\chi_{xxxx}^{(3)}) \qquad (1.25)$$

The temporal phase of a signal pulse propagating through optical fibre thus varies as given by the following equation.

$$\phi^{NL}(t)=\frac{2\pi L_{eff}n_2|E(t)|^2}{\lambda} \qquad (1.26)$$

where λ is the signal wavelength. L_{eff} is the effective length of the optical fibre which is defined by $L_{eff}=\frac{1-\exp(-\alpha L)}{\alpha}$ where L is the actual fibre length. The time dependent phase change experienced by optical signal pulses may alternatively be regarded as a change in the instantaneous frequency of the signal, which is referred to as frequency chirp. The SPM induced spectral broadening is thus a consequence of the time dependence of the induced nonlinear phase changes. The generation of new spectral components if coupled with normal dispersion in the fibre will lead to increased temporal broadening of the pulse. By contrast in the anomalous dispersion regime pulse compression can be achieved, and with the correct conditions, stable pulse forms which propagate without broadening can be generated. These special pulses which have a well-defined pulse shape are called fundamental solitons.

The principle of SPM in optical fibres has been applied within a range of devices such as the nonlinear optical loop mirror [1.7], Mach-Zehnder interferometer [1.15], Kerr nonlinear gate [1.16] etc..

1.1.3 Cross-Phase Modulation (XPM)

When two optical signals propagate inside a fibre they can interact with each other through the fibre Kerr nonlinearity. Each signal experiences SPM and they also influence each other by changing the refractive index experienced by the other signal, resulting in phase modulation of the other signal. This phenomenon is known as cross-phase modulation (XPM). The nonlinear refractive index for each signal of a different frequency with the same polarisation in an optical fibre can thus be expressed as

$$n_i = n_i^L + n_2 I_i + 2 \cdot n_2 I_j \quad \text{(1.27)}$$

$$n_j = n_j^L + n_2 I_j + 2 \cdot n_2 I_i \quad \text{(1.28)}$$

where $n_{i,j}^L$ represent the linear refractive index for each signal and n_2 is the Kerr nonlinearity. $I_{i,j}$ represents the optical intensities of the two signals, respectively. The factor of 2 on the right hand side of Eq. (1.27) and (1.28) shows that XPM is twice as effective as SPM for the same intensity.

In order to better understand the origin of XPM, electromagnetic theory can also be adopted as done in Section 1.1.2. The rapidly varying part of the electric field can be written in the form

$$\vec{E}(\vec{r},t) = \frac{1}{2}\hat{x}[E_1 \exp(-i\omega_1 t) + E_2 \exp(-i\omega_2 t)] + c.c, \quad \text{(1.29)}$$

where $\hat{x}$ is the polarisation unit vector, ω_1 and ω_2 are the centre frequencies of the two pulses. The amplitudes of E_1 and E_2 are assumed to be slowly varying functions of time. By substituting Eq. (1.29) in Eq. (1.18), the nonlinear part of the induced polarisation is found to be

$$\begin{aligned}\vec{P}_{NL}(\vec{r},t) = \frac{1}{2}\hat{x}\{&P_{NL}(\omega_1)\exp(-i\omega_1 t) + P_{NL}(\omega_2)\exp(-i\omega_2 t)\\ &+ P_{NL}(2\omega_1 - \omega_2)\exp[-i(2\omega_1 - \omega_2 t)]\\ &+ P_{NL}(2\omega_2 - \omega_1)\exp[-i(2\omega_2 - \omega_1 t)]\} + c.c.\end{aligned} \quad \text{(1.30)}$$

where

$$P_{NL}(\omega_1) = \chi_{eff}(|E_1|^2 + 2|E_2|^2)E_1 \qquad (1.31)$$

$$P_{NL}(\omega_2) = \chi_{eff}(|E_2|^2 + 2|E_1|^2)E_2 \qquad (1.32)$$

$$P_{NL}(2\omega_1 - \omega_2) = \chi_{eff}E_1^2E_2^* \qquad (1.33)$$

$$P_{NL}(2\omega_2 - \omega_1) = \chi_{eff}E_2^2E_1^* \qquad (1.34)$$

$$\chi_{eff} = \frac{3\varepsilon_0}{4}\chi_{xxxx}^{(3)} \qquad (1.35)$$

The induced nonlinear polarisation of Eq. (1.30) exhibits new frequency components at $2\omega_1 - \omega_2$ and $2\omega_2 - \omega_1$. These new components are generated from the phenomenon of four-wave mixing which is discussed in next Section (Section 1,1.4) and are negligible unless special efforts are made to satisfy the associated phase matching condition (momentum conservation). The remaining two terms contribute to the refractive index. Similar to Eq. (1.19), $P_{NL}(\varpi_j)$ can be written in the form (*j = 1, 2*)

$$P_{NL}(\omega_j) = \varepsilon_0\varepsilon_j^{NL}E_j \qquad (1.36)$$

After combining it with the linear part, the total induced polarisation can be expressed as

$$P(\omega_j) = \varepsilon_0\varepsilon_jE_j \qquad (1.37)$$

If the imaginary part of $\chi^{(3)}$ related to the absorption coefficient is ignored.

$$\varepsilon_j = \varepsilon_j^L + \varepsilon_j^{NL} = (n_j^L + \Delta n_j)^2 \qquad (1.38)$$

where n_j^L is the linear part of the refractive index and Δn_j is the change due to the third-order nonlinear effects. Under the approximation $\Delta n_j << n_j^L$ and the assumption $n_1^L \cong n_2^L = n_0$, the nonlinear part of the refractive index is found to be

$$\Delta n_j \cong \varepsilon_j^{NL} \Big/ 2n_j \cong n_2(|E_j|^2 + 2|E_{3-j}|^2) \quad (1.39)$$

where the nonlinear index coefficient n_2 is

$$n_2 = \frac{3}{8n_0} \mathrm{Re}(\chi_{xxxx}^{(3)}) \quad (1.40)$$

As the signal pulse propagates through the fibre, it obtains an intensity-dependent nonlinear phase given by

$$\phi_j^{NL}(t) = \frac{2\pi L_{eff} n_2}{\lambda} [|E_j|^2 + 2|E_{3-j}|^2] \quad (1.41)$$

The first term accounts for SPM discussed in Section 1.1.2 and the second is responsible for XPM.

The XPM-induced coupling is also observed between optical waves of the same frequency but different polarisation. Interestingly, XPM between the two waves of orthogonal polarisation is less effective than that between two waves of different frequencies as it shows a factor of 2/3 rather than 2 in Eq's (1.27) and (1.28) although the qualitative behaviour is same. The XPM effect in an optical fibre has a range of applications, for example a Kerr shutter based on XPM induced nonlinear birefringence [1.17], wavelength conversion using a dual wavelength nonlinear optical loop mirror [1.2], optical data demultiplexing [1.4], etc..

1.1.4 Four-Wave Mixing (FWM)

Four-wave mixing (FWM) can occur when two or more frequencies of light propagate through an optical fibre. Providing a condition known as phase matching (momentum conservation) is satisfied, light is generated at new frequencies by converting optical power at the original signal wavelengths. The equation that defines the frequency of a FWM product is given by

$$\omega_{ijk} = \omega_i + \omega_j - \omega_k \quad (1.42)$$

The generation of new frequencies from two partially non-degenerate input signals is shown schematically in Fig. 1.1.

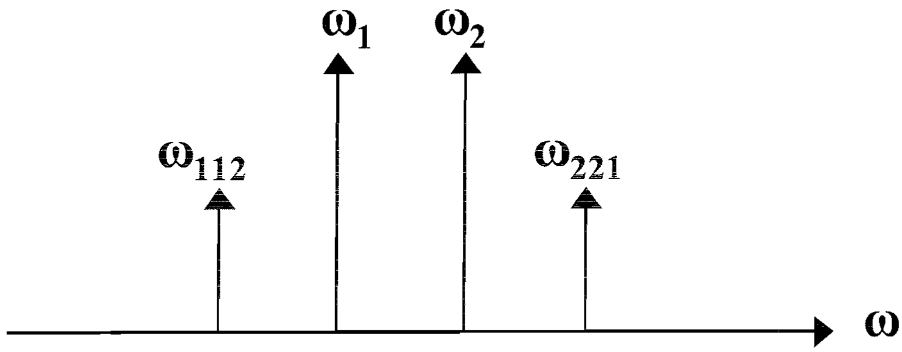

Figure 1.1: Schematic diagram of additional frequency generation through FWM for the partially non-degenerate case.

The main features of four-wave mixing can also be understood by taking into account the third-order polarisation term in Eq. (1.19). Consider four optical waves oscillating at frequencies ω_1, ω_2, ω_3, and ω_4 which are propagating in the same direction z and linearly polarised along the x axis. The total electric field can be written as

$$\vec{E} = \hat{x}\frac{1}{2}\sum_{1}^{4} E_j \exp[i(k_j z - \omega_j t)] + c.c. \quad (1.43)$$

where $k_j = {}^{n_j\omega_j}\!/_{c}$, and n_j is the refractive index. After substituting Eq. (1.43) in Eq. (1.18), $\vec{P}_{NL}$ exhibits the following form.

$$\vec{P}_{NL} = \hat{x}\frac{1}{2}\sum_{1}^{4} P_j \exp[i(k_j z - \omega_j t)] + c.c. \quad (1.44)$$

P_j is found to consist of a large number of terms involving the three products of three electric fields. For example, P_4 can be expressed as

$$P_4 = \frac{3\varepsilon_0}{4}\chi^3_{xxxx}\{[|E_4|^2 + 2(|E_1|^2 + |E_2|^2 + |E_3|^2)]E_4 + 2E_1E_2E_3\exp(i\theta_+) + 2E_1E_2E_3^*\exp(i\theta_-) + \cdots\} \quad (1.45)$$

$$\theta_+ = (k_1 + k_2 + k_3 - k_4)z - (\omega_1 + \omega_2 + \omega_3 - \omega_4)t \quad (1.46)$$

$$\theta_- = (k_1 + k_2 - k_3 - k_4)z - (\omega_1 + \omega_2 - \omega_3 - \omega_4)t \quad (1.47)$$

The term proportional to E_4 in Eq. (1.45) accounts for SPM and XPM effects which are discussed in Section 1.1.2 and 1.1.3, respectively. The remaining terms are responsible for four-wave mixing. The efficiency of the FWM terms depends on the relative phase between E_4 and P_4 which is given by θ_+, θ_-. Efficient FWM requires frequency matching as well as phase matching. Of the two FWM terms in Eq. (1.45) the latter term is more readily used in optical fibre with high efficiency. In this case two photons at frequencies ω_1 and ω_2 are annihilated with the simultaneous creation of two photons at frequencies ω_3 and ω_4.

$$\omega_3 + \omega_4 = \omega_1 + \omega_2 \quad (1.48)$$

The phase matching condition to be achieved can be expressed as

$$\Delta k = k_3 + k_4 - k_1 - k_2 = {}^{(n_3\omega_3 + n_4\omega_4 - n_1\omega_1 - n_2\omega_2)}\!/_{c} = 0 \quad (1.49)$$

In the particular case of $\omega_1 = \omega_2$ (degenerate case), it is relatively easy to satisfy $\Delta k = 0$

The generation of new optical components through four-wave mixing has serious negative implications within wavelength division multiplexed (WDM) transmission systems, however it can be used to obtain data demultiplexing [1.18], wavelength conversion [1.19], dispersion compensation in long-haul optical fibre links [1.20], and the like.

1.1.5 Stimulated Raman Scattering (SRS)

As well as the electronic response of a nonlinear optical medium to intense optical fields, another sort of nonlinearity related to the interaction between the optical photons and phonons (vibrational state) is also important in optical systems. Since these inelastic nonlinear effects can be regarded as the scattering of a pump beam off a phonon, with the resultant transfer of energy into a lower energy beam, they are called scattering phenomena. First of all, spontaneous scattering transfers a small portion of the input beam power (typically $\sim 10^{-6}$) to another optical beam at a frequency down shifted by an amount determined by the optical phonon vibrational modes of the medium. This phenomenon is called the Raman effect. The incident beam behaves as a pump for generating frequency downshifted light (referred to as the Stokes wave). The spontaneous scattering process is typically a rather weak process which can occur as the result of the medium optical property fluctuations (typically in the dielectric constant) excited mainly by thermal effects. However, when the intensity of the incident beam is large enough to modify the optical properties of the medium, highly efficient light scattering, so called stimulated scattering occurs.

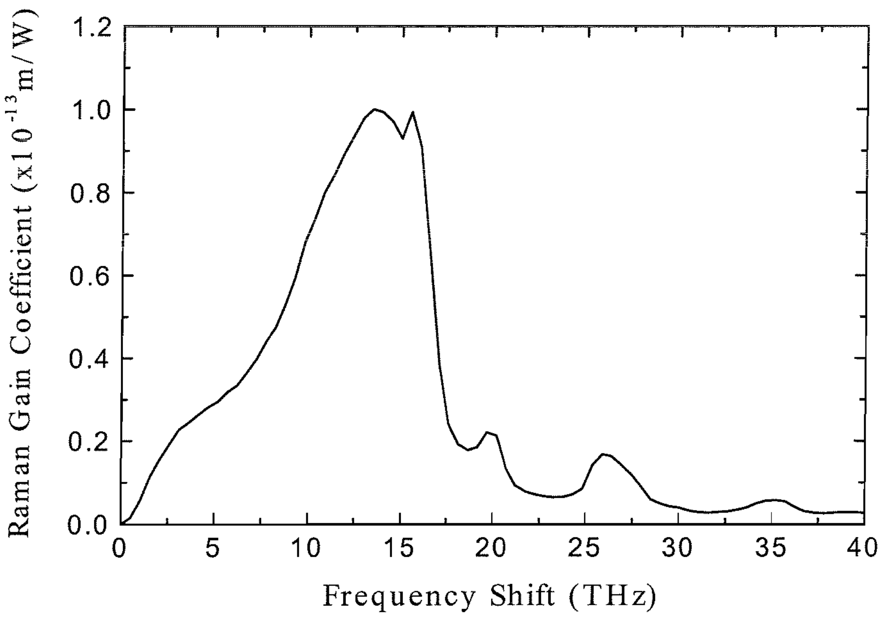

Figure 1.2: The Raman gain spectrum for silica (after Ref. [1.21]).

Stimulated Raman scattering (SRS) is a very strong scattering process and ten percent or more of the energy of the incident beam is often converted into the Stokes wave. Another difference between spontaneous and stimulated Raman scattering is that the spontaneous process leads to nearly isotropic emission, whilst the stimulated process leads to emission in the forward and backward directions.

The evolution of the Stokes wave in optical fibre under CW or quasi-CW conditions, can be expressed as

$$\frac{dI_s}{dz} = g_R I_p I_s \qquad (1.50)$$

where I_s is the Stokes intensity, I_p is the pump intensity, and g_R is the Raman gain coefficient. Measurements of the Raman gain coefficient g_R for silica fibres were reported in Ref [1.22]. The Raman gain coefficient g_R depends on the material composition of the fibre core, the waveguide structure, and the pump wavelength.

Fig. 1.2 shows the Raman gain coefficient g_R for fused silica as a function of frequency shift at a pump wavelength of 1 μm, extending from zero frequency shift up to 40 THz. The peak gain is observed at a frequency shift of 13 THz from the pump and the gain has a bandwidth of 10 THz.

To find the Raman threshold in optical fibre, the interaction between the pump and Stokes waves should be considered. In the CW case this interaction is governed by the following set of two coupled equations,

$$\frac{dI_s}{dz} = g_R I_p I_s - \alpha_s I_s \qquad (1.51)$$

$$\frac{dI_p}{dz} = -\frac{\omega_p}{\omega_s} g_R I_p I_s - \alpha_p I_p \qquad (1.52)$$

where α_s and α_p represents the fibre loss at the Stokes and pump wavelengths. Assuming pump depletion is negligible, Eq. (1.52) can be readily solved. If the solution is substituted in Eq. (1.51), the following equation is obtained.

$$\frac{dI_s}{dz} = g_R I_0 \exp(-\alpha_p z) I_s - \alpha_s I_s \quad (1.53)$$

where I_0 is the incident pup intensity at $z = 0$. The solution of Eq. (1.53) is expressed as

$$I_s(L) = I_s(0)\exp(g_R I_0 L_{eff} - \alpha_s L) \quad (1.54)$$

$$L_{eff} = \frac{1-\exp(-\alpha_p L)}{\alpha_p} \quad (1.55)$$

In order to calculate the Stokes power, an integration over the whole range of the Raman-gain bandwidth should be performed considering each frequency component of energy $\hbar\omega$.

$$P_s(L) = \int_{-\infty}^{\infty} \hbar\omega \exp[g_R(\omega) I_0 L_{eff} - \alpha_s L] d\omega \quad (1.56)$$

where the fibre is assumed to support a single transverse mode. Using the fact that the main contribution to the integral comes from a narrow region near the gain peak at $\omega = \omega_s$ (see Fig 1.2), the integral of Eq. (1.54) can be evaluated and the result is

$$P_s(L) = P_{s0}^{eff} \exp[g_R(\omega_s) I_0 L_{eff} - \alpha_s L] \quad (1.57)$$

$$P_{s0}^{eff} = \hbar\omega B_{eff} \quad (1.58)$$

$$B_{eff} = \left(\frac{2\pi}{\left|g_R^{"}(\omega_s)\right| I_0 L_{eff}} \right)^{1/2}, \quad g_R^{"}(\omega_s) = \left(\frac{\partial^2 g_R}{\partial \omega^2} \right)_{\omega=\omega_s} \quad (1.59)$$

Physically B_{eff} is the effective bandwidth of the Stokes radiation at the gain peak at $\omega = \omega_s$. The Raman threshold is defined as the input pump power which generates the same amount of Stokes power as residual pump power at the fibre output.

$$P_s(L) = P_p(L) = P_0 \exp(-\alpha_p L) \quad (1.60)$$

where $P_0 = I_0 A_{eff}$. P_0 and A_{eff} are the input pump power and the effective mode area, respectively. Assuming $\alpha_p = \alpha_s$, the threshold condition becomes

$$P_{s0}^{eff} \exp\left(g_R P_0 L_{eff} / A_{eff} \right) = P_0 \quad (1.61)$$

The solution of Eq. (1.61) gives the critical pump power to reach the Raman threshold but is not straightforward to obtain since P_{s0}^{eff} is also a function of P_0. Under the assumption of a Lorentzian Raman-gain spectrum, the critical pump power can be expressed as following [1.23].

$$g_R P_0^{cr} L_{eff} / A_{eff} \cong 16 \quad (1.62)$$

For SRS in the backward direction, the threshold condition is still the same as Eq. (1.62) but with the number of 16 replaced by 20. A reasonable prediction of the Raman threshold can be obtained by using Eq. (1.62) although the various approximations are made in the derivation of it. For example, if we use the typical values for fibres used in 1.55 µm communication systems, $A_{eff} = 50\mu m^2$ and $L_{eff} \cong 20km$, the predicted Raman threshold is $P_0^{cr} \cong 600mW$. SRS is not likely to occur in single-channel optical communication systems since the optical power into the fibre is much below the critical value.

The important applications of the SRS phenomenon in optical fibres include Raman fibre lasers [1.24] and broadband Raman amplifiers [1.8]. In particular fibre based Raman amplifiers have attracted huge research attention for ultra-broadband WDM systems applications nowadays since the amplification band can be applied anywhere of the fibre transparency window by simply changing the pump wavelength.

1.1.6 Stimulated Brillouin Scattering (SBS)

Stimulated Brillouin scattering is similar to SRS since it also generates a Stokes wave downshifted from the frequency of the incident pump beam. However, the main features of SBS are different from those of SRS. For example, the Stokes wave of SBS propagates only in the backward direction in contrast with SRS that occurs in both directions. SBS has a very narrow gain bandwidth of around 10~50 MHz at the frequency shift of ~10 GHz from the pump, which is much smaller than that of SRS. The threshold pump power for SBS depends on the spectral bandwidth of the pump light. Basically SBS is associated with scattering from acoustic phonons whilst optical phonons participate in SRS. The phase matching condition for the SBS process is thus much more stringent due to the nature of the acoustic phonon energy momentum relationship, as compared to the SRS process. Acoustic waves generated through the process of electrostriction by a pump wave cause a periodic modulation of the refractive index in an optical fibre. The index grating scatters the pump wave through Bragg diffraction and the scattered light thus propagates backward relative to the pump wave at a down-shifted frequency due to the Doppler shift associated with the motion of the grating which moves at the acoustic velocity

For the case of scattering at an angle θ, the Stokes scattering can be illustrated as the diagram in Fig. 1.3. The frequencies and the wave vectors of the related three wave components can thus be expressed by

$$\Omega = \omega_p - \omega_s \qquad (1.63)$$

$$\vec{q} = \vec{k}_p - \vec{k}_s \qquad (1.64)$$

where Ω, ω_p and ω_s are the frequencies, and $\vec{q}$, $\vec{k}_p$ and $\vec{k}_s$ are the wave vectors of the acoustic, pump and Stokes waves, respectively. Since $|\vec{k}_p|$ is almost equal to $|\vec{k}_s|$ (because Ω is much smaller than ω_p), the frequency Ω and the wave vector $\vec{q}$ of the acoustic wave satisfy the dispersion relation

$$\Omega = |\vec{q}| v_A = 2 v_A |\vec{k}_p| \sin(\theta/2) \qquad (1.65)$$

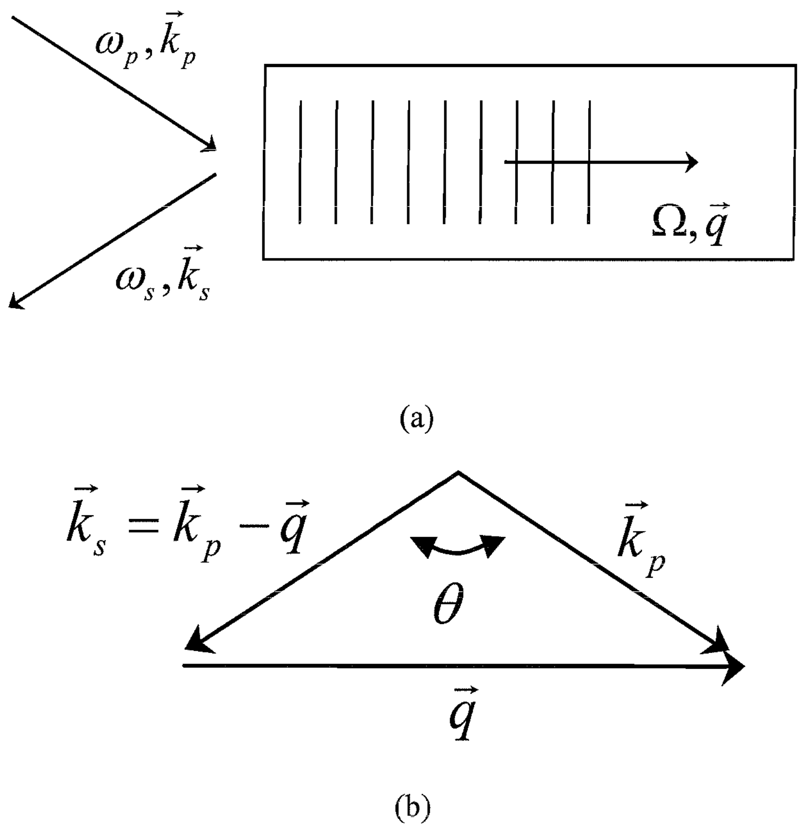

Figure 1.3: Illustration of the Stokes scattering based on Brillouin effect.

Eq. (1.65) shows that the frequency shift of the Stokes wave depends on the scattering angle. Note that the Stokes shift Ω is equal to zero for forward scattering and is maximum for backscattering ($\theta = \pi$). Eq. (1.65) predicts that the Brillouin scattering in optical fibre should thus occur only in the backward direction although small amount of spontaneous or thermal Brillouin scattering can occur in the forward direction due to the guide nature of acoustic waves [1.25]. The Brillouin frequency shift in the backward direction can be expressed as

$$\nu_B = \frac{\omega_A}{2\pi} = \frac{2n\nu_A}{\lambda_p} \quad (1.66)$$

where n and λ_p are the refractive index and the pump wavelength, respectively.

In contrast to the case of SRS, the spectral width $\Delta\nu_B$ of the Brillouin gain spectrum is very small (~10 MHz). The spectral bandwidth is associated with the damping time of acoustic waves, that is the phonon lifetime T_B. Assuming that an acoustic wave decays as $\exp\left(-t/T_B\right)$, the Brillouin gain coefficient will exhibit a Lorentzian spectral profile as follows.

$$g_B(\nu) = \frac{\left(\Delta\nu_B/2\right)^2}{(\nu-\nu_B)^2 + \left(\Delta\nu_B/2\right)^2} g_B(\nu_B) \quad \text{.......(1.67)}$$

where $\Delta\nu_B$ is 3dB spectral bandwidth and can be expressed as $\Delta\nu_B = 1/\pi T_B$. The peak value of the Brillouin gain coefficient at $\nu = \nu_B$ is given by [1.26]

$$g_B(\nu_B) = \frac{2\pi n^7 p_{12}^2}{c\lambda_p \rho_0 v_A \Delta\nu_B} \quad \text{.......(1.68)}$$

where p_{12} is the longitudinal electro-optic coefficient, ρ_0 is the material density, and λ_p is the pump wavelength.

In order to find the SBS threshold, the mutual interaction between the pump and Stokes waves governed by the coupled-intensity equations similar to Eqs. (1.51) and (1.52) needs to be considered. However as opposed to the SRS case, the sign of dI_s/dz should be changed to account for the counter-propagating nature of the Stokes wave relative to the pump wave. Note that the fibre loss is nearly same for the pump and Stokes waves, i.e. $\alpha_p \cong \alpha_s = \alpha$ due to the relatively small value of the Brillouin shift, $\omega_p \cong \omega_s$. Assuming the pump and Stokes waves are linearly polarised along the same direction and maintain their polarisation along the fibre, the coupled equations can be expressed as

$$\frac{dI_s}{dz} = -g_B I_p I_s + \alpha I_s \qquad (1.69)$$

$$\frac{dI_p}{dz} = -g_B I_p I_s - \alpha I_p \qquad (1.70)$$

If pump depletion is neglected, the Stokes intensity is found to be given by

$$I_s(0) = I_s(L)\exp\left({g_B P_0 L_{eff}} \big/ {A_{eff}} - \alpha L \right) \qquad (1.71)$$

With a similar approach to that of Section 1.1.5, the Brillouin threshold, to a good approximation, is given by [1.23]

$$g_B P_0^{cr} L_{eff} \big/ A_{eff} \cong 21 \qquad (1.72)$$

The numerical factor 21 is only approximate as it is a function of the Brillouin gain linewidth. It can also change by a factor between 1 and 2 depending on the polarisation status of pump and Stokes waves. Eq. (1.72) is nonetheless is useful for estimating the Brillouin threshold. For conventional, structurally uniform optical fibres used in 1.55μm optical communication systems, $A_{eff} = 50\mu m^2$, $L_{eff} \cong 20km$, and $g_B \cong 5\times10^{-11} m/W$, Eq. (1.72) predicts a critical pump power $P_0^{cr} \cong 1mW$. Such a low Brillouin threshold makes SBS a dominant nonlinear process in optical fibres.

SBS is unlikely to find applications for signal amplification in telecommunication systems because of its narrow gain bandwidth. However, SBS based fibre lasers have been successfully demonstrated [1.27].

1.1.7 The Nonlinear Properties of Semiconductor Optical Amplifiers (SOA's)

The use of semiconductor optical amplifiers as a nonlinear medium for optical signal processing devices is of great interest. SOA's have been successfully used to implement various nonlinear device functions, including wavelength conversion [1.28], and data demultiplexing [1.29, 1.30]. Since the microscale long active device has nonlinear properties comparable to those of several km's of conventional optical fibre, it is particularly attractive for integration with other photonic components. The useful nonlinear processes associated with SOA's are (i) Cross-Gain modulation (XGM) [1.31], (ii) Cross-phase modulation (XPM) [1.32], and (iii) four-wave mixing (FWM) [1.3], each of which is discussed below.

A. Cross-Gain Modulation (XGM)

The signal gain in a SOA saturates as the optical power level inside the SOA increases. The amplifier gain experienced by one signal can thus be modulated using a second signal.

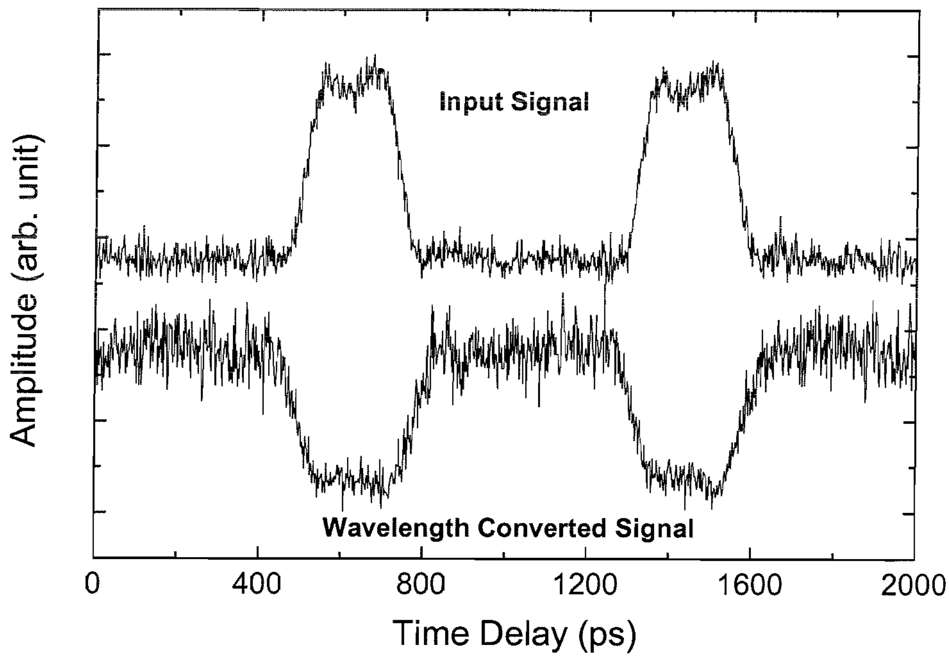

Figure 1.4: Measured waveforms for the input signal and wavelength converted signal through a commercially available SOA at 10 Gbit/s; Input signal wavelength: 1545 nm, probe CW signal wavelength: 1551 nm.

Such a phenomenon can be readily applied to wavelength conversion, in which a weak CW signal at the desired output wavelength can be modulated by a gain variation that follows the temporal pattern of a strong saturating input signal at a second wavelength. Fig. 1.4 shows experimentally measured waveforms of both input- and wavelength converted-signals at 10 Gbit/s. The wavelength-converted signal has an inverted pattern relative to the input signal and has a relatively poor extinction ratio as compared to the input signal. However, XGM is a simple and polarisation independent method. Error-free wavelength conversion at rates up to 100 Gbit/s has been reported [1.31].

B. Cross-Phase Modulation (XPM)

Optical signals travelling through a SOA experience a relatively large phase modulation due to a mechanism similar to SPM and XPM in an optical fibre. The XPM effect is used in interferometric switches such as Mach-Zehnder interferometers and Sagnac interferometers to perform functions such as wavelength conversion [1.32], data demultiplexing [1.33], and the like.

C. Four-Wave Mixing (FWM)

FWM is a more complex mechanism relative to XGM and XPM in a SOA due to its strong dependence on the state of the light polarisation and optical phase.

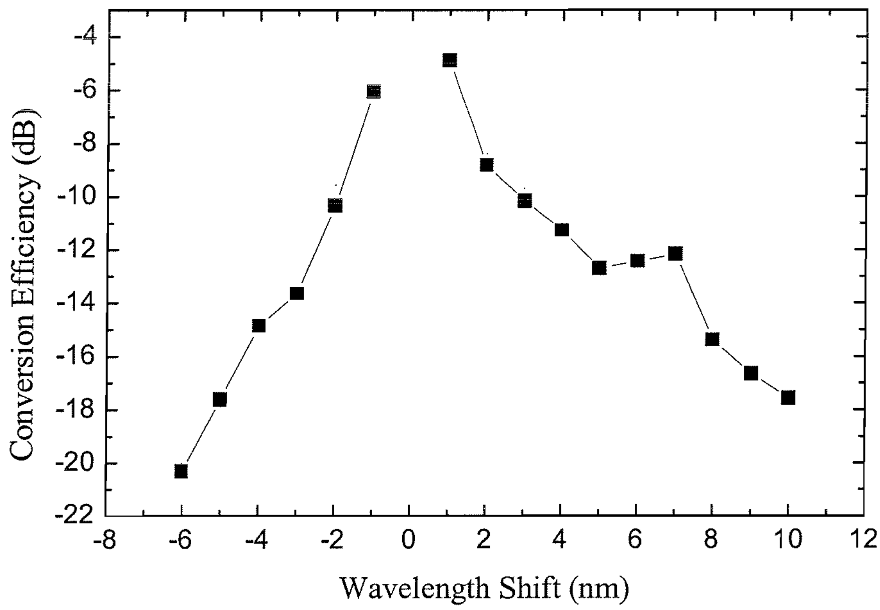

Figure 1.5: Measured efficiency of wavelength conversion as a function of wavelength detuning; Pump power: 3 mW, input signal power: 0.1 mW.

However, the unique advantage of being transparent to the modulation format, as well as the bit rate, enables us to find a greater number of applications in the high-speed communication systems. The main applications are to be found in wavelength conversion [1.34] and data demultiplexing [1.29]. In general the conversion efficiencies that can be achieved are somewhat low and frequently the conversion efficiency is a strong function of wavelength as shown in Fig. 1.5, however recently techniques have been developed to avoid these problems [1.35].

1.2 Superstructured Fibre Bragg Grating (SSFBG) Technology

Superstructured fibre Bragg Grating (SSFBG) fabrication technology is now well established and is finding many applications in optical communication systems. A SSFBG can be defined as a standard fibre grating, i.e. a grating with a rapidly varying refractive index modulation of uniform amplitude and pitch, onto which a slowly varying refractive index modulation has been applied along its length. It can be readily proven that the impulse response of a weakly reflecting SSFBG (reflectivity less than ~ 20 %) follows precisely the same form as the slowly varying, superstructure refractive index profile [1.36, 1.37]. SSFBG's can thus be designed and fabricated with a wide range of complex tailored impulse response functions with precise amplitude and phase characteristics. SSFBG's should find application within a variety of optical pulse processing systems [1.38, 1.39, 1.40], including use within both direct sequence - optical code division multiple access (DS-OCDMA) code generation and recognition devices, and all-optical pulse shaping devices for which precise control of the amplitude and phase of the temporal pulse profile is essential. SSFBG technology represents an attractive means to produce compact, and potentially low-cost components for such applications

This Section is organised as follows. In Section 1.2.1 a theoretical background of SSFBG based pulse shaping is presented. Section 1.2.2 describes the fabrication process for SSFBG's.

1.2.1 Theoretical Background of SSFBG

In the weak SSFBG grating limit, where the grating strength is such that light penetrates the full grating length and the individual elements of the grating contribute more or less equally to the reflected response, the wave vector response *F(κ)* can be shown to be given simply by the Fourier transform of the spatial superstructure refractive index modulation profile *A(x)* used to write the grating [1.36] i.e.

$$F(\kappa) = \frac{1}{2\pi} \int_{-\infty}^{+\infty} A(x) e^{j\kappa x} dx \quad (1.73)$$

The underlying uniform rapid refractive index modulation simply defines the central frequency/wavelength of the grating's reflection band. Similarly, the impulse response of a fibre grating *h(t)* is given by the inverse Fourier transform of its frequency response *H(ω)*

$$h(t) = \int_{-\infty}^{+\infty} H(\omega) e^{-j\omega t} d\omega \quad (1.74)$$

From the above equations, and the fact that κ the wave vector is proportional to the optical frequency ω , it is clear that the impulse response of a weak grating has a temporal profile given by the complex form of the refractive index superstructure modulation profile of the grating. For example, in the instance that the grating superstructure is simply amplitude modulated, i.e. the grating phase is uniform, the impulse response follows precisely the amplitude modulation profile used to write the grating [1.41]. (The scaling factor $t = 2nx/c$ is used to convert from the spatial to temporal domain where n is the refractive index and c is the speed of light).

Fig. 1.6 shows the basic principle of SSFBG based pulse synthesis. When a short but finite bandwidth pulse, (i.e. not an impulse pulse) is reflected from a SSFBG it is transformed into a pulse with a temporal shape given by the convolution between the input pulse and the impulse response of the grating i.e. [1.39]

$$y(t) = x(t) * h(t) \quad (1.75)$$

The process is described in the frequency domain by the product of the Fourier transform of the incident signal $X(\omega)$ with the frequency response of the grating $H(\omega)$.

$$Y(\omega) = X(\omega) \cdot H(\omega) \quad (1.76)$$

Thus it can be appreciated that for well-specified input and target output pulse forms, one can design and fabricate an SSFBG to perform the required shaping operation (subject to the usual laws of causality and the limits of SSFBG fabrication technology). SSFBG's are attractive for many pulse-shaping applications since they offer the advantages associated with fibre components, for example easy integration into fibre base systems and low coupling losses. Furthermore they are potentially low-cost devices.

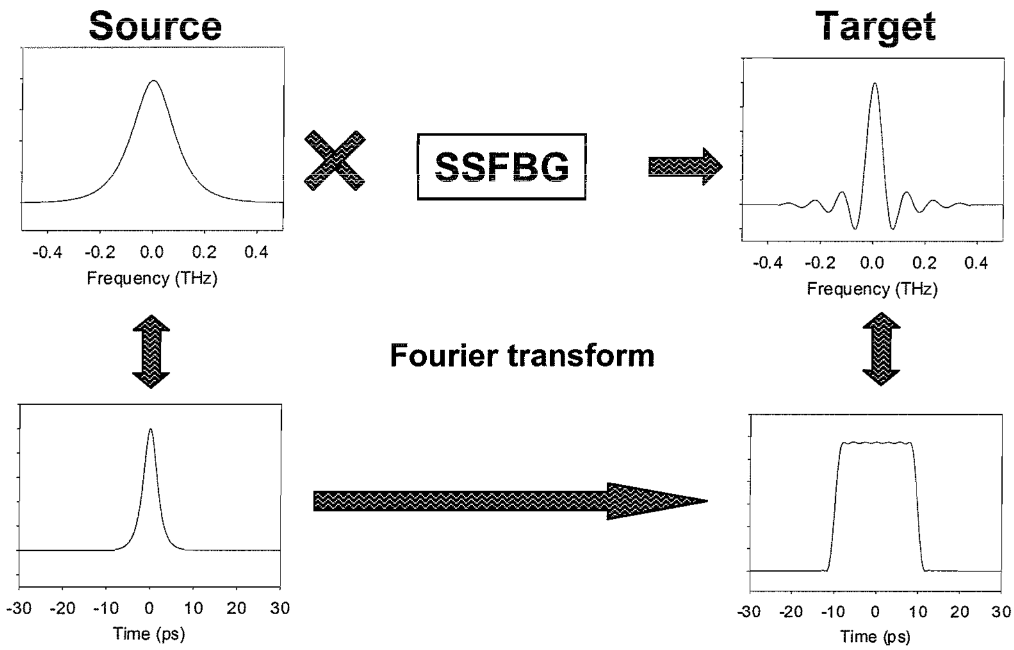

Figure 1.6: Principle of SSFBG based pulse synthesis as applied to rectangular pulse generation.

1.2.2 SSFBG Fabrication

The continuous grating writing technique, developed at the University of Southampton effectively writes gratings on a grating plane by grating plane basis and allows for the fabrication of gratings with truly complex refractive index profiles [1.41]. This technique uses a simple phase mask with uniform pitch and relies upon precise control of the positioning of the fibre relative to the phase mask and controlled exposure to the index modifying UV light used to write the grating. A single-phase mask can thus be used to write a wide range of complex grating structures. This is to be contrasted with traditional grating fabrication techniques where the induced refractive index pattern is written into the phase mask itself, and simply imprinted into the fibre [1.42]. The conventional approach limits both the quality and the length of the gratings that can be written to those that can be achieved for current phase-mask production itself, which is considerably inferior to what can be achieved using the superstructured fibre Bragg grating writing technique. The practical benefits of this SSFBG approach regarding flexibility, manufacturability and grating quality should be self-evident.

Figure 1.7 shows the continuous grating writing apparatus. The laser used is a continuous wave (CW) laser producing ultraviolet (UV) beam with a power of up to 100mW at a lasing wavelength of 244nm. It delivers a UV-beam to a photosensitive fibre through a phase mask (via a mirror and an acousto-optic modulator (AOM)). The photosensitive fibre is mounted on a translation stage, which is used to move the fibre relative to the phase mask under computer control. The control is implemented through a decision logic unit and an interferometer that is used to provide position measurements from the moving part of the translation stage.

By placing the photosensitive fibre in the interference pattern consisting of regions of high and low UV intensity generated by the phase mask, a grating will be formed with a period given by the periodicity of the interference pattern. The fibre-waveguide is then translated continuously at a constant velocity along the axis perpendicular to the interference fringes with sub-nanometre precision provided by an interferometer. To avoid obliterating the grating structure, the writing beam (interference pattern) is digitally modulated on and off at least once within one grating period using the AOM. The on/off position determines the phase-coherence between adjacent grating periods. The actual on/off positions are determined by feedback from the interferometer.

Therefore, this technique allows for very the accurate positioning of phase-shifts and the magnitude of the phase-shifts between adjacent chips in the grating can be accurately defined. The precision with which each grating plane is written is sub-nanometre. Furthermore, the length of the grating formed is no longer limited by the length of the phase-mask but by the length of the translation equipment holding the fibre. This allows for fabrication of fibre Bragg gratings up to 1000 mm in length.

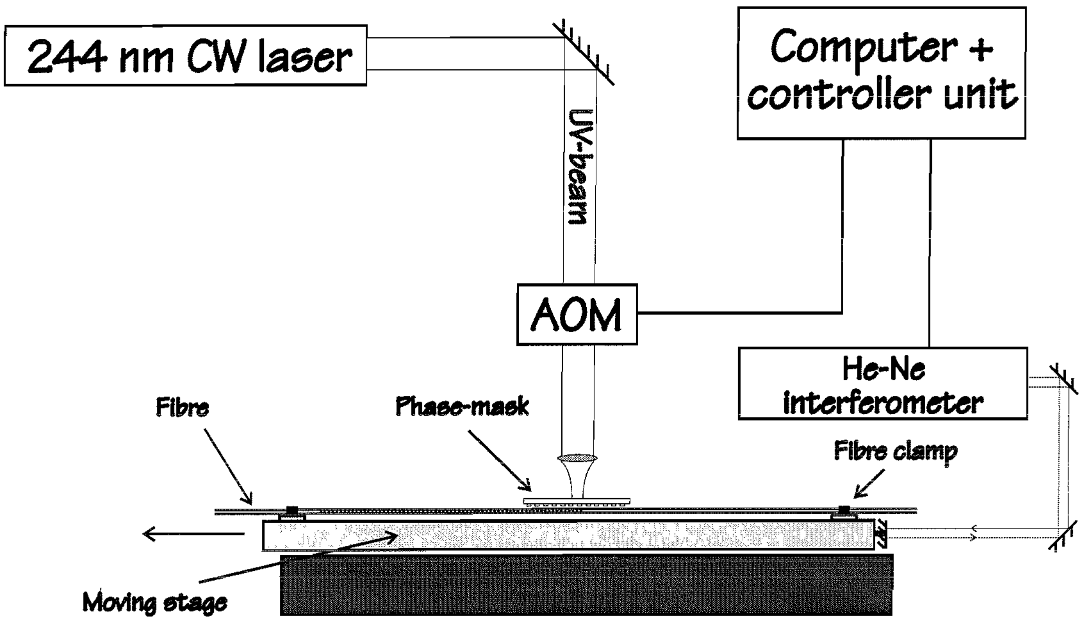

Figure 1.7: Continuous grating writing setup.

By exposing the photosensitive fibre on a plane-by-plane basis, the UV exposure on the fibre occurs always under the same part of the phase mask, while any amplitude or phase modulation are imposed by reducing the incident UV flux or dephasing the fibre relative to the phase mask [1.43]. Thus, any errors introduced during the writing process, or imperfections in the phase mask, are averaged out since the fibre is exposed to different parts of the phase mask many times during the writing process.

1.3 Holey Fibre Technology

The area of Holey Fibre (HF) technology has progressed rapidly in recent years and has resulted in the development of a wide range of optical fibres with unique and highly useful optical properties [1.44, 1.45]. Holey fibres (HF's) are a class of microstructured fibre which possess a solid core surrounded by a cladding region that is defined by a fine array of air holes that extend along the full fibre length. Fig. 1.8 shows an idealised HF structure. HF's are typically made of a single material, usually pure silica, and guide light through a modified form of total internal reflection since the volume average index in the core region of the fibre is greater than that of the surrounding microstructured cladding. Note that the hole diameter (d) and pitch (Λ=hole to hole spacing) which are the critical design parameters used to specify the structure of an HF are typically on the scale of the wavelength of light. Fig. 1.9 shows scanning electron microscope (SEM) images of various HF's fabricated at the University of Southampton

The fundamental physical differences between HF's and conventional fibre types arise from the way that the guided mode experiences the cladding region. In a conventional fibre, this is largely independent of wavelength to first-order. However, in a HF, the large index contrast between glass and air and the small structure dimensions combine to make the effective cladding index a strong function of wavelength. Short wavelengths remain tightly confined to the core, and so the effective cladding index is only slightly lower than the core index. However, at longer wavelengths, the mode samples more of the cladding, and so the effective index contrast is larger. This unusual wavelength dependence leads to a host of unique and tailorable optical properties. One striking property is that fibres with a low air fill fraction ($d/\Lambda < 0.4$) can be single-moded regardless of operating wavelength [1.46]. This property is particularly significant for broadband or short wavelength applications. Tailoring the scale of the cladding features allows the effective fundamental mode area of a holey fibre at 1.55μm to be varied over three orders of magnitude from ~ 1 μm^2 to >1000 μm^2 [1.45]. HF's can thus be seen to have a significantly broader range of optical properties than conventional optical fibres, which as well as being of fundamental scientific interest, should also open up the possibility for new and technologically important fibre devices.

This Section is organised as follows. In Section 1.3.1 the HF fabrication process is described. Section 1.3.2 provides a qualitative explanation of a broadband single mode operation in HF. Dispersion properties and nonlinear properties of HF are briefly discussed in Section 1.3.3 and 1.3.4, respectively.

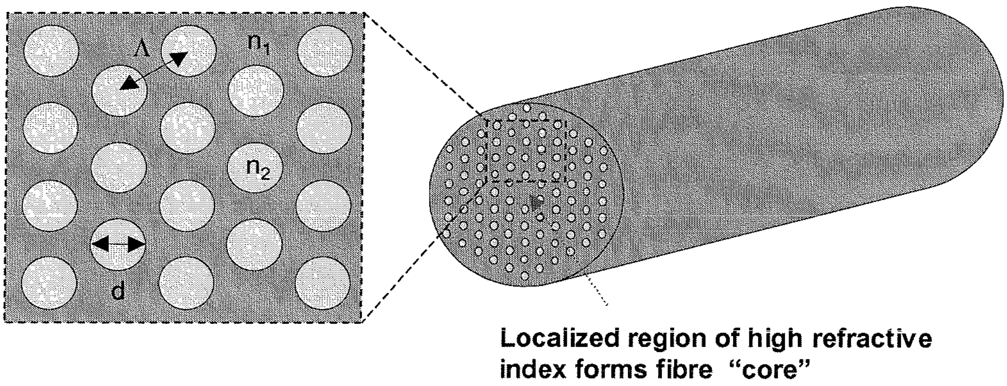

Figure 1.8: An idealised structure of HF.

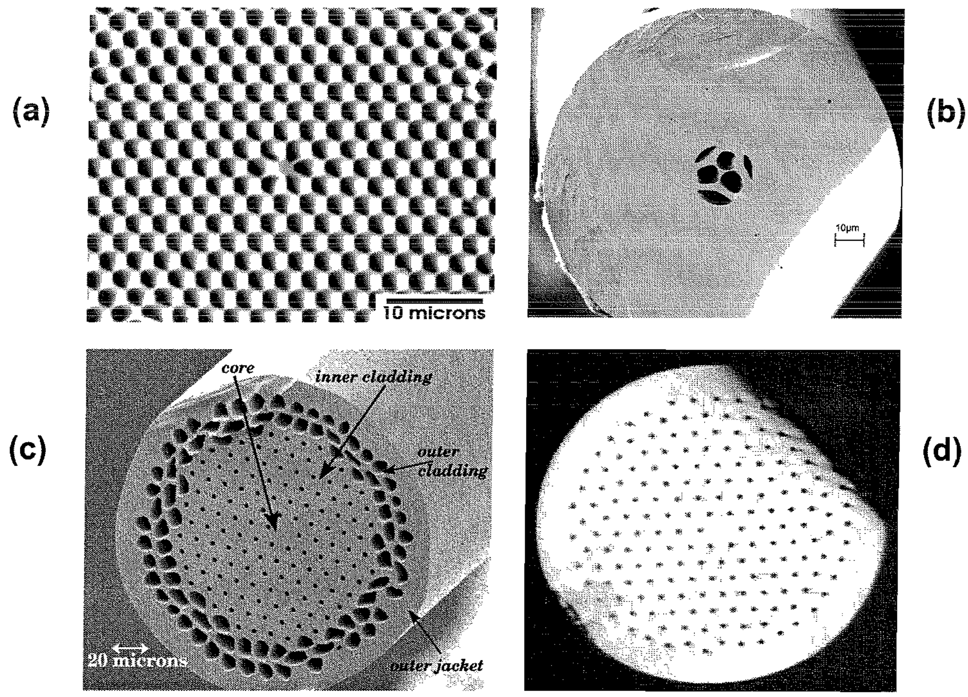

Figure 1.9: SEMs of various HF's fabricated at University of Southampton: (a) small effective area silica HF, (b) high nonlinearity HF in Schott SF57 glass, (c) Yb^{3+} doped, air-clad, LMA HF, (d) LMA-HF.

1.3.1 Fabrication of HF

HF's are typically fabricated by stacking an array of capillaries in a hexagonal configuration around a solid rod, which defines a core. This resulting stack, the so called preform, is then drawn down to fibre dimensions using a conventional fibre drawing tower. By controlling the conditions under which the fibre is drawn, a range of HF's with different optical properties can be produced from a single preform. Fig. 1.10 shows a simplified procedure for HF fabrication.

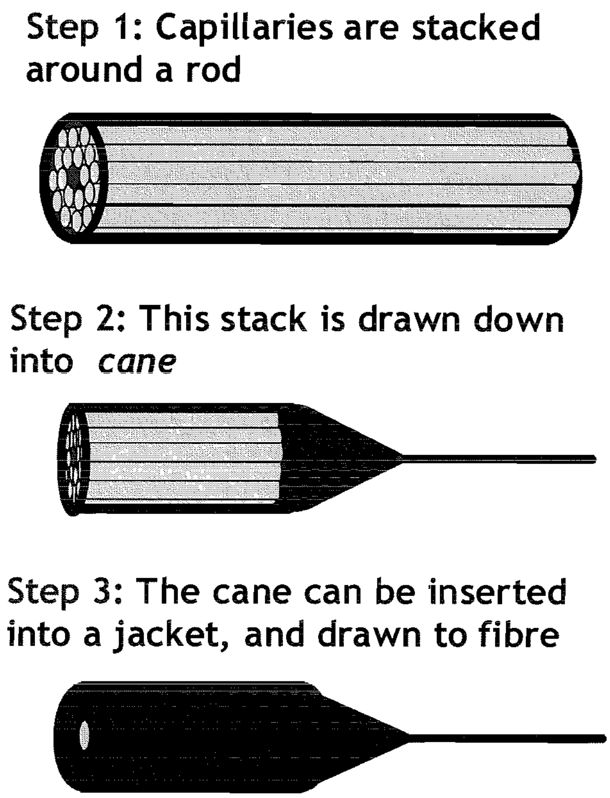

Figure 1.10: A simplified procedure of HF fabrication.

Recently the University of Southampton demonstrated a new and simple HF preform fabrication technique, which uses extrusion of glasses with lower softening temperatures (~600 °C for SF57 versus ~2000 °C for silica) through a die rather than stacking capillaries [1.47].

1.3.2 Single Mode Operation and Dispersion Properties of HF

HF's can have a single mode operation over a broad wavelength bandwidth. The wide single-mode operation of HF with a low air fill fraction ($d/\Lambda < 0.4$) can be understood qualitatively as following. In a standard step-index fibre the number of guided modes is determined by the normalized frequency, or V value [1.48].

$$V = 2\pi/\lambda \cdot \rho \cdot \sqrt{(n_{co}^2 - n_{cl}^2)} \quad (1.77)$$

where n_{co} and n_{cl} represent core and cladding indices, respectively. ρ is core radius. The V value should be less than 2.405 for single mode operation in fibre, which means most standard single mode fibres are multi-mode at short wavelengths For example, SMF28 has a single mode cut-off wavelength of ~ 1.2 μm. In HF the light field confines itself in the silica core area rather than distributing itself across the air cladding at shorter wavelengths. Thus, the corresponding effective cladding index increases at the shorter wavelengths, keeping the V value nearly constant and extending the single-mode bandwidth. A more detailed, quantified study of endless single-mode operation of HF's can be found in Ref. [1.46].

The unusual wavelength dependence of the effective refractive index in HF also leads to a range of novel dispersion properties and which are relevant for both linear and nonlinear device applications [1.49]. For example, silica fibres with a small pitch (Λ<2 μm) and large air holes ($d/\Lambda > 0.5$) can exhibit anomalous dispersion down to wavelength as low as 550 nm [1.50]. This has made the generation and propagation of optical solitons in the near-IR and visible regions of the spectrum a reality [1.51, 1.52] and is something not possible in conventional single mode fibres. Fig. 1.11 shows the GVD of a HF as a function of wavelength for a range of different hole sizes when the hole spacing is fixed [1.45].

It is also possible to design HF's with extremely high values of normal dispersion [1.53] and for example values as high as -2000 ps/nm-km have been predicted, which suggests that these fibres may find application in dispersion compensation. Other work has shown that broadband dispersion-flattened holey fibres can also be designed [1.50], a property that is likely to be useful for the development of broadband WDM devices.

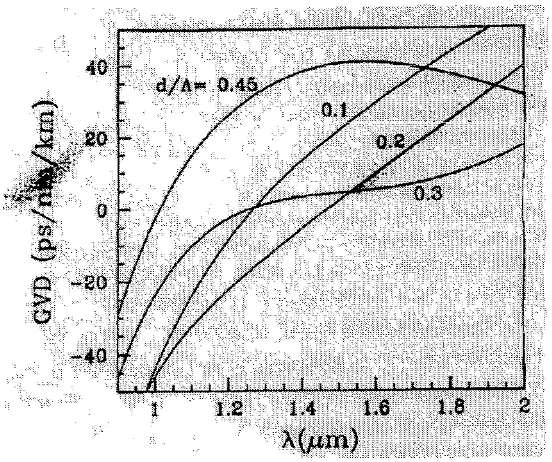

(a)

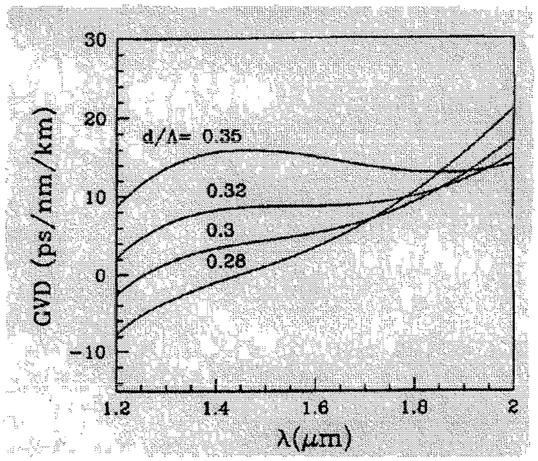

(b)

Figure 1.11: (a) GVD for holey fibres with d/Λ = 0.1, 0.2, 0.3, and 0.45 for Λ = 2.3 μm. Both waveguide and material dispersion have been included. (b) GVD for holey fibres with d/Λ = 0.28, 0.3, 0.32, and 0.35 in order of increasing GVD at a wavelength of 1.4 μm for Λ = 2.3 μm. Both waveguide and material dispersion have been included (after Ref. [1.45]).

1.3.3 Nonlinearity of HF

Arguably, the most exciting possibility afforded by HF technology is the opportunity to develop fibres with a very high optical nonlinearity per unit length [1.55, 1.56]. Holey fibres with small-scale features (small Λ) and a large air-filling fraction (large d/Λ) can confine the guided mode tightly within the core, resulting in extremely small mode areas (see Fig. 1.9(a)). In such a fibre, modest optical powers can induce significant nonlinear effects. The state-of-the-art HF technology allows the fabrication of fibres with very tightly confined modes, and thus very high optical nonlinearities per unit length. Indeed, a silica holey fibre can have a nonlinearity 10 ~ 100 times higher than that of a conventional silica fibre. Nonlinear devices based on HF can thus in principle be 10 ~100 times shorter than similar devices based on conventional fibre technology, offering a route to the development of truly practical, ultrafast fibre based nonlinear devices [1.57, 1.16].

Note that further significant increases in fibre nonlinearity should be achievable using fibres made of other glasses, such as the Chalcogenides [1.58], which have around two orders of magnitude higher nonlinear optical coefficient than silica. Indeed, recently University of Southampton produced the first results in this direction and demonstrated a HF in SF57 lead glass with $\gamma = 550\ W^{-1} \cdot km^{-1}$, about 500 times more nonlinear than conventional SMF28 fibre [1.47]. Note that this particular fibre was produced from a preform manufactured using extrusion technique as explained in Section 1.3.1. The SEM image of the HF is shown in Fig. 1.12(a) and the results of nonlinear phase shift as a function of launched optical power is plotted in Fig. 1.12(b).

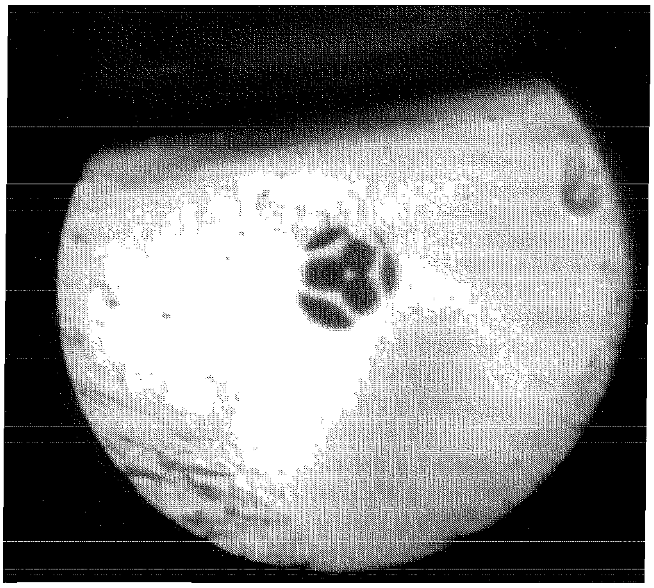

(a)

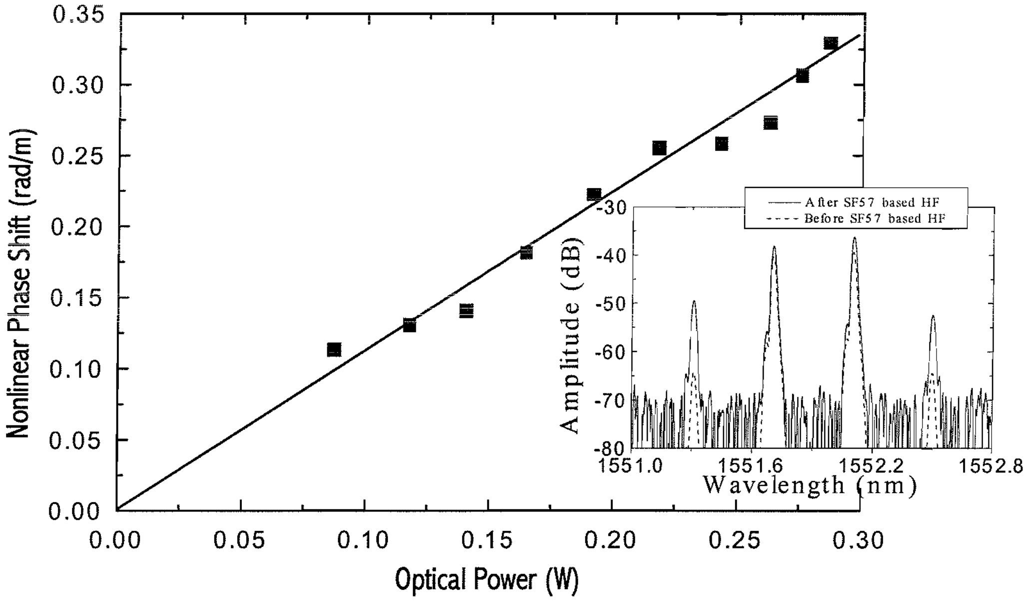

(b)

Figure 1.12: (a) SEM of SF57 based highly nonlinear HF. (b) Nonlinear phase shift versus launched power for the SF57 HF which yields an estimated value of the effective nonlinearity parameter γ = 550 $W^{-1}{\cdot}km^{-1}$; Inset: Spectral sidebands of high power dual frequency beat signal.

1.4 References

[1.1] B.-E. Olsson, P. Ohlen, L. Rau, and D. J. Blumenthal, "A simple and robust 40-Gb/s wavelength converter using fiber cross-phase modulation and optical filtering," *IEEE Photon. Technol. Lett.*, vol.12, no.7, pp. 846-848, 2000.

[1.2] J. Yu, X. Zheng, C. Peucheret, A. T. Clausen, H. N. Poulsen, and P. Jeppesen, "40-Gb/s all-optical wavelength conversion based on a nonlinear optical loop mirror," *J. Lightwave Technol.*, vol.18, no.7, pp.1001-1006, 2000.

[1.3] A. D'Ottavi, F. Girardin, L. Graziani, F. Martelli, P. Spano, A. Mecozzi, S. Scotti, R. Dall'Ara, J. Eckner, and G. Guekos, "Four-wave mixing in semiconductor optical amplifiers: a practical tool for wavelength conversion," *IEEE J. Select. Topics Quantum Electron.*, vol.3, no.2, pp.522-528, 1997.

[1.4] T. Yamamoto, E. Yoshida, and M. Nakazawa, "Ultrafast nonlinear optical loop mirror for demultiplexing 640Gbit/s TDM signals," *Electron Lett.*, vol.34, no.10, pp.1013-1014, 1998.

[1.5] I. D. Phillips, A. D. Ellis, H. J. Thiele, R. J. Manning, and A. E. Kelly, " 40Gb/s all-optical data regeneration and demultiplexing with long pattern lengths using a semiconductor nonlinear interferometer," *Electron Lett.*, vol.34, no.24, pp.2340-2342, 1998.

[1.6] I. Y. Khrushchev, I. D. Phillips, A. D. Ellis, R. J. Manning, D. Nesset, D. G. Moodie, R. V. Penty, and I. H. White, "OTDM applications of dispersion imbalanced fiber loop mirror," *Electron Lett.*, vol.35, no.14, pp.1183-1185, 1999.

[1.7] J. H. Lee, P. C. Teh, P. Petropoulos, M. Ibsen and D. J. Richardson, "Reduction of interchannel interference noise in a two-channel, grating based OCDMA system using a nonlinear optical loop mirror," *IEEE Photon. Technol. Lett*, vol.13, no.5, pp.529-531, 2001.

[1.8] Y. Emori, and S. Namiki, "100nm bandwidth flat gain Raman amplifiers pumped and gain-equalized by 12-wavelength-channel WDM high power laser diodes," in *Proc. Optical Fiber Communications Conference (OFC'1999)*, March 1999, Postdeadline paper PD19.

[1.9] P. C. Reeves-Hall, D. A. Chestnut, C. J. S. De Matos, and J. R. Taylor, "Dial wavelength pumped L- and U-band Raman amplifier," *Electron. Lett.*, vol.37, no.14, pp.883-884, 2001.

[1.10] D. M. Patrick, and R. J. Manning, " 20Gbit/s all-optical clock recovery using semiconductor nonlinearity," *Electron. Lett.*, vol.30, no.2, pp.151-152, 1994.

[1.11] P. V. Mamyshev, "All-optical data regeneration based on self-phase modulation," in *Proc. European Conference on Optical communication (ECOC'98)*, pp.475-476, 1998.

[1.12] M. Jinno, T. Sakamoto, J.-I. Kani; S. Aisawa, K. Oda, M. Fukui, H. Ono, M. Yamada, K. Oguchi, "1580-nm band, equally spaced 8/spl times/10 Gb/s WDM channel transmission over 360 km (3/spl times/120 km) of dispersion-shifted fiber avoiding FWM impairment," *IEEE Photon. Technol. Lett.*, vol.10, no.3 , pp.454-456, 1998.

[1.13] P. M. Kjeldsen, M. Obro, J. S. Madsen, and S. K. Nielsen, "SRS induced depletion of 1540nm signal copropagating with 1630nm OTDR pulses," *Electron. Lett.*, vol.32, no.20, pp.1914-1916, 1996.

[1.14] G. P. Agrawal, *Nonlinear fiber optics*, Academic Press, Second Edition 1995, Chapter 2.

[1.15] N. J. Doran, and D. Wood, "Soliton processing element for all-optical switching and logic," *J. Opt. Soc. Am. B*, vol.4, no.11, 1843, 1987.

[1.16] P. Petropoulos, T. M. Monro, W. Belardi, K. Furusawa, J. H. Lee, and D. J. Richardson, "A 2R-regenerative all-optical switch based on a highly nonlinear fiber", *Optics Lett.*, vol. 26, no.16, pp.1233-1235, 2001.

[1.17] M. Asobe, T. Kanamori, and K. Kubodera, "Ultrafast all-optical switching using highly nonlinear Chalcogenide glass fiber," *IEEE Photon. Technol. Lett.*, vol.4, no.4 , pp.362-365, 1992

[1.18] K. Inoue, and H. Toba, "Wavelength conversion experiment using fiber four-wave mixing," ", *IEEE Photon. Technol. Lett.*, vol.4, no.1 , pp.69-72, 1992.

[1.19] A. T. Clausen, L. Oxenlowe, C. Peucheret, H. N. Poulsen, P. Jeppesen, S. N. Knudsen, and L. Gruner-Nielsen, "10-GHz return-to-zero pulse source tunable in wavelength with a single- or multiwavelength output based on four-wave mixing in a newly developed highly nonlinear fiber", *IEEE Photon. Technol. Lett.*, vol.13, no.1 , pp.70-72, 2001.

[1.20] S. Watanabe, T. Naito, T. Chikama, "Compensation of chromatic dispersion in a single-mode fiber by optical phase conjugation", *IEEE Photon. Technol. Lett.*, vol.5, no.1 , pp.92-94, 1993.

[1.21] G. P. Agrawal, *Nonlinear fiber optics*, Academic Press, Second Edition 1995, p. 318.

[1.22] S. T. Davey, D. L. Williams, B. J. Ainslie, W. J. M. Rothwell, and B. Wakefield, "Optical gain spectrum of GeO2-SiO2 Raman fiber amplifiers," *IEE Proc.-J*, vol136, no.6, pp.301-306, 1989.

[1.23] R. G. Smith, "Optical power handling capacity of low loss optical fibers as determined by stimulated Raman and Brillouin scattering", *Appl. Optics*, vol.11, no.11, pp.2489-2494, 1972.

[1.24] V. E. Perlin, H. G. Winful, "Distributed feedback fiber Raman laser," *IEEE J. Quantum Electron.*, vol.37, no.1, pp.38-47, 2001.

[1.25] R. M. Shelby, M. D. Levenson, and P. W. Bayer, "Resolved forward Brillouin scattering in optical fibers", *Phys. Rev. Lett.*, vol.54, no.9, pp.939-942, 1985.

[1.26] C. L. Tang, "Saturation and spectral characteristics of the Stokes emission in the stimulated Brillouin process", *J. Appl. Phys.*, vol.37, no.8, pp.2945-2955, 1966.

[1.27] Y. Tanaka, K. Hotate, "Analysis of fiber Brillouin ring laser composed of single-polarization single-mode fiber," *J. Lightwave Technol.* Vol.l5, no.5, pp.838-844, 1997.

[1.28] M. Asghari, I. H. White, and R. V. Penty, "Wavelength conversion using semiconductor optical amplifiers," *J. Lightwave Technol.* Vol.l5, no.7, pp.1181-1190, 1997.

[1.29] K. Uchiyama, S. Kawanishi, and M. Saruwatari, "100-Gb/s multi-channel output all-optical OTDM demultiplexing using multchannel four-wave mixing in a semiconductor optical amplifier," *IEEE Photon. Technol. Lett.*, vol.10, no.6, pp.890-892, 1998.

[1.30] I. Glesk, J. P. Sokoloff, and P. R. Prucnal, "Demonstration of all-optical demultiplexing of TDM data at 250Gbit/s," *Electron. Lett.*, vol.30, no.4, pp.339-341, 1994.

[1.31] A. D. Ellis, A. E. Kelly, D. Nesset, D. Pitcher, D. G. Moodie, and R. Kashap, " Error free 100 Gbit/s wavelength conversion using grating assisted cross-gain modulation in 2mm long semiconductor amplifier," *Electron. Lett.*, vol.34, no.20 , pp.1958-1959, 1998.

[1.32] T. Durhuus, B. Mikkelsen, C. Joergensen, S. L. Danielsen, and K. E. Stubkjaer, "All-optical wavelength conversion by semiconductor optical amplifiers," *J. Lightwave Technol.* Vol.14, no.6, pp.942-954, 1996.

[1.33] N. S. Patel, K. A. Rauschenbach, and K. L. Hall, "40-Gb/s demultiplexing using an ultrafast nonlinear interferometer (UNI)," *IEEE Photon. Technol. Lett.*, vol.8, no.12 , pp.1695-1697, 1996.

[1.34] A. E. Kelly, A. D. Ellis, D. Nesset, R. Kashyap, and D. G. Moodie, "100Gbit/s wavelength conversion using FWM in an MQW semiconductor optical amplifier," *Electron. Lett.*, vol.34, no.20, pp.1955-1956, 1998.

[1.35] G. Contestabile, F. Martelli, A. Mecozzi, L. Graziani, A. D'Ottavi, P. Spano, G. Gueskos, R. Dall'Ara, and J. Eckner, " Efficiency flattening and equalization of frequency up- and down-conversion using four-wave mixing in semiconductor optical amplifiers," *IEEE Photon. Technol. Lett.*, vol.10, no.10, pp.1398-1400, 1998.

[1.36] B. J. Eggleton, P. A. Krug, L. Poladian, and F. Ouellette, "Long period superstructure Bragg gratings in optical fibers," *Electron. Lett.*, vol.30, no.19, pp.1620-1622, 1994.

[1.37] M. Ibsen, M. K. Durkin, M. J. Cole, and R. I. Laming, "Sinc-sampled fiber Bragg gratings for identical multiple wavelength operation," *IEEE Photon. Technol. Lett.*, vol.10, no.6, pp.842-844, 1998.

[1.38] P. Petropoulos, M. Ibsen, M. N. Zervas and D. J. Richardson, "Generation of a 40-Ghz pulse stream by pulse multiplication with a sampled fiber Bragg grating," *Optics Lett.*, vol.25, no.8, pp.521-523, 2000.

[1.39] P. Petropoulos, M. Ibsen, A. D. Ellis, and D. J. Richardson, "Rectangular pulse generation based on pulse reshaping using a superstructured fiber Bragg grating," *J. Lightwave Technol.*, vol.19, no.5, pp.746-752, 2001.

[1.40] P. C. Teh, P. Petropoulos, M. Ibsen, and D. J. Richardson, "A comparative study of the performance of seven- and 63-chip optical code-division multiple-access encoders and decoders based on superstructured fiber Bragg gratings," *J. Lightwave Technol.*, vol.19, no.9, pp.1352-1365, 2001.

[1.41] H. Geiger, A. Fu, P. Petropoulos, M. Ibsen, D. J. Richardson, and R. I. Laming, "Demonstration of a simple CDMA transmitter and receiver using sampled fiber gratings," in *Proc. European Conference on Optical Communication (ECOC'1998)*, 1998.

[1.42] A. Grunnet-Jepsen, A. E. Johnson, E. S. Maniloff, T. W. Mossberg, M. J. Munroe, and J. N. Sweetser, "Demonstration of All-Fiber Sparse Lightwave CDMA based on Temporal Phase Encoding," *IEEE Photon. Techno. Let.,* vol. 11, pp.1283-1285, 1999.

[1.43] M. Ibsen, M. K. Durkin, M. J. Cole, M. N. Zervas, and R. I. Laming, "Recent advances in long dispersion compensating fiber Bragg gratings," *IEE Publications*, vol. 0963-3308-ref.no. 1999/023, 1999.

[1.44] J. C. Knight, T. A. Birks, P. St. J. Russell, and M. Atkin, "All-silica single-mode optical fiber with photonic crystal cladding," *Optics Lett.*, vol. 21, pp.1547-1549, 1996.

[1.45] T. M. Monro, D.J. Richardson, N.G.R. Broderick, P.J. Bennett, "Holey optical fibers: an efficient modal model," *J. Lightwave Technol.*, vol.17, no.6, pp.1093-1102, 1999.

[1.46] T. A. Birks, J. C. Knigth, and P. St. J. Russell, "Endlessly single-mode photonic crystal fiber," *Optics Lett.*, vol.22, no.13, pp.96-963, 1997.

[1.47] T. M. Monro, K. M. Kiang, J. H. Lee, K. Frampton, Z. Yusoff, R. Moore, J. Tucknott, D. W. Hewak, H. N. Rutt, and D. J. Richardson, "High nonlinearity extruded single-mode holey optical fibers," in *Proc. Optical Fiber Communications Conference (OFC 2002)*, FA1, Anaheim USA, March 2002 (Postdeadline paper).

[1.48] G. P. Agrawal, *Fiber optic communication systems*, Wiley Interscience, Second Edition 1997, pp. 30-39.

[1.49] J. H. Lee, D. J. Richardson, Z. Yusoff, W. Belardi, and T. M. Monro, "System applications of holey fibers," *15th Annual meeting of the IEEE Lasers & electro-Optics Society (LEOS'2002)*, Glasgow Scotland, November 2002 (Invited paper).

[1.50] J. C. Knight et al., "Anomalous dispersion in photonic crystal fiber," *IEEE Photon Technol. Lett.*, vol.12, no.7, pp.807-809, 2000

[1.51] W. J. Wadsworth et al., "Soliton effects in photonic crystal fibers at 850 nm," *Electron. Lett.*, vol.36, no.1, pp.53-55, 2000.

[1.52] J.H.V. Price et al., "A tuneable femtosecond pulse source operating in the range 1.06-1.33 microns based on an Yb doped holey fiber amplifier", in *Proc. Conference on Lasers and Electro-Optics (CLEO 2001)*, Postdeadline CPD1-1, May 2001.

[1.53] T. A. Birks, D. Mogilevtsev, J. C. Knight, P. St. J. Russell, "Dispersion compensation using single-material fibers," *IEEE Photon. Technol. Lett*, vol.11, no.6, pp.674-677, 1999.

[1.54] A. Ferrando, E. Silvestre, J. J. Miret, J. A. Monsoriu, M. V. Andres, P. St. J. Russell, "Designing a photonic crystal fiber with flattened chromatic dispersion," *Electron. Lett.*, vol.35, no.4, pp.325-327, 1999.

[1.55] N. G. R. Broderick, T. M. Monro, P. J. Bennett, and D. J. Richardson, "Nonlinearity in holey optical fibers: measurement and future opportunities", *Optics Lett.*, vol.24, no.20, pp.1395-1397, 1999.

[1.56] K.P. Hansen, J. R. Jensen, C. Jacobsen, H. R. Simonsen, J. Broeng, P. M. W. Skovgaard, A. Petersson, and A. Bjarklev, "Highly nonlinear photonic crystal fiber with zero dispersion at 1550nm", in *Proc. Optical Fiber Communications Conference (OFC 2002)*, FA9, Anaheim USA, March 2002 (Postdeadline paper).

[1.57] J. E. Sharping, M. Fiorentino, P. Kumar, R. S. Windeler, "All-optical switching in microstructured fiber", *IEEE Photon. Technol. Lett.*, vol.14, no.1, pp.77-79, 2002.

[1.58] T. M. Monro, Y. D. West, D. W. Hewak, N. G. R. Broderick, D. J. Richardson, "Chalcogenide holey fibers," *Electron. Lett.*, vol.36, no.24, pp.1998-2000, 2000.

CHAPTER TWO

THE USE OF NONLINEAR OPTICAL ELEMENTS FOR SIGNAL RECOGNITION SIGNATURE ENHANCEMENT IN A GRATING BASED ALL-OPTICAL CDMA CODING:DECODING SYSTEM

This Chapter reports results concerning the use of a self-switching, nonlinear optical loop mirror (NOLM) within a time-spreading direct sequence (DS) - optical code division multiplexing (OCDMA) system to act as a fast nonlinear thresholding device with which to improve the quality of the code recognition signature.

This Chapter is organised as follows. In Section 2.1 a brief introduction to the DS-OCDMA system and the corresponding nonlinear thresholding device is presented. Section 2.2 describes the results of a preliminary theoretical study into the pulse-shaping and signal-contrast enhancement effects that can be obtained by incorporating a suitably designed NOLM into a SSFBG based DS-OCDMA system. Calculations are presented for a specific 7-chip, bipolar 160 Gchip/s system based on M-sequence codes, and the results are then compared with experimental data. Section 2.3 describes the results of detailed system experiments using 63-chip, 160 Gchip/s bipolar coding and decoding SSFBG's in which the noise reduction benefits of using the NOLM within the decoder are more apparent. The performance benefits achieved are then quantified from a system perspective. Both single channel and multi-channel operation are investigated and the cancellation of both intra-channel, and inter-channel interference noise are successfully demonstrated. Section 2.4 presents conclusions regarding the results and discusses further extensions and applications of the technology.

2.1 SSFBG Based DS - OCDMA Systems and Nonlinear Thresholding Devices

The continued rapid growth in Internet traffic demands the development of optical networks of ever increasing capacity and functionality. It is clear that when developing such future networks it will be desirable, if not essential, to perform as much as possible of the processing and routing of signals directly within the optical domain. In this way many of the 'bottlenecks' currently imposed by optoelectronic conversion and electronic processing of data can be removed.

All-optical pattern generation and recognition are two such signal-processing functions that are likely to be required in future high-capacity optical networks. These functions will be needed for example for header recognition in ultra-fast OTDM packet switched networks, and for use within Optical Code Division Multiple Access (OCDMA) systems [2.1, 2.2]. OCDMA is the optical analogue of the CDMA technique that has been applied with such success to the field of mobile communications. CDMA is a spread-spectrum digital transmission technique which allows multiple users of a network to share the same relatively broad transmission bandwidth through the allocation of specific mathematically defined codes. These codes dictate how the individual users use/sample the available spectral bandwidth in order to both send and receive data. There are two main types of technique used to spectrally code and spread a data signal, these are the so-called Direct-Sequence (DS-) CDMA, and Frequency-Hopping (FH-) CDMA, however it is also possible to use hybrid approaches which seek to combine the two techniques [2.3]. In DS-CDMA the digital data is directly coded with pseudo-random patterns in the time-domain, and the receiver knows how to generate the same code and correlates the received signal with that code to extract the data. By contrast in FH-CDMA, the signal is rapidly, pseudo-randomly switched between different frequencies within the hopping bandwidth, and the receiver knows beforehand where to find the signal at any given time. OCDMA is still in the very earliest stages of technological development however it is attractive for a number of reasons which include amongst others the capacity for high connectivity, more flexible bandwidth usage, asynchronous access and improved system security.

Recently a number of DS-OCDMA systems based upon fibre Bragg grating encoding/decoding devices have been demonstrated [2.4]. These particular experiments showed the suitability of using superstructure fibre Bragg grating (SSFBG) technology for the generation, recognition and recoding of phase encoded optical code sequences containing as many as 63-chips at chip rates as high as 160 Gchip/s. Longer code sequences and higher chip rates should also be possible.

The SSFBG technology represents an attractive means to produce compact, and potentially low-cost components for such OCDMA applications relative to the more conventional technological approaches and which include the use of planar lightwave circuits [2.5], arrays of discrete fibre gratings [2.6], bulk grating based systems incorporating spatial light modulators [2.7], and arrays of fibre couplers [2.8].

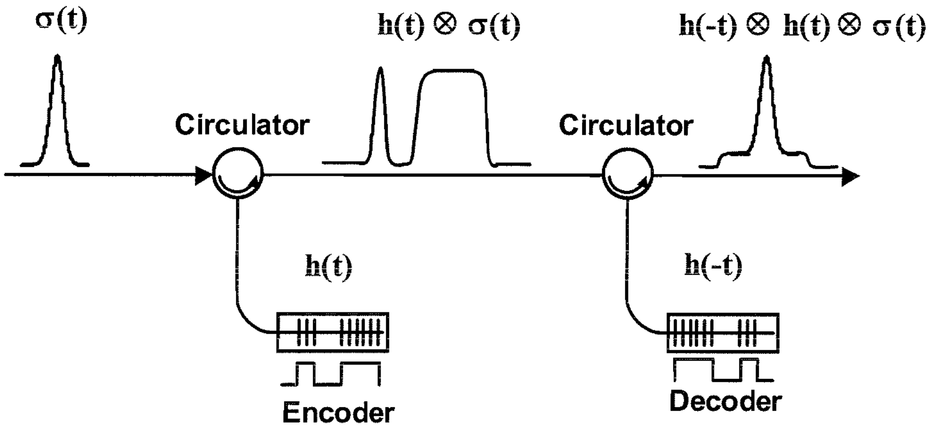

Figure 2.1: Basic principle of pulse encoding and decoding by SSFBG's.

Fig. 2.1 shows the basic principle of pulse encoding and decoding by SSFBG's. When a short pulse enters the SSFBG encoder, the resulting reflected signal represents a coded sequence of distinct, time-spread pulses (the individual pulses that make up the code sequences are commonly known as chips). The individual chip duration, the code sequence, and code length are defined by the SSFBG impulse response is given by the SSFBG refractive index profile. The coded pulse sequence is then transmitted along an optical fibre to the decoder/receiver. The decoder operates on the principle of matched filtering, and as such is based upon purely linear optical effects. The matched filtering operation is realised in practice by reflecting the coded pulses from a grating with the spatially reversed superstructure profile of the encoder grating, and which thus has the temporally inverted impulse response (phase conjugate frequency response).

Consequently the pulse reflected from the decoder grating represents the cross-correlation function between the codes used within the encoder and decoder SSFBG's. In the instance that the codes are matched the reflected pulse represents the autocorrelation function of the encoded pulse sequence.

High quality code generation and recognition in the time domain can be obtained by this method by restricting the codes used within the systems and those that have a distinct autocorrelation function and mutually low cross correlation functions [2.9]. Unfortunately though, as one moves to longer code lengths, higher data rates and multi-user operation, undesirable phenomena can come into play that reduce the quality and contrast of the pattern recognition signature and which begin to adversely affect the quality of the system performance. Such undesirable phenomena can include decoherence of the refractive index profile along the grating length due to fibre diameter inhomogeneity or errors in the writing process itself, adjacent code (intra-channel) interference, and inter-channel interference. However, one can envisage incorporating additional nonlinear components within SSFBG based processing schemes to either improve the performance in such instances, or to extend the functionality of this technical approach.

In the following Sections, both theoretical and experimental results concerning the use of a self-switching, nonlinear optical loop mirror (NOLM) within a time-spreading DS-OCDMA system to act as a fast saturable absorber with which to improve the quality of the code recognition signature, are reported. NOLM's have already been adopted for various other optical processing applications, these include amongst others; pulse laser compression [2.10], extinction ratio improvement of optical time domain multiplexing (OTDM) systems [2.11], all-optical channel demultiplexing [2.12] and filtering of amplified spontaneous emission (ASE) noise [2.13]. It is shown that a suitably designed NOLM can significantly improve the contrast of a degraded pattern recognition signature due to imperfect matching of SSFBG parameters, and that it can reduce both intra-channel and inter-channel interference noise.

2.2 Theoretical and Experimental Analysis an Improved Performance of a 7-Chip Time Spread DS-OCDMA System Using a NOLM

The configuration for the 7-chip time-spread DS-OCDMA system that were used to first validate the nonlinear, code recognition signature enhancement concept described above is shown in Fig. 2.2.

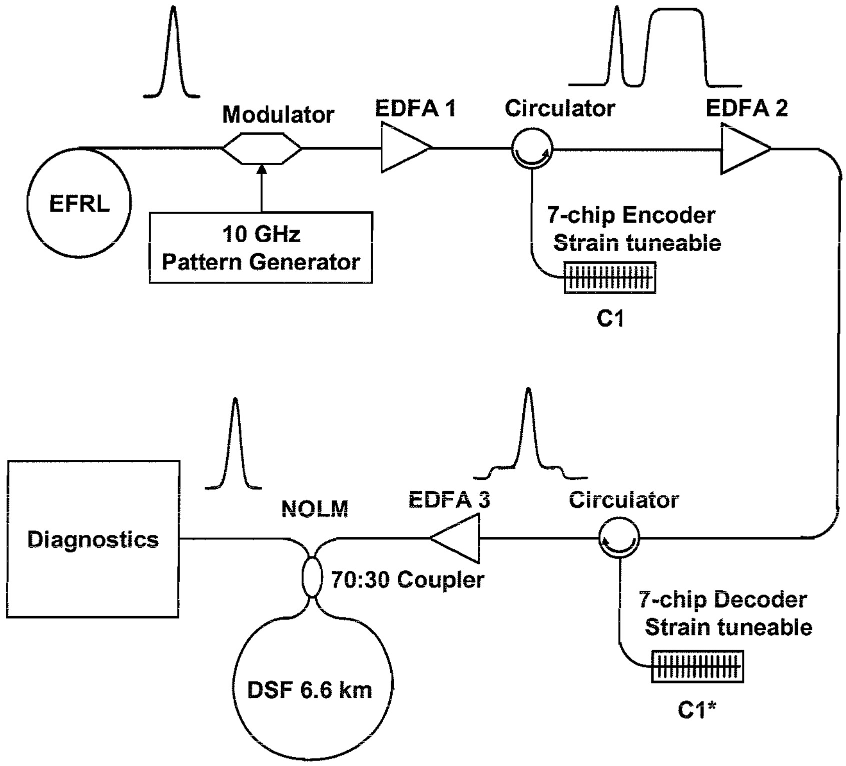

Figure 2.2: Configuration of a 7-chip time spread DS-OCDMA system incorporating a NOLM. The saturated output power from EDFA3 was 15 dBm. The length of DSF in the NOLM was 6.6 km and the dispersion of the DSF was 1.18 ps/nm-km.

The system comprised: a 2.5 ps, 10 GHz regeneratively mode locked erbium fibre ring laser (EFRL) with an external 10GHz 'pulse selector'; a 7-chip coding SSFBG; a matched 7-chip decoder SSFBG; various low-noise amplifiers to compensate for the system losses; a power amplifier to boost the power of the decoded signal; and a NOLM for nonlinear processing of the matched-filtered signal. Short pulses from the laser were launched onto the coding SSFBG resulting in the generation of a code sequence corresponding to the impulse response of the grating. In this instance the particular code was bipolar with the required phase-shifts distributed within the grating in accordance with the 7-chip M-sequence code '0100111'. The chip length of the gratings used in these experiments was 6.4 ps, corresponding to a chip rate of 160 Gchip/s. The coded pulse sequence had a total duration of ~45 ps. The coded pulses were then launched onto the decode grating. The temporal form of the pulses reflected from the decoder grating thus represented the cross-correlation function between the incoming encoded sequence and the decoder grating's impulse response function. Assuming that the encoder:decoder gratings are well matched then the specific choice of a 7-chip M-sequence ensures a good pattern recognition signature which has the form of a short, chip-length long autocorrelation spike on a relatively low-level broad pedestal. The pedestal has a total duration of twice the code length (i.e. 90 ps). The performance of the particular gratings used in these experiments, was quantified in an earlier work which showed that the precision of this grating writing was such that it was indeed possible to obtain excellent pattern recognition signatures using the matched filtering approach [2.4]. In the current experiments the decoded pulses were amplified to a high power and then were passed through the NOLM in order to selectively pass the correlation spike and filter out the low level pedestal prior to detection. This nonlinear processing serves to further improve the signal to noise ratio of the pattern recognition signature and to reshape the correlation spike.

In order to validate theoretically this system concept, and to establish an optimum NOLM design, the above system was first modelled as a function of the key parameters of the NOLM (e.g. coupling ratio, dispersion and length and the peak power of the decoded pulse incident to the NOLM). The SSFBG's were assumed to be perfectly matched and to behave as idealized 7-chip M-sequence coders and decoders. Pulse propagation within the NOLM was modelled using the nonlinear Schrödinger equation with group velocity dispersion, self-phase modulation, intrapulse Raman scattering, self-steepening, and shock formation at the pulses' leading edge [2.14] as described by Eq. (2.1).

$$\frac{\partial A}{\partial z}+\beta_1\frac{\partial A}{\partial t}+\frac{i}{2}\beta_2\frac{\partial^2 A}{\partial t^2}-\frac{1}{6}\beta_3\frac{\partial^3 A}{\partial t^3}+\frac{\alpha}{2}A=i\gamma|A|^2A-\frac{\gamma}{\omega_o}\frac{\partial}{\partial t}(|A|^2A)-i\gamma T_R A\frac{\partial|A|^2}{\partial t} \qquad (2.1)$$

where the pulse amplitude A is normalized such that $|A|^2$ represents the optical field strength within the fibre. β_1 is the group delay, β_2 is the first order group velocity dispersion (GVD), and β_3 is the second order GVD. α represents the absorption coefficient of optical power in the fibre and corresponds to 0.25dB/km, ω_o is the signal frequency, and $\gamma = \frac{n_2\omega_o}{cA_{eff}}$ is the nonlinearity coefficient where $n_2 = 2.6\times10^{-20}\, m^2/W$ and $A_{eff} = 50\mu m^2$ is the effective area of the fibre. T_R = 2 fs has its origin in the delayed Raman response and represents the first-order Raman gain effects. (Note that in fact neither Raman scattering, self-steepening, nor third-order dispersion play a significant role in the evolution of pulses of order the chip length over the ~6km propagation lengths considered herein.)

The above equation was solved using the symmetrised split step Fourier method [2.14]. A NOLM was modelled to be constructed from a 70:30 coupler and a length of dispersion shifted fibre (DSF). The 70:30 coupling ratio was chosen to obtain the best nonlinear switching performance suitable for this system after many numerical simulations with a range of different values. DSF was chosen in preference to standard single mode fibre (SMF) in order to reduce the power required to generate the necessary SPM/soliton effects due to both its higher nonlinearity and smaller dispersion relative to SMF. The values of the dispersion parameter (D), dispersion slope ($dD/d\lambda$), and nonlinearity coefficient (γ) assumed within these calculations were 1.18 ps/nm-km, 0.07 ps/nm^2/km and 1.55 W$^{-1}\cdot$km^{-1} respectively at the system-operating wavelength of 1558 nm, and corresponded to those of a fibre that was available within our laboratories. The fibre length was 6.6 km.

Fig. 2.3 shows the results of the theoretical calculation which demonstrate the predicted impact of the NOLM on both the autocorrelation signal reshaping and pedestal rejection as a function of input pulse power. In Fig. 2.3(a) the pulse shape evolution is plotted as a function of increasing input pulse peak power. Fig. 2.3(b) is a log scale plot of the same data. The pulse shape of the simple matched filtered decoded signal for the particular 7-chip bipolar pulse sequence used in these experiments is given by the '0 W' pulse form in Fig. 2.3(a). (Note that the individual pulse shape at each power is normalized with respect to the peak pulse amplitude). It can be seen that as the decoded signal power is increased the relative height of the ripple features associated with the pedestal decreases and the central autocorrelation feature narrows significantly.

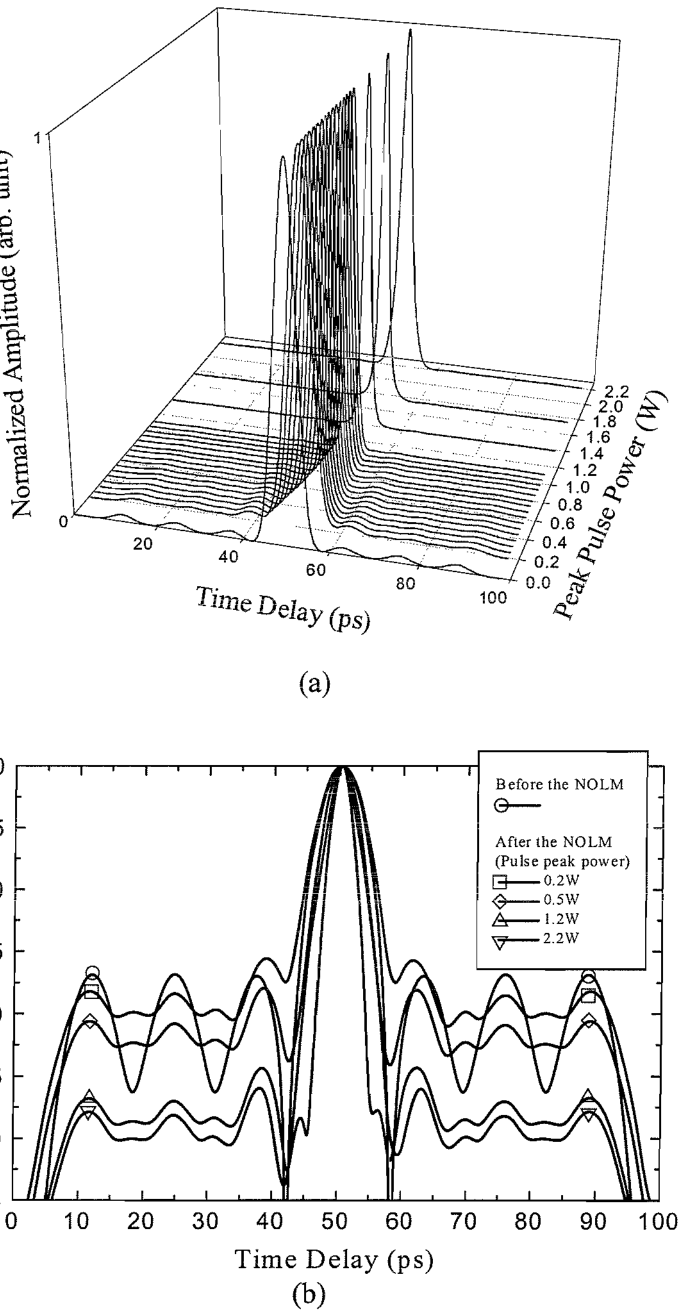

Figure 2.3: Theoretical calculation showing the predicted impact of the NOLM on both the autocorrelation signal reshaping and pedestal rejection as a function of input pulse power; (a) actual pulse shape evolution as a function of increasing input pulse peak power. (b) Same data plotted in a log scale.

These features are summarised more fully in Figs. 2.4(a), (b), and (c). In Fig. 2.4(a) the half width of the central autocorrelation feature is plotted as a function of input power. It is seen that optimum compression with compression factors approaching '3' are obtained at a pulse peak power of ~1.5 W. Note that for a peak power of 1.2 W the pulse duration is 2.5 ps, essentially the same as that of the input laser pulses.

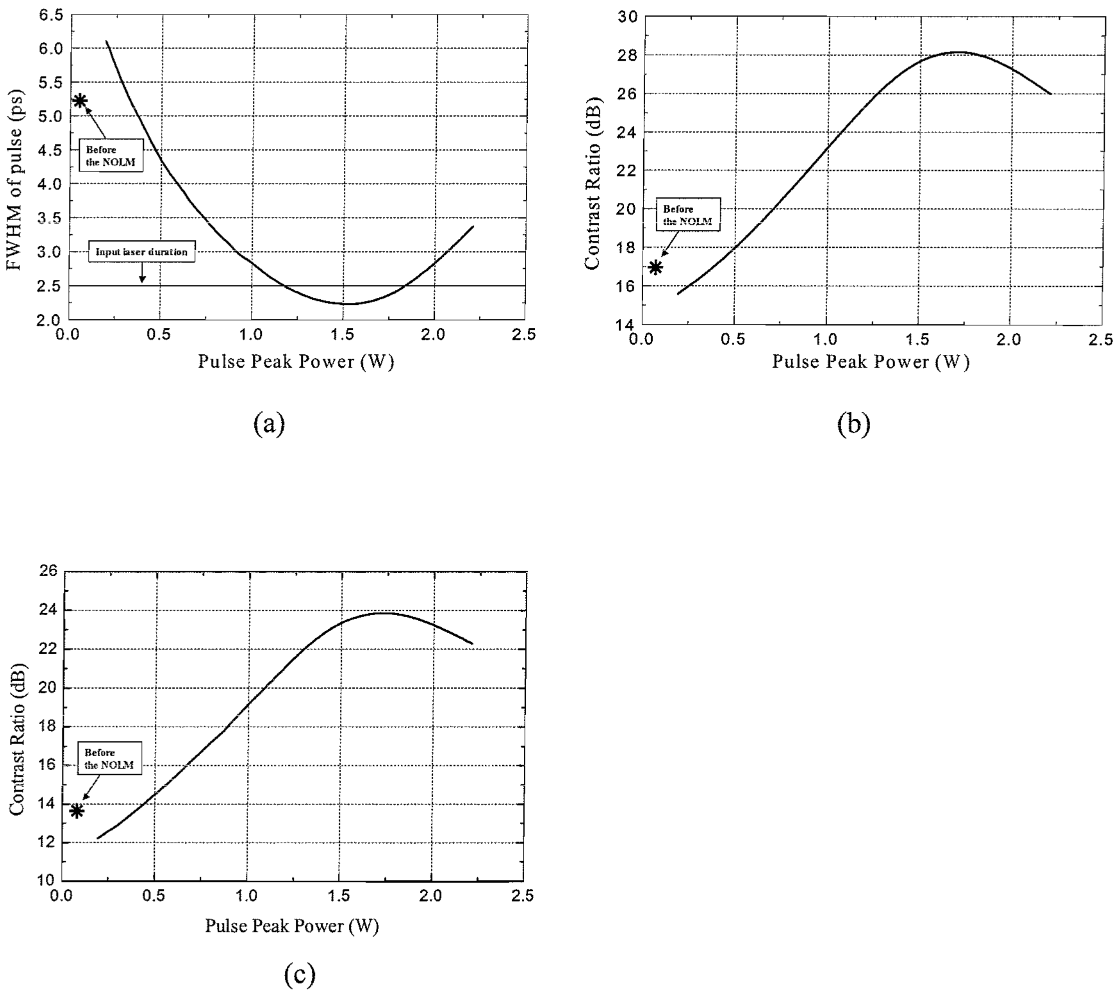

Figure 2.4: (a) FWHM of the central autocorrelation feature as a function of input power. (b) Corresponding value of the signal contrast defined as the ratio between the peak power of the output pulse to that of the first pedestal lobe. (c) Contrast ratio in terms of the measured SHG autocorrelation of the decoded pulse form.

Fig. 2.4(b) shows the corresponding value of the signal contrast which is defined as the ratio between the peak power of the output pulse to that of the first pedestal lobe. After simple matched filtering alone, (i.e. before the NOLM), this ratio is ~17 dB. However, this can be increased by as much as 10 dB to a value of ~28 dB at a peak power of 1.6W and which represents the optimum contrast enhancement in this instance. An 8-9 dB contrast enhancement is achieved at a peak power of 1.2 W. In Fig. 2.4(c) the improvement in contrast ratio is quantified in terms of the measured SHG autocorrelation of the decoded pulse form, since in practice it is this that was measured in the preliminary experiments. A factor of ~3 reduction in pulse width and a peak contrast ratio enhancement factor of order 10 dB are again predicted. The pulse width contraction and nonlinear filtering result from high order soliton effects within the NOLM [2.15]. These calculations, and others over a broader parameter space than described so far, show that for optimal pulse compression a ~70:30 coupling ratio, a soliton order of N = 3 within the 70 % coupling direction within the loop, and the loop length to be of order the soliton period are required. (The relevant pulse duration for calculating the soliton period and order in the above is given by the half width of the correlation spike incident to the loop).

Fig. 2.5 shows the predicted reflectivity of the NOLM as a function of input peak power. The NOLM is predicted to transmit ~12 % of the incident decoded pulse power at low intensities, with this percentage increasing to ~78 % at a pulse power of ~1.8 W. The reflectivity at ~1.5-1.6 W incident power, the optimum power in terms of minimum pulse duration/contrast enhancement, is ~70 %. In Fig. 2.5 the experimentally determined reflectivity is also plotted as a function of incident power. The amplifier used in this particular experiment limited the maximum achievable peak power to 1.2 W, which although slightly less than optimum, still allowed for significant switching, pulse shaping and contrast enhancement. The experimentally observed nonlinear increase in NOLM transmission closely follows the predicted theoretical form, and approaches 40 % at the 1.2 W level.

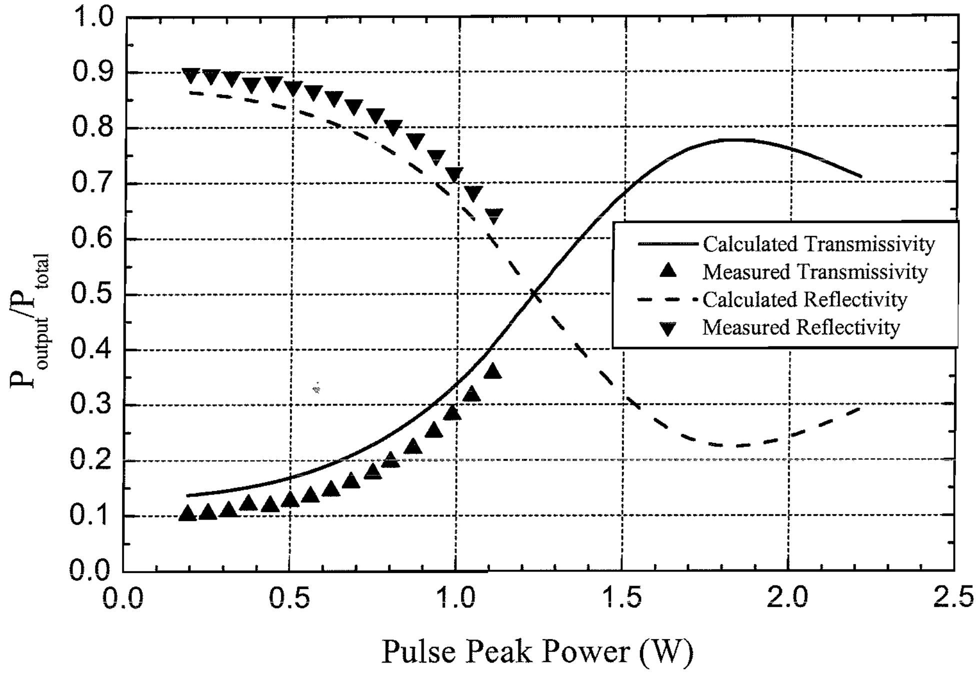

Figure 2.5: Predicted and measured reflectivity of the NOLM as a function of input peak power.

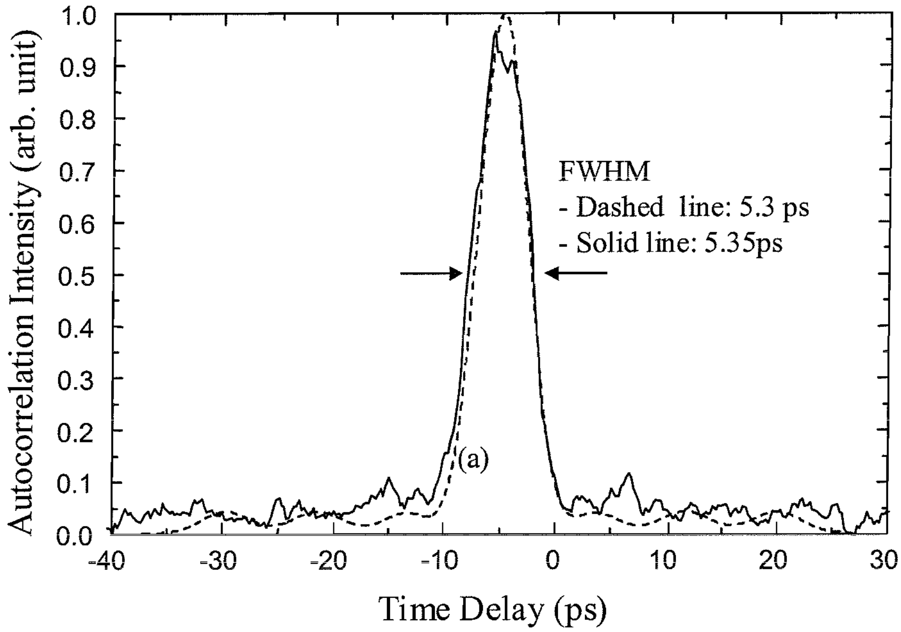

(a)

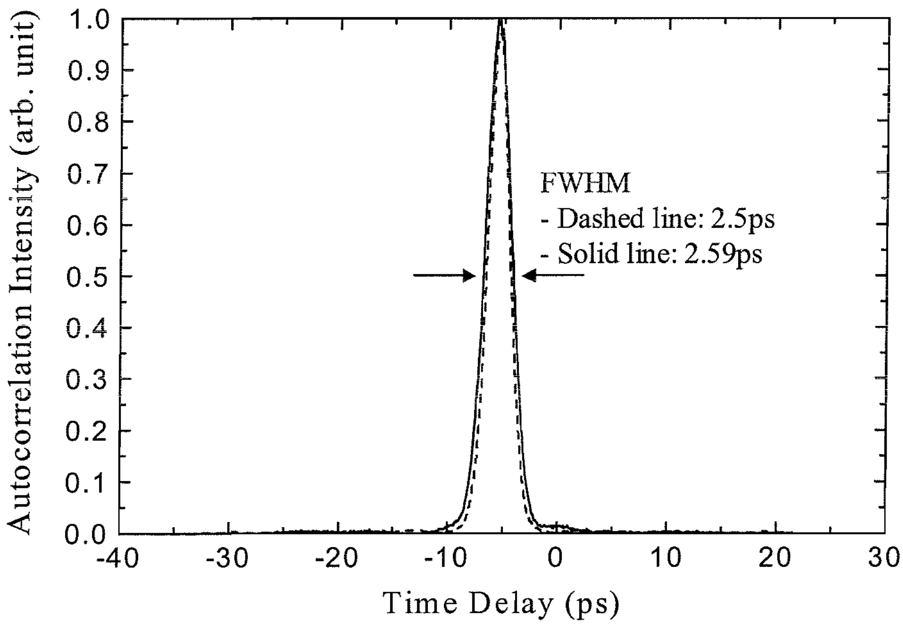

(b)

Figure 2.6: Experimental and theoretical SHG autocorrelation functions at a peak power of 1.2 W both (a) before and (b) after the NOLM. (solid lines: experimental measurements, dashed lines: theoretical calculations).

In Fig. 2.6 I show the experimental and theoretical SHG autocorrelation functions at a peak power of 1.2 W both before and after the NOLM. Good agreement between theory and experiment is observed in both cases in terms of both pedestal suppression, and pulse narrowing. The final deconvolved pulse duration after the NOLM is ~2.6 ps, essentially the same as the input pulse form and exactly as predicted in Fig. 2.4(a).

The preliminary experiments thus validate the theoretical predictions of pattern recognition signature clean up, and narrowing. As it happens the autocorrelation properties of this particular M-sequence, and the quality of these 7-chip bipolar gratings is so good, that error-free, penalty free operation can readily be achieved with matched filtering alone. The benefits of the NOLM as a pulse-cleaning element only really become evident from a system perspective as either longer code words are used, or when there are multiple users of the system. The use of longer code words dictates the use of longer coding/decoding gratings and which can lead to a degradation of decode signal quality as a result of the difficulty in maintaining coherence of the grating structure over the longer physical length of the grating during fabrication. Moreover, the use of longer codes means that interference noise due to temporal overlap of adjacent coded data bits occurs once the length of the decode signal (which is two times the code length) becomes longer than the reciprocal of the data rate. The presence of this interference noise can significantly impact the system performance even under single user operation of the system. Similar interference noise is also generated once there are simultaneous users of the system, transmitting either synchronously or asynchronously over the same fibre. In order to demonstrate these features detailed system measurements on an OCDMA system, similar to that described previously for 7-chip codes, only this time with 63-chip code sequence bipolar SSFBG's, were thus performed. These experiments are described in detail within the next Section. Note that the use of longer code words is desirable in real OCDMA systems since they support the use of a greater number of simultaneous users. In the case of 7-chip codes there are just two bipolar M-sequence codes which offer little scope for real system applications. In the case of 63 chip codes based on Gold sequences as used in these experiments there are 65 'orthogonal' bipolar code combinations [2.16], allowing accommodation of up to 65 simultaneous users.

2.3 Code Recognition Performance Improvement of A 63-Chip Time Spread Grating Based OCDMA System Using a NOLM

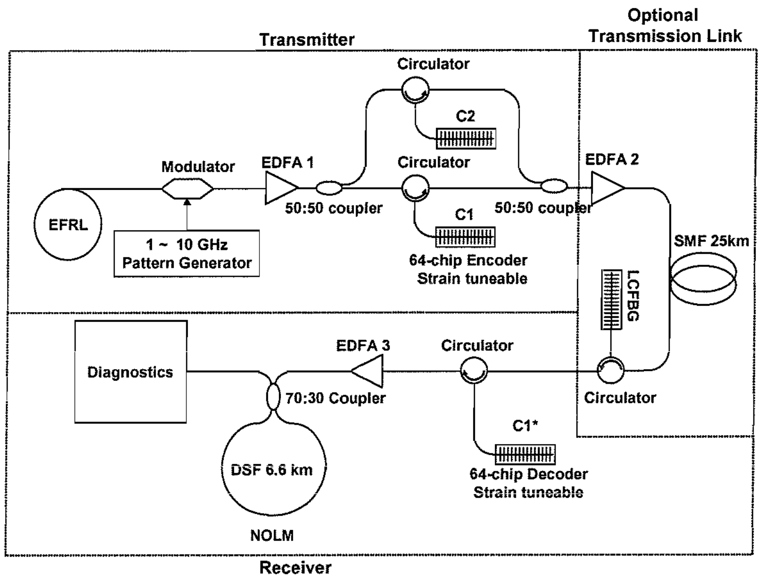

(a)

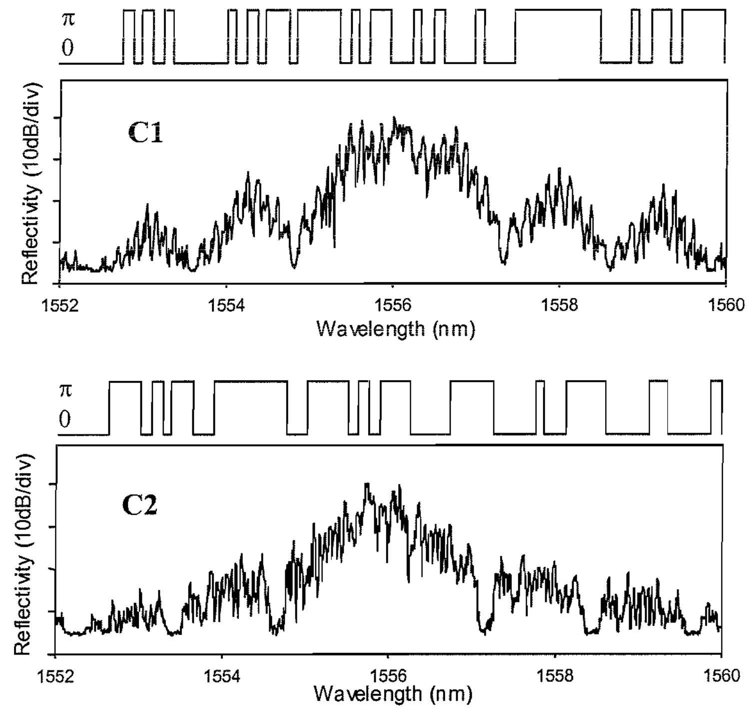

(b)

Figure 2.7: (a) Experimental setup for the 63-chip, 160 Gchip/s system experiments. (b) Two 63-chip bipolar Gold codes and the corresponding spectral profiles of the encoder SSFBG's that were fabricated.

The experimental setup for the 63 chip, 160 Gchip/s system experiments is shown in Fig. 2.7(a) and is similar in principle to the 7-chip set-up. In this instance the 2.5 ps pulses at 10 GHz were first gated down to a lower repetition frequency, and encoded with pseudorandom data at either 1.25, or 2.5 Gbit/s. The data pulses were then split using a 3 dB coupler and fed onto two separate encoder gratings, denoted C1 and C2 respectively, before being recombined into a single fibre using a second 3 dB coupler. The individual encoding SSFBG's contain phase-coding information within their refractive index profiles as defined by two 'orthogonal', 63-chip bipolar Gold codes. Once the data pulses are reflected from gratings C1 and C2 they generate two distinct data streams encoded with either one of these two distinct codes. Fig. 2.7(b) shows both the distribution of the phase changes along the gratings as defined by the two Gold sequences selected, and their corresponding spectral responses. The spiky reflectivity spectrum observed results from the multiple phase jumps within the spectrum and is as theoretically expected. The chip duration for these gratings is 6.4 ps, and the chip rate 160 Gchip/s.

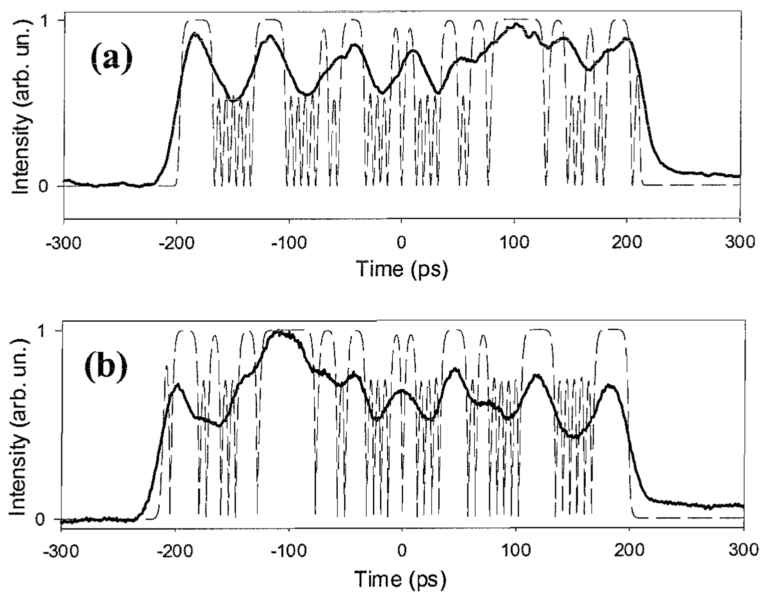

Figure 2.8: Theoretically predicted, and experimentally observed, response of (a) gratings C1 and (b) their corresponding conjugates C1 after excitation with 2.5 ps pulses. (solid lines: experimental measurements, dashed lines: theoretical plots). The detection bandwidth of the experimental measurement (~20 GHz) was not taken into consideration for the theoretical calculation.*

The coded data bits have a total duration of ~400 ps as illustrated in Fig. 2.8(a) and 2.8(b) in which both the theoretically predicted, and experimentally observed, response of gratings C1 and their corresponding conjugates C1* after excitation with 2.5ps pulses are plotted. Although the response time of the detection system used to measure these pulses was insufficient to precisely resolve the individual chips, a clear correlation between theory and the experimental data is observed, confirming the high quality of the gratings.

The coded data stream was then either fed directly to decode grating C1*, or else transmitted over 25 km of standard single mode fibre whose dispersion was compensated over a 5 nm bandwidth using a suitably linearly chirped fibre Bragg grating and then fed to grating C1*. Grating C1* was designed to provide a matched filter response to grating C1. The decoded output from grating C1* was then either detected directly, (or pre-amplified in EDFA3) before being passed through the NOLM prior to detection. The NOLM used in the 63-chip experiments was the same NOLM used in the previously described 7-chip experiments. The pulse shaping properties of the individual gratings, and of the gratings when used in conjunction with the NOLM, were characterised in the temporal domain using a fast pin diode and sampling oscilloscope of combined ~20 GHz bandwidth, and a SHG autocorrelator (<100 fs resolution). The system error rate performance was measured using a BER test set with up to 10 Gbit/s measurement capability. Note that it was ensured that there was a significant difference in passage time through the system for each of the individually coded data streams so as to remove any direct correlation between the data arriving at the receiver from the two channels. Moreover the relative passage time of the two channels could be fine-tuned to allow anywhere between zero and full temporal overlap of the coded data bits at the receiver.

2.3.1 Single Channel Operation

Disconnecting the fibres connected to grating C2 in Fig. 2.7(a) allowed us to make single user experiments using gratings C1 and C1*. Encoding:decoding and associated transmission experiments at data rates of both 1.25 and 2.5 Gbit/s were performed. Fig. 2.9(a) shows the SHG autocorrelations of the central correlation spikes of the decoded pulse forms prior to the NOLM and directly after the decoder grating for bit-rates of both 1.25 and 2.5 Gbit/s. This particular data was taken with no intermediate transmission of the coded data bits. The decoded pulse forms have a deconvolved temporal half-width of 6.4 ps at 2.5 Gbit/s, and 5.8 ps at 1.25 Gbit/s and exhibit an appreciable pedestal component which extends +/- 400 ps from the central correlation spike as can be seen in the eye diagrams shown in Fig. 2.10(b).

Whilst the pattern recognition signature obtained from simple matched filtering is very good, thereby confirming the quality of these coding:decoding gratings, the presence of the pedestal component can still have a significant impact on the pattern recognition signal to noise ratio. This is particularly true at data rates above 1.25 Gbit/s for which the 800 ps long correlation pulses arising from individual data bits can have significant overlap in the pulse tails with decoded bits originating from neighbouring bit slots. This overlap can result in significant amplitude noise associated with coherent interference between pedestals arising from adjacent/neighbouring '1' data bits. This increased noise level is apparent within Fig. 2.10(b) which shows the eye diagrams observed for data rates of 1.25 Gbit/s (no pedestal overlap), and at 2.5 Gbit/s (pedestal contribution from the two adjacent data slots). To quantify the system impact of this noise, detailed BER measurements were performed on the matched filtered pulse forms shown in Fig. 2.9(a) and 2.10(b) at data rates of both 1.25 and 2.5 Gbit/s. The results are summarised in Fig. 2.11. These measurements showed that high quality error-free performance could be obtained at both data rates albeit with a power penalty relative to back-to-back measurements. At a data rate of 1.25 Gbit/s this power-penalty was ~1.5 dB. The power-penalty increased to 4.5 dB at 2.5 Gbit/s due to the intra-channel interference noise arising from decode signal overlap as previously discussed. Note that at both data rates there was no significant additional power penalty associated with transmitting the coded bits over the 25 km dispersion-compensated transmission line.

In order to reduce the power penalties observed at both 1.25 and 2.5 Gbit/s the decoded code-correlation pulse forms were first amplified and fed into the input of the NOLM. The resulting nonlinearly switched pulse forms were then characterised as previously, and BER measurements performed. The improved pattern recognition contrast is clearly evident on comparing Figs. 2.9(a) and (b), and Figs. 2.10(b) and (c). The low-level pedestal obtained with simple matched filtering is almost entirely eliminated by passage through the nonlinear loop mirror. From Fig. 2.9 it is also seen that the shape and duration of the output pulses were restored to values close to the original input laser pulses.

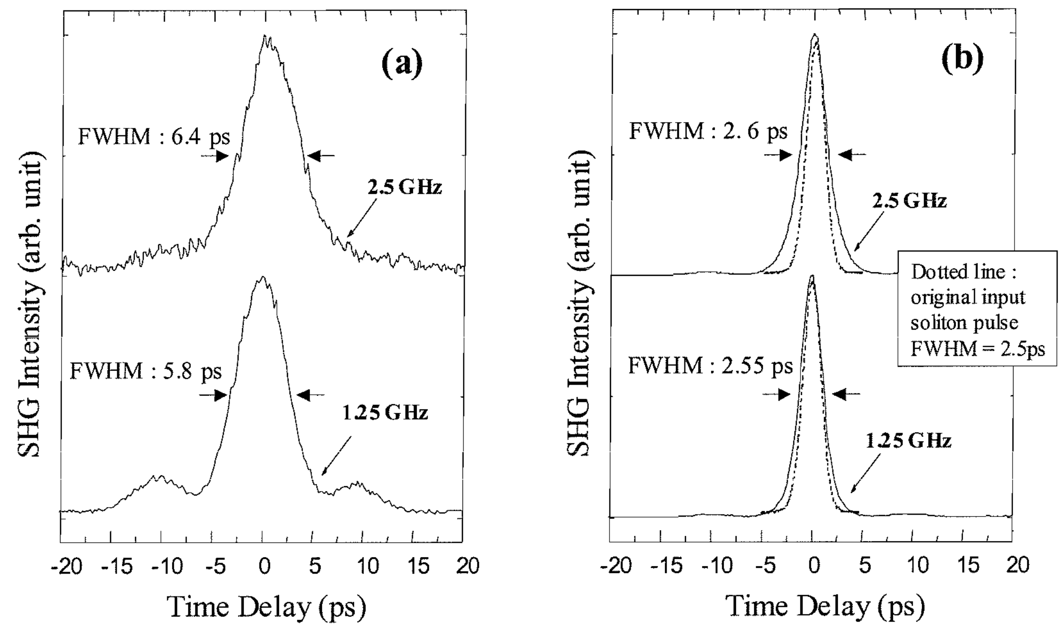

Figure 2.9: The SHG autocorrelations of the central correlation spikes of the decoded pulseforms, (a) prior to the NOLM and (b) directly after the decoder grating for bit-rates of both 1.25 and 2.5 Gbit/s.

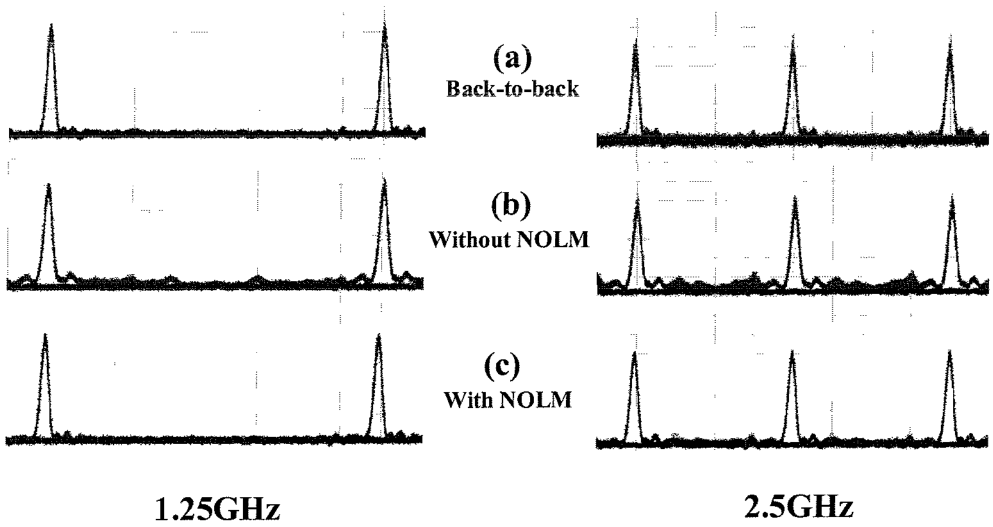

Figure 2.10: Eye diagrams of (a) the input 2.5ps pulses, (b) the pulses after matched filtering and (c) the matched filtered pulses after nonlinear switching by the NOLM for the data rates of 1.25 GHz and 2.5 GHz, each (100 ps/div).

The benefits of the pedestal rejection from a system perspective are highlighted in Fig. 2.11. The previously observed power penalties associated with the matched filtering are entirely eliminated. This is true even in the presence of considerable autocorrelation tail overlap at the bit-rate of 2.5 Gbit/s. Note again that for both data rates there was no power penalty associated with transmitting the coded bits over the 25 km dispersion-compensated transmission line.

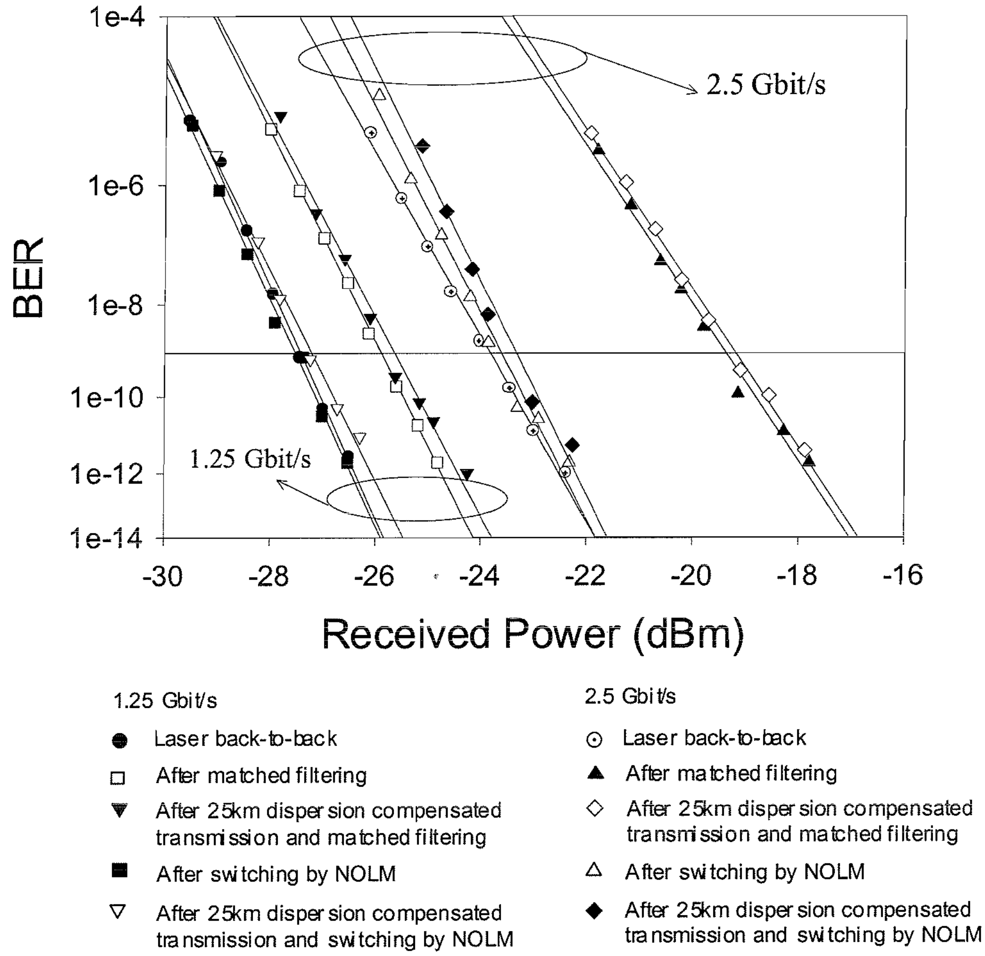

Figure 2.11: Measured BER versus received optical power for single-user operation at 1.25 Gbit/s and 2.5 Gbit/s.

These results are significant from a single-channel data rate perspective since they show that use of a NOLM to filter intra-channel coherence noise can allow for higher data rates than possible with simple matched filtering alone. To investigate this aspect further, experiments at a bit-rate of 10 Gbit/s were performed. At this data rate a given bit-slot receives contributions from as many as 16 neighbouring data bits, resulting in considerable interference noise. The eye diagrams obtained with and without the use of the NOLM are shown in Fig. 2.12(a) and highlight the significant performance improvements that can be obtained by nonlinear processing of the signal. After simple matched filtering alone at 10 Gbit/s the eye is completely closed, however after nonlinear processing a clear, open eye is restored. The system performance benefits were again quantified by BER measurements as shown in Fig. 2.12(b).

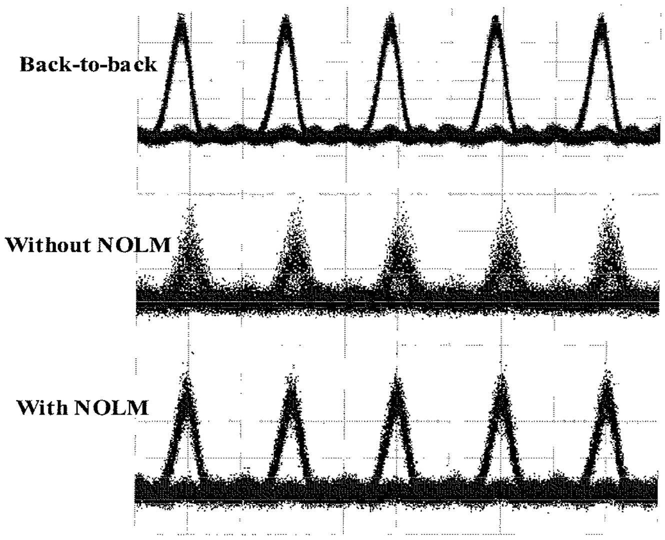

(a)

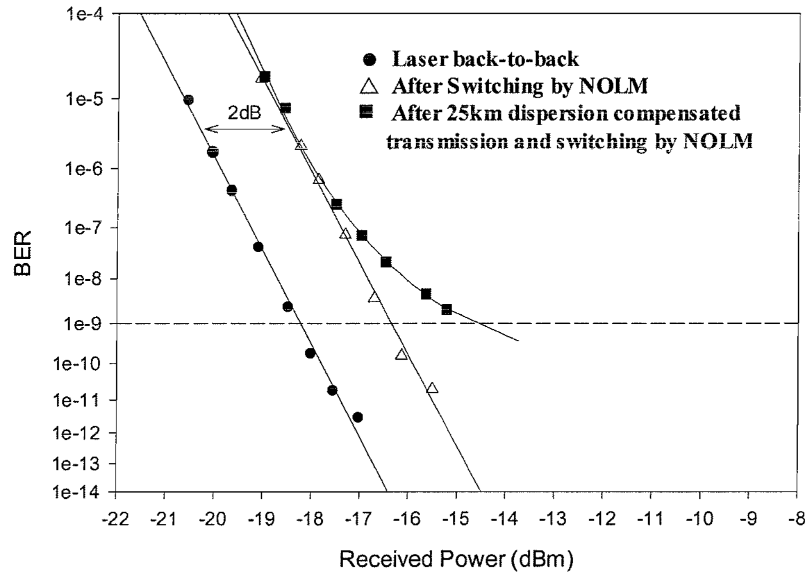

(b)

Figure 2.12: For single-channel operation at 10 Gbit/s, (a) eye diagrams (50 ps/div) and (b) BER versus received optical power.

Without the NOLM it was impossible to measure a meaningful error rate, however with the NOLM error-free performance was obtained albeit with a power penalty of ~2 dB. Interestingly though in this instance an error floor at the 10^{-9} BER level was observed after transmission through the dispersion compensated transmission line. Whilst the cause of this error floor has yet to be fully established, it is not considered to be fundamental to the technique itself but is believed to be associated with the additional loss of the transmission line (~10 dB) and the specifics of the noise characteristics of the high-power (20 dBm) Er^{3+}/Yb^{3+}amplifier used for this particular experiment.

2.3.2 Multi-User Operation (2-channel)

The experimental setup was next reconfigured for multi-user operation by reconnecting grating C2. System tests were performed at the data repetition rates of 1.25 Gbit/s and 2.5 Gbit/s. The pulses in each channel were set to fully overlap temporally at the detector so as to maximize the impact of interchannel interference.

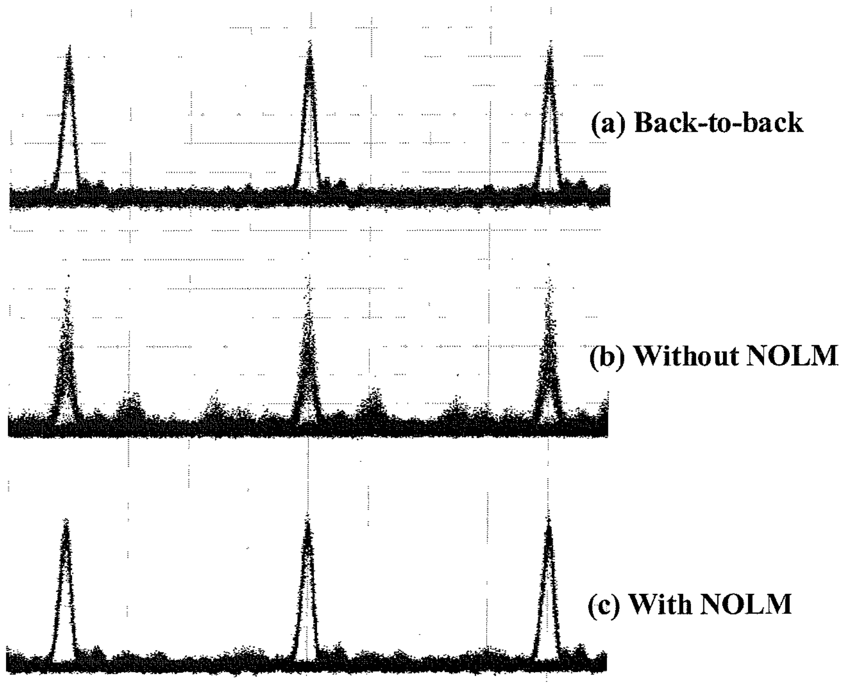

Figure 2.13: Eye diagrams for 2-channel operation at 2.5 Gbit/s (100 ps/div).

As can be seen comparing the eye diagrams in Fig. 2.13 (a) and (b) the temporal overlap of the two orthogonal codes results in severe interference noise at the receiver without the NOLM in place. However, as can be seen in Fig. 2.13 (c) the quality of the eye opening is again drastically improved by nonlinear filtering of the matched filtered signal, resulting in a substantial improvement in the BER performance. The measured BER plots are summarised in Fig. 2.14.

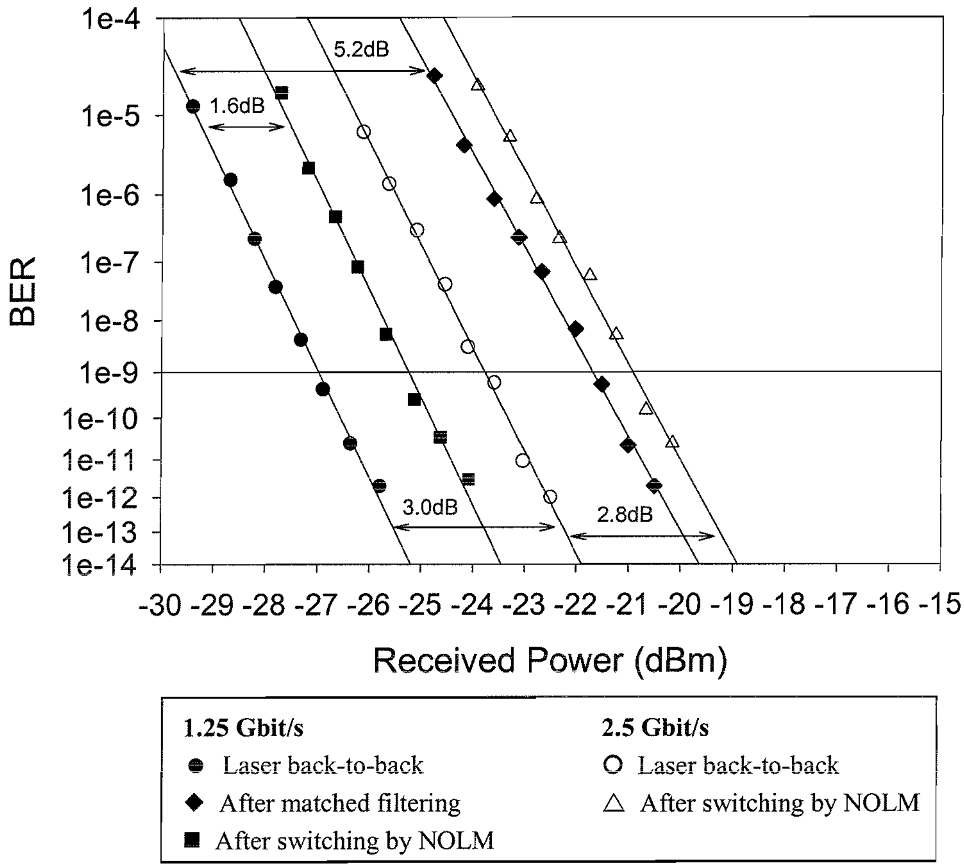

Figure 2.14: Measured BER versus received optical power for 2-channel operation at 1.25 Gbit/s and 2.5 Gbit/s.

For a data rate of 1.25 Gbit/s error-free operation with a 3.6 dB power penalty reduction relative to simple matched filtering alone is obtained through the use of the NOLM. The residual power penalty of ~1.5 dB is comparable to that achieved previously for single channel operation without the NOLM. The penalty in the two channel experiments is believed to be due primarily to the contribution to the received average power made by imperfect suppression of the second ('orthogonal') channel by the NOLM. The benefits of using the NOLM at the higher data rate of 2.5 Gbit/s are even more manifest. In this instance it was not possible to get error free operation without the use of the NOLM. The power penalty relative to the back to back in this instance was 2.8 dB, and which again was similar to that previously obtained for conventional single channel operation at this data rate. Note that as previously discussed the individual pattern recognition signatures overlap at a data rate of 2.5 Gbit/s providing an additional element of intrachannel interference noise, and hence the slightly increased power penalty relative to the 1.25 Gbit/s case in which no such overlap occurs.

2.4 Conclusion

The benefits to be obtained from incorporating a nonlinear switch (in this case a NOLM) within SSFBG based OCDMA and associated all-optical processing and code recognition schemes, have been numerically and experimentally reported. Error-free, penalty-free operation of a 63-chip, 160 Gchip/s OCDMA transmitter/receiver was reliably obtained through the addition of a simple nonlinear optical switch. In this experiment a fibre based NOLM was used however, semiconductor based nonlinear devices should offer similar system benefits. The improved performance observed at the repetition rate of 10 Gbit/s as well as both at 2.5 Gbit/s and 1.25 Gbit/s, offers the possibility of higher capacity data delivery than previously considered viable for coherent, direct-sequence OCDMA systems. Moreover the fact that error-free and penalty-free operation in two channel multiplexing experiments has been achieved, implies that the approach should give equivalent system benefits when used in OCDMA systems operating under more significant multi-user operation. Indeed the use of a NOLM in 4-channel OCDMA experiments has been subsequently demonstrated [2.17] and a NOLM for pulse quality restoration has been successfully used to allow bit regeneration and recoding within an IP node [2.18]. The above experiments represent just one example of the sorts of optical processing function that will be enabled by the combination of SSFBG technology and nonlinear optical devices.

The next two Chapters describe the use of SSFBG's to improve the switching characteristics of a nonlinear optical switch.

2.5 References

[2.1] K. Kitayama, and N. Wada, "Photonic IP routing," *IEEE Photon. Technol. lett.*, vol.11, no.12, pp.1689-1691, 1999.

[2.2] I. Saeki, S. Nishi, and K. Murakami, "All-optical code division multiplexing switching network based on self-routing principle," in *IEICE Trans. Commun.*, vol.E82-B, no.2, pp.239-245, 1999.

[2.3] W. C. Y. Lee, "Overview of cellular CDMA," *IEEE Trans. Veh. Technol.*, vol.40, no.2, pp.291-302, 1991.

[2.4] P. C. Teh, P. Petropoulos, M. Ibsen and D. J. Richardson, "A comparative study of the performance of seven- and 63-chip optical code-division multiple-access encoders and decoders based on superstructured fiber Bragg gratings," *J. Lightwave Technol.*, vol.19, no.9, pp.1352-1365, 2001.

[2.5] N. Wada, and K. Kitayama, "A 10Gb/s optical code division multiplexing using 8-chip optical bipolar code and coherent detection", *J. Lightwave Technol.*, vol.17, no.10, pp.1758-1765, 1999.

[2.6] D. B. Hunter, and R. A. Minasian, "Programmable high-speed optical code recognition using fiber Bragg grating arrays," *Electron. Lett.*, vol.35, no.5, pp.412-414, 1999.

[2.7] C. -C. Chang, H. P. Sardesai, and A. M. Weiner, "Code-division multiple-access encoding and decoding of femtosecond optical pulses over a 2.5km fiber link," *IEEE Photon. Technol. Lett.*, vol.10, no.1, pp.171-173, 1998.

[2.8] K. P. Jackson, S. A. Newton, B. Moslehi, M. Tur, C. C. Cutler, J. W. Goodman, and H. J. Shaw, "Optical fiber delay-line signal processing," *IEEE Trans. Microwave Theory Tech.*, vol. MTT-33, no.3, pp.193-209, 1985.

[2.9] P. C. Teh, P. Petropoulos, M. Ibsen, and D. J. Richardson, "160Gbit/s, 64-bit all-optical code generation and recognition using superstructured fiber Bragg gratings", in *Proc. European Conference on Optical Communication (ECOC'2000),* 2000, vol.1, pp.13-14.

[2.10] A. L. Steele, "Pulse compression by an optical fiber loop mirror constructed from two different fibers," *Electron. Lett.*, vol.29, no.22, pp.1972-1974, 1993.

[2.11] I. Y. Krushchev, I.D. Philips, A. D. Ellis, R. J. Manning, D. Nesset, D. G.

Moodie. R. V. Penty, and I. H. White, "OTDM applications of dispersion-imbalanced fiber loop mirror," *Electron. Lett.*, vol.35, no.14, pp.1183-1185, 1999.

[2.12] D. M. Patrick, A. D. Ellis, and D. M. Spirit, "Bit-rate flexible all-optical demultiplexing using a nonlinear optical loop mirror," *Electron. Lett.*, vol.29, no.8, pp.702-703, 1993.

[2.13] B. -E. Olsson, and P. A. Andrekson, "Noise filtering with the nonlinear optical loop mirror," *J. Lightwave Technol.*, vol.13, no. 2, pp.213-215, 1995.

[2.14] G. P. Agrawal, *Nonlinear fiber optics*, Academic Press, 1995, pp.43-55.

[2.15] L. Chusseau and E. Delevaque, "250-fs optical pulse generation by simultaneous soliton compression and shaping in a nonlinear optical loop mirror including a weak attenuation," *Optics Lett.*, vol.19, no.10, pp.734-736, 1994.

[2.16] E. H. Dinan, and B. Jabbari, "Spreading codes for direct sequence CDMA and wideband CDMA cellular networks," *IEEE Commun. Mag.*, pp.48-54, September 1998.

[2.17] P. C. Teh, M. Ibsen, L.B. Fu, J. H. Lee, Z. Yusoff, and D. J. Richardson, "A 16-channel OCDMA system (4 OCDMA X 4WDM) based on 16-chip, 20 Gchip/s superstructure fibre Bragg gratings and DFB laser transmitters," *Optical Fiber Communications Conference (OFC'2001)*, ThEE1, Anaheim USA, March 2002 (Invited paper).

[2.18] B. C. Thomsen, P. C. Teh, M. Ibsen, J. H. Lee, and D. J. Richardson, "A multi-hop optical packet switching demonstration employing all-optical grating based header generation and recognition," *28th European Conference on Optical Communication (ECOC'2002),* 5.5.3, Copenhagen Denmark, September 2002.

CHAPTER THREE

ALL-OPTICAL MODULATION AND DEMULTIPLEXING SYSTEMS WITH SIGNIFICANT TIMING JITTER TOLERANCE THROUGH INCORPORATION OF PULSE-SHAPING FIBRE BRAGG GRATINGS

This Chapter discusses timing jitter issue in high-speed optical time division multiplexing (OTDM) systems and reports the use of a superstructured fibre Bragg grating based pulse-shaper to achieve a rectangular switching window in an optical demultiplexer to provide a 5-10-fold reduction in timing jitter sensitivity.

This Chapter is organised as follows. Section 3.1 presents a brief introduction to timing jitter in high-speed OTDM systems and the concept of a switching window. Section 3.2 describes the system configurations for the OTDM switching experiments I conducted and the general principle of the pulse-shaping technique that I used to reduce the timing jitter sensitivity based on the use of a superstructured fibre Bragg grating. Experimental results are then presented for grating based square pulse generation. In Section 3.3 I show the results of a preliminary theoretical study into a NOLM based wavelength conversion technique which allowed me to obtain a pair of synchronised solitons at different wavelengths as required to undertake my experiments. Calculations are presented for wavelength converted 10 GHz pulse streams from an optimally designed NOLM and these are then compared with the experimental results. In Section 3.4 the results of detailed system experiments using 20 ps wide square control pulses in optical switches based on either a fibre NOLM or four-wave mixing in the SOA, are presented. The performance benefits achieved are then quantified from a system perspective and are compared to those of short control pulse driven switches. In Section 3.5, conclusions are drawn regarding the results, and further extensions and applications of the technology are discussed.

3.1 Timing Jitter Issue and Switching Window in High-Speed OTDM Systems

Single channel data rates approaching the Tbit/s level have now been reported for optical time division multiplexing (OTDM) systems placing increased demands and tolerances on the techniques used to multiplex and demultiplex the optical data bits [3.1]. Consider for example the case of optical demultiplexing. As OTDM data rates increase, and the pulses used get correspondingly shorter, the synchronization requirements placed on the locally generated pulses used to control the switch operation can become a limiting practical issue. The key to reducing time jitter tolerance in such devices is to establish a rectangular temporal switching window [3.2, 3.3]. This reduces the absolute accuracy for temporal bit alignment and provides optimal resilience to timing jitter-induced errors.

Fig. 3.1 shows a comparison of the operation of an optical switch with a conventional switching window (assumed to approximate to a Gaussian) and a switch with a rectangular shape switching window. Conventional optical switches are seen to generate a large intensity variation of the output signals with relative timing drift between the input and timing signals due to the window shape, which can then result in a significant system power penalty. However, a flat-top rectangular switching window enables us to operate the switching system with considerable tolerance to relative timing difference over relatively wide timing drift ranges. This provides increased resilience to timing jitter.

A fibre based nonlinear optical loop mirror (NOLM) demultiplexing scheme that provides good ultrafast performance and tolerance to timing-jitter of either, or both, of the control and data signals has been demonstrated previously [3.3, 3.4]. This scheme uses the difference in group velocity and the resultant 'walk-off' between the control and data signals within the nonlinear medium to define the rectangular switching window. This consequently requires tight specification and control of both the data and signal wavelengths, and the dispersion characteristics of the fibre. Whilst this approach is applicable to fibre based switches it is complex and cannot be applied to switches based on highly nonlinear semiconductors and within which there are no appreciable dispersive propagation effects over the length scales of relevance. Simple, robust techniques that can help reduce time jitter tolerances, and that are applicable to a variety of switching mechanisms, are thus of great interest.

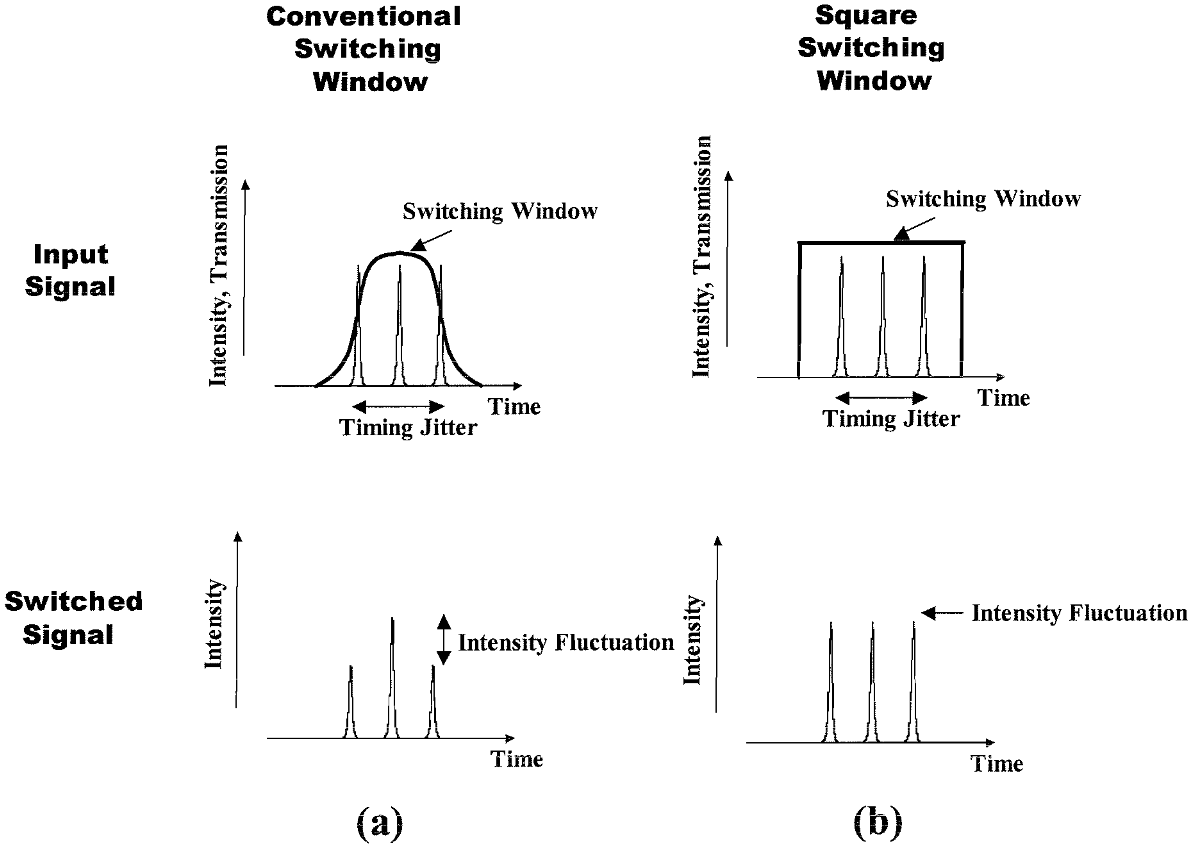

Figure 3.1: Comparison of functionality between conventional switching window and rectangular shape switching window

The most obvious way to generate a rectangular switching window is to use rectangular control pulses and to eliminate, or at least minimize, all dispersive effects within the device. However, until recently it has not been straightforward to reliably generate suitably short (<20 ps) rectangular pulses.

In the following Sections, the use of superstructured fibre Bragg gratings (SSFBG's) to convert the output of an actively mode-locked, 2.5 ps fibre laser, a source of short pulses of a well-defined soliton shape, to 20 ps rectangular pulses [3.5] is demonstrated. These pulses are then used to control the operation of two sorts of nonlinear switch. The basic principle of square pulse OTDM switching by a SSFBG is illustrated in Fig. 3.2. High quality, ~15-20 ps rectangular switching windows are obtained, providing +/-7 ps, 15 ps timing jitter tolerance, in switches based on both the Kerr effect in dispersion shifted fibre (DSF), and four-wave mixing in a semiconductor amplifier (SOA).

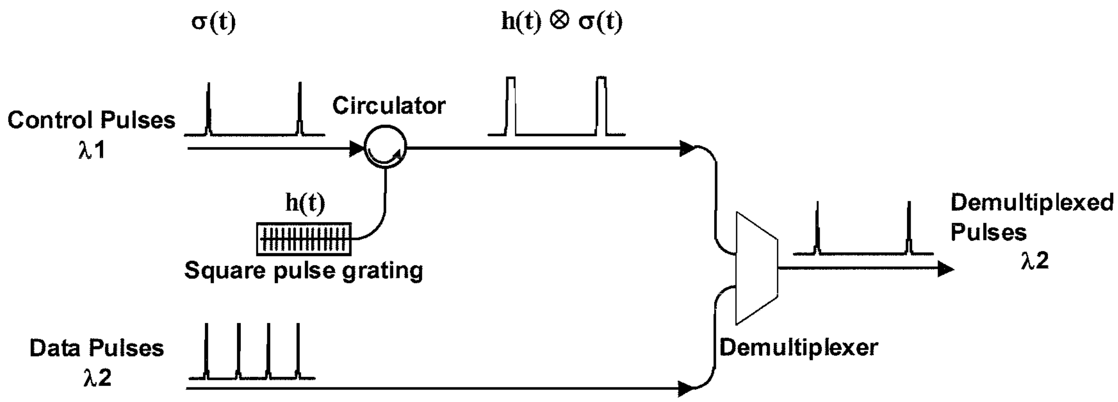

Figure 3.2: Principle of square pulse OTDM switching by a SSFBG.

3.2 Experiment Setup and Pulse Shaping Using a Fibre Bragg Grating

The experimental setup is shown in Fig. 3.3. Pulses from a 2.5 ps, 10 GHz, regeneratively mode locked erbium fibre ring laser (EFRL) operating at 1557nm were first split using a 50:50 coupler into two separate channels. The first channel was modulated to provide a pseudorandom data sequence of 2.5 ps pulses at 2.5 Gbit/s. These pulses were then fed onto a pulse-shaping SSFBG fabricated with the correct phase and amplitude reflectivity profile to convert the 2.5 ps solitons into 20 ps rectangular pulses.

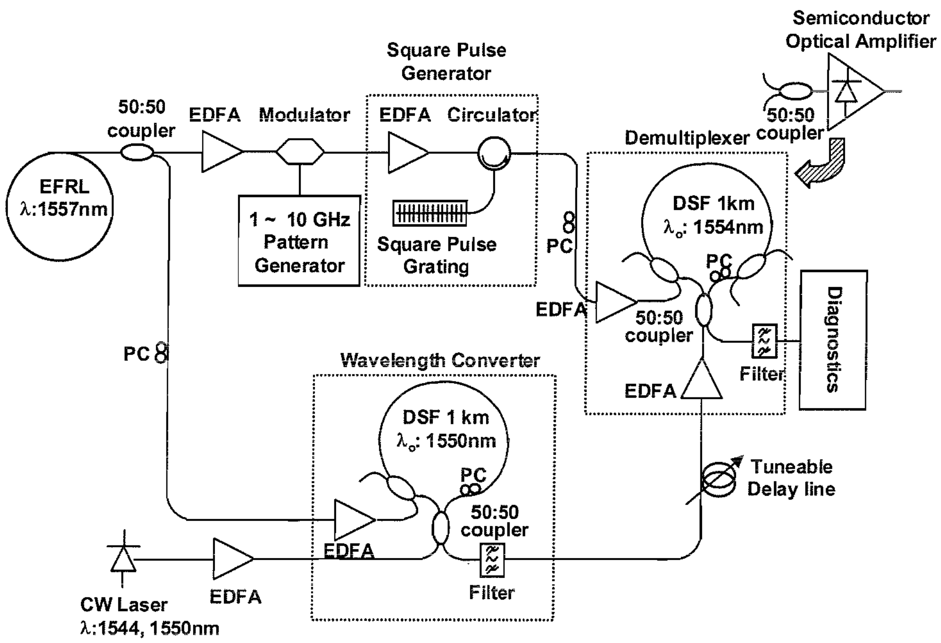

Figure 3.3: Experimental setup.

Fig. 3.4(a) shows both the theoretical and experimental spectral response of a superstructured fibre Bragg grating for the square pulse generation. 13 spectral lobes were accommodated to obtain a close approximation to an ideal Sinc function ($\sin(x)/x$) which is the counterpart in the spectral domain to a temporal square shape pulse. The corresponding refractive index superstructure required to achieve this response is shown in Fig. 3.4(b) and highlights the precision required and achieved within the grating writing process. The temporal length of the grating is 100 ps, corresponding to a grating length of 10.3 mm. The characteristics of the particular grating and details of how it both operates and performs as a rectangular pulse generator have been previously reported [3.5]. The measured SHG triangular autocorrelation profile of the rectangular pulses so generated is shown in Fig. 3.5(a), along with the calculated shape of square pulses.

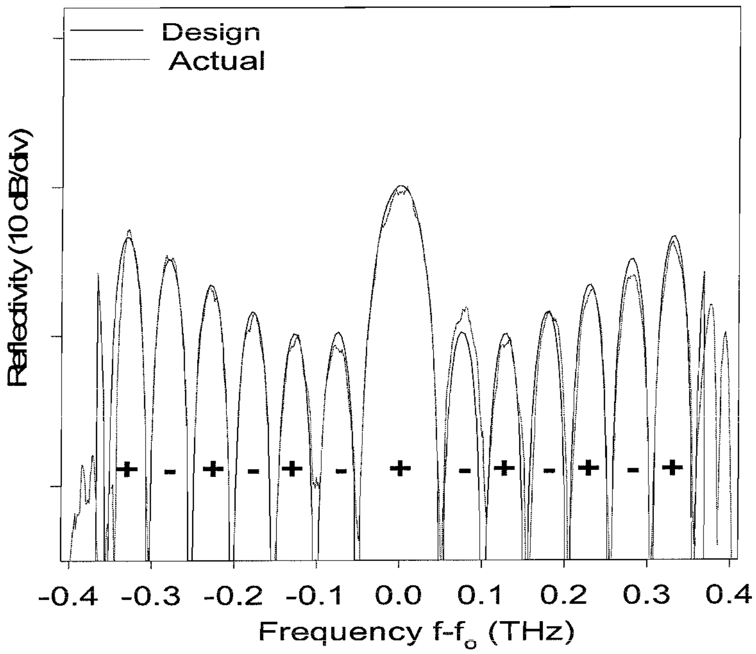

(a)

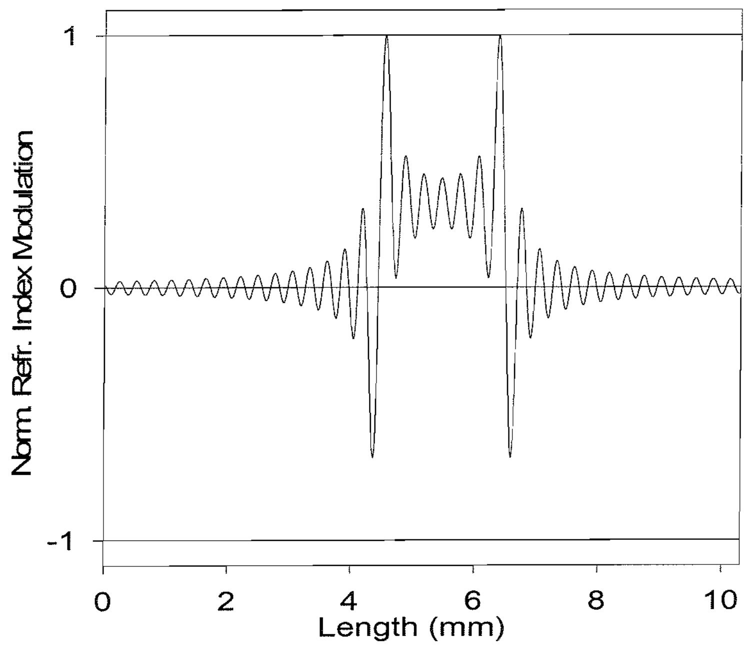

(b)

Figure 3.4: (a) Spectral response of the SSFBG's performing pulse shaping of solitons into square pulses, and (b) the corresponding refractive index modulation profile.

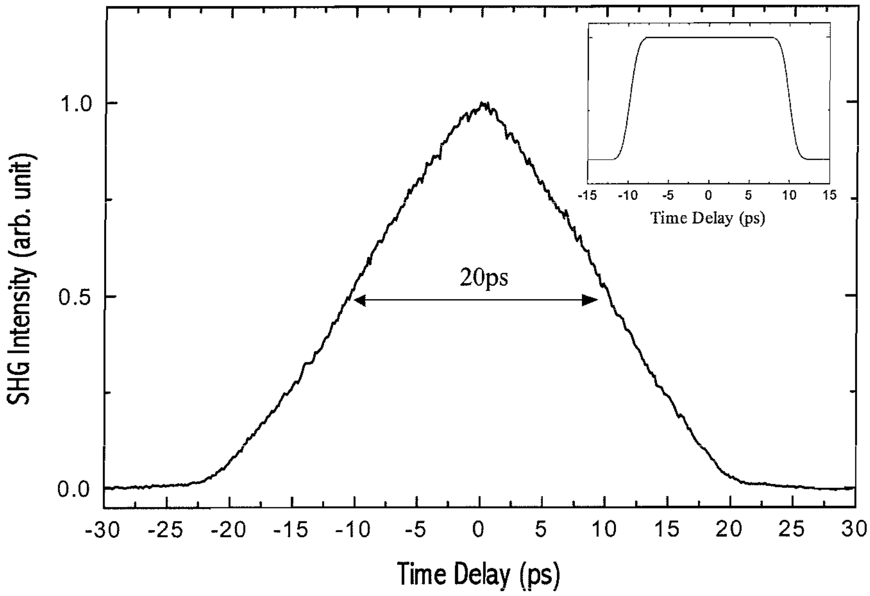

(a)

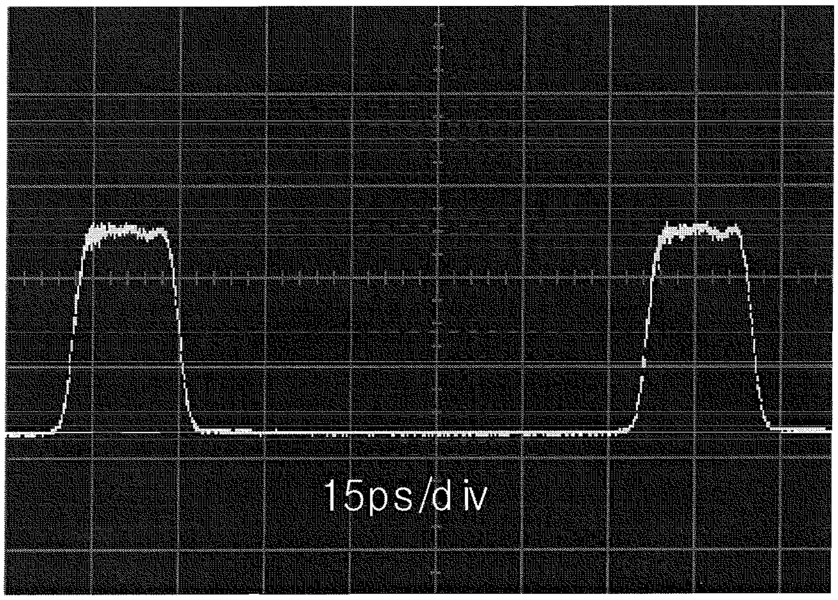

(b)

Figure 3.5: (a) Measured autocorrelation profile of the rectangular pulses generated through a SSFBG, inset: the calculated shape of square pulses. (b) Measured optical sampling scope trace of the rectangular pulses with 2 ps temporal resolution.

A 20 ps FWHM triangular trace represents a rectangular pulse shape as wide. To resolve in real time the formation of rectangular pulses, the optical sampling oscilloscope measurement based on four-wave mixing in highly nonlinear fibre was performed with 2 ps temporal resolution. The high quality of the 20 ps rectangular pulses was readily confirmed as shown in Fig. 3.5(b). The detailed information on the optical sampling oscilloscope used is fully described in Ref. [3.6]. The amplitude contrast of 14 dB between the central peak and the first side lobe peak in the spectrum of Fig. 3.6 is comparable to the value of 13.3 dB of an ideal Sinc function, which means that high quality square pulses are generated using the superstructured fibre Bragg grating.

The other component of the 10 GHz, 2.5 ps pulse stream split-off from the laser was first amplified and then fed to the control port of a dual-wavelength NOLM that was employed as a wavelength converter (WC). This nonlinear switch allowed us to modulate the output of a continuous-wave DFB laser using the 1557 nm control pulses. By appropriately setting the loss and polarisation of light within the WC-NOLM, and filtering out the 1557 nm control pulses at the loop output, a 10 GHz train of high-quality, 3.5 ps pulses was generated at 1544 nm. Importantly, for this demonstration, this pulse train was synchronised to the 2.5 Gbit/s data stream generated within the first channel. By generating two synchronised pulse streams at two different wavelengths, the switching window characteristics of two-wavelength nonlinear switches controlled by either 2.5 Gbit/s, 20 ps rectangular pulses, or 2.5 ps soliton pulses at 1557 nm could now be measured.

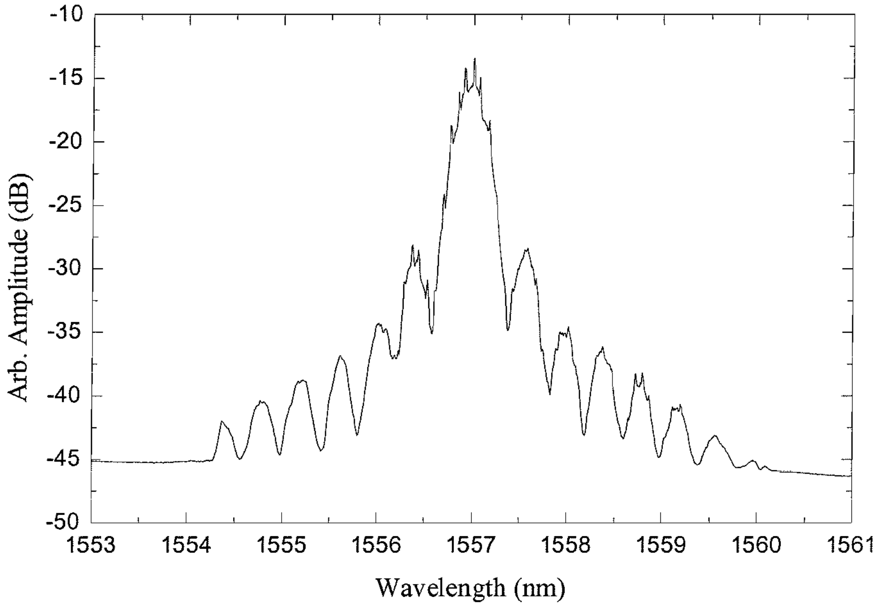

Figure 3.6: Measured spectral shape of the rectangular pulses.

3.3 Wavelength Conversion through a Nonlinear Optical Loop Mirror

To obtain synchronised data pulse streams from the soliton laser pulses used for the control of the data-demultiplexers, a wavelength conversion technique using a dual-wavelength nonlinear optical loop mirror (NOLM) was adopted. Compared to other more common wavelength conversion techniques which are based on cross-phase modulation (XPM) [3.7], cross-gain modulation (XGM) [3.8], four-wave mixing (FWM) [3.9] in semiconductor based active devices, fibre NOLM based wavelength converters offer significant advantages for applications in high capacity telecommunication systems [3.10]. For example using optical fibres, Tbit/s switching operation is achievable due to the ultrafast optical nonlinearity inside an optical fibre, wide wavelength tuning ranges can be achieved with proper control of the walk-off time between control pulses and probe signal, and the pulses can be of a very high quality.

In order to establish the optimum design of a WC-NOLM, a wavelength converter was first modelled as a function of the key parameters of the NOLM such as the coupling ratio, dispersion, length of fibre, walk-off time of the probe signal relative to the control pulses, and the peak power of control pulses. Propagation of both control pulses and a probe signal within the NOLM was modelled using two coupled nonlinear Schrödinger equations with group velocity, group velocity dispersion, and self-phase modulation [3.11] described by Eq. (3.1) and Eq. (3.2).

$$\frac{\partial A_1}{\partial z}+\frac{1}{v_{g1}}\frac{\partial A_1}{\partial t}+\frac{i}{2}\beta_{21}\frac{\partial^2 A_1}{\partial t^2}-\frac{1}{6}\beta_{31}\frac{\partial^3 A_1}{\partial t^3}+\frac{\alpha_1}{2}A_1=i\gamma_1\left(|A_1|^2+2|A_2|^2\right)A_1 \quad ....(3.1)$$

$$\frac{\partial A_2}{\partial z}+\frac{1}{v_{g2}}\frac{\partial A_2}{\partial t}+\frac{i}{2}\beta_{22}\frac{\partial^2 A_2}{\partial t^2}-\frac{1}{6}\beta_{32}\frac{\partial^3 A_2}{\partial t^3}+\frac{\alpha_2}{2}A_2=i\gamma_2\left(|A_2|^2+2|A_1|^2\right)A_2 \quad ....(3.2)$$

where the pulse amplitudes $A_{1,2}$ are normalized such that $|A_{1,2}|^2$ represent the optical field strength for the probe and control signals, each within the fibre. $v_{g1,2}$ are the group delays, $\beta_{21,22}$ are the first order group velocity dispersions (GVD's), and $\beta_{31,32}$ are the second order GVD's. $\alpha_{1,2}$ represent the absorption coefficient of optical power in the fibre and corresponds to 0.25dB/km, and $\gamma_{1,2} = \frac{n_2 \omega_{1,2}}{c A_{eff}}$ are the nonlinearity coefficients where $n_2 = 2.6 \times 10^{-20}\, m^2/W$ and $A_{eff} = 50 \mu m^2$ is the effective area of the fibre.

The above coupled equations were solved using the symmetrised split step Fourier method [3.11]. A dual wavelength NOLM was modelled to be constructed from two 50:50 couplers and a length of dispersion shifted fibre (DSF) (See Fig. 3.3). A probe wavelength of 1544 nm was used, corresponding to the wavelength of a particular DFB laser available to us. The control wavelength was chosen to be 1557 nm. The wavelength separation (13 nm) was adequate to allow sufficient extinction between control and probe beams at the switch output using a 1.3 nm filter available to us.

The 10 GHz soliton control pulses split from the ring laser were launched into the loop through a 50:50 coupler (The coupler would ideally have been replaced with a 1544/1557 nm WDM coupler if one had been available) into the loop. DSF with a zero dispersion wavelength (λ_0) of 1550 nm was chosen within the loop so as to reduce walk-off effects between the control pulses and the probe signal. The measured dispersion slope ($dD/d\lambda$) was 0.074 ps/nm^2/km and the fibre length was 1km.

Fig. 3.7(a) shows both experimental and theoretical SHG autocorrelation functions of the wavelength converted signal and the original soliton control. Excellent agreement between theory and experiment is observed in terms of pulse shape and the duration of the output pulses from the WC-NOLM. The temporal width of the wavelength converted pulses is ~3.5 ps which is larger than the 2.5 ps FWHM of the soliton control pulses. This originates mainly due to walk-off effects caused by the difference in group velocity between the control pulses and the CW-probe signal. The high quality of the converted pulses which exhibits a spectral modulation depth of more than 20 dB is clearly evident from the spectrum in Fig. 3.7(b).

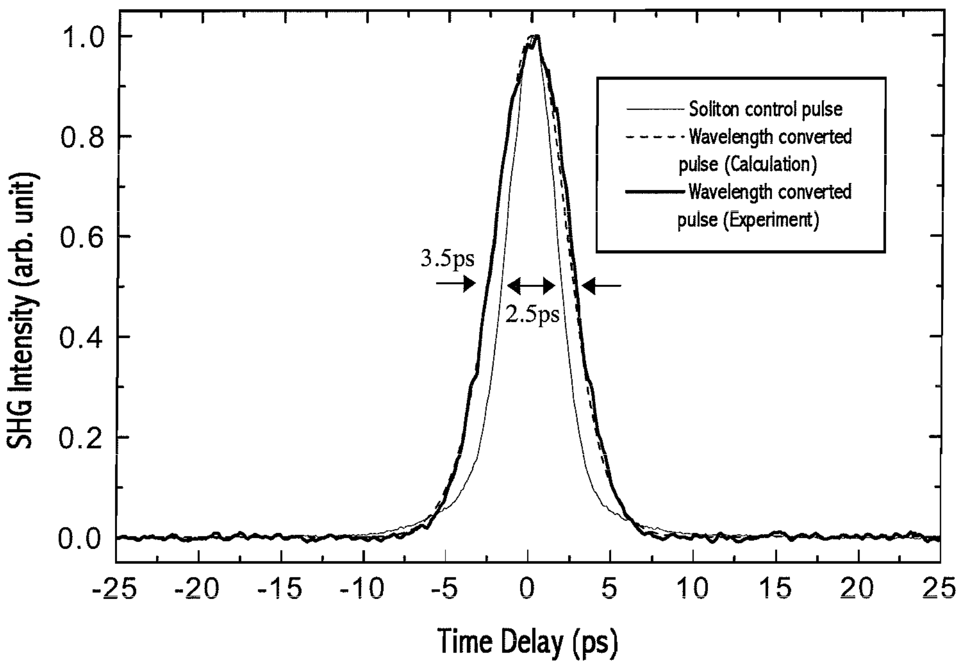

(a)

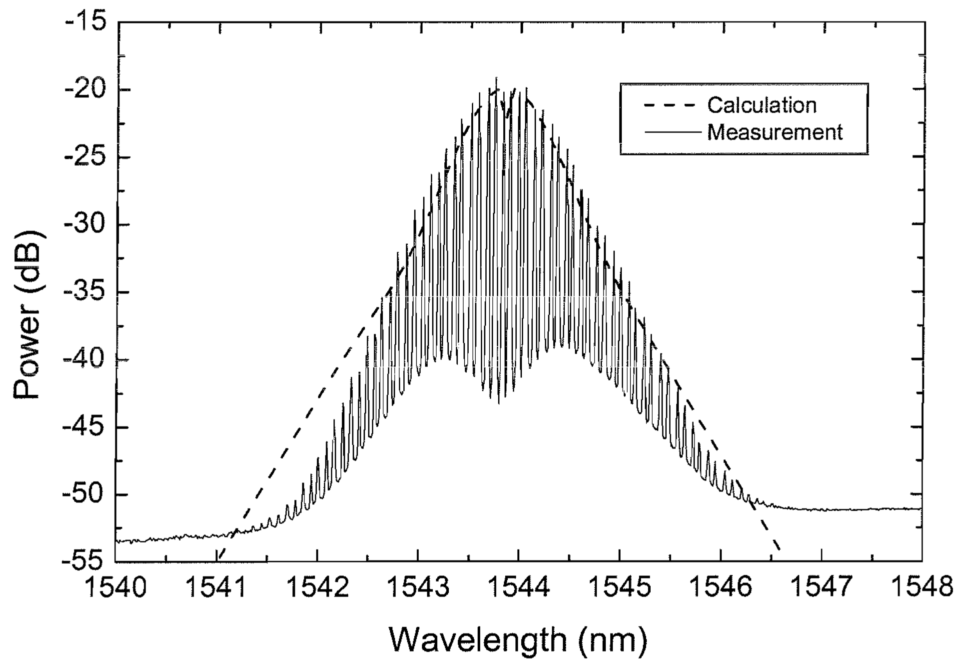

(b)

Figure 3.7: (a) Experimental and theoretical SHG autocorrelation functions of a wavelength converted signal with that of original soliton control pulses. (b) Measured spectrum of the wavelength converted signal.

3.4 Improvement of System Performance through the Use of Square Control Pulses Generated by Reshaping Soliton Pulses Using a SSFBG

The first switch to be investigated was a dual-wavelength NOLM similar to that used for the wavelength conversion process. In this instance however, the control signal was now a data-modulated signal, and the signal to be switched was a 10 GHz train of 3.5ps optical pulses at 1544 nm. The system thus operated as an all-optical modulator in this configuration and which for convenience I refer to as an M-NOLM. Note that by reversing the input and control signals the system could be configured to act as an all-optical demultiplexer. The 1544 nm pulse train incident to the switch was first passed through a tuneable delay line to allow for adjusting the arrival time of the 1544 nm pulses relative to the rectangular control pulses. By adjusting and measuring this relative arrival time delay and monitoring the loop output at the wavelength of 1544 nm for a suitable control pulse power, the switching window of the device and its sensitivity to timing-jitter could be readily determined. I also modelled the operation of the M-NOLM switch using Eq. (3.1) and Eq. (3.2) with square switching pulses defined by the pulse-shaping SSFBG (See the inset of Fig. 3.5(a)).

Fig. 3.8 shows both the experimentally observed and theoretically predicted switching window of the M-NOLM operating at 1544 nm using both 20 ps square and 2.5 ps control pulses. A good rectangular switching characteristic with a 3 dB width of 20 ps is obtained using the rectangular control pulses as opposed to a value of 4 ps when driving the switch directly with pulses from the laser. Note the slight asymmetry in the switching window that is both predicted theoretically and observed experimentally. This arises from pulse walk-off effects between the pump and probe beams within the NOLM. The effect though is small since the DSF used in the M-NOLM had a length of only 1km, a zero-dispersion wavelength of 1554 nm, and a dispersion slope of 0.07 ps/nm^2/km. These results show that it can expected to achieve around 5 times greater tolerance to timing-jitter by converting the control pulses to rectangular pulses in this instance.

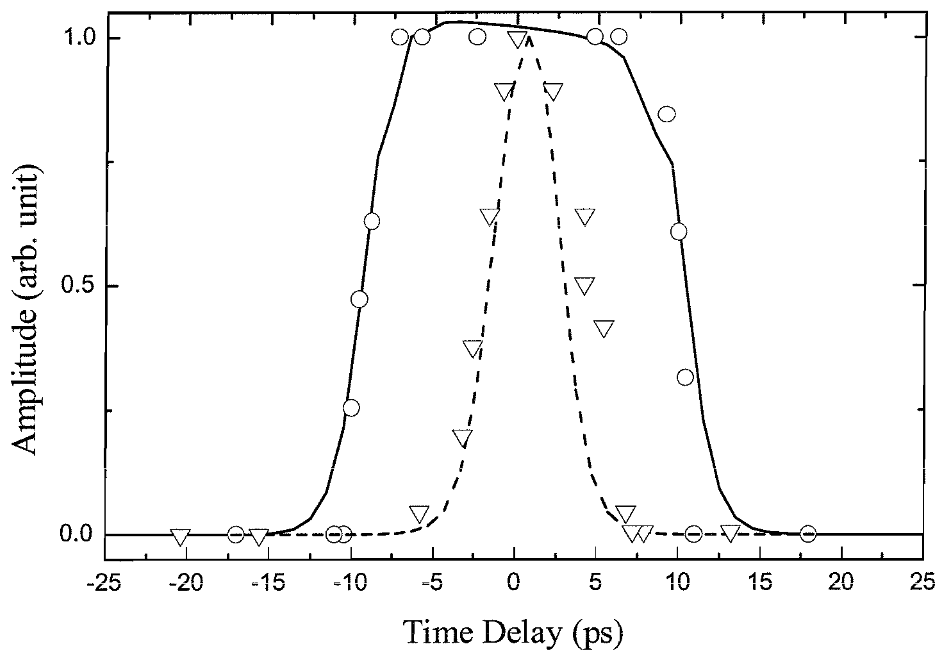

Figure 3.8: Switching windows of the NOLM based OTDM demultiplexer with respect to relative timing mismatch between control pulses and data pulses; solid line (—): calculation for rectangular control pulses, dashed line (---): calculation for soliton control pulses, circle (O): experiment for rectangular control pulses, triangle (▽): experiment for soliton control pulses.

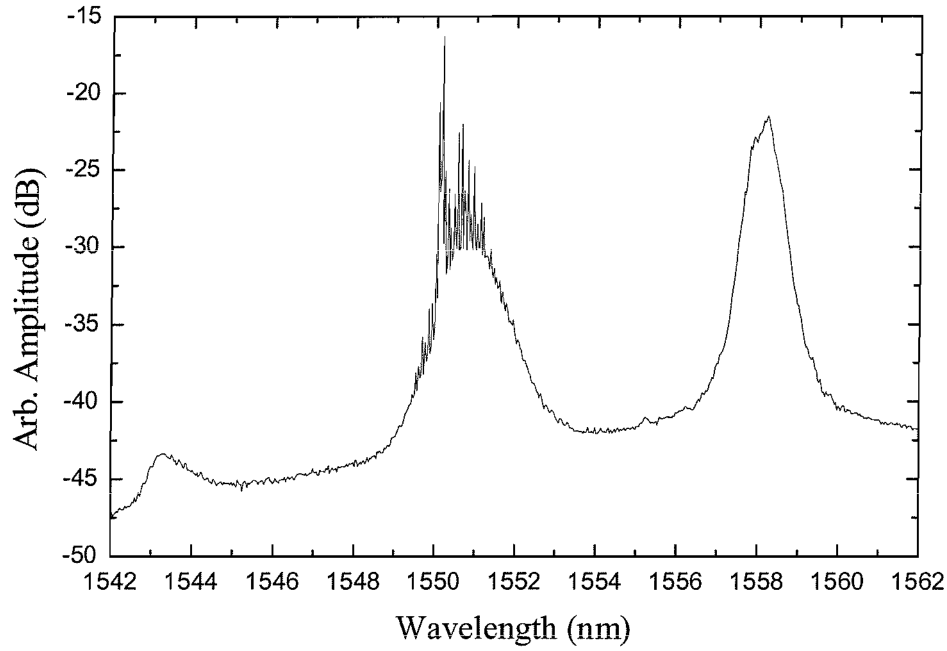

(a)

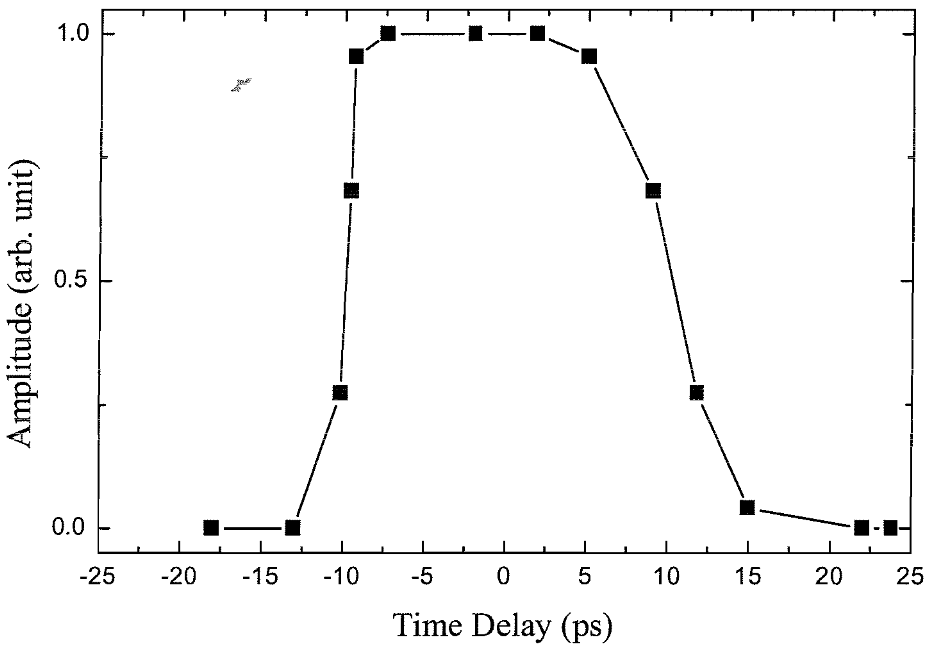

(b)

Figure 3.9: (a) Output spectrum of the SOA after four-wave mixing process. (b) experimentally determined switching window of a SOA based switch.

Next the switching window of a SOA based switch employing four-wave mixing (FWM) as the optical switching mechanism, was investigated. The experimental set up was essentially the same as that used for the NOLM. It is to be appreciated that the optimum switching powers required for the SOA based scheme (~7 dBm average power at 10 Gbit/s) were substantially lower than those required for the NOLM (~15 dBm at 2.5 Gbit/s). Note also that the wavelength of the 10 GHz switching pulses had to be changed from 1544 nm to 1550 nm to achieve an adequate phase matching condition within the SOA. A demultiplexed FWM signal is evidently observed at the wavelength of 1543 nm, as shown in the SOA output spectrum of Fig. 3.8(a). The experimentally measured switching window is plotted in Fig. 3.8(b). As with the fibre based switch an excellent rectangular switching window is obtained, allowing for timing jitter tolerance of +/-7 ps.

In order to confirm the system impact of using rectangular control pulses BER measurements on the M-NOLM switch performance were carried out. These results are summarised in Fig. 3.9. At first the BER was measured on the optically modulated signals at the fixed received power of –20 dBm as a function of relative time delay for both the switched output using 20 ps square control pulses and switched output using 2.5 ps soliton control pulses. This allowed us to assess the relative timing jitter tolerance of the system. Error-free, penalty-free performance was readily achieved over a +/-7 ps delay range for the rectangular pulse driven switch versus a +/-1 ps range for the switch driven directly with the 2.5 ps laser pulses as shown in Fig. 3.10(a). To ensure reasonable comparison under the same operating conditions of the system BER measurements on optically modulated signals were performed as a function of received optical power under optimal time synchronization between control pulses and data pulses for both switches. No power penalty with respect to laser back-to-back is observed as shown in Fig. 3.10(b), which confirms the system performance comparison was performed on a reasonably equivalent basis for both a square pulse driven and a soliton pulse driven switch.

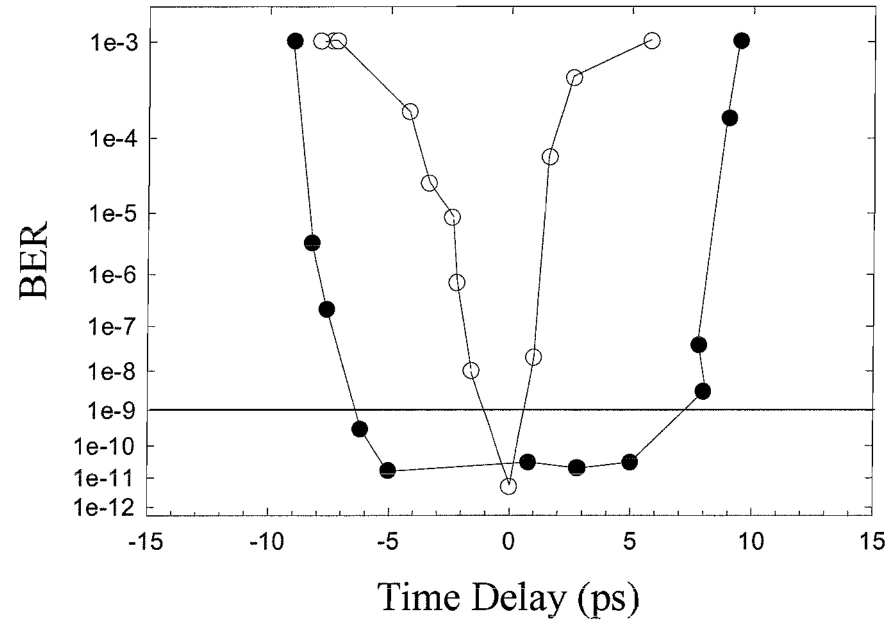

(a)

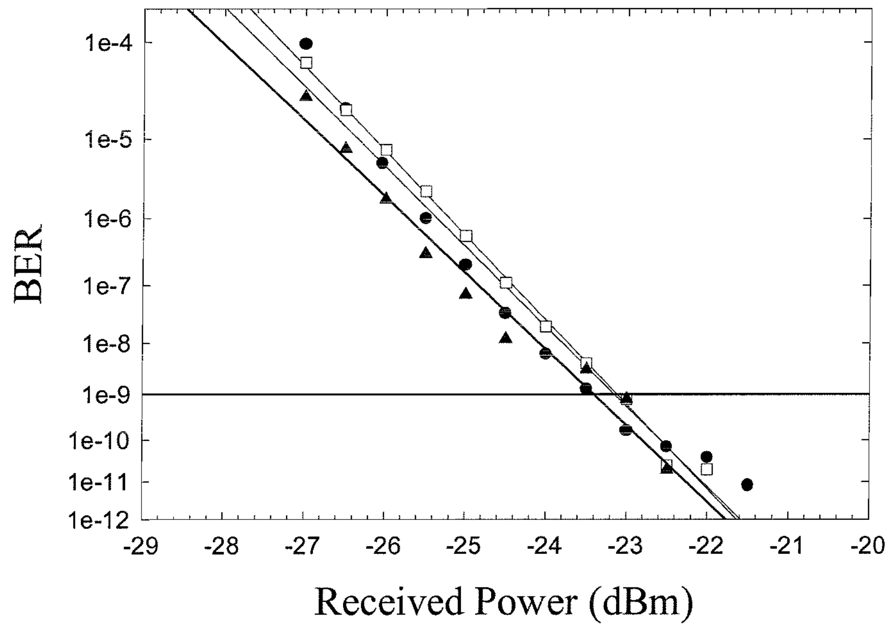

(b)

Figure 3.10: (a) BER on the optically modulated signals at the fixed received power of -20 dBm (●: 20 ps rectangular control pulses, O: 2.5ps soliton control pulses), and (b) BER as a function of received power under optimal time synchronization between control pulses and data pulses (□: wavelength converted signal, ●: switched output using 20 ps square control pulses, ▲: switched output using 2.5 ps soliton control pulses).

3.5 Conclusion

I have experimentally demonstrated that SSFBG's can be used to reliably re-shape ultrashort optical pulses in order to provide more optimal and jitter-tolerant operation of nonlinear optical switches based on both fibre and semiconductor nonlinear components. This approach could be particularly attractive for use with SOA based switching devices for which there is no easy and ready way of shaping the switching window other than through direct control of the pulse shape. The tera-hertz optical asymmetric demultiplexer (TOAD) [3.12] and the ultrafast nonlinear interferometer (UNI) [3.13] are two main switches incorporating SOA's that are commonly used nowadays. Both of those switches can be designed to provide a switching window with a desired temporal width by introducing an internal delay which describes the relative difference of arrival time of the two travelling data pulses at the SOA. However, note that a flat-top, rectangular shape switching window in both cases is not easily achievable due to the nonlinearity recovery (~1 ps recovery time) associated with carrier heating and carrier density changes (1 ns recovery time) [3.14]. The next Chapter reports that the SSFBG based rectangular pulse switching technology can be readily applied for 80 Gbit/s OTDM data demultiplexing.

3.6 References

[3.1] M. Nakazawa, T. Yamamoto, and K. R. Tamura, "1.28 Tbit/s-70km OTDM transmission using third- and fourth-order simultaneously dispersion compensation with a phase modulator," in *Proc. 26th European Conference on Optical communication (ECOC'2000)*, Munich Germany, September 2000, Postdeadline paper 2.6.

[3.2] K. Uchiyama, T. Morioka, "All-optical signal processing for 160Gbit/s channel OTDM/WDM systems", in *Proc. Optical Fibre Communications Conference (OFC'2001)*, Anaheim USA, March 2001, paper ThH2.

[3.3] M. Jinno, "Effects of crosstalk and timing jitter on all-optical time-division demultiplexing using a nonlinear fiber Sagnac interferometer switch", *IEEE J. Quantum Electron.*, vol.30, no.12, pp.194-201, 1994.

[3.4] N. A. Whitaker, Jr., H. Avramopoulos, P. M. W. French, M. C. Gabriel, R. E. LaMarche, D. J. Di Giovanni, and H. M. Presby, "All-optical arbitrary demultiplexing at 2.5Gbit/s with tolerance to timing jitter," *Optics Lett.*, vol.16, no.23, pp.1838-1840, 1991.

[3.5] P. Petropoulos, M. Ibsen, A. D. Ellis, and D. J. Richardson, "Rectangular pulse generation based on pulse reshaping using a superstructured fiber Bragg gratings," *J. Lightwave Technol.*, vol.19, no.5, pp.746-752, 2001.

[3.6] F. Parmmigiani, P. Petropoulos, P. Almeida, M. Ibsen, J. H. Lee, and D. J. Richardson, "A direct assessment of the performance of pulse shaping superstructured fiber Bragg gratings using an optical sampling oscilloscope," in *Proc. Optical Fibre Communications Conference (OFC'2001)*, Atlanta USA, March 2003, paper MF36.

[3.7] A. D. Ellis, A. E. Kelly, D. Nesset, D. Pitcher, D. G. Moodie, and R. Kashap, "Error free 100Gbit/s wavelength conversion using grating assisted cross-gain modulation in 2mm long semiconductor amplifier," *Electron. Lett.*, vol.34, no.20, pp.1958-1959, 1998.

[3.8] T. Durhuus, B. Mikkelson, C. Joergensen, S. L. Danielson, and K. E. Stubkjar, "All-optical wavelength conversion by semiconductor optical amplifier," *J. Lightwave Technol.*, vol.14, no.6, pp.942-954, 1996.

[3.9] A. D'Ottavi. F. Girardin, L. Graziani, F. Martelli, P. Spano, A. Mecozzi, S. Scotti, R. Dall'Ara, J. Eckner, and G. Guekos, "Four-wave mixing in semiconductor optical amplifiers: a practical tool for wavelength conversion," *IEEE J. Select. Topics Quantum Electron.*, vol.3, no.2, pp.522-528, 1997.

[3.10] J. Yu, X. Zheng, C. Peucheret, A. T. Clausen, H. N. Poulsen, and P. Jeppsen, "40-Gb/s all-optical wavelength conversion based on a nonlinear optical loop mirror," *J. Lightwave Technol.*, vol.18, no.7, pp.1001-1006, 2000.

[3.11] G. P. Agrawal, *Nonlinear fiber optics*, Academic Press, Second edition 1995, pp. 50-55 and pp. 238-247.

[3.12] G. Toptchiyski, K. Petermann, S. Diez, E. Hillinger, C. Schmidt, R. Ludwig, and H. G. Weber, "Evaluation of switching windows for fast optically-controlled SOA switches," in *Proc. Optical Fibre Communications Conference (OFC'2000)*, Baltimore USA, March 2000, paper ThF4.

[3.13] G. Toptchiyski, S. Randel, K. Petermann, C. Schmidt, J. Berger, and H. G. Weber, "Comparison of switching windows of an all-optical 160 Gbit/s demultiplexer with base data rates of 10 Gbit/s and 40 Gbit/s," in *Proc. Optical Fibre Communications Conference (OFC'2000)*, Anaheim USA, March 2000, paper MB5.

[3.14] B. S. Robinson, K. I. Hall, "Experimental analysis of switching windows in semiconductor based all optical switches," in *Proc. Conference on Laser and Electro-Optics (CLEO'2000),* San Francisco USA, May 2000, CWK58.

CHAPTER FOUR

ALL-OPTICAL TDM DATA DEMULTIPLEXING AT 80 GBIT/S WITH SIGNIFICANT TIMING JITTER TOLERANCE USING A FIBRE BRAGG GRATING BASED RECTANGULAR PULSE SWITCHING TECHNOLOGY

In this Chapter the pulse-shaping SSFBG rectangular switching technology described in Chapter 3, is applied to reducing timing jitter sensitivity in an 80 Gbit/s OTDM demultiplexing system. Note that these measurements were made in conjunction with the COM center, Technical University of Denmark who has an 80 Gbit/s test bed.

This Chapter is organised as follows. Section 4.1 presents a brief review of various schemes to obtain timing jitter rectangular switching windows in high-speed OTDM demultiplexing systems. Section 4.2 describes the design and the characterisation of the pulse-shaping superstructured fibre Bragg grating used to convert 1.7 ps soliton pulses into 10 ps rectangular pulses. In Section 4.3 the results of detailed system experiments using 10 ps rectangular control pulses in a NOLM based 80 Gbit/s demultiplexer are presented. The performance benefits achieved are then quantified from a system perspective and are compared to those of a short control pulse driven demultiplexer. In Section 4.4, conclusions are drawn regarding the results.

4.1 Timing Jitter in an 80 Gbit/s OTDM System

As the single channel data rates increase, OTDM systems suffer increased sensitivity to source noise, and the effects of nonlinearity, group velocity dispersion (GVD), polarisation mode dispersion (PMD) and environmental sensitivity associated with the transmission line. These effects generally manifest themselves in terms of increased amplitude jitter, timing jitter and absolute timing drift at the receiver [4.1]. A data demultiplexer with a rectangular switching window should provide enhanced timing jitter tolerance at the receiver [4.2, 4.3, 4.4]. To this end the University of Southampton has demonstrated a simple and robust method to generate a rectangular switching window within nonlinear optical devices based on pulse-shaping superstructured fibre Bragg gratings (SSFBG) as described in Chapter 3 [4.5]. In the first demonstration of this approach, 2.5 ps soliton control pulses were converted into 20 ps wide rectangular pulses using SSFBG's and then applied to optical switches based on either optical fibre or a semiconductor optical amplifier (SOA). Rectangular switching windows with +/-7 ps error-free jitter tolerance were readily achieved. Recently C. Schubert et al. demonstrated a pulse shaper based on both a HiBi fibre and a polarisation beam splitter which can be used to obtain a rectangular switching window [4.6]. However, the polarisation sensitivity of this approach could be a practical limiting issue for its application within real systems.

In the following Sections, the SSFBG based rectangular pulse switching technology is used for data demultiplexing at a data rate of 80 Gbit/s in a high-speed OTDM system. 1.7 ps transform-limited soliton pulses from a harmonically mode-locked erbium fibre ring laser are converted into 10 ps rectangular pulses using a polarisation-insensitive pulse-shaping SSFBG. These pulses are then used to control a high-speed optical demultiplexer based on a nonlinear optical loop mirror (NOLM). High-performance, error-free demultiplexing operation with +/-3 ps timing jitter tolerance was achieved with 1 dB power penalty relative to the 10 Gbit/s base rate back-to-back measurement. A 2 dB power-penalty improvement was also achieved with respect to data demultiplexing without the SSFBG.

4.2 Pulse-Shaping Superstructured Fibre Bragg Gratings

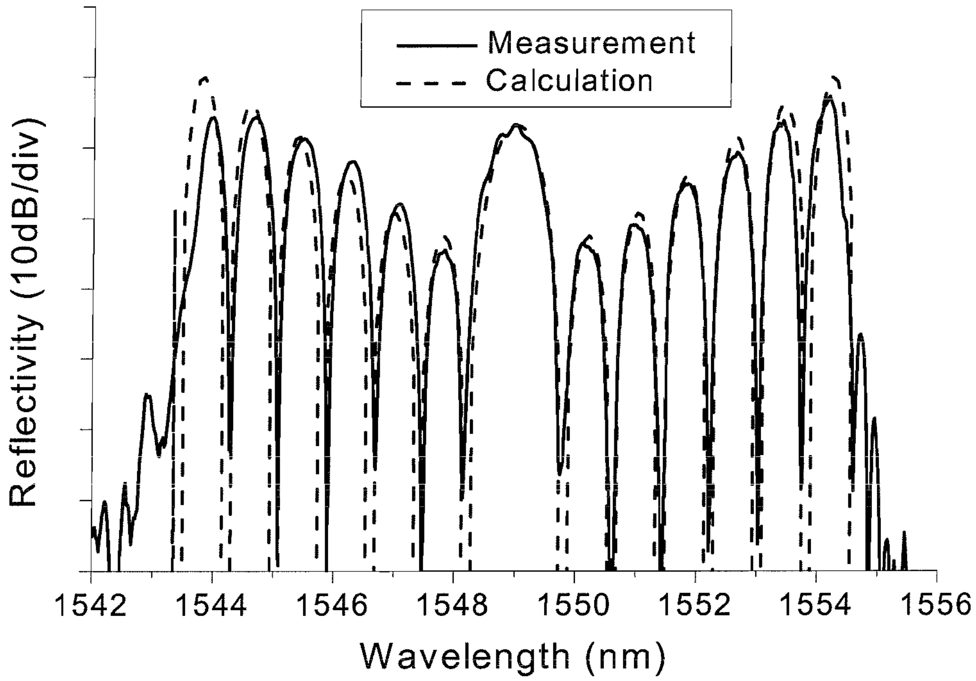

(a)

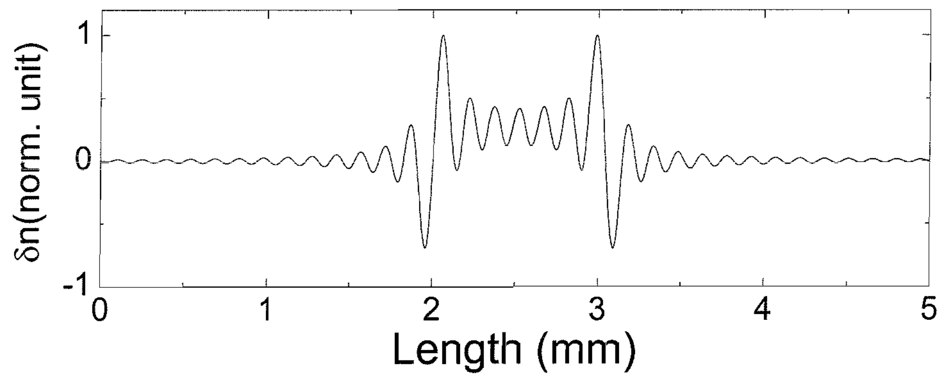

(b)

Figure 4.1: (a) The spectral reflectivity profile of the pulse-shaping SSFBG converting 1.7 ps soliton pulses into 10 ps rectangular pulses. (b) The corresponding refractive index modulation profile of the SSFBG.

Since the SSFBG based pulse-shaping technique is a purely passive-filtering process, a well-defined input pulse form to filter and thereby reshape are required. For this experiment soliton pulses generated from a harmonically mode-locked erbium-doped fibre ring laser were used. The grating was designed and fabricated with the correct phase and amplitude reflectivity profile to convert the input 1.7 ps transform-limited soliton pulses into 10 ps rectangular pulses [4.7]. The refractive index modulation profile and the corresponding spectral response of the SSFBG are shown in Fig. 4.1.

13 spectral lobes were accommodated within the available 12 nm spectral bandwidth. The grating was designed to apodize the output spectrum using a Gaussian profile to reduce temporal shape distortion (Gibbs phenomenon) due to the spectral truncation. The length of the grating was 5.1 mm, corresponding to t = 50 ps in the time domain. Note the high (<10 μm) spatial superstructure resolution required of the grating writing process as shown in Fig. 4.1(b). The measured optical spectrum of the pulses from the SSFBG is shown Fig. 4.2 together with that of the theoretically calculated single rectangular pulse. Excellent agreement between theory and experiment is obtained highlighting the quality of the grating writing process.

Temporal characterisation of the rectangular pulses was next performed. First, the autocorrelation trace measurement was performed using a SHG autocorrelator (resolution <100 fs). The measured and theoretically calculated triangular autocorrelation traces are shown in Fig. 4.3(a) together with the calculated temporal shape of the rectangular pulses. Excellent agreement between theory and measurement is obtained implying the quality of the rectangular pulses. Next, the optical sampling oscilloscope measurement based on four-wave mixing in highly nonlinear fibre was performed with 2 ps temporal resolution. The measured sampling scope trace of the pulses is shown in Fig. 4.3(b). The high quality of the 10 ps rectangular pulses is clearly evident. The detailed information on the optical sampling oscilloscope is fully described in Ref. [4.8].

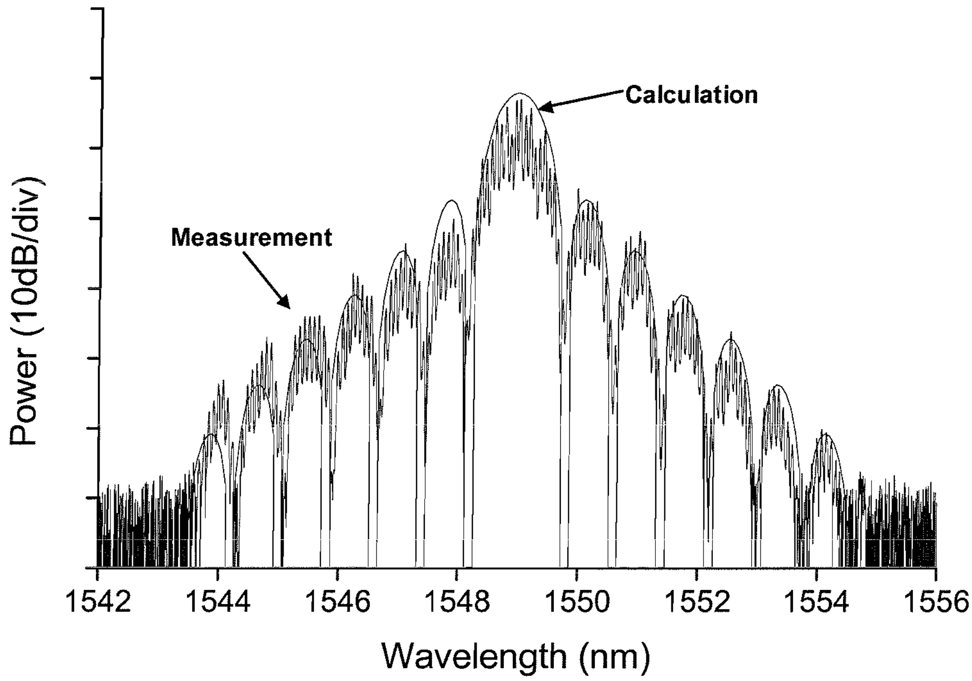

Figure 4.2: Optical spectrum of the rectangular pulses from the SSFBG described in Fig. 4.1.

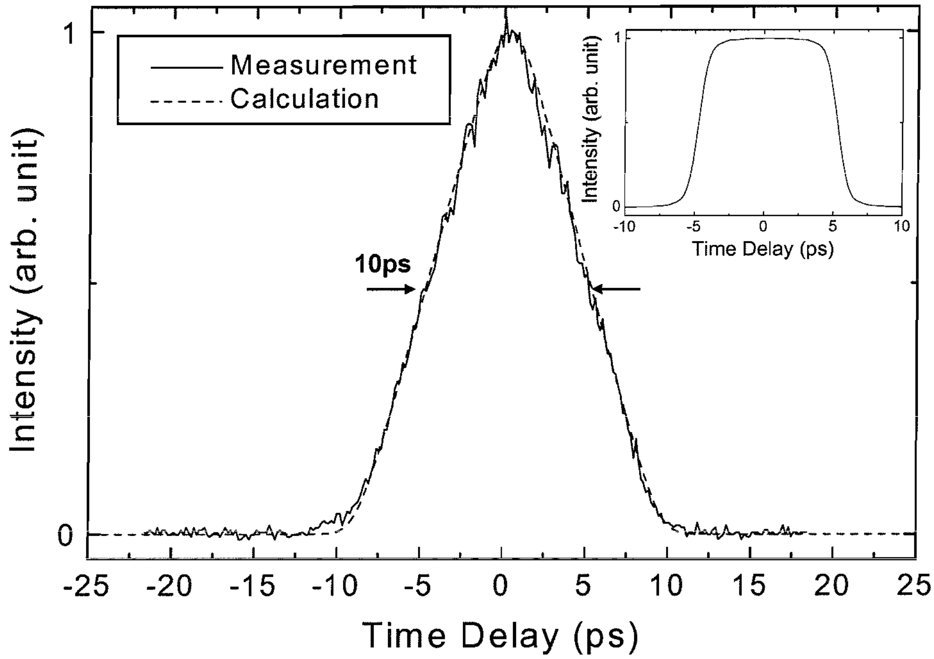

(a)

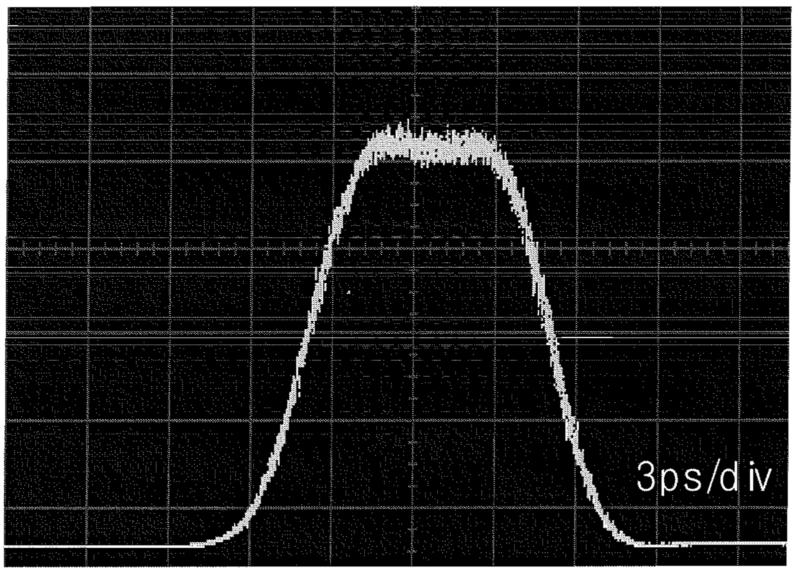

(b)

Figure 4.3: (a) SHG autocorrelation traces of the rectangular pulse; Inset: Theoretically calculated temporal shape of the rectangular pulse. (b) Optical sampling scope trace of the 10 ps rectangular pulses.

4.3 Experimental Setup and Results for 80 Gbit/S OTDM Data Demultiplexing

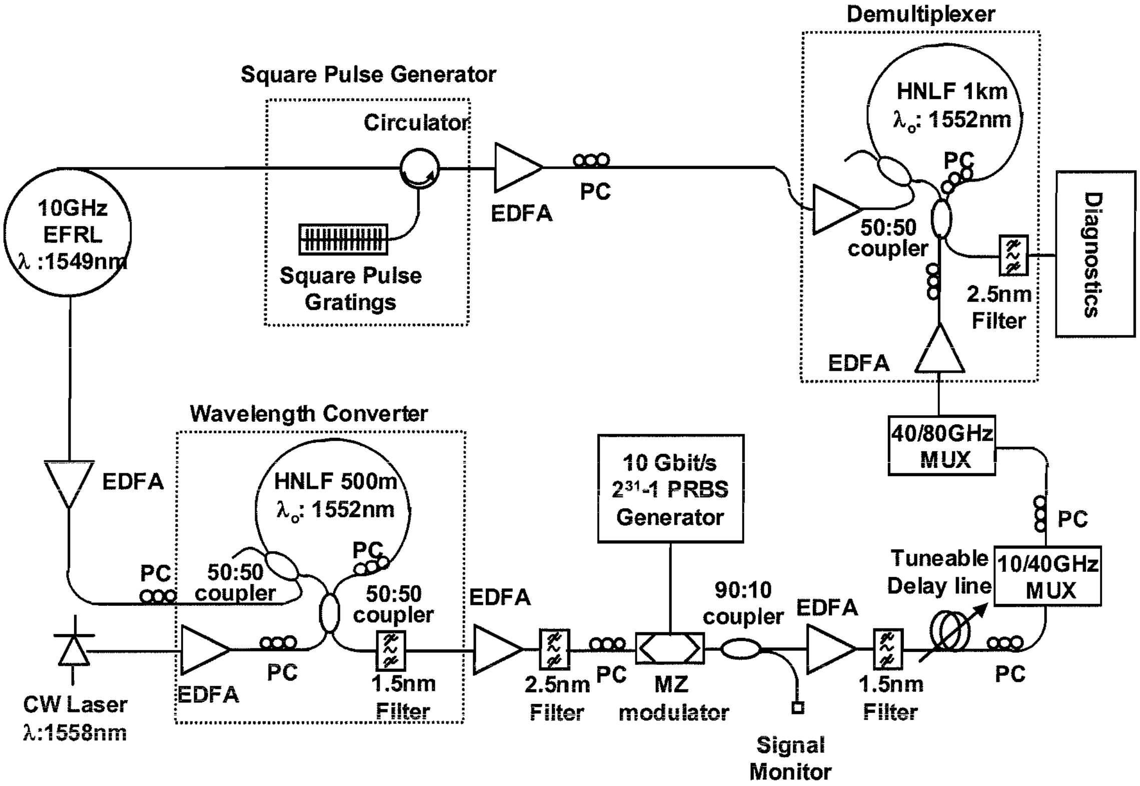

Figure 4.4: Experimental setup for 80 Gbit/s OTDM data demultiplexing.

The experimental setup for 80 Gbit/s OTDM data demultiplexing is shown in Fig. 4.4. 1.7 ps soliton pulses were first generated from a 10 GHz harmonically mode-locked erbium-fibre ring laser (EFRL) with two output channels. The first channel was fed onto the pulse-shaping SSFBG described in Section 4.2. The generated 10 ps wide, 10 Gbit/s rectangular pulses were then amplified and used as a control signal for the 80 Gbit/s demultiplexer based on NOLM. The other channel of the 10 GHz 1.7 ps pulse stream was first amplified and then fed into the control port of a dual-wavelength NOLM that was employed as a wavelength converter with which to generate a synchronized data stream [4.9]. The NOLM incorporated a 500 m long highly nonlinear fibre (HNLF) with a nonlinearity coefficient γ = 10.9 $W^{-1}km^{-1}$ and a zero dispersion wavelength λ_0 = 1552 nm. The output from a continuous wave (CW) external cavity feedback laser at an operating wavelength of 1558 nm was used as a probe signal for the wavelength converter. A 10 GHz train of high-quality 3.3 ps pulses at 1558 nm were readily generated by appropriately setting the polarisation of the light within the NOLM and filtering out the 1549 nm control pulses at the output port. The measured autocorrelation traces of the wavelength-converted pulses and the original soliton pulses are shown in Fig. 4.5. Stable and synchronized data pulses were readily achieved using the HNLF based NOLM. These wavelength converted pulses were modulated to provide a 2^{31}-1 pseudorandom data sequence at 10 Gbit/s using a high-speed $LiNBO_3$ modulator. The 10 Gbit/s pseudorandom data stream was multiplexed up to an aggregate bit rate of 80 Gbit/s using a two-stage passive multiplexer (MUX) and subsequently sent into the data port of the 80 Gbit/s demultiplexer.

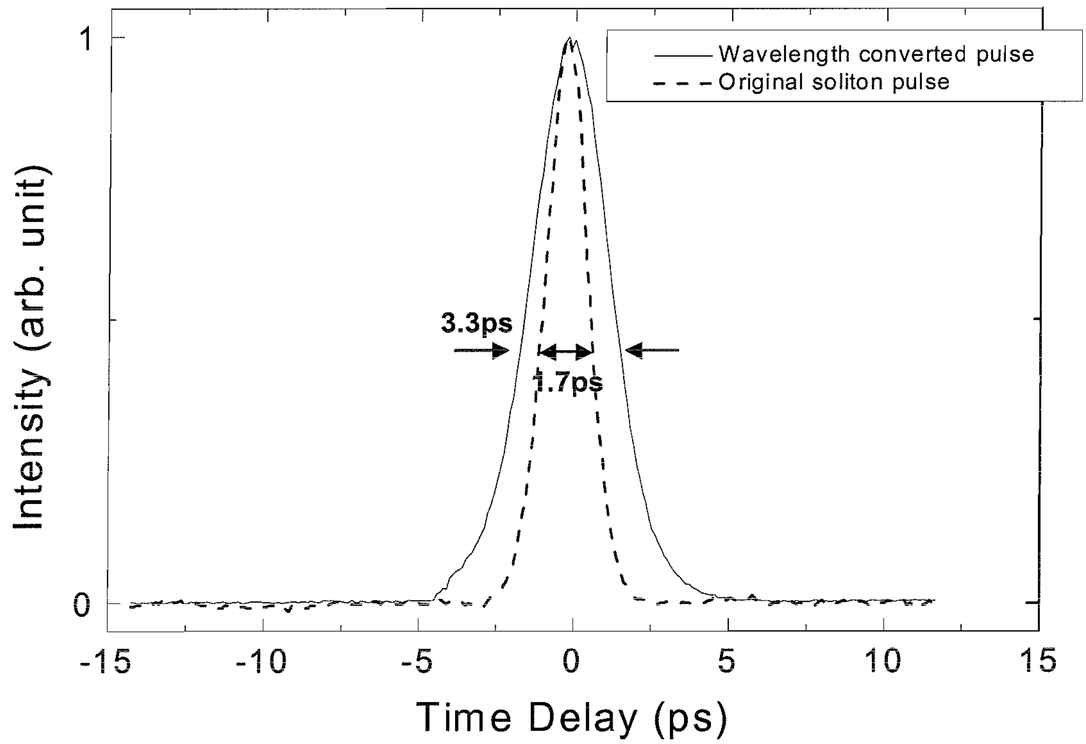

Figure 4.5: Measured autocorrelation traces of the wavelength-converted pulses and the original soliton pulses.

The high-speed data demultiplexer used in this experiment was also based on a NOLM using a 1 km length of the HNLF [4.10]. In order to properly demultiplex 3.3 ps data pulses without any additional power penalty, the NOLM was designed to generate a minimum ~3 ps FWHM switching window for the 1.7 ps soliton control pulse. This was achieved by careful selection of clock and data wavelengths relative to zero dispersion wavelength of the fibre in order to use the walk-off effect between the control and data pulses inside the NOLM. The 1558 nm 80 Gbit/s data stream incident to the demultiplexer was passed through a tuneable optical delay line to allow for adjustment of the arrival time of the data pulses relative to the 1549 nm rectangular control pulses.

Switching window measurements were performed by launching a CW probe signal into the data port of the demultiplexer and measuring the temporal width of autocorrelation traces of the switched signal. As shown in Fig. 4.6 a good switching window characteristic with a ~10 ps FWHM triangular trace was obtained using the rectangular control pulses. By contrast a value of ~4 ps was measured when driving the demultiplexer directly with pulses from the EFRL. These results show that a maximum10 ps timing jitter tolerance can be expected by using the rectangular control pulses.

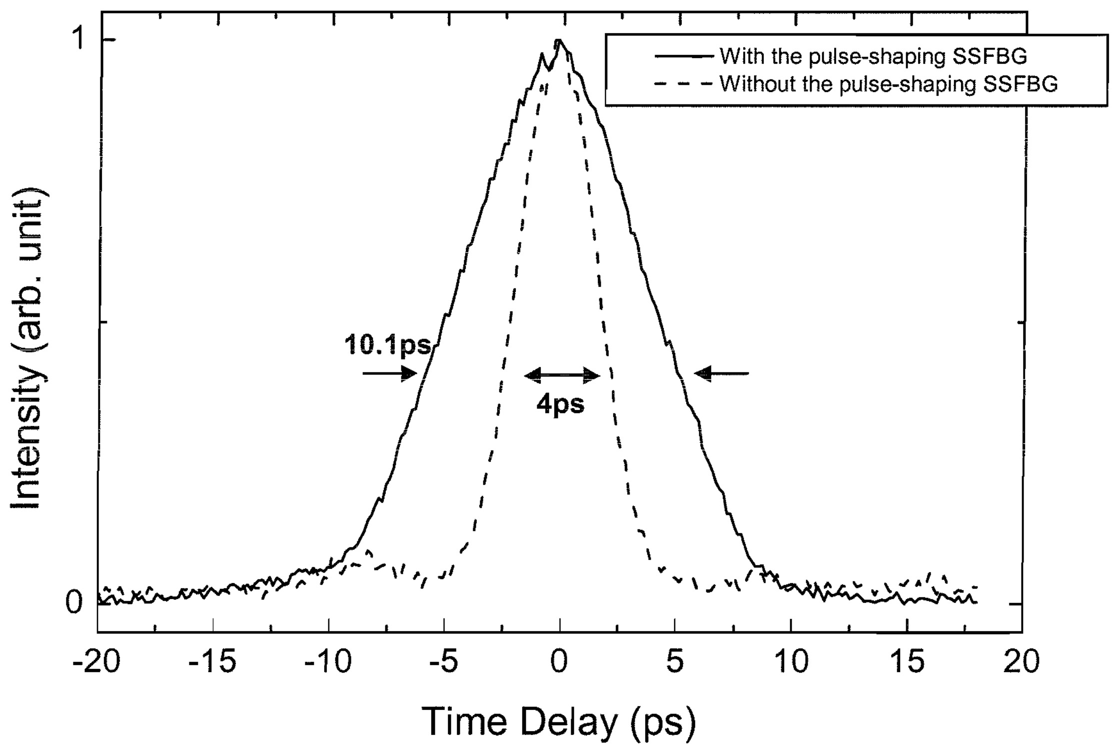

Figure 4.6: The autocorrelation traces of the switching windows measured by launching a CW probe signal into the data port of the demultiplexer.

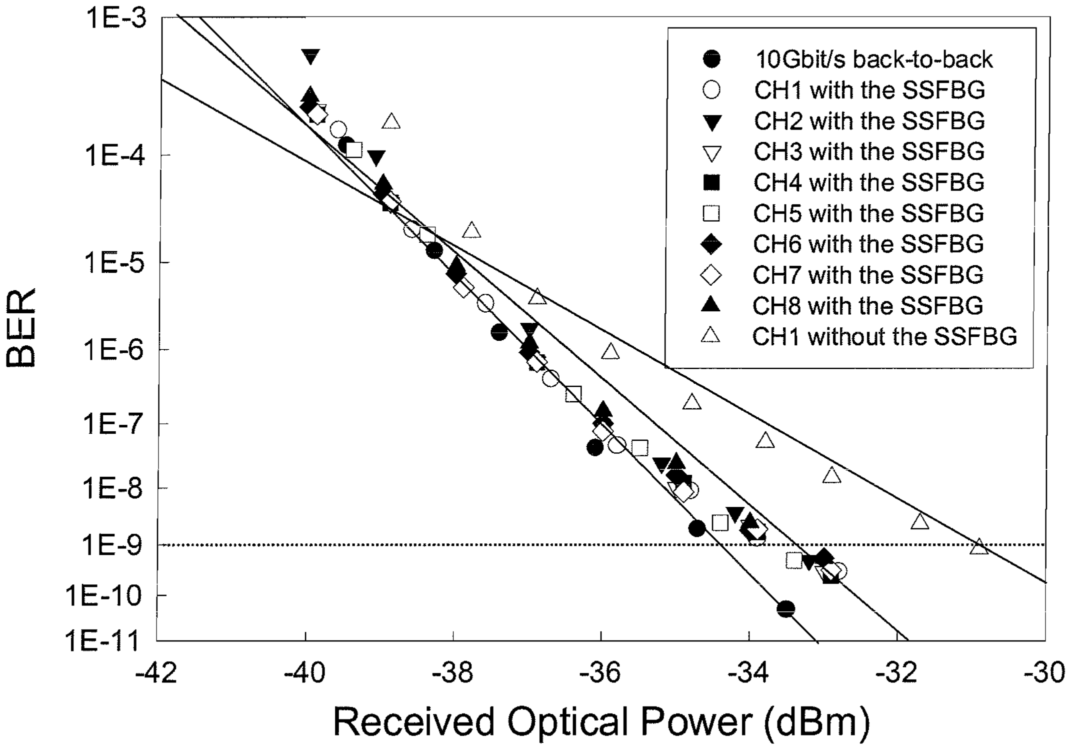

(a)

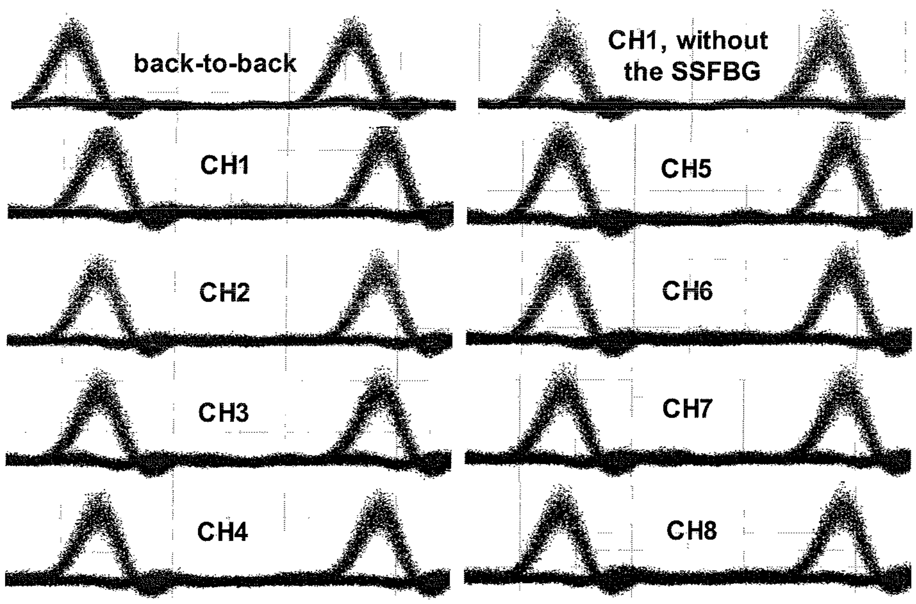

(b)

Figure 4.7: (a) BER and (b) Eye diagrams at –32 dBm, on the 80 Gbit/s to 10 Gbit/s demultiplexed signals as a function of received optical power under optimal time synchronization between control and data pulses.

In order to confirm the benefits of using rectangular control pulses in practical high-speed OTDM demultiplexing systems, bit-error-rate (BER) measurements on the 80 Gbit/s demultiplexer were performed. At first the BER was measured under optimal time synchronization between control and data pulses for both cases i.e. with and without the pulse shaping SSFBG. The results are summarised in Fig. 4.7(a).

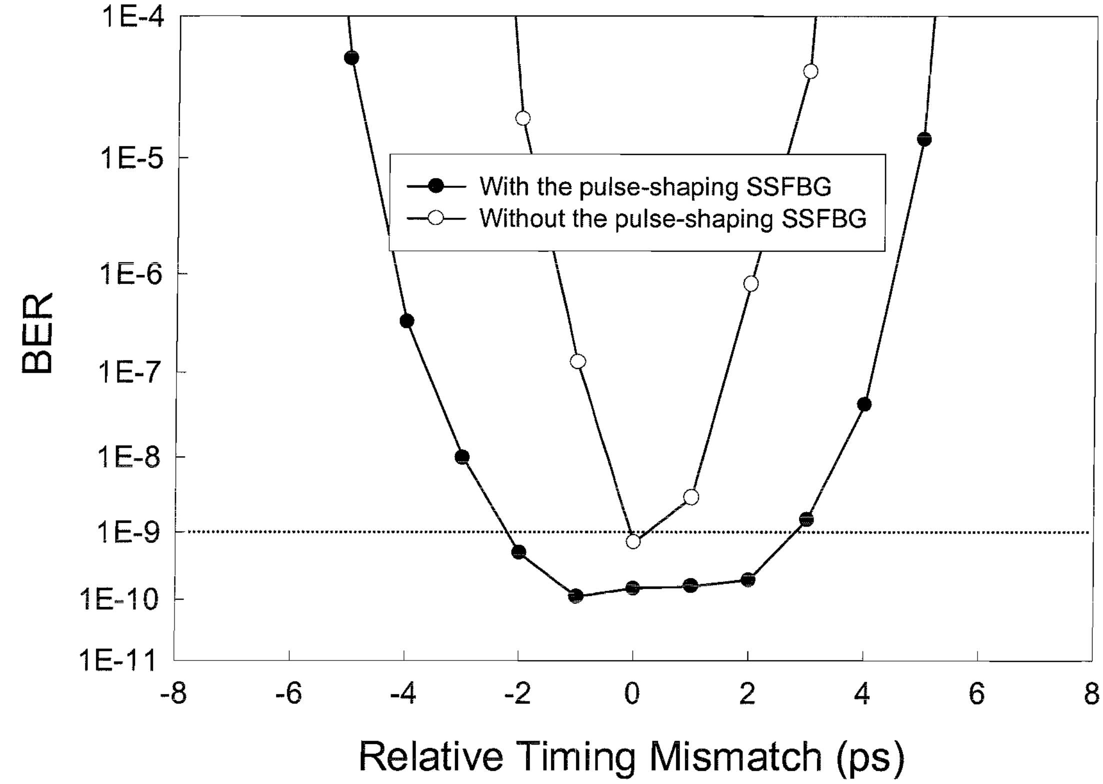

Figure 4.8: The BER measured at a fixed received optical power of –31 dBm as a function of relative timing mismatch between control and data pulses.

Error-free demultiplexing operation for all 8-channels was achieved using the 10 ps wide rectangular shape control pulses with 1 dB power penalty relative to the 10 Gbit/s base rate back-to-back. A 2 dB power-penalty improvement was also achieved with respect to data demultiplexing without the SSFBG. This penalty improvement can be attributed to the enhanced tolerance to ~ sub-picosecond timing drift inherent to this particular experimental setup caused by environmental temperature/air flow variations during this particular experiment. The corresponding eye diagrams are shown in Fig. 4.7(b). Both intensity noise and timing jitter are clearly evident in the eyes of channel no.1 using soliton control pulses without the pulse-shaping SSFBG compared to those of all 8-channels under rectangular control pulses. Next, the BER at a fixed received optical power of –31 dBm was measured as a function of relative timing mismatch between control and data pulses and the results are shown in Fig. 4.8. Error-free performance was readily achieved over a +/-3 ps timing mismatch range for the rectangular pulse driven demultiplexer versus a +/-0.5 ps range for the demultiplexer driven directly with the soliton pulses.

4.4 Conclusion

I have experimentally demonstrated that the SSFBG based rectangular pulse switching technology can be used to provide improved timing jitter tolerance in a high-speed 80 Gbit/s OTDM demultiplexing system. Error-free demultiplexing operation with ~6 ps timing jitter tolerance was achieved using a ~10 ps rectangular control pulses generated through an SSFBG. The 2 dB power-penalty improvement compared to the demultiplexing without the SSFBG highlights that significant OTDM demultiplexer performance enhancements can be achieved simply by adding a SSBFG to the system. This approach could be applied to 160 Gbit/s OTDM systems since state-of-the art SSFBG technology should be capable of producing high-quality gratings capable of generating rectangular pulses with rise/fall time less than 1 ps.

4.5 References

[4.1] M. C. Gross, M. Hanna, K. M. Patel, and S. E. Ralph, "Reduction of power fluctuations in ultrafast optically time-division-multiplexed pulse trains by use of a nonlinear amplifying loop mirror," *IEEE Photon. Technol. Lett.*, vol.14, pp.690-692, 2002.

[4.2] K. Uchiyama, and T. Morioka, "All-optical signal processing for 160Gbit/s channel OTDM/WDM systems," in *Proc. Optical Fiber Communications Conference (OFC'2001)*, Paper ThH2, 2001.

[4.3] M. Jinno, "Effects of crosstalk and timing jitter on all-optical time-division demultiplexing using a nonlinear fiber Sagnac interferometer switch," *IEEE J. Quantum Electron.*, vol.30, pp.194-202, 1994.

[4.4] N. A. Whitaker, Jr., H. Avramopoulos, P. M. W. French, M. C. Gabriel, R. E. LaMarche, D. J. Di Giovanni, and H. M. Presby, "All-optical arbitrary demultiplexing at 2.5Gbit/s with tolerance to timing jitter," *Optics Lett.*, vol.16, pp.1838-1840, 1991.

[4.5] J. H. Lee, P. C. Teh, P. Petropoulos, M. Ibsen, and D. J. Richardson, " Timing jitter tolerant all-optical modulator and demultiplexing systems incorporating pulse-shaping fiber Bragg gratings," in *Proc. Optical Fiber Communications Conference(OFC'2001)*, Postdeadline Paper PD30, 2001.

[4.6] C. Schubert, R. Ludwig, S. Watanabe, F. Futami, S. Ferber, J. Berger, C. Schmidt, and H. G. Weber, "Improved performance of a 160Gbit/s fibre based all-optical switch using rectangular gating pulses," in *Proc. European Conference on Optical Communications (ECOC'2002)*, Copenhagen Denmark, September 2002, Paper P.8.3.7.

[4.7] P. Petropoulos, M. Ibsen, A. D. Ellis, and D. J. Richardson, "Rectangular pulse generation based on pulse reshaping using a superstructured fiber Bragg grating," *J. Lightwave Technol.*, vol.19, pp.746-752, 2001.

[4.8] F. Parmmigiani, P. Petropoulos, P. Almeida, M. Ibsen, J. H. Lee, and D. J. Richardson, "A direct assessment of the performance of pulse shaping superstructured fiber Bragg gratings using an optical sampling oscilloscope," in *Proc. Optical Fibre Communications Conference (OFC'2001)*, Atlanta USA, March 2003, paper MF36.

[4.9] J. Yu, Y. Qian, P. Jeppesen, and S. N. Knudsen, "Broad-band and pulsewidth-maintained wavelength conversion based on a high-nonlinearity DSF nonlinear optical loop mirror," *IEEE Photon. Technol. Lett.*, vol.13, pp.344-346, 2001.

[4.10] K. J. Blow, N. J. Doran, and B. P. Nelson, " Demonstration of the nonlinear fibre loop mirror as a ultrafast all-optical demultiplexer," *Electron. Lett.*, vol.26, pp.962-964, 1990.

CHAPTER FIVE

A HOLEY FIBRE BASED NONLINEAR THRESHOLDING DEVICE FOR OPTICAL CDMA RECEIVER PERFORMANCE ENHANCEMENT.

This Chapter reports experimental results concerning the use of holey fibre (HF) technology to realise a nonlinear thresholding device within an OCDMA receiver.

This Chapter is organised as follows. Section 5.1 gives a brief introduction to the use of holey fibre technology for nonlinear thresholding devices in OCDMA systems. In Section 5.2 characterisation results on the holey fibre used for these experiments are presented. Section 5.3 describes the results of detailed system experiments using 255-chip, 320 Gchip/s quadrapolar coding and decoding SSFBG's in which the noise reduction benefits of using a nonlinear switch based on a short length of holey fibre within the decoder are more apparent. In Section 5.4, conclusions are drawn regarding the results and further applications of the technology are discussed.

5.1 Holey Fibre Technology for Nonlinear Thresholding Device Applications in DS-OCDMA Systems

In SSFBG based OCDMA schemes the reflection of a short pulse from one SSFBG (the encoder) results in the generation of a code sequence [5.1]. This code can then be recognised (at a particular receiver) by subsequent reflection from a second SSFBG (the decoder) that has a spatially reversed refractive index profile relative to that of the encoder. This process results in the generation of a pulse form in the time domain with a temporal structure corresponding to the autocorrelation function of the code. Simple intensity discrimination techniques can then be used to detect code recognition provided that only code sequences are used within the system that have: (a) a distinctive autocorrelation characteristic comprising a short, relatively intense pulsed feature, (which is in general unavoidably accompanied by an extended low level pedestal), and (b) mutually low cross correlation characteristics. Whilst good operation of such 'linear' optical systems can be achieved, nonlinear optical techniques that can eliminate the extended low-level pedestal associated with the matched filtering process are desirable (as shown in Chapter 2), since removal of this pedestal enhances the contrast of the pattern recognition signature. This is particularly important within OCDMA systems since a particular coded signal generally needs to be recognised in the presence of other orthogonally coded signals, each of which also gives rise to low level pedestal signals when filtered, and which can interfere with the decoded signal.

The use of fast, fibre based nonlinear thresholding devices within OCDMA receivers has been previously demonstrated, and these devices were based on either the filtering of spectrally broadened signal components generated through Kerr nonlinearity [5.2], or soliton effects in a nonlinear optical loop mirror as shown in Chapter 2 [5.3]. Both of these devices employed conventional silica fibres and were impractical since the relatively low nonlinearity of these fibre types means that long fibre lengths (several kms) are required.

Holey fibre (HF) technology however now allows the fabrication of fibres with very tightly confined modes, and thus very high optical nonlinearities per unit length. Indeed, a silica holey fibre can have a nonlinearity 10~100 times that of a conventional silica fibre. Nonlinear devices based on HF can thus in principle be 10 ~100 times shorter than similar devices based on conventional fibre technology, offering a route to the development of truly practical, ultrafast fibre based nonlinear devices [5.4].

In the following Sections, experimental results concerning the use of a HF nonlinear thresholding device within an OCDMA receiver is presented. Using a short (8.7 m) length of HF enhanced code recognition quality was achieved in a 255-chip, 320 Gchip/s superstructured fibre Bragg grating (SSFBG) based OCDMA code:decode system. Error-free, penalty-free system performance is obtained and the ~3 dB power penalty observed for pure matched filtering alone is eliminated.

5.2 Characterisation of the Holey Fibre (WBHNL12-125)

In order to obtain a HF with a high nonlinearity appropriate for this special experiment, a structure with large air holes and a small core was designed and fabricated. A cross sectional SEM image of the HF (WBHNL12-125) used in this experiment is shown in Fig. 5.1.

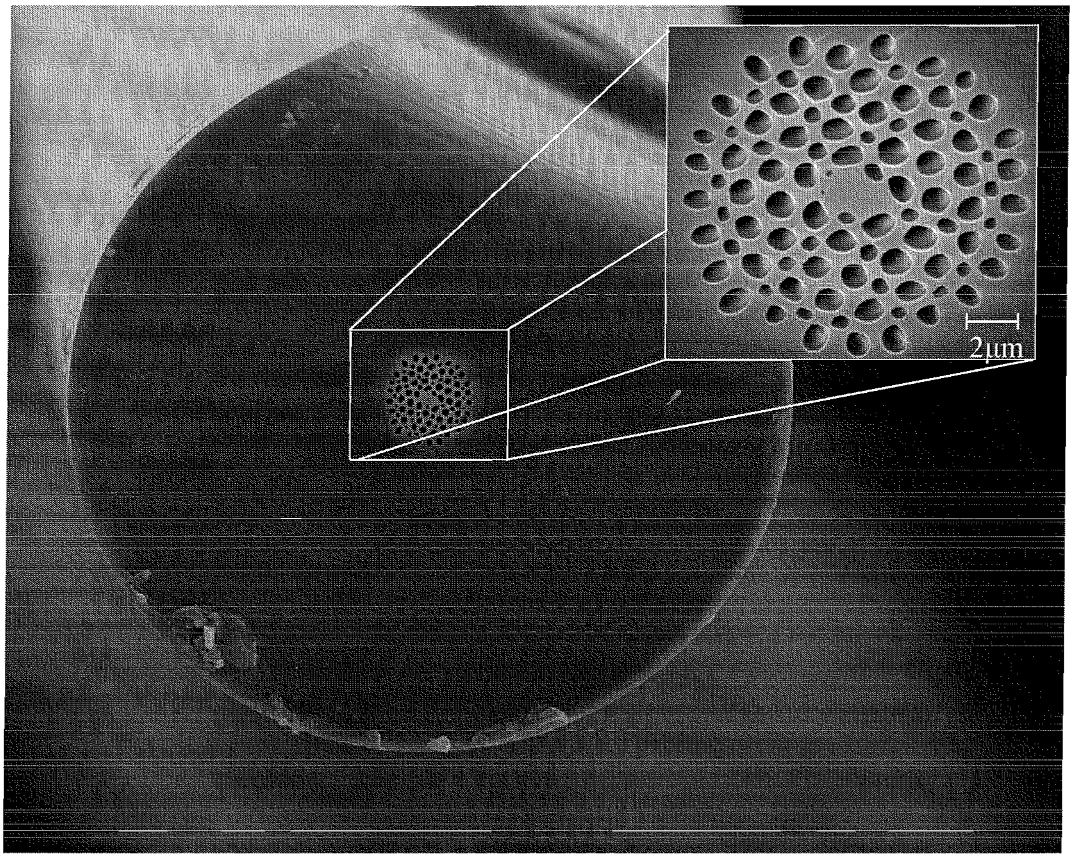

Figure 5.1: A SEM image of the HF (WBHNL12-125) used for the switching experiment.

The core diameter is ~2.0 μm and the outer diameter of this fibre is 125 μm. The 66 m long HF (WBHNL12-125) was fabricated using the conventional procedure of stacking microscopic silica tubes (2 mm diameter) around a silica rod which is used to define a higher refractive index core. The resultant structure was then pulled down to a pre-designed dimension through a conventional fibre drawing tower.

The nonlinear coefficient γ of the guided mode in this fibre was measured at 1552 nm using a direct CW measurement of the nonlinear phase shift suffered by a beat signal propagating in the fibre [5.5]. Output signals from two tuneable DFB lasers with a relative wavelength offset of 0.5 nm were first combined using a 50:50 coupler to generate a beat signal and amplified with an erbium-doped fibre amplifier to obtain an adequate power level to generate four-wave mixing effects inside the HF (WBHNL12-125). The polarised beat signal was coupled onto one polarisation axis of the HF (WBHNL12-125) using translation stages and an appropriate combination of lenses. The fibre Kerr nonlinearity generates spectral side bands and the relative intensity ratio between the signal peak and the first side band peak gives the nonlinear phase shift through the following equation.

$$\frac{I_0}{I_1} = \frac{J_0^2(\phi_{SPM}/2) + J_1^2(\phi_{SPM}/2)}{J_1^2(\phi_{SPM}/2) + J_2^2(\phi_{SPM}/2)} \quad \text{.......(5.1)}$$

where $I_{0,1}$ are the intensities of the signal peak and the first side lobe peak, respectively, and J_n is the nth Bessel function. ϕ_{SPM} represents the nonlinear Kerr phase shift expressed as

$$\phi_{SPM} = \frac{2\omega_0 n_2 L_{eff} P}{cA_{eff}} \quad \text{.......(5.2)}$$

where ω_0 is a beat signal frequency and P is power of the beat signal. L_{eff} and A_{eff} represents the effective length and area, respectively. n_2 is the Kerr nonlinear coefficient which depends on the material composition of the fibre.

From the measured SPM nonlinear phase shift versus launched optical power as shown in Fig. 5.2, a value of $\gamma = 31\text{W}^{-1}\ \text{km}^{-1}$ was obtained and an estimate of A_{eff} = 2.93(+/-0.3) μm^2 was subsequently estimated for the effective area (assuming the Kerr nonlinear coefficient of pure silica $n_2 = 2.16 \times 10^{-20}\ m^2/W$ [5.5]). This nonlinearity is ~20 times higher than that of a conventional dispersion shifted fibre.

The polarisation maintaining properties of the fibre were also investigated by measuring the birefringence of the fibre at 1550 nm. The spectral transmission characteristics of broadband light source were measured using an optical spectrum analyser (OSA) with properly adjusted polarisers and polarisation controllers located at input and output of the HF (WBHNL12-125). The fibre was found to be highly birefringent with a beat length of 0.437 mm and showed a polarisation extinction of 19 dB (measured over a 1.1 m length of the fibre). The measured group velocity dispersion (GVD) at the wavelength of 1550 nm was 98 ps/nm-km and the fibre loss was measured to be 50 dB/km.

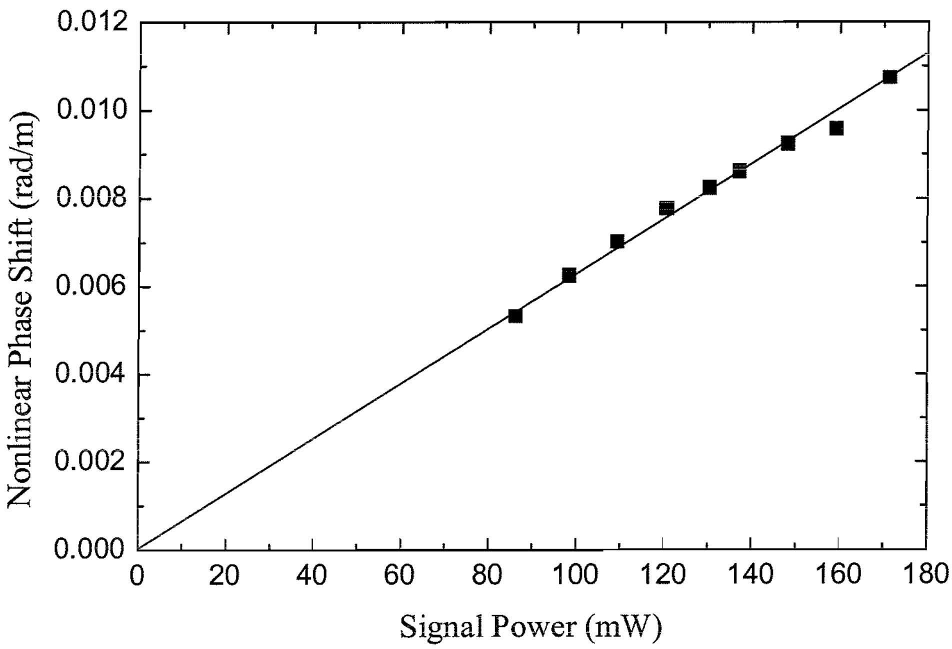

Figure 5.2: Experimentally measured nonlinear phase shift of the HF (WBHNL12-125) with respect to input signal power. The linear fit line to the experimental data is shown.

5.3 Enhancement of Code Recognition Signature Contrast in a 255-Chip, 320 Gchip/s Superstructured Fibre Bragg Grating (SSFBG) Based OCDMA Code:Decode System Using a Short Length Holey Fibre Based Nonlinear Switch

The experimental set up is shown in Fig. 5.3. 2.5 ps pulses at 10 GHz are first generated using a regeneratively mode locked erbium fibre ring laser (EFRL) operating at 1553 nm. These were then gated down in frequency and then modulated to obtain a 1.25 Gbit/s data stream. The 1.25 Gbit/s, short pulse data stream was then launched onto an SSFBG encoder (C1) containing 255-chip, 320 Gchip/s quaternary phase code sequence coding information. The chip duration was thus 3.2 ps and the coded data pulses had a total duration of ~800 ps. The particular code used is a member of the Family $\mathcal{A}$ sequences that have been applied within wireless CDMA communications

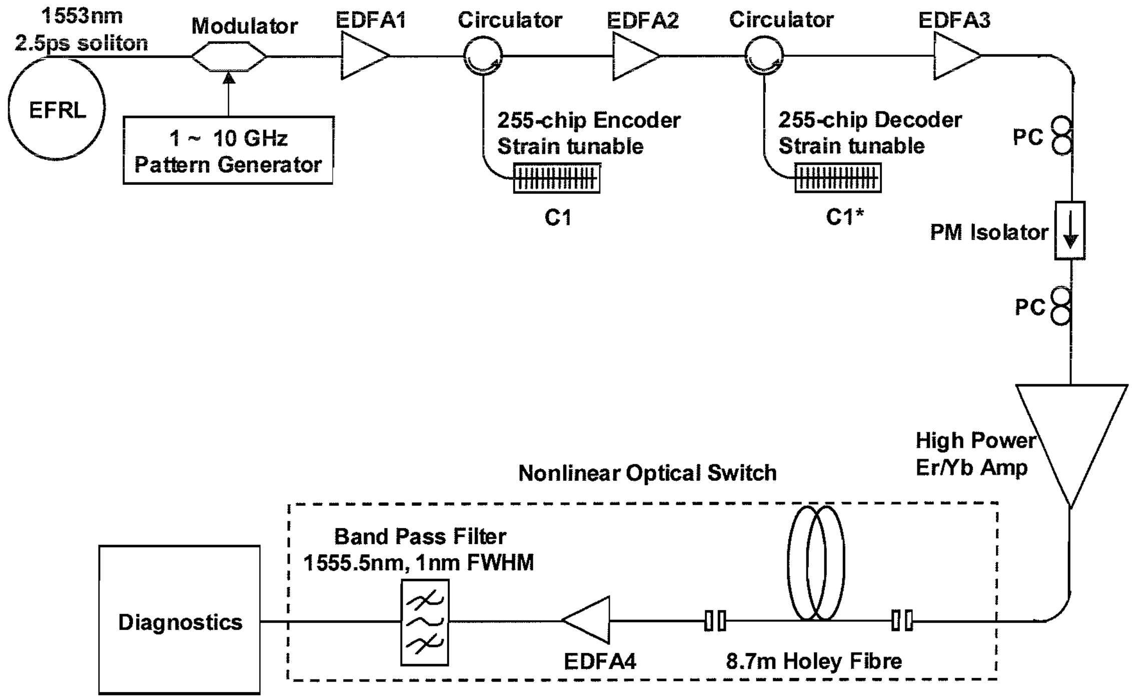

Figure 5.3: Experimental setup

Fig. 5.4 shows the 255-chip quadra-polar code sequence used for this experiment, and the theoretical and experimental spectra of the corresponding particular gratings. The high quality of the gratings is readily evident from the good agreement between the theoretical and experimental spectra. The particular gratings are more fully described in Ref. [5.1]. The resulting code sequence is defined by the impulse response of the grating and follows the actual refractive index superstructure profile written into the grating. The chip duration was 3.2 ps and the coded data pulse, which had a total duration of ~800 ps, was then fed directly to the associated matched (spatially reversed) decode grating filter (C1*).

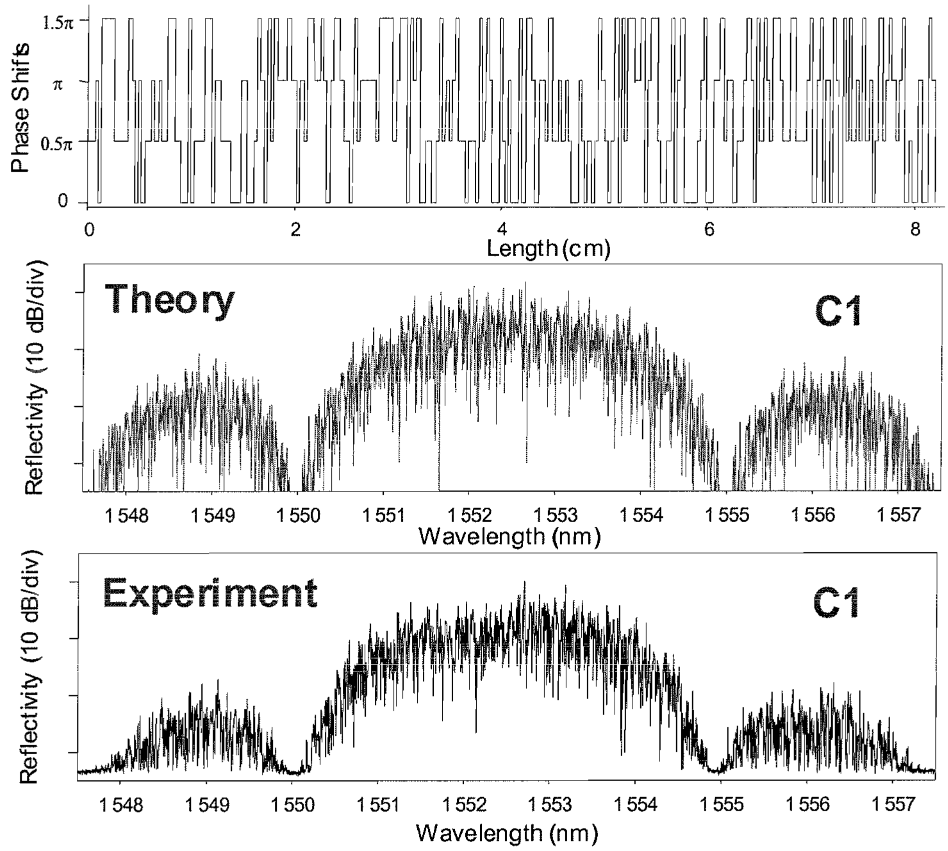

Figure 5.4: The 255-chip quadra-polar code sequence used for this experiment, and the theoretical and experimental spectra of the corresponding particular gratings.

When the code and decode gratings are matched then the decode output exhibits a short, chip length long autocorrelation spike on a relatively low-level broad (1.6 ns) pedestal as shown in Fig. 5.5. A nonlinear optical switch based on an 8.7 m long holey fibre (WBHNL12-125) was located after the decoder grating to increase the contrast between decoded pulse forms and low-level pedestal noise. Within this scheme the noisy decoded pulses are first amplified and then fed to the nonlinear medium in which mainly self-phase modulation (SPM) takes place.

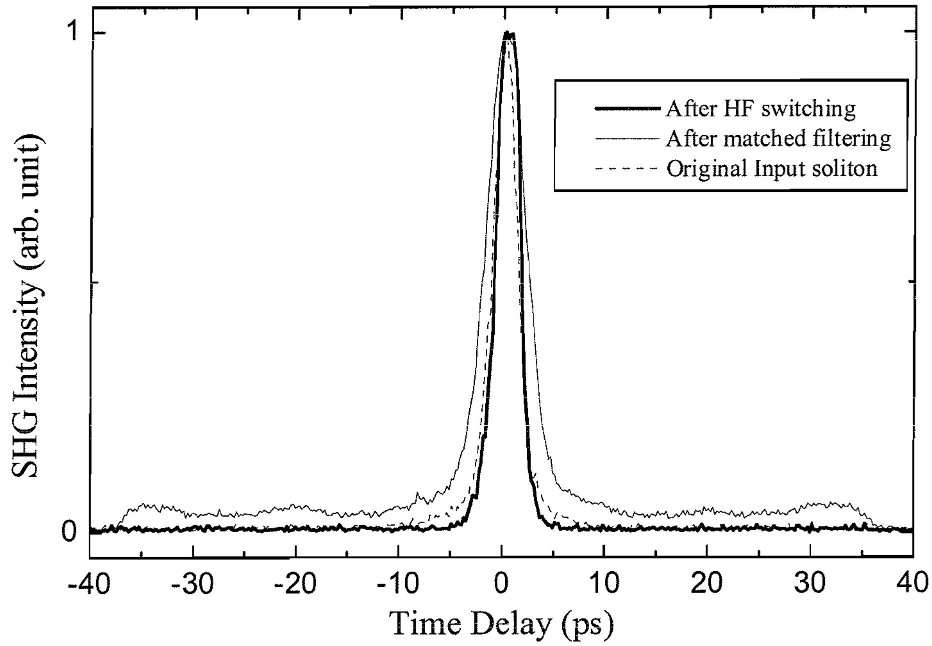

Figure 5.5: Experimental SHG autocorrelation functions of the input 2.5 ps soliton pulses, the pulses after matched filtering, and the matched filtered pulses after nonlinear switching by the HF (WBHNL12-125) switch for the data rate of 1.25 Gbit/s.

The self-switched signal is obtained by filtering the spectrally broadened signal with a narrowband filter which has its centre-wavelength offset relative to the peak wavelength of the incident signal. The decoded signal was amplified through EDFA3 to obtain a power level sufficient to saturate a high power Er^{3+}/Yb^{3+} Amplifier. The maximum pulse peak power achievable using the setup was ~15 W, which was strong enough to obtain significant spectral broadening of the output pulses. A polarisation maintaining (PM) isolator was used with an input polarisation controller (PC) to make sure that incoming light was linearly polarised and another PC was included just after the PM isolator to ensure that light was coupled onto just one of the principal polarisation axes of the HF (WBHNL12-125). Signal light was coupled into the HF (WBHNL12-125) through translation stages combined with an appropriate choice of lenses at an efficiency of ~35 %. Fig. 5.6 shows the spectral broadening of the incoming pulses through the HF (WBHNL12-125) with respect to the spectrum of the input pulses. The input peak power of the pulses was ~3 W. Significant spectral broadening occurs which allows for good switching performance. An angle-tuned dielectric filter centered at a wavelength of 1555.5 nm which is 2.5 nm away from the centre-wavelength of the original soliton laser, was used to extract the switched/cleaned pulses. A filter 3 dB bandwidth of 1.0 nm was chosen to ensure that the switched output pulses had roughly the same temporal width as the original soliton pulses.

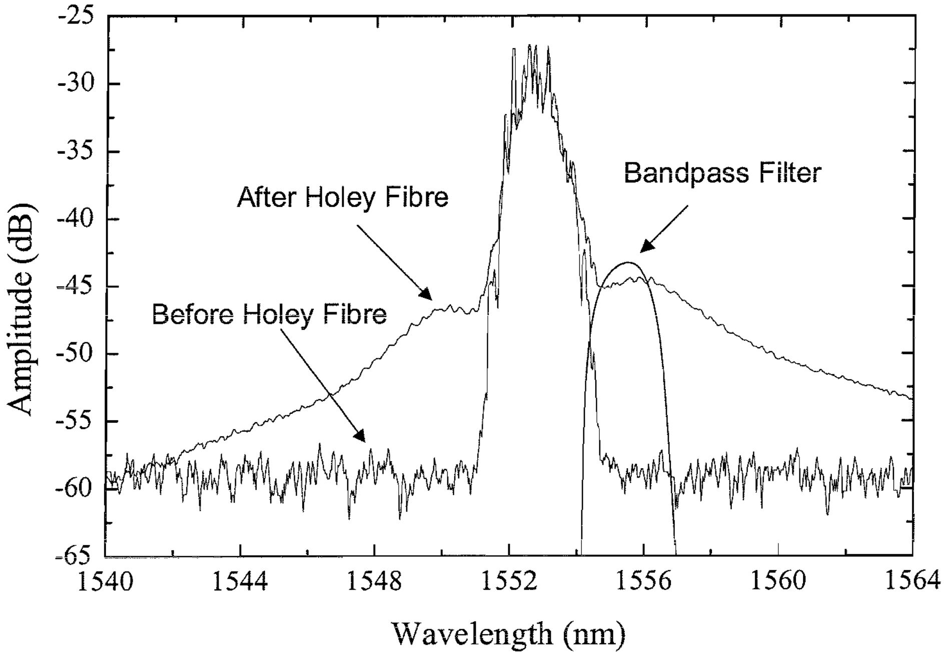

Figure 5.6: Signal spectrum both before and after the 8.7 m HF (WBHNL12-125) at an input pulse peak power of ~3 W.

In Fig. 5.7 the experimentally measured power transmission characteristic of the HF (WBHNL12-125) switch is plotted as a function of input pulse peak power. A good binary transfer characteristic for the nonlinear switch is clearly shown in the graph, implying that both low intensity and high intensity noise on the decoded pulses can be readily removed by setting the input peak power at the optimum operating point (~1.7 W).

In order to assess the impact of using the HF (WBHNL12-125) switch as an optical thresholder the eye diagrams were first measured. The improved pattern recognition contrast is clearly evident on a 20 ps timescale by comparing the eyes and background noise levels in Fig. 5.8, and on a ps timescale in Fig. 5.5. The low-level pedestal obtained with simple matched filtering is almost completely eliminated. Note that the switched-output pulses have a quality close to that of the original soliton pulses in terms of the shape and temporal width as shown in Fig. 5.5, which indicates that further all-optical signal processing steps can be readily taken after the OCDMA receiver.

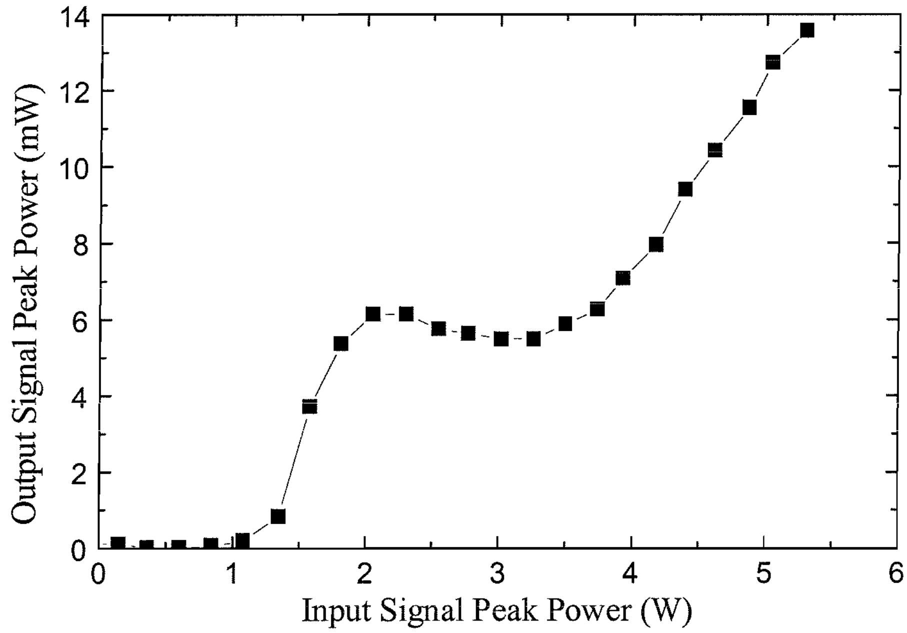

Figure 5.7: Experimentally obtained power transmission characteristic of the HF (WBHNL12-125) switch as a function of the input peak power.

To quantify the benefits of the pedestal rejection from a system perspective BER measurements were performed as shown in Fig. 5.9. The observed ~3 dB power penalty associated with matched filtering alone is totally eliminated. It should be mentioned that since the fibre has anomalous dispersion (D ~100 ps/nm-km) the filtering process results in additional noise on the 'one' bits (see Fig. 5.8) due to coherence degradation [5.6, 5.7]. However, for this particular application this does not appear to lead to any penalty. Indeed, a ~1 dB penalty improvement relative to the laser back-to-back case was obtained due to clean up of residual radiation in the zero bit slots due to the poor (~-14 dB) extinction ratio of the external data modulator (see Fig. 5.8: back to back trace).

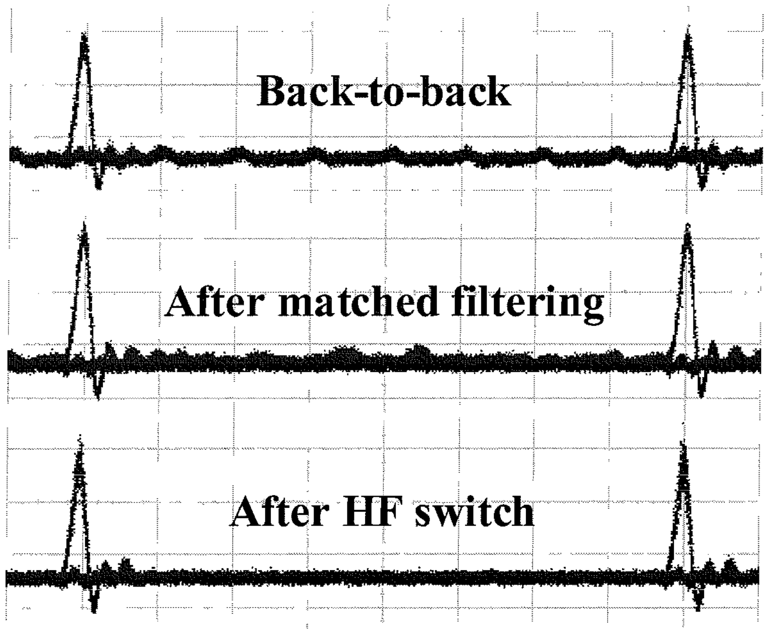

Figure 5.8: Eye diagrams of the input 2.5 ps soliton pulses, the pulses after matched filtering, and the matched filtered pulses after nonlinear switching by the HF switch for the data rate of 1.25 Gbit/s.

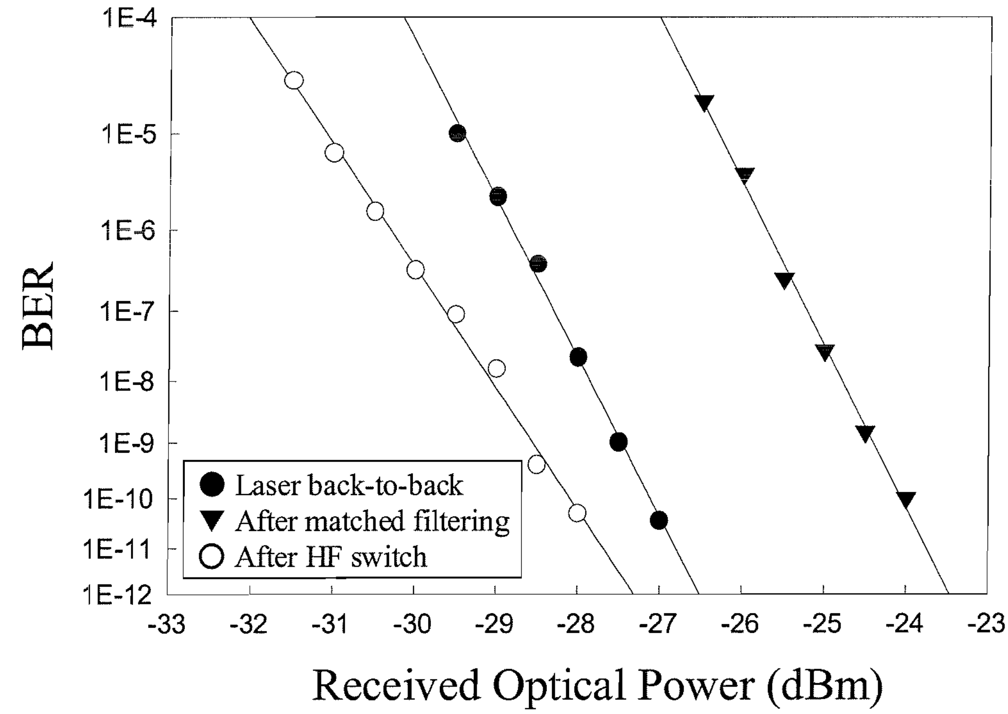

Figure 5.9: Measured BER versus received optical power at 1.25 Gbit/s.

5.4 Conclusion

I have experimentally demonstrated that a short, highly nonlinear holey fibre based optical switch can be readily used to enhance code recognition contrast in a SSFBG based OCDMA code:decode system. This experiment represents just the first example of an application of nonlinear devices based on a short length of holey fibre for real fibre-optic communication systems. Such short length, fibre based devices are particularly attractive for integration with other photonic components. This is the first of many such demonstrations and the next five Chapters are devoted to more device applications of highly nonlinear holey fibre for fibre-optic communication systems.

5.5 References

[5.1] P. C. Teh, M. Ibsen, J. H. Lee, P. Petropoulos, and D. J. Richardson, "A 4-channel WDM/OCDMA system incorporating 255-chip, 320 Gchip/s quaternary phase coding and decoding gratings," in *Proc. Optical Fiber Communications Conference (OFC'2001)*, Anaheim USA, March 2001, Postdeadline paper PD37.

[5.2] H. P. Sardesai, C.-C. Chang, and A. M. Weiner, "A femtosecond code-division multiple access communication system test bed," *J. Ligthwave Technol.*, vol.16, no.11, pp.1953-1964, 1998.

[5.3] J. H. Lee, P. C. Teh, P. Petropoulos, M. Ibsen and D. J. Richardson, "Reduction of interchannel interference noise in a two-channel, grating based OCDMA system using a nonlinear optical loop mirror," *IEEE Photon. Technol. Lett*, vol.13, no.5, pp.529-531, 2001.

[5.4] P. Petropoulos, T. M. Monro, W. Belardi, K. Furusawa, J. H. Lee, and D. J. Richardson, "A 2R-regenerative all-optical switch based on a highly nonlinear fiber", *Optics Lett.*, vol. 26, no.16, pp.1233-1235, 2001.

[5.5] A. Boskovic, S. V. Chernikov, J. R. Taylor, L. Gruner-Nielsen, and O. A. Levring, "Direct continuous measurement of n_2 in various types of telecommunication fiber at 1.55μm," *Optics Lett.*, vol.21, no.24, pp.1966-1968, 1996.

[5.6] S. Taccheo, and L. Boivin, " Investigation and design rules of supercontinuum sources for WDM applications," in *Proc. Optical Fiber Communications Conference (OFC'2000)*, Baltimore USA, March 2000, Paper ThA1.

[5.7] N. Nakazawa, H. Kubota, and K. Tamura, "Random evolution and coherence degradation of a high-order optical soliton train in the presence of noise," *Optics Lett.*, vol.24, no.5, pp.318-320, 1999.

CHAPTER SIX

A HIGHLY NONLINEAR HOLEY FIBRE BASED RAMAN AMPLIFIER AND ALL-OPTICAL MODULATOR

This Chapter reports the use of HF technology to reduce the length/power levels required for nonlinear telecommunication devices based on the Raman effect; (i) a HF Raman amplifier and (ii) an all-optical, HF Raman modulator.

This Chapter is organised as follows. Section 6.1 contains a brief introduction to HF technology applications within Raman effect based nonlinear devices. In Section 6.2 the results of a characterisation of a holey fibre used for the experiments are presented. Section 6.3 gives the results of Raman amplification experiments using a holey fibre, in which the signal gain and noise figure in the wavelength band 1610~1640 nm are characterised and presented. In Section 6.4, the experimental results of signal modulation through the Raman effect in a holey fibre are presented. In Section 6.5 conclusions are drawn regarding the results and further applications of the technology are discussed.

6.1 Holey Fibre Technology for Raman Effect Based Nonlinear Devices

Fibre amplifiers based on the Raman effect have attracted huge research attention in recent years due to the fact that the amplification band can be applied anywhere within the transparency window of optical fibre simply by changing the pump wavelength. In particular the ever-increasing demand for optical data transmission capacity expansion in telecommunications has generated enormous interest in optical communication bands (S-, L-band) outside of the conventional EDFA gain bandwidth (C-band) [6.1, 6.2, 6.3]. Fibre Raman amplifiers with over 100 nm gain-bandwidth have previously been demonstrated covering the S- and L-bands [6.4, 6.5], and also a realisation of a U-band (1625~1675 nm) amplifier through Raman effect in a conventional fibre has recently been proposed [6.6]. As well as signal amplification, the Raman effect in an optical fibre can also be used for all-optical ultra-fast signal processing applications due to its fast response time (< 10 fs). Ultra-high speed (>500 Gbit/s) data modulation and packet header erasure functions can easily be achieved using Raman effect and these principles have already been experimentally demonstrated [6.7]. However optical devices based on the Raman effect in optical fibres often suffer drawbacks which are not straightforward to overcome. For example long lengths of fibre are required (~10 km) for reasonable pump powers and the related issue of Rayleigh scattering in such fibres compromises their performance [6.8]. The use of a relatively short length of holey fibre could probably provide an easy solution to such problems. To obtain an adequate Raman amplification signal gain in a short length of optical fibre specialty fibres with either a very high Raman gain coefficient or a small effective area is needed. Holey fibre which allows for extremely tightly confined mode is thus a suitable candidate.

In the following Sections, I show that HF technology can indeed be used to reduce the length/power levels required for two Raman effect based devices, specifically; (i) a HF Raman amplifier and (ii) an all-optical, HF Raman modulator.

6.2 Characterisation of the Holey Fibre (WBHNL12-100)

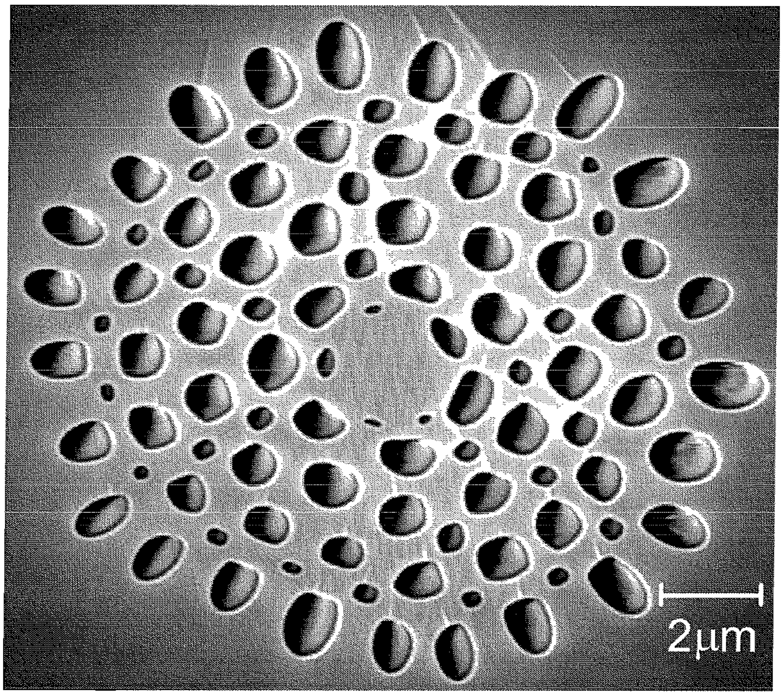

Figure 6.1: Cross sectional SEM image of the HF (WBHNL12-100) used.

A cross sectional Scanning Electron Micrograph (SEM) image of the HF (WBHNL12-100) used in these experiments is shown in Fig. 6.1. The fibre has a core diameter of ~1.6 μm and an outer diameter of 100 μm. The relatively large hole sizes result in a high optical nonlinearity and their asymmetric arrangement ensures that the fibre is linearly birefringent with a measured beat length of ~0.4 mm at 1.55 μm. A length of 75 m of this fibre was used in all of the experiments/measurements reported herein. The loss of this fibre was measured using the cut back technique to be 40 dB/km. The 75 m of HF (WBHNL12-100) thus has an effective nonlinear length L_{eff} of just 54 m. The nonlinear coefficient γ of the guided mode in this fibre was measured at 1535 nm using the CW beat signal measurement of the SPM induced nonlinear phase shift described in Chapter 5.2. A value of $\gamma = 32$ W^{-1} km^{-1} was obtained. The measured nonlinear phase shift of the HF (WBHNL12-100) with respect to input signal power is shown in Fig. 6.2. Using the quoted value of the Kerr nonlinear coefficient of silica of $n_2 = 2.16\text{x}10^{-20}$ m^2/W, an estimate of A_{eff} = 2.85(+/-0.3) μm^2 was obtained for the effective area of the HF (WBHNL12-100). This value is in very good agreement with a theoretical prediction of 2.87 μm^2 based on the SEM image shown inset in Fig. 6.1. The fibre was shown to be highly birefringent (beat length ~0.5mm) with a polarisation extinction of ~21 dB and the fibre loss is 40 dB/km.

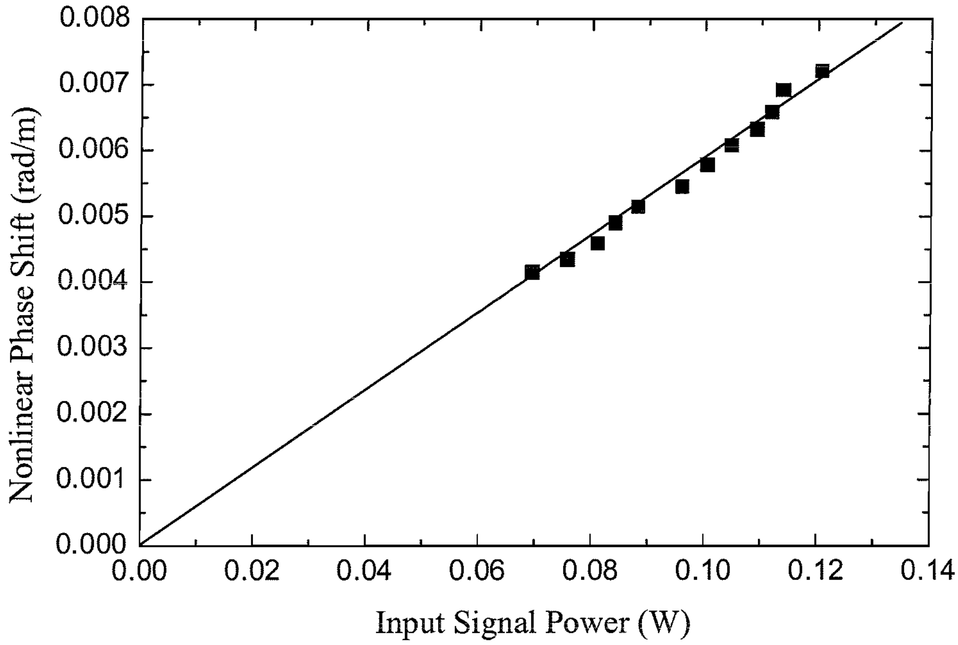

Figure 6.2: Experimentally measured nonlinear phase shift of the HF (WBHNL12-100) with respect to input signal power. The linear fit line to the experimental data is shown.

6.3 L^+-Band Raman Amplification with High Signal Gain Using a 75 m Long Holey Fibre

The experimental Raman amplifier setup is shown in Fig. 6.3. The amplifier was configured for copropagating pump and signal. The pump source, based on a diode seeded, fibre amplifier based MOPA configuration, was operated in a pulsed mode with 20 ns square pulses at 500 kHz repetition rate, corresponding to a 100:1 pump duty cycle.

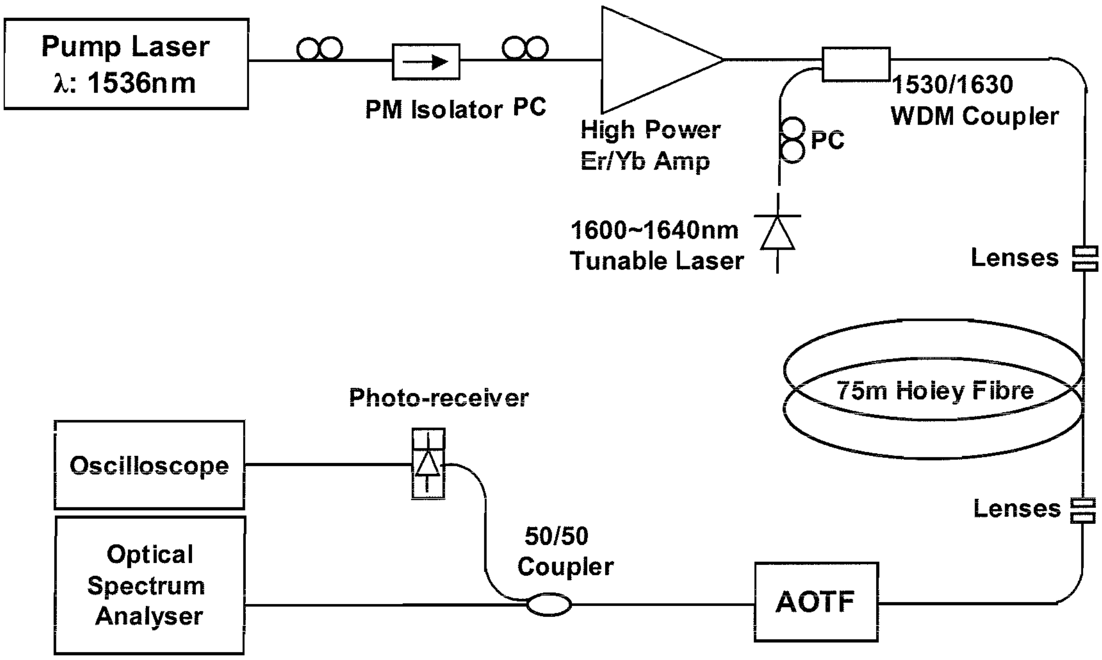

Figure 6.3: Experimental setup.

The pump wavelength was 1536 nm. The pump and the input signal beams were combined together using a 1530/1630 nm WDM coupler prior to launching the light into the HF Raman amplifier. The signal light was generated from a continuous wave external cavity laser tuneable in the range 1600 ~ 1640 nm. Polarisation controllers were included on both the pump and signal launching paths into the HF (WBHNL12-100) so that both beams could be launched onto a single polarisation axis of the polarisation maintaining HF. Both the pump and signal light were coupled with up to 40 % efficiency into the HF Raman amplifier using an appropriately matched lens combination. The maximum peak pump power coupled into the HF (WBHNL12-100) was ~6.7 W, and the maximum launched signal power ~ -10 dBm. An acousto-optic tuneable filter (AOTF) was placed at the output of the fibre to allow us to filter the amplified signal beam from the pump with sufficiently high isolation (>60 dB) to permit accurate gain measurements. The Raman gain measurements were made by analysing the temporal response of the signal beam to the pulsed pump beam.

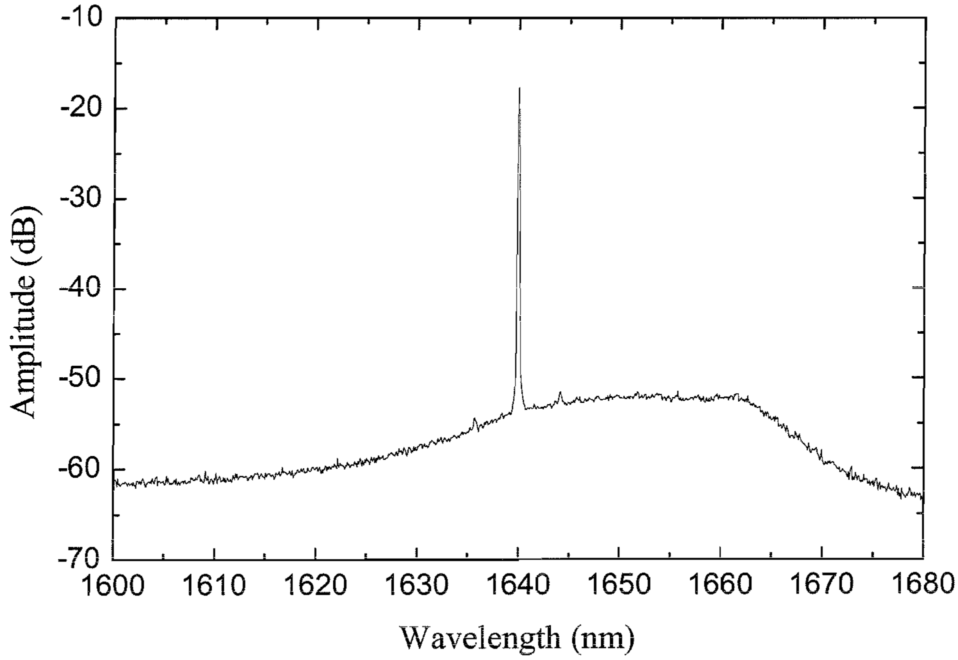

Figure 6.4: Measured (high gain) amplifier spectrum showing Raman ASE spectrum

Fig. 6.4 shows a measured time-averaged output spectrum from the HF (WBHNL12-100) where a 1640 nm probe signal with –10 dBm power was amplified under pumping of 6.7 W peak power. According to the optical spectrum of background ASE in the graph 1647 nm was found to be the Raman gain peak which has 13.2 THz frequency separation from the pump wavelength of 1535 nm.

Fig. 6.5 shows internal Raman gain and noise figure for various probe signal wavelengths and fixed pump/signal powers. Higher gain and lower noise figure are observed as the probe signal wavelength approaches the peak of the Raman gain curve around 1650 nm, corresponding to the peak Raman shift of 13.2 THz (see Fig. 6.4). Small signal gains as large as 42.8 dB, and noise figures as low as 6 dB were obtained at 1640 nm (the longest wavelength to which the signal laser used could be tuned). The observed variation in gain with wavelength was in good agreement with the expectations based on published data on the Raman lineshape of silica [6.9].

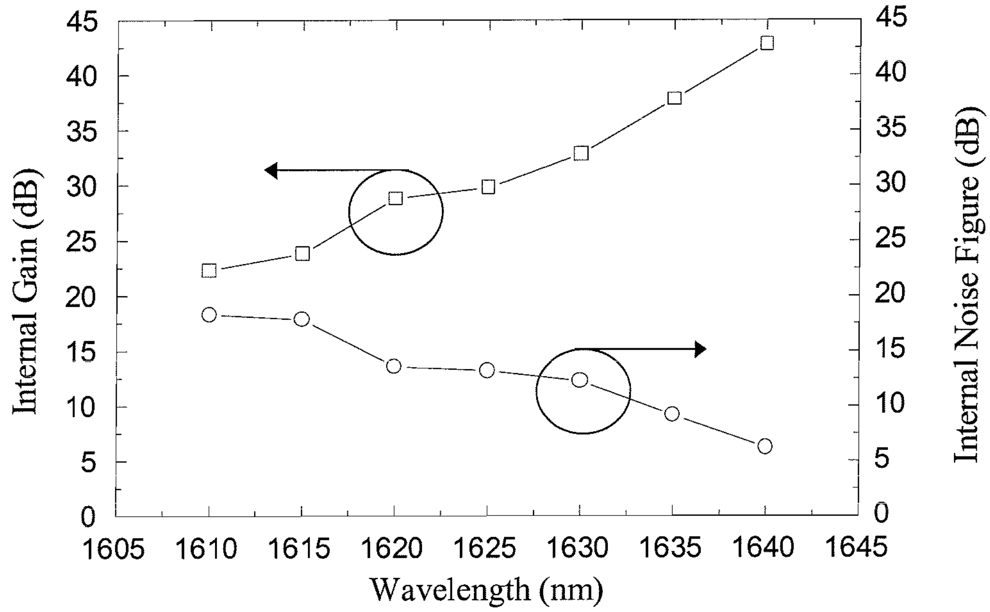

Figure 6.5: Internal Raman gain and noise figure for various probe signal wavelengths (signal power: -10 dBm, pump peak power: 6.7 W).

The internal gain was also measured as a function of pump peak power for a signal wavelength of 1635 nm. The input signal power was again fixed at -10 dBm. This plot is shown in Fig. 6.6.

Using the following equation $Gain(dB) = 10 \cdot \log_{10}(\exp(g_R P L_{eff} / A_{eff}) - \alpha L)$ [6.9], the measured value of gain efficiency (6 dB/W), and the directly measured value of L_{eff} / A_{eff}, the Raman gain coefficient g_R at the gain peak was estimated to have a value of 7.6 10^{-14} m/W. This value is in good agreement with the number for pure silica reported in the Ref. [6.10].

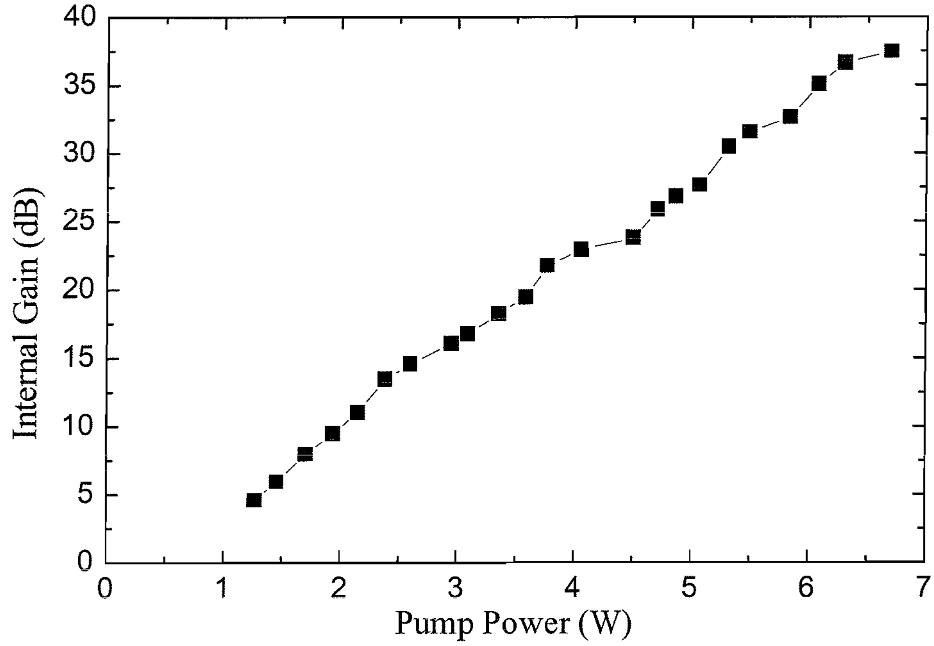

Figure 6.6: Measured internal gain versus pump power at 1635 nm.

6.4 Signal Modulation Using Ultra-Fast Raman Effects in Holey Fibre

As well as investigating the performance of the HF (WBHNL12-100) as a pure Raman amplifier a Raman modulator/erasure experiment was also carried out. In this instance a strong pump beam at a long wavelength is used to induce loss for a copropagating beam at shorter wavelengths [6.7]. The same experimental configuration as in the Raman amplification experiment was used (see Fig. 6.3) other than that the tuneable 1600 nm signal source was exchanged for a 20 dBm, 1458 nm CW semiconductor diode laser. (The 1530/1630 nm WDM coupler can also be used to combine light at 1536 nm and 1458 nm). In the presence of the pump pulses, the signal beam experiences stimulated Raman scattering (SRS), resulting in an effective nonlinearly induced signal loss. This manifests itself in the time domain through the formation of 'dark' pulses at the signal wavelength where the signal overlaps the pump pulses. Measured oscilloscope traces are shown in Figs. 6.7.

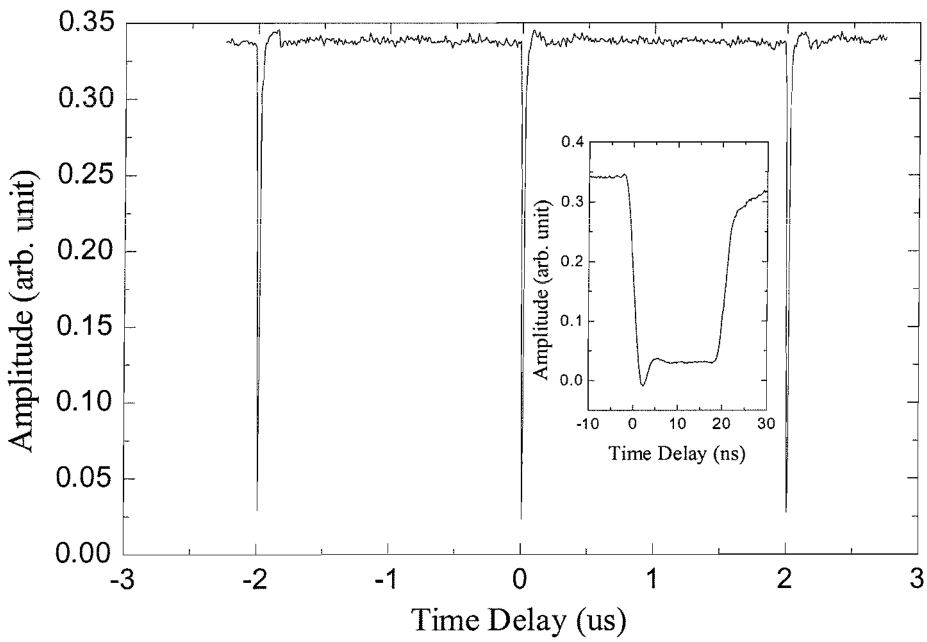

Figure 6.7: Temporal profile of dark pulses at the SRS modulator output; inset: Close up view of the square-shaped dark pulse (the temporal dip at the falling edge is due to ringing of the photo-receiver).

To quantify the performance of the SRS signal modulator the modulator extinction ratio which is defined as the hole depth relative to the background CW level was measured, as a function of pump pulse peak power. The results are summarised in Fig. 6.8, where it is seen that extinction ratios in excess of ~11 dB were obtained for peak powers of ~5 W and above. It should be possible to obtain even higher extinction ratios by tuning the frequency separation of the signal and pump (10.5 THz in these experiments) to lay closer to the peak Raman shift value, and by better alignment of the polarisation of the two beams relative to a principal axis of the fibre.

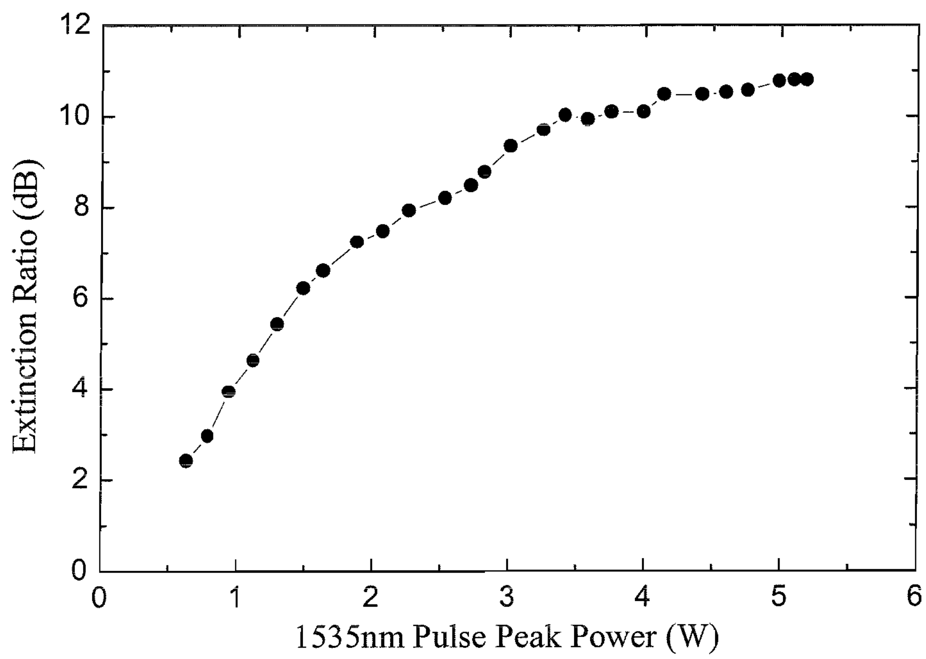

Figure 6.8: Extinction ratio of SRS based signal modulation versus pump pulse peak power.

6.5 Conclusion

I have experimentally demonstrated two Raman based devices using high nonlinearity HF. These experiments highlight the improvements that can be obtained in terms of reduced device lengths/power requirements relative to Raman devices based on conventional fibre types. As well as being significant from a packaging /environmental stability perspective, the reduced device lengths could also prove advantageous in terms of reducing the deleterious impact of double Rayleigh scattering on Raman amplifier noise [6.11], allowing this has yet to be studied in detail. Rayleigh scattering coefficient and capture cross-sections within such optical fibres need to be measured and better understood. HF technology could prove to be a powerful technology for the development of a wide range of practical nonlinear optical devices such as Raman amplifiers, optical limiters and wavelength converters.

6.6 References

[6.1] M. N. Islam, "Raman amplifiers for telecommunications," *IEEE J. Sel. Topic on Quantum Electron.*, vol.8, no.3, pp.548-559, 2002.

[6.2] E. M.Dianov, "Advances in Raman amplifier fibers," in *Proc. Optical Fiber Communications Conference (OFC'2001)*, Anaheim USA, March 2001, MA1.

[6.3] T. Sakamoto, "S-band fiber optic amplifier," in *Proc. Optical Fiber Communications Conference (OFC'2001)*, Anaheim USA, March 2001, TuQ1.

[6.4] H. Masuda, A. Mori, K. Shikano, K. Oikawa, K. Kato, and M. Shimizu, " Ultra-wide-band Raman amplifier using tellurite and silica fibres," *Electron. Lett.*, vol.38, no.16, pp.867-868, 2002.

[6.5] Y. Emori, and S. Namiki, "100nm bandwidth flat gain Raman amplifiers pumped and gain-equalized by 12-wavelength-channel WDM high power laser diodes," in *Proc. Optical Fiber Communications Conference (OFC'1999)*, March 1999, Postdeadline paper PD19.

[6.6] P. C. Reeves-Hall, D. A. Chestnut, C. J. S. De Matos, and J. R. Taylor, "Dual wavelength pumped L- and U-band Raman amplifier," *Electron. Lett.,* vol.37, no.14, pp.883-884, 2001.

[6.7] G. Burdgel, S. Alam, A. Grudinin, I. Khrushchev , M. Durkin, M. Ibsen, and I. White, "Ultrafast Intensity Modulation via Raman Gain for All-Optical In-Fiber Processing," *Optics. Lett.,* vol.23, no.8, pp.606-608, 1998.

[6.8] P. B. Hansen, L. Eskildsen, A. J. Stentz, T. A. Strasser, J. Judkins, J. J. DeMarco, R. Pedrazzani, and D. J. DiGiovanni, "Rayleigh scattering limitations in distributed Raman pre-amplifiers," *IEEE Photon. Technol. Lett.*, vol.10, no.1, pp.159-161, 1998.

[6.9] G. P. Agrawal, *Nonlinear fiber optics*, Academic Press, Second Edition 1995, pp.316-322.

[6.10] S. T. Davey, D. L. Williams, B. J. Ainslie, W. J. M. Rothwell, and B. Wakefield, "Optical gain spectrum of GeO_2-SiO_2 Raman fibre amplifiers," *IEE Proc.-J*, vol136, no.6, pp.301-306, 1989.

[6.11] S. H. Chang, S. K. Kim, M.-J. Chu, and J.-H. Lee, "Limitations in fibre Raman amplifiers imposed by Rayleigh scattering of signals," *Electron. Lett.*, vol.38, no.16, pp.865-867, 2002.

CHAPTER SEVEN

INVESTIGATION OF BRILLOUIN EFFECTS IN SMALL CORE HOLEY OPTICAL FIBRE: LASING AND SCATTERING

This Chapter reports that HF technology can also be applied for building a Brillouin laser and provides an investigation of spontaneous/stimulated Brillouin scattering characteristics in an HF.

This Chapter is organised as follows. Section 7.1 describes a brief introduction to HF technology applications on Brillouin effect based nonlinear devices. In Section 7.2 the experimental results on the observation of an HF based Brillouin laser are presented. Section 7.3 gives a systematic investigation into increase of stimulated Brillouin scattering threshold in holey fibre due to its structural nonuniformity. In Section 7.4 conclusions are drawn regarding the results and further applications of the technology are discussed.

7.1 Holey Fibre Technology for Brillouin Effect Based Nonlinear Devices

A number of research groups have studied nonlinear effects in HF and demonstrated a variety of results such as four-wave mixing [7.1], soliton self-frequency shift [7.2], third harmonic generation [7.3], and so on. As discussed in Chapter 5 and 6, it has also been illustrated that holey fibre technology could provide a powerful way to realise a variety of practical nonlinear optical devices for fibre-optic communication systems. For example, the use of a nonlinear thresholding device based on the Kerr effect in just 8.7 m of HF with a mode area of ~2.93 μm^2 in a superstructured fibre Bragg grating-based 255-chip, DS-OCDMA system [7.4] and the achievement of ~ 42 dB signal gain in an L^+-band Raman amplifier based on just 75 m length of a HF [7.5]. Both demonstrations highlight the improvements that can be obtained in terms of reduced device lengths/power requirements due to the high effective nonlinearity of the fibre.

In the following Sections, it is shown that HF technology can also be applied to another important class of nonlinear fibre-optic devices - namely those devices based on the Brillouin effect; more specifically, a HF based Brillouin laser. Also, the Brillouin gain line shapes within the fibre (for two different fibre lengths) were measured and compared with the lineshape of conventional dispersion shifted fibre (DSF). The results show that structural variations along the HF length give a substantial increase in Brillouin linewidth.

7.2 Holey Fibre Based Brillouin Laser

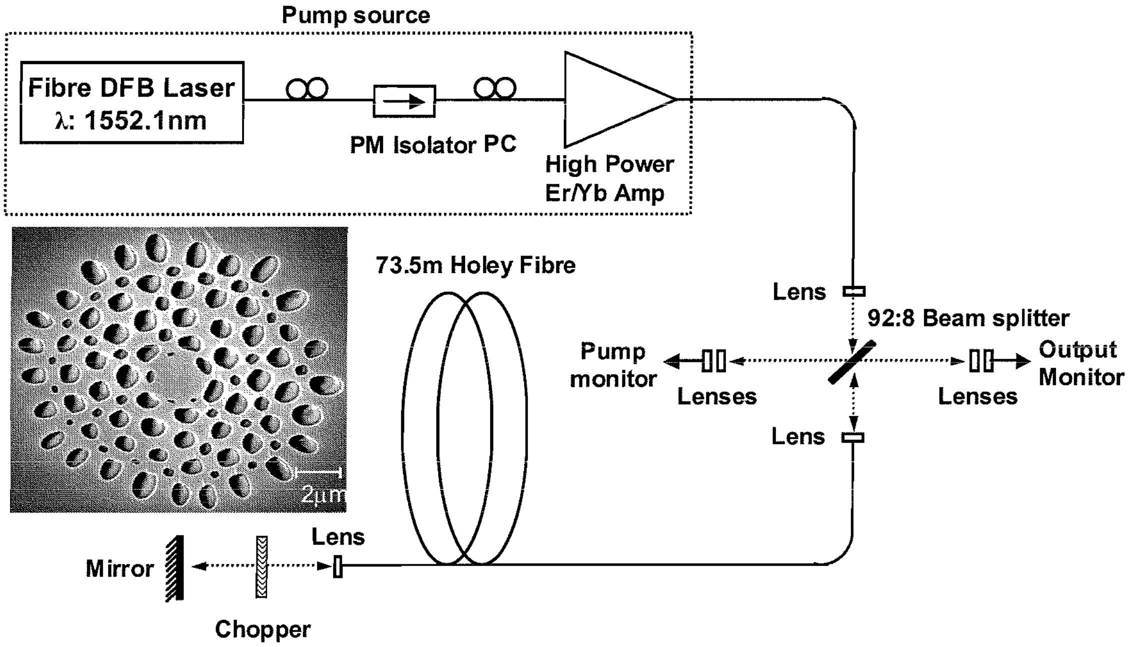

Figure 7.1: Experimental setup. Inset, cross sectional scanning electron microscope image of the holey fibre (WBHNL12-100) used in this experiment. PC, polarisation controller.

The experimental setup is shown in Fig. 7.1. The pump source is based on an Erbium fibre DFB seed laser followed by a high power Er^{3+}/Yb^{3+} Amplifier. The source has a linewidth of ~35 kHz, a centre wavelength of 1552.1 nm and provides a maximum output power of ~750 mW. The Fabry-Perot resonator incorporates a 73.5 m long holey fibre (WBHNL12-100), a lens-coupled high-reflectivity cavity mirror and a 96 % output coupler defined by the Fresnel reflection from the cleaved fibre facet at the pump launch end of the cavity. Both polarisation controllers and a polarisation maintaining (PM) isolator were used in order that the pump beam could be lens-coupled onto one of the principal axes of the HF (WBHNL12-100). A launch efficiency of ~50 % was measured. A 92:8 beam splitter was located at the pump launch end of the HF (WBHNL12-100) to monitor both the Brillouin laser output, and the incident pump power. A mechanical chopper was located in front of the HR mirror to facilitate alignment of the cavity.

The holey fibre (WBHNL12-100) used in this experiment has a core diameter of ~1.6 μm and has a measured effective area of 2.85 μm^2 and a loss of 40 dB/km at 1550 nm. The effective length ($L_{eff} = \frac{1-e^{-\alpha L}}{\alpha}$ where α is fibre loss and L is fibre length) of the fibre is 53 m. The fibre is polarisation maintaining by virtue of the structural hole asymmetry evident in the cross sectional Scanning Electron Micrograph (SEM) shown in the inset of Fig. 7.1, and has a measured beat length of ~ 0.4 mm around 1550 nm. This fibre is more fully described in Chapter 6.2 [7.5].

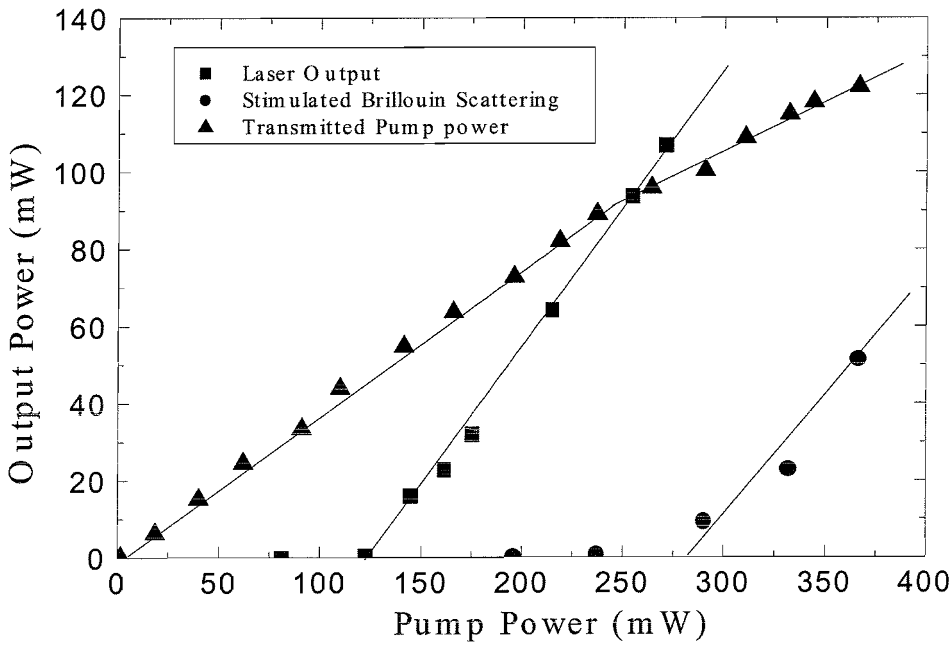

Figure 7.2: (i) Laser output, (ii) stimulated Brillouin scattering (backward), and (iii) transmitted pump power as a function of launched pump power (stimulated scattering only).

First, the performance investigation of the fibre was carried out under laser operation (i.e. with feedback from the HR mirror end of the cavity). Laser operation rather than stimulated scattering was confirmed by modulating the cavity loss using the free space chopper, and looking for correspondingly modulated laser output as shown in Fig. 7.3. Fig. 7.2 shows experimental data of the Brillouin laser output power as a function of the input pump power. The laser threshold was found to be 125 mW, and the slope efficiency was ~70 %. The RF spectrum of the beat signal between the laser output and the pump beam was measured using an RF spectrum analyser, which showed that the frequency of the Brillouin laser output was downshifted by 10.6 GHz relative to the pump frequency as shown in Fig. 7.4.

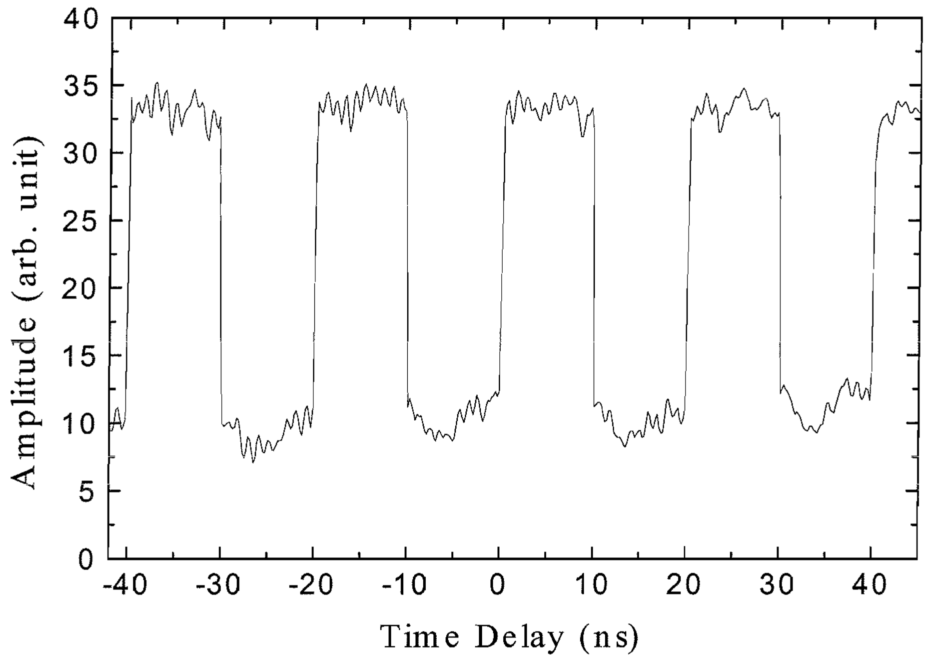

Figure 7.3: Oscilloscope trace of output square-shaped pulses from the Brillouin laser under cavity modulation with the chopper.

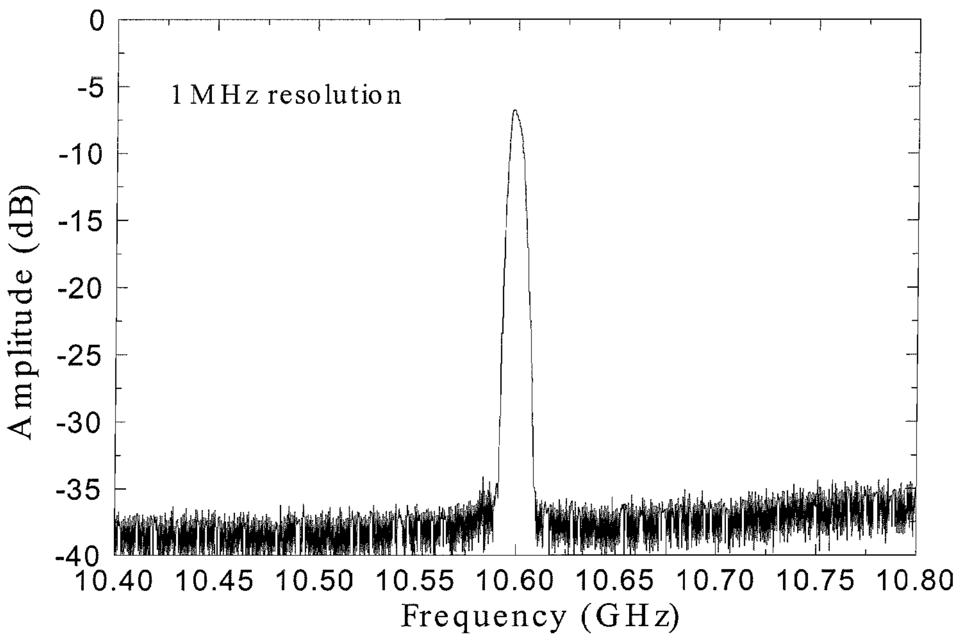

Figure 7.4: RF frequency trace of the beat signal between the Stokes and the pump beams.

7.3 Increase of Stimulated Brillouin Scattering Threshold in Holey Fibre with Structural Nonuniformity

Next, the investigation into the stimulated Brillouin scattering (SBS) threshold within the HF (WBHNL12-100) was performed. Feedback from the HR mirror was removed, and any possibility of Fresnel reflection from the terminated fibre at this end of the cavity was eliminated by immersing the fibre in index matching liquid. A SBS threshold was experimentally observed to be ~ 280 mW as shown in Fig. 7.2.

This stimulated threshold value, (and indeed the laser threshold), was substantially higher (by roughly an order of magnitude) than what was expected from simple estimates based on the established Brillouin gain coefficient for pure silica, and the measured values of HF mode area and loss. It was postulated that this was due to structural variations along the HF (WBHNL12-100) since it is well established in conventional fibres that Brillouin shift is strongly dependent on the fibre structure and that any variation in structure along a fibre can result in effective Brillouin line broadening and reduced Brillouin gain [7.6]. This particular HF (WBHNL12-100) was drawn without active diameter control during the drawing process and was known to have a (slow) variation of to +/-3 μm diameter along its length, a far greater variation than is usual for conventional commercial fibre types (and indeed for other HF's that the University of Southampton has drawn).

Theoretically if the pump laser linewidth is negligible relative to the Brillouin gain bandwidth, the SBS threshold can be approximated by the following equation as suggested by K. Shiraki et al. [7.6].

$$P_{th} \cong 21\frac{KA_{eff}}{G(\nu_{\max})} \qquad (7.1)$$

The effective gain coefficient $G(\nu)$ is expressed as

$$G(\nu) = \int_0^L g_B(\nu, z)\cdot \exp(-\alpha z)dz \qquad (7.2)$$

where K and A_{eff} are the polarisation factor (K = 1 for a polarisation maintaining fibre) and the effective area of the fibre, respectively. $\nu_{\max}$ represents the frequency at which $G(\nu)$ is maximized. $g_B(\nu,z)$ is the Brillouin gain spectrum whose Lorentzian profile is given by

$$g_B(\nu,z)=\frac{g_0}{1+\left(\frac{\nu-\nu_B(z)}{\Delta\nu_B/2}\right)^2} \qquad (7.3)$$

where $\nu_B(z)$ is the Brillouin frequency shift at the location of z, $\Delta\nu_B$ is the intrinsic Brillouin gain bandwidth, and g_0 is the peak Brillouin gain coefficient. A fibre with structural variations shows a smaller effective gain coefficient than a uniform fibre ($G(\nu_{\max})=g_0\cdot L_{eff}$ for uniform fibre) due to the irregular Brillouin shift distribution along the fibre, as can be understood through the relation of $g_B(\nu,z)\le g_0$ [7.6]. Thus, the Brillouin threshold increases while the effective gain coefficient $G(\nu_{\max})$ decreases in a structurally nonuniform fibre.

In order to confirm the suspicions the spontaneous Brillouin scattering lineshape was measured for two different lengths (73.5 m, 40 m) of the fibre, using a hetrodyne-detection technique that relies upon beating the spontaneously scattered light with the pump beam [7.7]. Also the result was compared to that of a standard DSF fibre. These Brillouin gain bandwidth measurements are summarised in Fig. 7.5. The spontaneous Brillouin linewidth of the 73.5 m long HF (WBHNL12-100) is seen to be approximately an order of magnitude greater than that of pure silica and has a non-Lorentzian shape. More specifically, the 73.5 m HF (WBHNL12-100) has ~7 times broader bandwidth than DSF silica fibre in terms of the 3-dB bandwidth. The theoretical prediction of the threshold of the HF (WBHNL12-100) based on the observed line broadening is ~240 mW and which is in reasonable agreement with the measured value of 280 mW mentioned above. The Brillouin gain bandwidth of a 40 m length of the same HF (WBHNL12-100) (L_{eff} = 33 m) was also measured, and the bandwidth was observed to be approximately half the value found in the 73.5 m length, and in addition a small increase in the Brillouin frequency shift was observed (see Fig. 7.4). This thus represents compelling evidence that structural variation along the fibre is indeed responsible for the variation in Brillouin frequency shift and corresponding linewidth broadening, and consequently to the increased SBS threshold. It will certainly be possible to obtain much lower SBS thresholds in HF in which greater attention is paid to reducing the diameter fluctuations along the length. Note that the 40 m HF (WBHNL12-100) was measured to have a SBS threshold of 290 mW, which is comparable to that of the 73.5 m HF (WBHNL12-100).

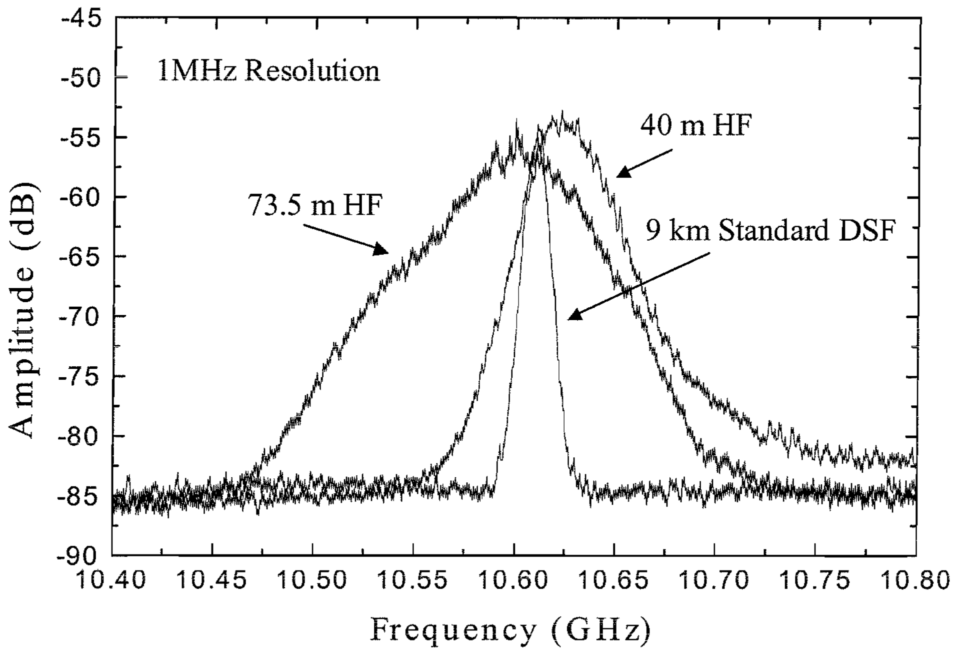

Figure 7.5: RF frequency trace of the beat signals between spontaneous Brillouin scattered beam and the pump for 73.5 m HF (WBHNL12-100), 40 m HF (WBHNL12-100), and a 9 km standard DSF fibre.

7.4 Conclusion

It has been experimentally demonstrated a CW Brillouin laser based on a highly nonlinear HF. A good laser power conversion efficiency of ~70 % and a Brillouin shifted output power of 110 mW were readily achieved at a wavelength of 1552.18 nm using a simple Fabry-Perot resonator scheme. Investigation of the stimulated Brillouin scattering characteristics of the HF was performed and it was established that structural variation along this particular HF was responsible for broadening the Brillouin gain lineshape. With better control of the HF diameter during drawing it will be possible to reduce this line broadening allowing the full benefits of the tight mode confinement within these fibres to be exploited more fully in terms of reduced device lengths/power requirements for a variety of Brillouin effect based optical devices. Further study on structural variation of HF is underway in order to understand how Brillouin frequency shift varies with structure, and the sensitivity of effective mode area and GVD to structural variations.

7.5 References

[7.1] J. E. Sharping, M. Fiorentino, A. Coker, P. Kumar, and R. S. Windeler, " Four-wave mixing in microstructure fiber," *Optics Lett.*, vol.26, pp.1048-1050, 2001.

[7.2] X. Liu, C. Xu, W. H. Knox, J. K. Chandalia, B. J. Eggleton, S. G. Kosinski, and R. S. Windeler, " Soliton self-frequency shift in a short tapered air-silica microstructure fiber," *Optics Lett.*, vol.26, pp.358-360, 2001.

[7.3] F. G. Omenetto, A. J. Taylor, M. D. Moores, J. Arriaga, J. C. Knight, W. J. Wadsworth, and P. St. J. Russell, "Simultaneous generation of spectrally distinct third harmonics in a photonic crystal fiber," *Optics Lett.*, vol.26, pp.1158-1160, 2001.

[7.4] J.H. Lee, P.C. Teh, Z. Yusoff, M. Ibsen, W. Belardi, T.M. Monro, and D.J. Richardson, "A holey fiber based nonlinear thresholding device for optical CDMA receiver performance enhancement," *IEEE Photon. Technol. Lett.,* vol.14, no.6, pp.876-878, 2002.

[7.5] J.H. Lee, Z. Yusoff, W. Belardi, T.M. Monro, P.C. Teh, and D.J. Richardson, "A holey fibre Raman amplifier and all-optical modulator," in *Proc. 27th European Conference on Optical Communication (ECOC' 2001)*, Amsterdam the Netherlands, September 2001, PD.A.1.1, pp.46-47.

[7.6] K. Shiraki, M. Ohashi, and M. Tateda, "SBS threshold of a fiber with a Brillouin frequency shift distribution," *J. Lightwave Technol.*, vol.14, pp.50-57, 1996.

[7.7] R. W. Tkach, A. R. Chraplyvy, and R. M. Derosier, "Spontaneous Brillouin scattering for single-mode optical-fibre characterisation," *Electron Lett.*, vol.22, pp.1011-1013, 1986.

CHAPTER EIGHT

A TUNEABLE WDM WAVELENGTH CONVERTER BASED ON CROSS PHASE MODULATION EFFECTS IN HOLEY FIBRE

This Chapter reports that HF technology can be applied for tunable WDM wavelength conversion, an important function in high-capacity WDM systems. The wavelength conversion is based on cross phase modulation and passive filtering.

This Chapter is organised as follows. Section 8.1 provides a brief introduction to HF technology applications within tuneable wavelength conversion. In Section 8.2 experimental results on wavelength conversion based cross phase modulation and filtering in holey fibre are described. In Section 8.3 conclusions are drawn regarding the results and a method to obtain further performance improvement is discussed.

8.1 Holey Fibre Technology for Wavelength Conversion

All-optical wavelength conversion is another important nonlinear function required within high-capacity wavelength division multiplexing (WDM) systems and the related all-optical networks [8.1]. The capacity of WDM based networks is mainly limited by the number of channels used, wavelength congestion at network nodes, and system management requirements for data re-routing on link failure. The use of wavelength converters within the networks will thus increase the flexibility of data traffic management schemes [8.2].

So far a variety of types of wavelength converters have been reported; for example, those based on four-wave mixing (FWM) in optical fibre and semiconductor optical amplifiers [8.3, 8.4], nonlinear optical loop mirror types based on cross-phase modulation (XPM) [8.5, 8.6], and those based on cross gain modulation (XGM) in SOA [8.7, 8.8]. Recently a simple and robust, optical fibre based wavelength converter scheme has been proposed, which uses XPM and spectral filtering [8.9, 8.10]. The principle of operation in this scheme is based on XPM between the control signal and the CW beams, which generates additional spectral components on the CW laser beam. A wavelength-converted signal is obtained by passing one of the generated spectral components through a narrowband filter which also serves to eliminate the residual unchirped CW signal. Fig. 8.1 shows the principle of XPM and spectral filtering based wavelength conversion using a HF.

In the following Sections, I report that HF technology can also be applied for tunable WDM wavelength conversion. Multiple wavelength conversion over ~20 nm bandwidth is demonstrated at a data rate of 10 Gbit/s using a combination of XPM in a short length of HF and narrowband spectral filtering. As well as a much shorter device in contrast to previously reported wavelength conversion based on the XPM and filtering [8.9, 8.10], the use of a compression-tuned narrowband apodized fibre Bragg grating (FBG) filter is demonstrated to obtain accurate, high quality spectral definition of the wavelength converted signal. The use of an apodized grating filter allows for a very good extinction of the associated residual continuous wave (CW) and pump beams, as well as for adjacent wavelength converted channels.

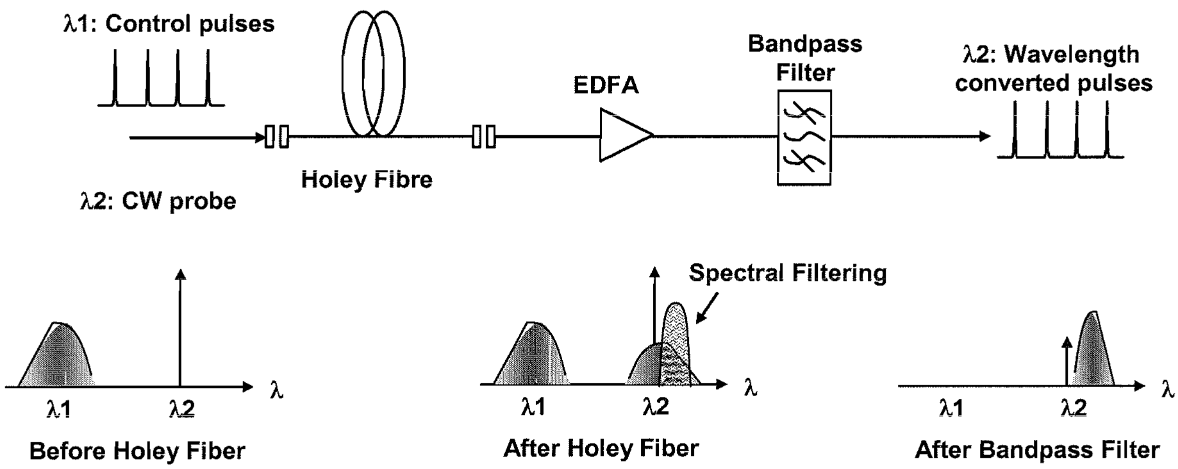

Figure 8.1: Principle of XPM and spectral filtering based wavelength conversion.

8.2 Tuneable Wavelength Conversion Based on Cross Phase Modulation and Filtering in Holey Fibre

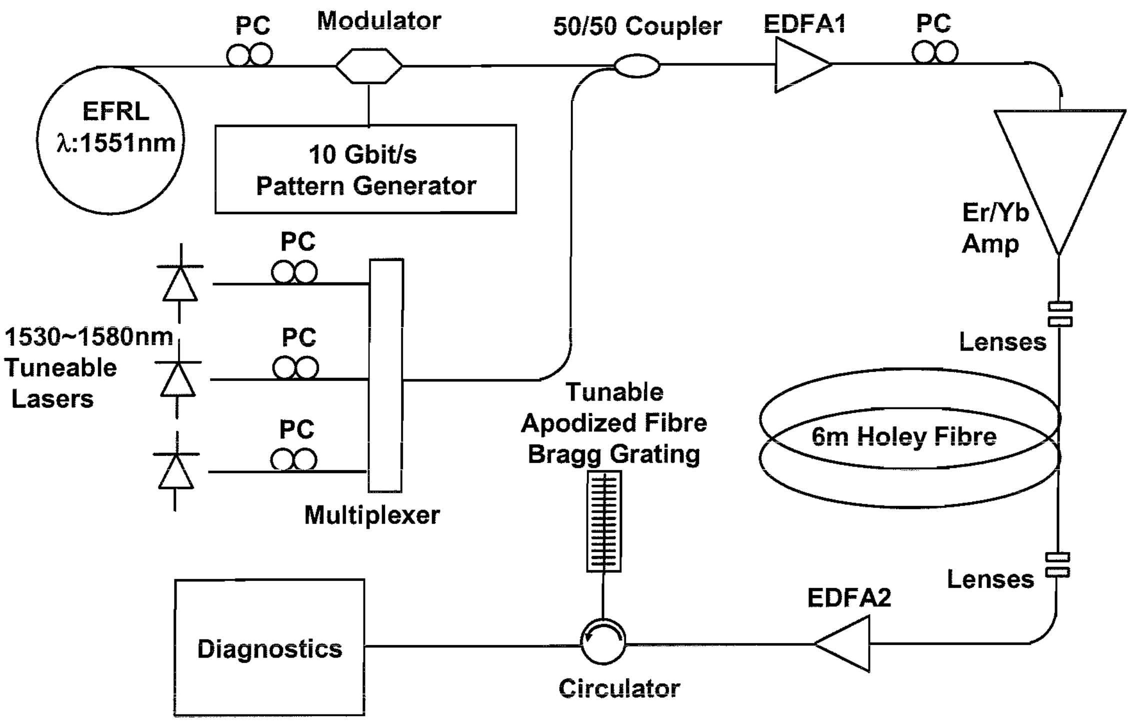

(a)

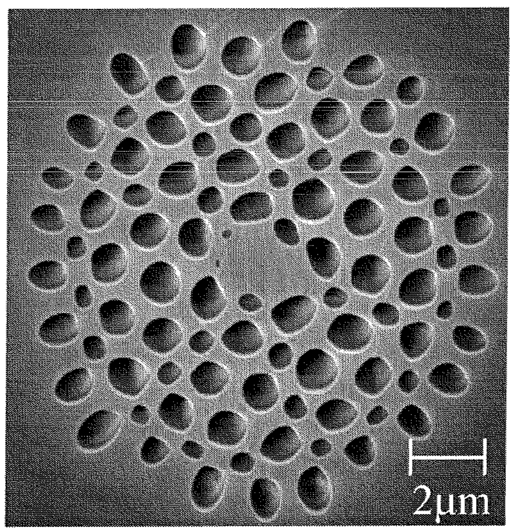

(b)

Figure 8.2: (a) Experimental setup. (b) Cross-sectional SEM image of the holey fibre (WBHNL12-125) used.

The experimental set up is shown in Fig. 8.2(a). 2.5 ps pulses at a repetition rate of 10 GHz are first generated using a regeneratively mode locked erbium fibre ring laser (EFRL) operating at a wavelength of 1551 nm. These pulses are then modulated to obtain a 10 Gbit/s, 2^{15} - pseudorandom control pulse stream. The control pulses and three probe beams were combined together using a combination of 50/50 couplers prior to launching the light into the HF (WBHNL12-125). The probe beams were generated from CW external cavity lasers tunable in the range 1530 ~ 1580 nm. Polarisation controllers were included on both the control and probe launching paths into the HF so that all of the beams could be launched onto a single polarisation axis of the polarisation maintaining HF. Both the control and probe signals were amplified using an Er/Yb amplifier with a maximum saturated output power of ~800 mW, and were then lens coupled into a 6m length of the HF (WBHNL12-125) with a coupling efficiency of 40 %. A cross-sectional SEM profile of the highly nonlinear HF (WBHNL12-125) used in this experiment is shown in Fig. 8.2(b). The core diameter is ~2.0 μm and the outer diameter is 125 μm. The measured dispersion at the wavelength of 1550 nm was +100 ps/nm-km and the measured loss was 50 dB/km. From a measurement of the SPM induced nonlinear phase shift versus launched optical power, the nonlinearity coefficient γ was estimated to be $31W^{-1}\ km^{-1}$ and an estimated effective area A_{eff} to be 2.93(+/-0.3) μm^2. This nonlinearity is ~20 times higher than that of a conventional dispersion shifted fibre.

XPM between the control signal and the CW beams results in chirping of the CW laser beam where these beams overlap temporally within the fibre. This frequency chirping can then be converted to a frequency converted signal by passing this chirped signal through a narrowband filter which serves to eliminate the residual unchirped CW signal as well as to select one of the two XPM-induced side bands [8.10]. The measured output spectrum from the HF (WBHNL12-125) is shown in Fig. 8.3(a). It is clearly evident that each probe beam is spectrally broadened due to XPM with the control signal, whilst the control signal itself also shows a small amount of spectral broadening caused by self-phase modulation. In this experiment, an apodized FBG was used for the spectrum-slicing filter. The filter has a 3 dB bandwidth of 0.55 nm and a 30 dB bandwidth of 1.5 nm as shown in the inset of Fig. 8.3(b). The FBG was embedded in a layered flexible plate that when bent allowed for 20 nm wavelength tuning of the filter due to the resulting compressive strain on the FBG [8.11].

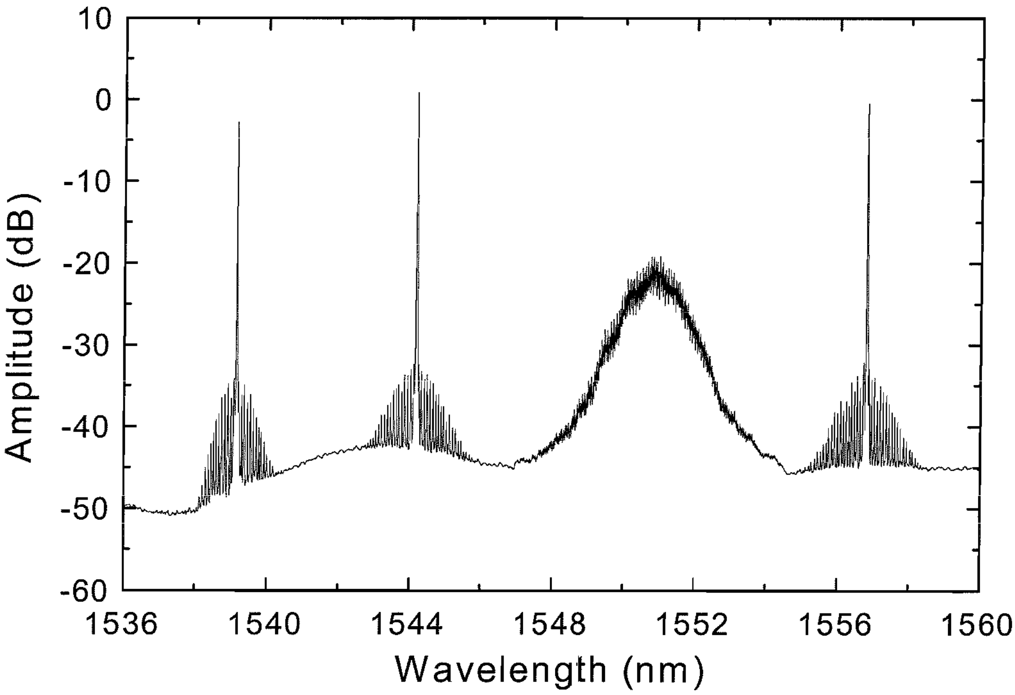

(a)

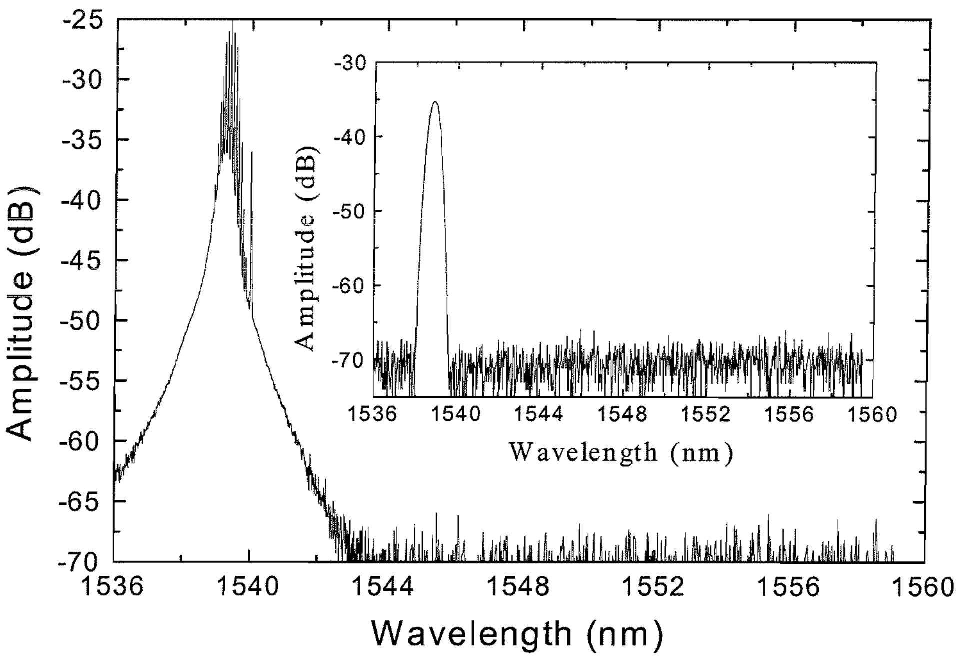

(b)

Figure 8.3: (a) Measured optical spectrum of three probe signals with control pulses after the HF (WBHNL12-125). (b) Measured optical output spectrum after the HF (WBHNL12-125) and the grating filter; Inset: Spectral response of the apodized fibre Bragg grating filter used (3 dB bandwidth of 0.55 nm, 30 dB bandwidth of 1.5 nm).

The FBG provides both high precision and high efficiency spectral slicing as well as significant suppression of all residual CW components, pump beams and adjacent wavelength channels as shown in the spectrum of Fig. 8.3(b).

Initially the performance of this wavelength converter was characterised in the temporal domain using a SHG autocorrelator (<100 fs resolution). The measured temporal width of the wavelength-converted pulses as a function of probe beam wavelength is plotted in Fig. 8.4. The pulsewidths of the converted pulses were observed to be almost constant at ~11 ps over the full, ~20 nm wavelength tuning wavelength range of the FBG. The time-bandwidth product of the converted pulses was ~0.5 which, although somewhat larger than that of the original control soliton pulses (0.32, transform-limited), still indicates high-quality pulses. However, a degree of amplitude noise was observed on the converted signals and which can be attributed to coherence degradation due to the anomalous dispersion of this particular HF (WBHNL12-125) [8.12]. This noise could be eliminated by the use of an HF with normal dispersion at the operating wavelength rather than anomalous dispersion. The production of such fibres could be achieved quite easily by relatively minor changes to the structure of the existing HF.

It is well known that the use of a saturable absorber can also reduce intensity noise to a significant extent [8.13] and so a semiconductor optical amplifier (SOA) was incorporated in the experimental setup to help eliminate this amplitude noise, and to allow us to make some system measurements of the HF based wavelength converter. BER measurements were performed on one channel at a wavelength of 1540 nm. Fig. 8.5 shows both the measured BER and eye diagrams for the soliton control and wavelength converted 10 Gbit/s pulses. An approximately 4 dB power penalty was observed together with an error floor at the 10^{-9} BER level relative to that of the soliton control pulses. It should be pointed out again though that the use of normal dispersion fibre would have eliminated these coherence related penalties.

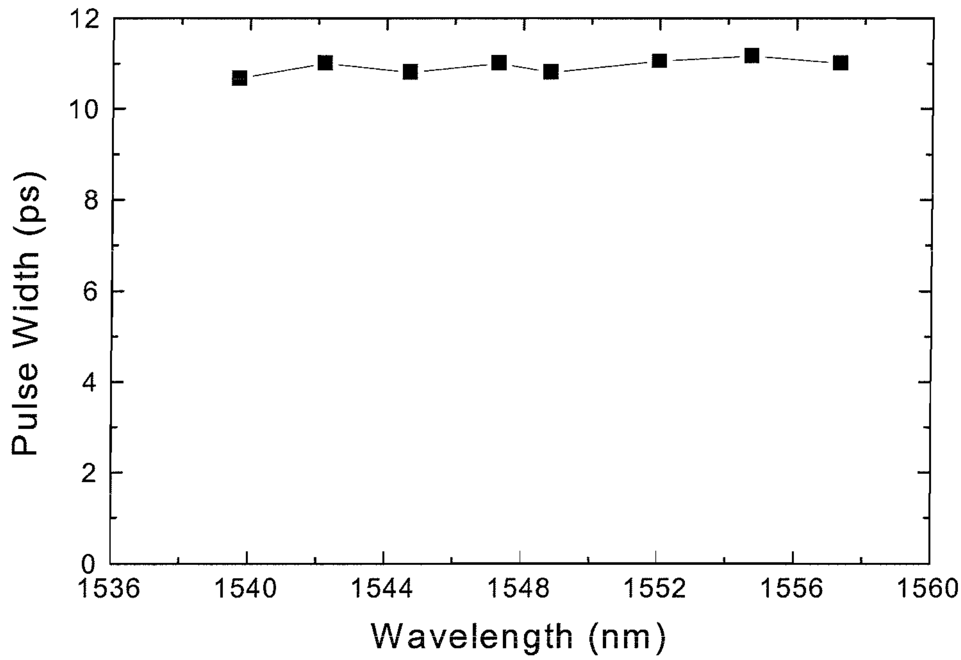

(a)

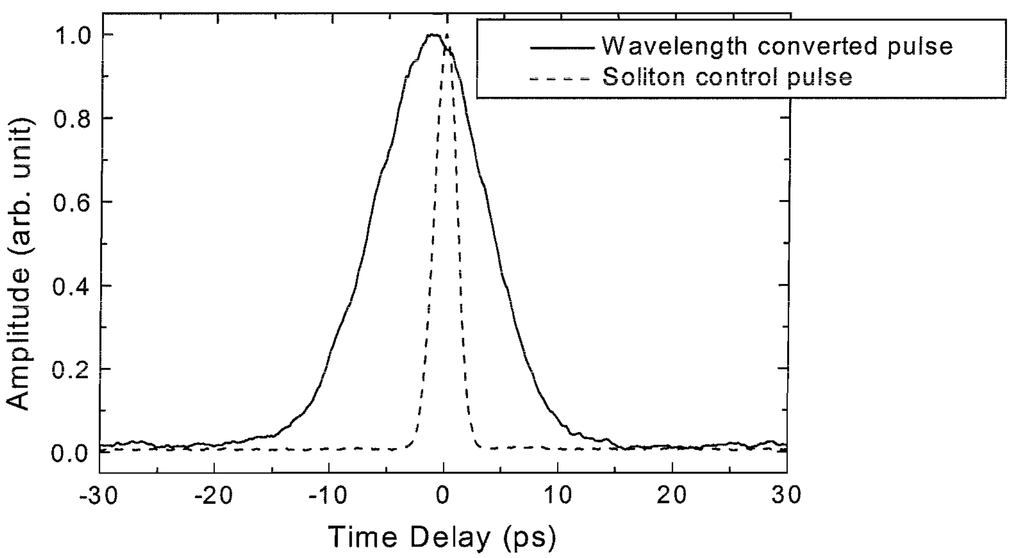

(b)

Figure 8.4: (a) Measured FWHM of wavelength converted pulses as a function of probe beam wavelength at a single channel case. (b) SHG autocorrelation traces of wavelength converted pulses at 1540 nm.

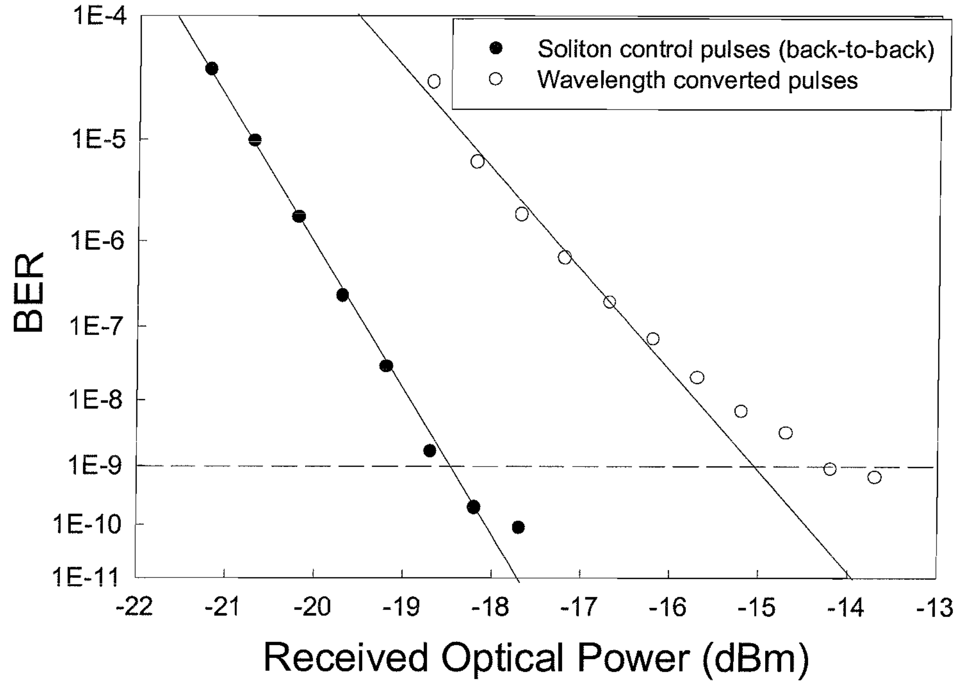

(a)

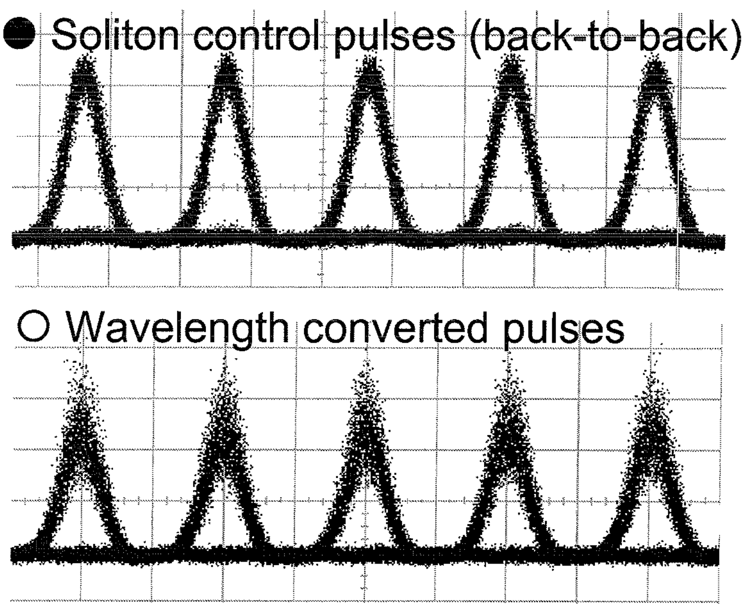

(b)

Figure 8.5: (a) Measured BER versus received optical power for wavelength conversion of 10 Gbit/s data pulses at a wavelength of 1540 nm. (b) The corresponding eye diagrams.

8.3 Elimination of Coherence Degradation Induced Intensity Noise Using Normal Dispersion Holey Fibre

In order to prove the postulation that use of a holey fibre with normal rather than anomalous dispersion would lead to performance improvement without coherence degradation, further wavelength conversion experiments with a normal GVD HF were subsequently performed.

The same experimental configuration as in the wavelength conversion with a anomalous GVD HF was used (see Fig. 8.2(a)) other than that the 6 m long anomalous GVD HF (WBHNL12-125) was exchanged for a 5.8 m long normal GVD HF (WBHNL17). A cross-sectional SEM profile of the highly nonlinear normal dispersion HF (WBHNL17) used in this experiment is shown in Fig. 8.6.

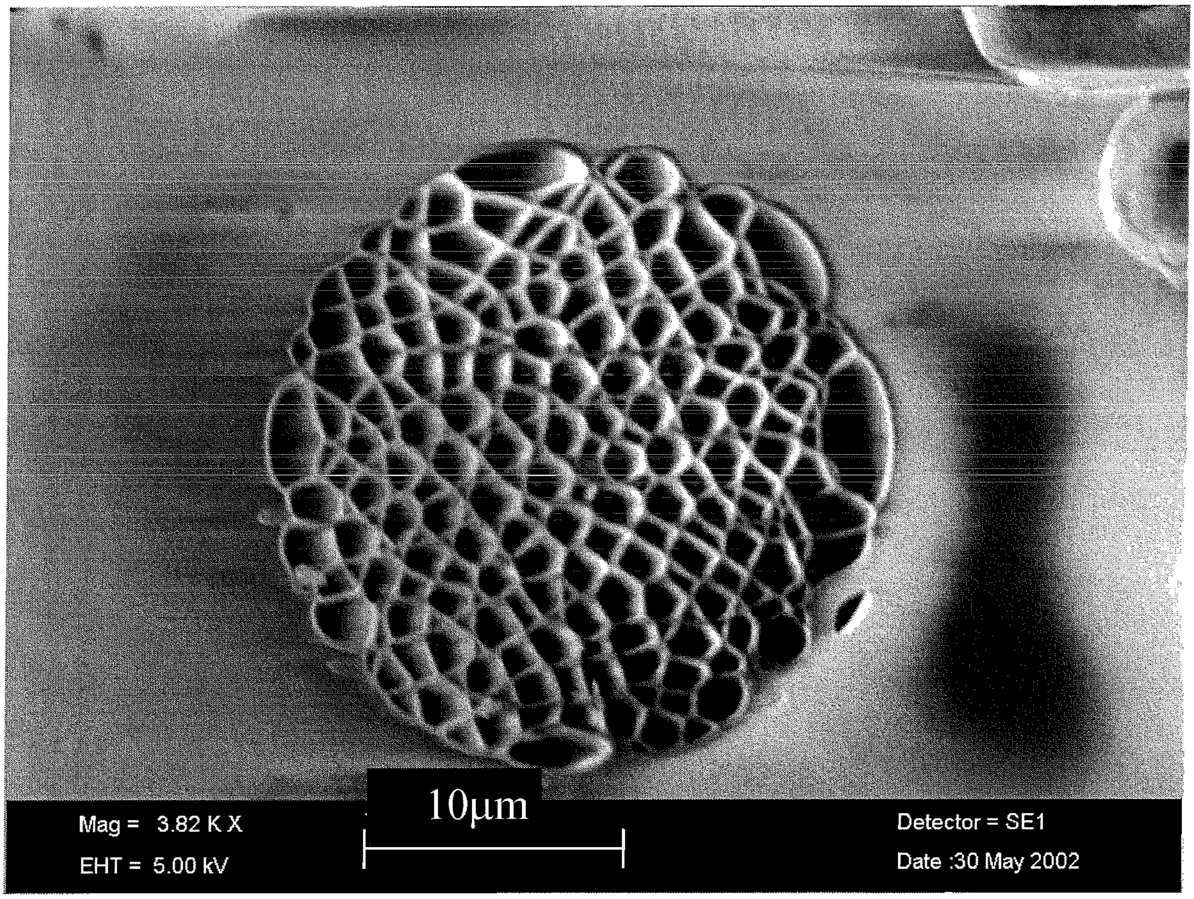

Figure 8.6: Cross-sectional SEM image of the normal dispersion holey fibre (WBHNL17) used within this experiment.

The core is elliptical in shape (axis ratio of ~1.5) with a minimum axis dimension of ~1.0 μm. The outer diameter of the HF (WBHNL17) is 100 μm. The measured dispersion at the wavelength of 1550 nm was ~ -350 ps/nm-km and the measured loss was 300 dB/km. From a measurement of the SPM induced nonlinear phase shift versus launched optical power, an estimated value of γ = ~ 60 W^{-1} km^{-1} was obtained for the nonlinearity coefficient corresponding to an estimated effective area of A_{eff} = 1.5(+/-0.2) μm^2. This nonlinearity is ~30 times higher than that of a conventional dispersion shifted fibre.

The measured output spectrum from the HF (WBHNL17) is shown in Fig. 8.7. It is clearly evident that each probe beam is spectrally broadened due to XPM induced by the control signal. The control signal itself also shows a small amount of spectral broadening caused by self-phase modulation. XPM among three CW's and SPM of each CW's could be generated in some degree. However, the corresponding frequency chirping would be very small compared to that from XPM between CW's and pump due to the lower peak powers of the CW pumps.

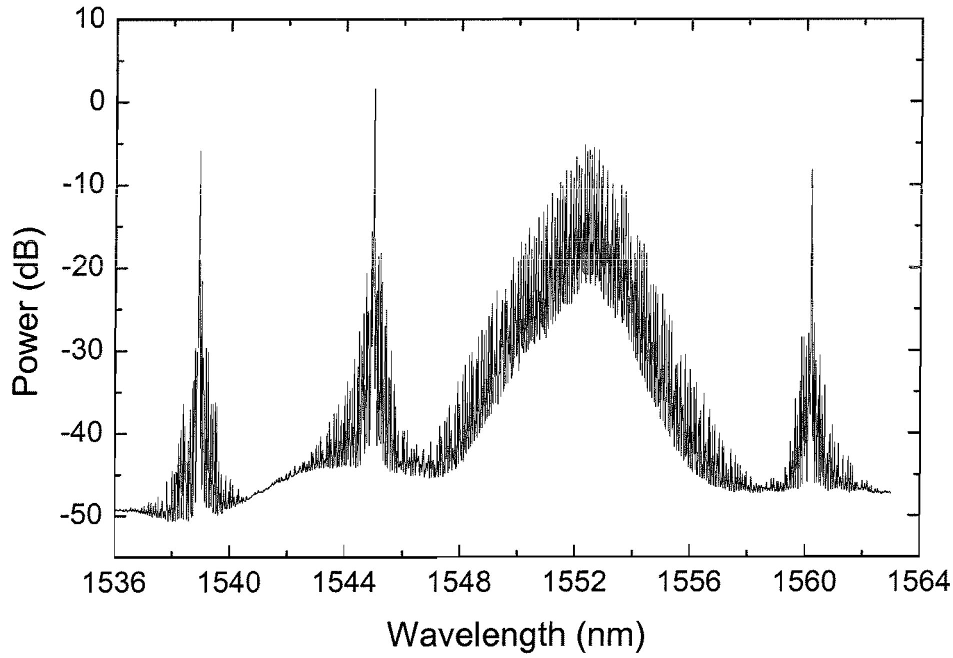

Figure 8.7: Measured optical spectrum of the three wavelength converted signals and of the control pulses after the HF (WBHNL17).

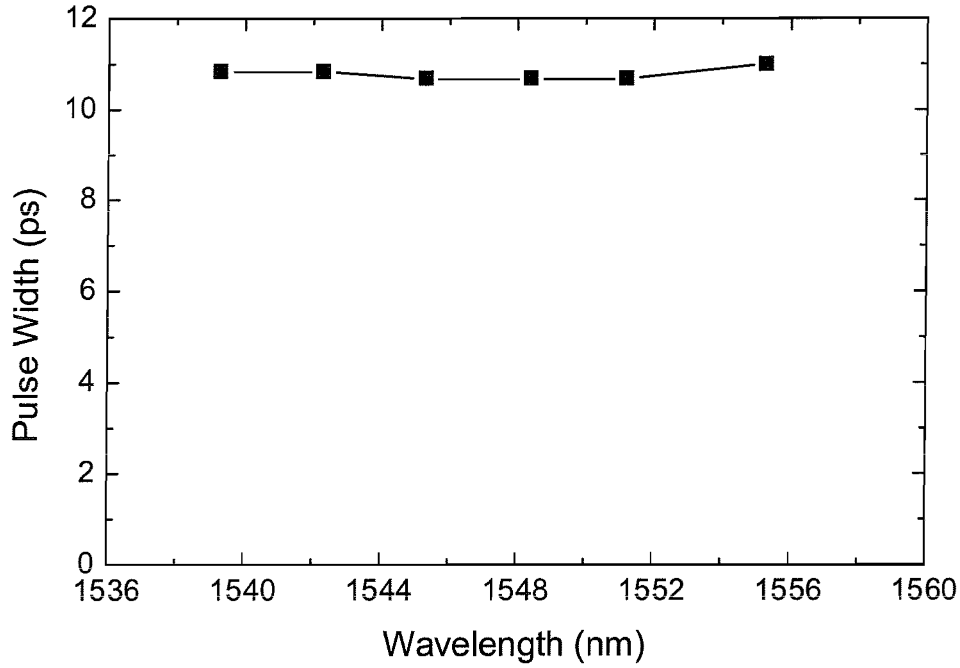

(a)

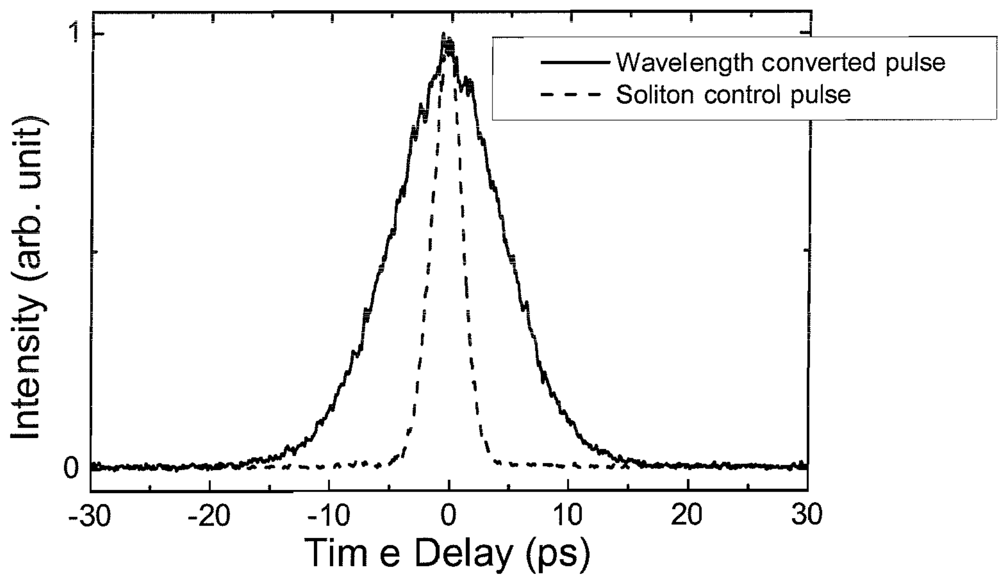

(b)

Figure 8.8: (a) Measured FWHM of the wavelength converted pulses as a function of the probe beam wavelength for the case of wavelength conversion of a single channel. (b) SHG autocorrelation traces of the wavelength converted pulses at 1545 nm, and the input pulses.

Initially the performance of this wavelength converter was characterised in the temporal domain using a SHG autocorrelator (<100 fs resolution). The measured temporal width of the wavelength-converted pulses as a function of probe beam wavelength is plotted in Fig. 8.8. The pulsewidths of the converted pulses were observed to be almost constant at ~11 ps over the full, ~15 nm wavelength tuning wavelength range of the FBG. The walk-off between pump and signal was indeed quite significant and would have generated uneven output pulsewidths over the 15 nm tuning range without bandwidth reduction. However, the use of a narrow bandpass filter (0.5 nm 3 dB bandwidth) restricted the output signal spectrum such that the temporal pulse shape was almost entirely determined by the filtered spectral bandwidth. The time-bandwidth product of the converted pulses was ~0.5 which, although somewhat larger than that of the original control soliton pulses (0.32, transform-limited), still indicates high-quality pulses. The amplitude noise observed on the converted pulses in the previous experiments as shown in Section 8.2, which can be attributed to coherence degradation due to the anomalous dispersion of the particular HF (WBHNL12-125) used [8.12], was eliminated as was anticipated [8.14] (see the eye diagrams of Fig. 8.9). A detailed, numerical study on the coherence degradation problem associated with dispersion in HF could be found from the recent work by J. M. Dudley et al. [8.15]. BER measurements were performed on one channel at a wavelength of 1545 nm. Fig. 8.9 shows both the measured BER and eye diagrams for the soliton control and wavelength converted 10 Gbit/s pulses. Error-free, almost penalty-free (~0.5 dB power penalty) wavelength conversion performance was achieved. Compared to the performance of the highly nonlinear fibre based device in Ref. [8.9], a benefit of using HF is clearly obvious in terms of length/power product since the result shows a lower value of 1.2 (m W) than the 10 (m W) reported in Ref. [8.9]. Both of the results show output pulsewidths that are almost constant over the device operating bandwidth, although relatively broader output temporal pulsewidths are observed in the HF based wavelength converter.

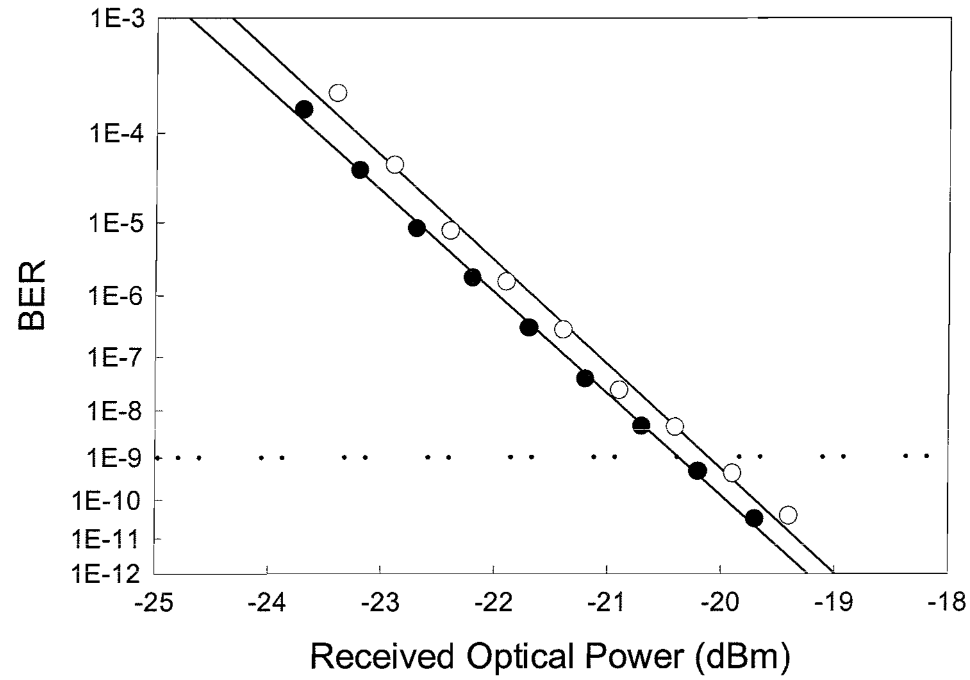

(a)

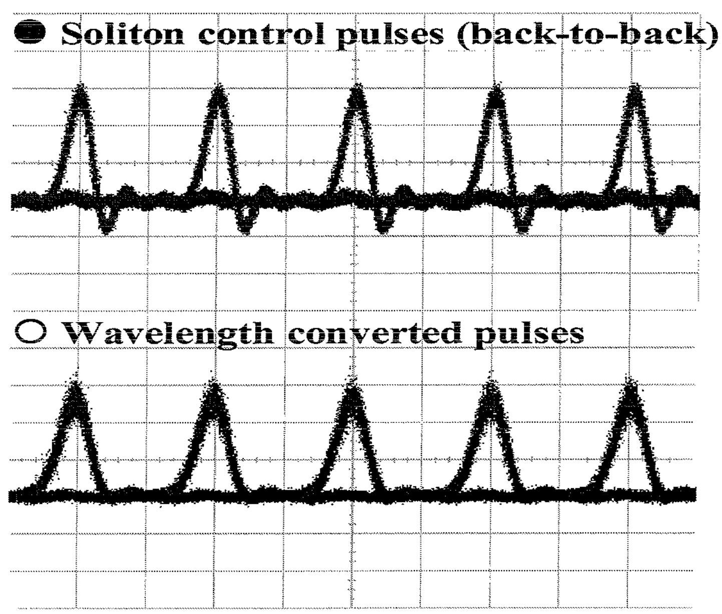

(b)

Figure 8.9: (a) Measured BER versus received optical power for wavelength conversion of 10Gbit/s data pulses to a wavelength of 1545 nm. (b) Measured eye diagrams.

8.4 Conclusion

A high-performance, HF based WDM wavelength converter using XPM and spectral filtering has been reported. Error-free, penalty-free multiple wavelength conversion of 10 Gbit/s RZ data pulses over a ~15 nm bandwidth was reliably obtained using a combination of just 5.8 m of highly nonlinear, normally dispersive HF and an apodized fibre Bragg grating filter. Use of an apodized grating filter with high extinction ratio allows for excellent suppression of residual CW light, pump beams and adjacent wavelength converted channels. The use of a short length of high nonlinearity HF with normal dispersion eliminates coherence degradation effects and reduces walk-off effects. High performance WDM wavelength conversion is thus obtained. In the next Chapter a four-wave mixing based wavelength converter in HF, which is another important, more attractive wavelength conversion technique is reported.

8.5 References

[8.1] I. H. White, R. V. Penty, M. Webster, Y. J. Chai, A. Wonfor, and S. Shahkooh, "Wavelength switching components for future photonic networks," *IEEE Communications Magazine*, vo.40, no.9, pp.74-81, 2002.

[8.2] M. Asghari, I. H. White, and R. V. Penty, "Wavelength conversion using semiconductor optical amplifiers," *J. Lightwave Technol.*, vol.15, no.7, pp.1181-1190, 1997.

[8.3] K. Inoue, and H. Toba, "Wavelength conversion experiment using fiber four-wave mixing," *IEEE Photon. Technol. Lett.*, vol.4, pp.69-72, 1992.

[8.4] A. E. Kelly, A. D. Ellis, D. Nesset, R. Kashyap, and D. G. Moodie, "100 Gbit/s wavelength conversion using FWM in an MQW semiconductor optical amplifier," *Electron. Lett.,* vol.34, no.20, pp.1955-1956, 1998.

[8.5] T. Sakamoto, F. Futami, K. Kikuchi, S. Takeda, Y. Sugaya, S. Watanabe, S, "All-optical wavelength conversion of 500-fs pulse trains by using a nonlinear-optical loop mirror composed of a highly nonlinear DSF," *IEEE Photon. Technol. Lett.*, vol.13, no.5, pp. 502 –504, 2001

[8.6] J. E. Sharping, M. Fiorentino, P. Kumar, and R. S. Windeler, "All-optical switching based on cross-phase modulation in microstructure fiber," *IEEE Photon. Technol. Lett.*, vol.14, pp.77-79, 2002.

[8.7] K. Obermann, S. Kindt, D. Breuer, and K. Petermann, "performance analysis of wavelength converters based on cross-gain modulation in semiconductor-optical amplifiers," *J. Lightwave Technol.*, vol.16, no.1, pp.78-85, 1998.

[8.8] X. Zheng, F. Liu, and A. Kloch, "Experimental investigation of the cascadability of a cross-gain modulation wavelength converter," *IEEE Photon. Technol. Lett.*, vol.12, no.3, pp.272-274, 2000.

[8.9] J. Yu, and P. Jeppesen, "80-Gb/s wavelength conversion based on cross-phase modulation in high-nonlinearity dispersion-shifted fiber and optical filtering," *IEEE Photon. Technol. Lett.*, vol.13, pp.833-835, 2001.

[8.10] P. Ohlen, B. -E. Olsson, and D. Blumenthal, " Wavelength dependence and power requirements of a wavelength converter based on XPM in a dispersion-shifted optical fiber," *IEEE Photon. Technol. Lett.*, vol.12, pp.522-524, 2000.

[8.11] S. Y. Set, B. Dabarsyah, C. S. Goh, K. Katoh, Y. Takushima, K. Kikuchi, Y. Okabe, and N. Takeda, "A widely tunable fiber Bragg grating with a wavelength tenability over 40nm," in *Proc. Optical Fiber Communications Conference (OFC'2001),* Anaheim USA, 2001, Paper MC4.

[8.12] N. Nakazawa, H. Kubota, and K. Tamura, "Random evolution and coherence degradation of a high-order optical soliton train in the presence of noise," *Optics Lett*., vol.24, pp.318-320, 1999.

[8.13] S.-J. Kim, J.-H. Han, J.-S. Lee, and C.-S. Park, "Intensity noise suppression in spectrum-sliced incoherent light communication systems using a gain-saturated semiconductor optical amplifier," *IEEE Photon. Technol. Lett*., vol.11, pp.1042-1044, 1999.

[8.14] J. H. Lee, Z. Yusoff, W. Belardi, M. Ibsen, T. M. Monro, B. Thomsen, and D. J. Richardson, "A holey fiber based WDM wavelength converter incorporating an apodized fiber Bragg grating filter," in *Proc. Conference on lasers and Electro-Optics (CLEO'2002)*, Long beach California, May 2002, Postdeadline CPDB5.

[8.15] J. M. Dudley, and S. Coen, "Numerical simulations and coherence properties of supercontinuum generation in photonic crystal and tapered optical fibers," *IEEE Sel. Topic on Quantum Eletron.,* vol.8, no.3, pp.651-659, 2002.

CHAPTER NINE

FOUR-WAVE MIXING BASED, 10 GBIT/S TUNEABLE WAVELENGTH CONVERSION USING A HOLEY FIBRE WITH A HIGH STIMULATED BRILLOUIN SCATTERING THRESHOLD

This Chapter discusses the use of holey fibre for 10 Gbit/s tuneable wavelength conversion based four-wave mixing (FWM) effect. The HF used for this particular experiment was fabricated so as to exhibit a very high stimulated Brillouin scattering threshold.

This Chapter is organised as follows. Section 9.1 provides a brief introduction to HF technology for four-wave mixing based wavelength conversion. In Section 9.2 characterisation results on the HF with a very high SBS threshold is reported. The experimental results on wavelength conversion based on FWM in the HF are described in Section 9.3. Conclusions are drawn regarding the results and a method to obtain further performance improvement is discussed in Section 9.4.

9.1 Holey Fibre Technology for Four-Wave Mixing Based Wavelength Conversion

A high-speed wavelength converter is likely to be an essential nonlinear device within high capacity all-optical WDM networks and there is thus considerable interest in the development of practical wavelength converters. The applicability of HF technology to this area was discussed in Chapters 8, 9 and a high-performance HF based WDM wavelength converter using a cross-phase modulation (XPM) and filtering approach was correspondingly demonstrated [9.1]. Error-free conversion operation was readily achieved in the experiment. An alternative, and more flexible approach is however based on four-wave mixing (FWM). FWM is particularly attractive for wavelength conversion due to its relative transparency to both bit-rate and modulation format. Highly efficient, broadband wavelength conversion based on FWM in optical fibre requires high nonlinearity, low dispersion, a low dispersion slope, and a short fibre length so as to reduce the phase mismatch between the interacting waves [9.2, 9.3, 9.4]. The reduction of stimulated Brillouin scattering (SBS) effects is a key issue in such devices and is required to suppress SBS induced pump power loss [9.5].

In the following Sections, I report FWM based, tuneable conversion using a highly nonlinear HF with a high SBS threshold. The high SBS threshold is obtained due to broadening of the Brillouin lineshape through structural variation along the fibre length [9.6]. The 15 m HF has a nonlinearity coefficient γ ~70 (+/-10) W^{-1} km^{-1}. The measured SBS threshold is more than 130 mW which is over three times higher than that of a uniform pure silica fibre. Error-free wavelength conversion over a ~10 nm bandwidth of a 10 Gbit/s NRZ data rate is obtained with good efficiency. The elimination of modulation instability related amplitude noise associated with the wavelength conversion process is observed by ensuring that the HF has normal dispersion [9.7].

9.2 Characterisation of the Holey Fibre (DHNL06_15) with a High Stimulated Brillouin Scattering (SBS) Threshold

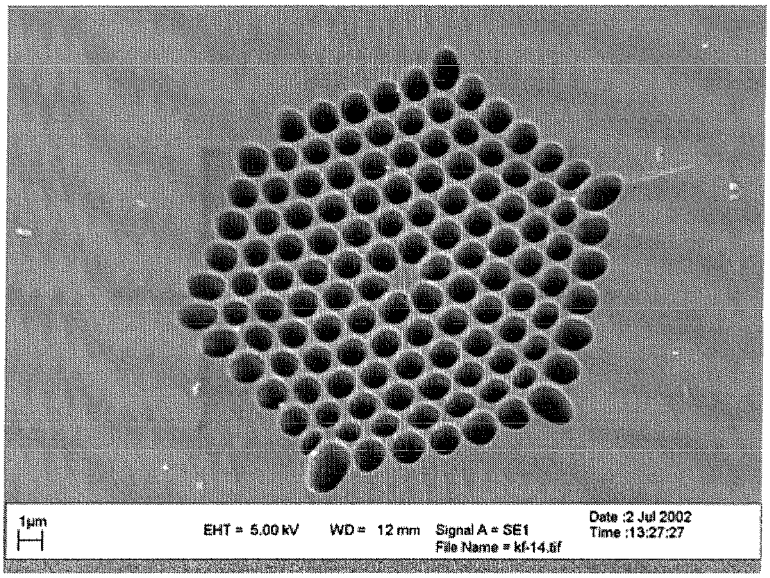

Figure 9.1: Cross-sectional SEM image of the high SBS threshold holey fibre (DHNL06_15) used within these experiments.

A highly nonlinear HF with a high SBS threshold for the experiment was obtained by ensuring structural non-uniformity long its length during the fibre fabrication process through variation of the external fibre diameter [9.6]. The structural variation of the holey fibre (DHNL06_15) was not precisely specified in this instance since the active diameter feedback control ordinarily used when drawing fibre was simply switched off. This resulted in a HF with larger than normal diameter fluctuations. A cross-sectional SEM image of the HF (DHNL06_15) used in this experiment is shown in Fig. 9.1. The core diameter is ~1.2 μm and the outer diameter is ~150 μm. The measured loss was 190 dB/km at 1550 nm and thus the effective length of the 15 m HF (DHNL06_15) was only 11 m. The nonlinearity coefficient γ was measured to be ~70 (+/-10) W^{-1} km^{-1}, which is ~40 times higher than that of conventional dispersion shifted fibres (DSF's), using a direct CW measurement of the nonlinear phase shift suffered by a beat signal propagating in the fibre. The measurement procedure is fully described in Chapter 5.2 and Ref. [9.8]. The accurate derivation of the nonlinear coefficient γ from the measured phase shift is dependent on measurements of the fibre loss and optical coupling. These measurements are somewhat more difficult to measure with accuracy using HF and thus the error quoted is somewhat larger than might be considered usual for the technique when applied to standard fibre types. Such a high nonlinearity allows for a reduction in the device length which is one of key factors required in order to achieve broadband wavelength conversion [9.3, 9.4]. The measured group velocity dispersion (GVD) of the HF (DHNL06_15) is ~ -30 ps/nm-km at a wavelength of 1550 nm. Due to the relatively short length of the fibre, and relatively narrow operating bandwidth of the measurement set up used, it was impossible to get a reliable measurement of the dispersion slope. The best estimate from numerical simulations of the structure would be that the average zero dispersion wavelength along the fibre would be located around 1550 nm, although it should be appreciated that this is likely to vary along the fibre length due to the structural non-uniformity. The predicted average dispersion slope is approximately -0.6 ps/nm^2/km. Then, SBS properties of the 15 m long HF (DHNL06_15) were characterised. The spontaneous Brillouin scattering lineshape of the 15 m HF (DHNL06_15) was first measured, using a hetrodyne-detection technique that relies upon beating the spontaneously scattered light with the pump beam [9.6]. Fig. 9.2(a) shows the measured spontaneous Brillouin spectrum. A non-Lorentzian lineshape comprising two distinct peaks with ~75 MHz frequency separation is clearly observed and results from the structural non-uniformity along the fibre length. The spontaneous Brillouin 3dB bandwidth of one of the two peaks is seen to be approximately 50 MHz, which is over five times broader than would be expected for a silica fibre with a uniform cross-sectional profile [9.6].

The SBS threshold of the 15 m HF (DHNL06_15) used for wavelength conversion was estimated to be higher than 130 mW since it was impossible to observe stimulated Brillouin scattering due to the limited output power of the high-power amplifier used (maximum pump power inside the HF: ~130 mW). The SBS threshold of a 20 m length of nominally the same fibre was measured to be ~100 mW as shown in Fig. 9.2(b), which is around two times higher than would be expected for a silica fibre with a uniform cross-sectional profile.

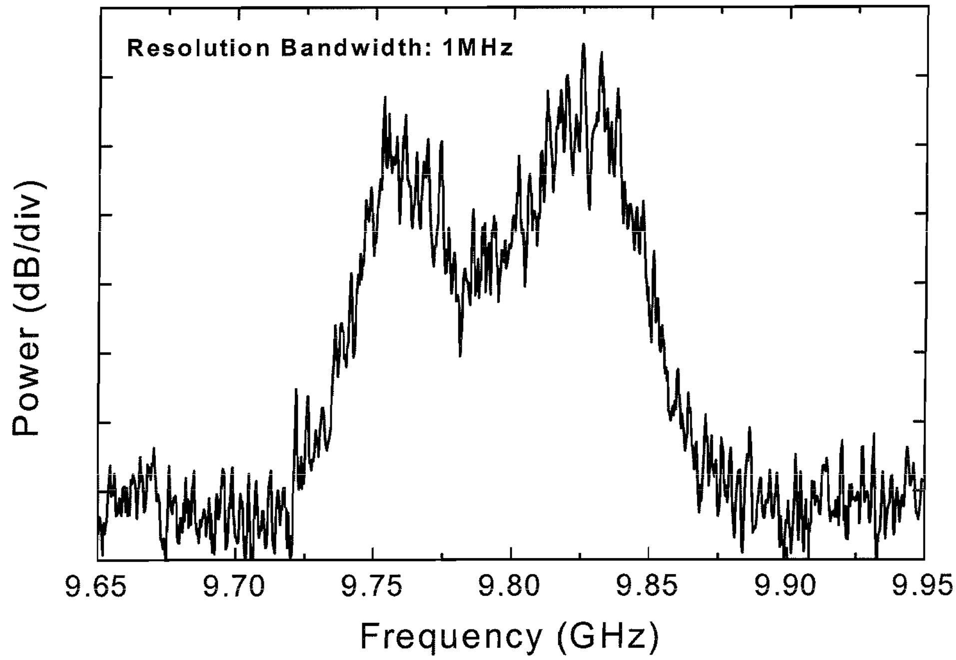

(a)

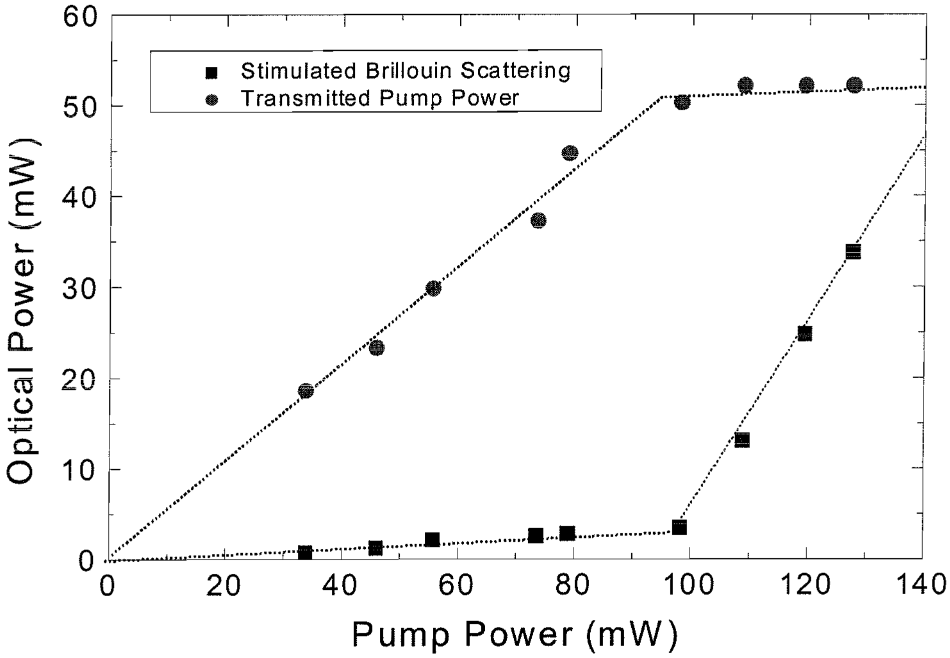

(b)

Figure 9.2: (a) RF frequency trace of the beat signals between spontaneous Brillouin scattered beam and the pump, using the 15 m long HF (DHNL06_15) described in Fig. 1(a). (b) Stimulated Brillouin scattering and transmitted pump power as a function of launched pump power, using a 20 m length of nominally the same fibre.

9.3 Experimental Results on Wavelength Conversion Based on FWM in the Holey Fibre

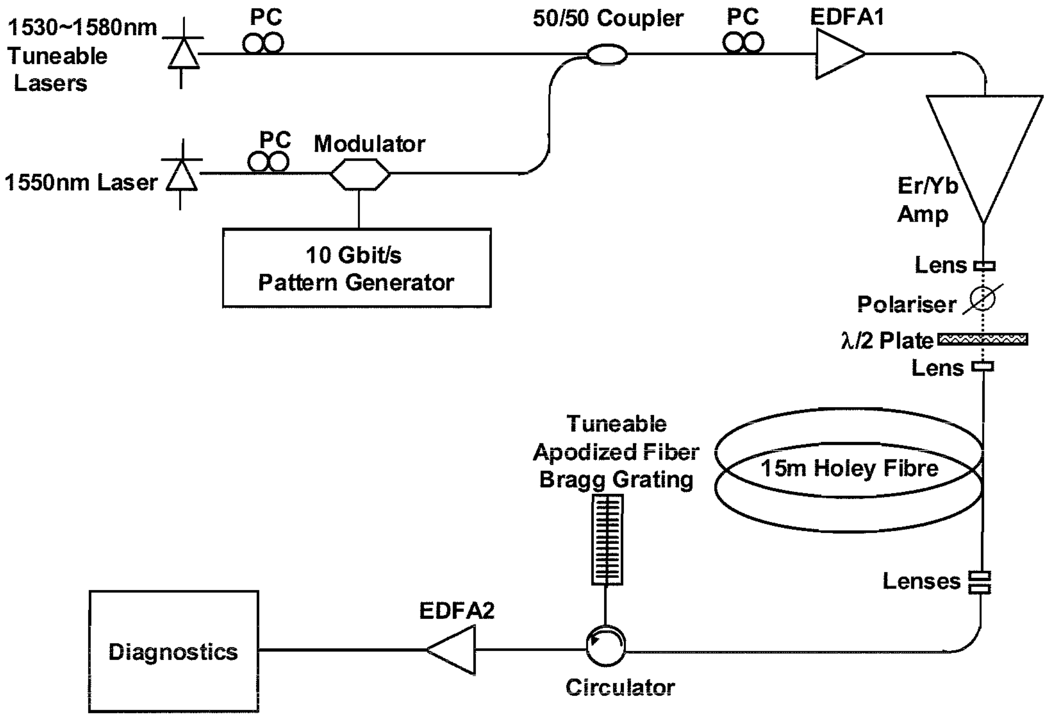

Figure 9.3: Experimental setup

The schematic of the experiment is shown in Fig. 9.3. Both the pump and the signal beams were derived from tuneable, continuous wave, external cavity lasers operating in the range 1530~1580 nm. The signal beam at a fixed wavelength of 1550 nm was modulated with a $2^{15} - 1$ pseudorandom data sequence at a data rate of 10 Gbit/s and then combined with the pump beam using a 50/50 coupler. The two beams were then amplified using an Er/Yb amplifier with a maximum saturated power of ~700 mW and then lens coupled into the 15 m long HF (DHNL06_15) with a coupling efficiency of ~20 %. Polarisation controllers (PC's), a polarizer, and a λ/2 plate were used to ensure that both beams were launched onto a single polarisation axis of the polarisation maintaining HF, which had a beat length of ~ 0.5 mm and a polarisation extinction ratio of 17 dB.

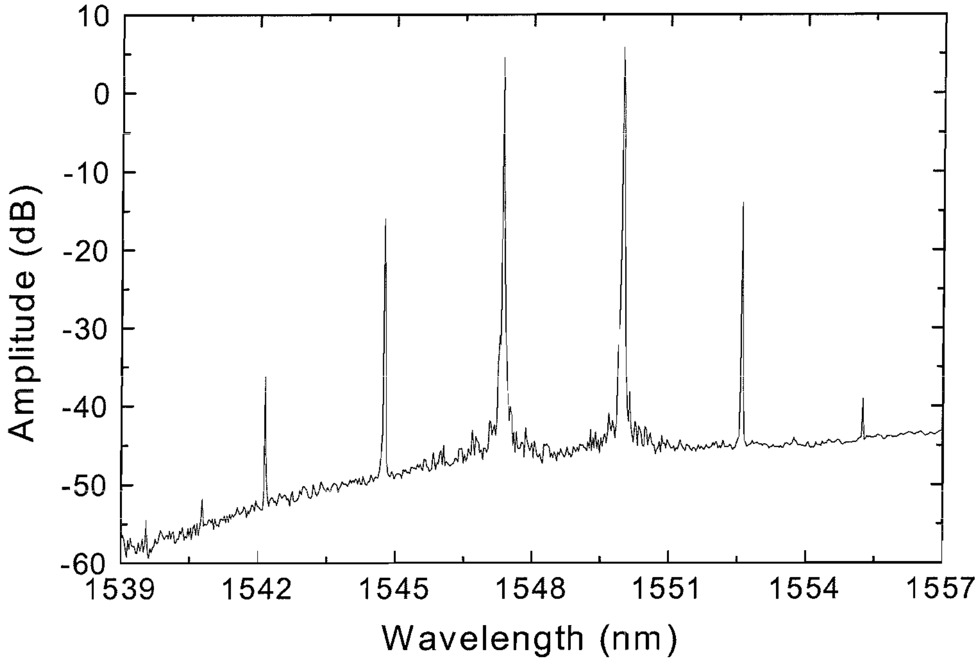

(a)

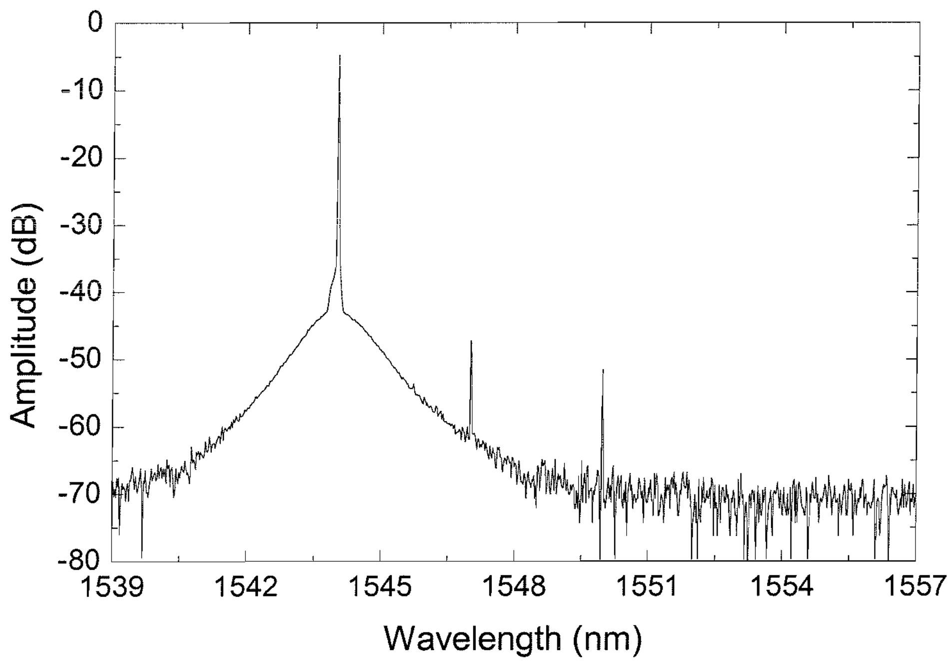

(b)

Figure 9.4: (a) Output FWM spectrum after the HF (DHNL06_15) only (input signal at λ = 1550 nm, pump at λ =1547 nm). (b) Wavelength converted signal spectrum after the apodized fibre Bragg grating filter.

The HF (DHNL06_15) output spectrum is shown in Fig. 9.4(a). The wavelengths of the initial signal and the pump beams are 1550 nm and 1547 nm, respectively. A strong FWM wavelength converted signal is clearly evident at a wavelength of 1544 nm despite the short fibre length used and both second and third order idler beams are also observable. After the HF (DHNL06_15) a compression tuneable, apodized fibre Bragg grating (FBG) filter with a 3 dB bandwidth of 0.55 nm and a 30 dB bandwidth of 1.5 nm was used to efficiently suppress the input signal and pump beams and to pick out the wavelength converted signal [9.1]. The spectrum of the converted signal after the two-stage FBG filter is shown in Fig. 9.4(b). A ~40 dB extinction ratio between the idler and the pump was achieved.

Fig. 9.5 shows the measured conversion efficiency, which is defined as the ratio of output wavelength-converted signal power to the input signal power. A maximum conversion efficiency of −16 dB was achieved over a 3 dB bandwidth of ~10 nm.

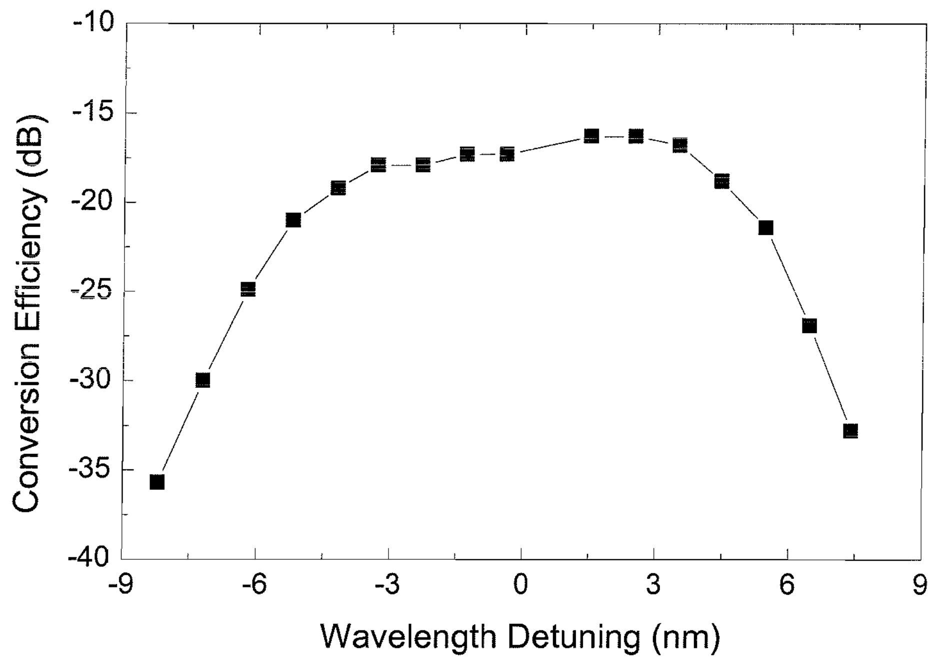

Figure 9.5: Measured conversion efficiency versus wavelength detuning relative to a fixed signal wavelength of 1550 nm.

In order to analyse the system impact of using this HF based FWM wavelength converter in practical WDM applications BER measurements were performed on the wavelength converted channel at 1544 nm (see Fig. 9.4(a)). Fig. 9.6 shows both the measured BER and eye diagrams for both the 10 Gbit/s NRZ input signal and wavelength converted output signal. Error-free (BER < 10^{-9}) wavelength conversion performance was obtained with a ~2 dB power penalty relative to that of the back-to-back input signal. The conversion efficiency will be a function of pump wavelength and the BER performance will also depend on the pump and signal wavelengths since the HF (DHNL06_15) is operated in a wavelength regime in which the dispersion slope is relatively high and the net GVD is small.

A small amount of timing jitter and intensity noise is observed from the eye diagrams, which is believed to be due to polarisation coupling in this highly birefringent small core fibre. However, since the fibre had normal dispersion, no modulational instability induced intensity noise was observed [9.7]. In order to ensure the benefits of the use of normal dispersion fibres in the realisation of this sort of nonlinear fibre devices, similar FWM based wavelength conversion experiments were carried out using a HF with an anomalous dispersion of +10 ps/nm-km. The intensity noise, which can be attributed to modulational instability in anomalous dispersion regime, was so severe that BER measurements could not be performed.

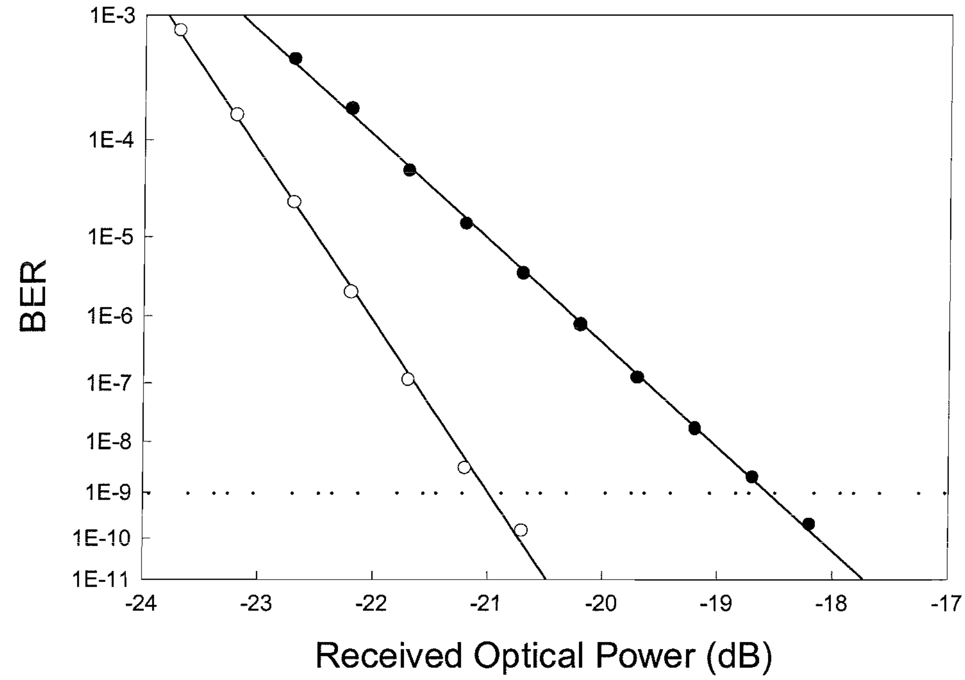

(a)

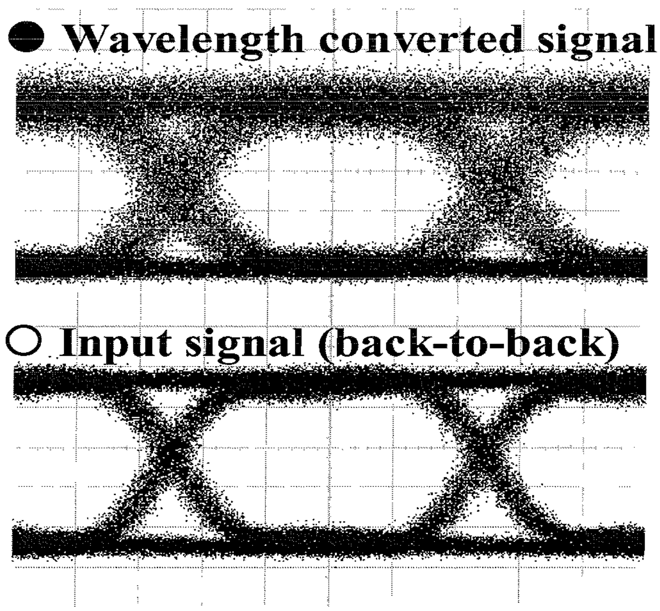

(b)

Figure 9.6: (a) Measured BER versus received optical power for wavelength conversion of a 10 Gbit/s NRZ signal at a wavelength of 1544 nm. (b) Eye diagrams.

9.4 Conclusion

A HF based tuneable wavelength converter using FWM has been experimentally demonstrated. Error free wavelength conversion of 10 Gbit/s NRZ data signals over a ~10 nm bandwidth was reliably achieved using just 15 m of highly nonlinear HF with a high SBS threshold. Although the HF based FWM wavelength converter shows slightly worse performance in terms of conversion efficiency and tuning bandwidth compared to the results achieved with highly nonlinear fibre (HNLF) [9.3], the use of a highly nonlinear HF with lower and flatter GVD should allow for further improvements. However, non-uniform HF technology has offers significant advantages in terms of reduced device length, reduced power requirements and ease of use since it eliminates the need for active schemes to reduce pump power loss caused by Brillouin scattering.

9.5 References

[9.1] J. H. Lee, Z. Yusoff, W. Belardi, M. Ibsen, T. M. Monro, B. Thomsen, and D. J. Richardson, "A holey fiber based WDM wavelength converter incorporating an apodized fiber Bragg grating filter," in *Proc. Conference on lasers and Electro-Optics (CLEO'2002)*, Long beach California, May 2002, Postdeadline CPDB5.

[9.2] K. Inoue, and H. Toba, "Wavelength conversion experiment using fiber four-wave mixing," *IEEE Photon. Technol. Lett.*, vol.4, pp.69-72, 1992.

[9.3] O. Aso, S. Arai, T. Yagi, M. Tadakuma, Y. Suzuki, and S. Namiki, "Broadband four-wave mixing generation in short optical fibre," *Electron. Lett.*, v.36, p.709-711, 2000.

[9.4] J. E. Sharping, M. Fiorentino, A. Coker, P. Kumar, and R. S. Windeler, "Four-wave mixing in microstructure fiber," *Optics Lett.*, vol.26, pp.1048-1050, 2001.

[9.5] J. Hansryd, F. Dross, M. Westlund, P. A. Antrekson, and S. N. Knudsen, "Increase of the SBS threshold in a short highly nonlinear fiber by applying a temperature distribution," *J. Lightwave Technol.*, vol.19, pp.1691-1697, 2001.

[9.6] J.H. Lee, Z. Yusoff, W. Belardi, M. Ibsen, T. M. Monro, B. Thomsen, and D. J. Richardson, "Investigation of Brillouin effects in small-core holey optical fiber: lasing and scattering," *Optics Lett.*, vol.27, pp.927-929, 2002.

[9.7] D. F. Grosz, C. Mazzali, S. Celaschi, A. Paradisi, and H. L. Fragnito, "Modulation instability induced resonant four-wave mixing in WDM systems," *IEEE Photon. Technol. Lett.*, vol.11, pp.379-381, 1999.

[9.8] A. Boskovic, S.V Chernikov, J.R. Taylor, L. Gruner-Nielsen, and O.A. Levring, "Direct continuous-wave measurement of n_2 in various types of telecommunication fiber at 1.55 μm," *Optics Lett.*, vol.21, pp.1966-1968, 1996.

CHAPTER TEN

CONCLUSION

The overall objective of the works reported in this thesis was to improve nonlinear optical signal processing device technologies and to find appropriate applications of those devices for fibre-optic communication systems. This has been achieved in two aspects.

Firstly, overall system performance improvement using a combined technology of nonlinear optical devices and superstructured fibre Bragg gratings has been investigated, specifically in time-spreading DS-OCDMA systems and high-speed OTDM systems. The SSFBG approach is now considered to represent an extremely powerful and flexible way of manipulating the temporal characteristics of pulses and I believe that it could play an important role in future high-speed, high capacity optical communication systems and networks.

Secondly holey fibre technology has been investigated as a strong candidate for implementation of a range of nonlinear telecommunication devices such as nonlinear thresholding devices, Raman amplifier, Brillouin lasers, and wavelength converters. Further applications are certain to be found in near future. However further study is still required to investigate issues such as coupling efficiency, polarisation sensitivity, loss, and optimisation of dispersion characteristics associated with the use of such devices in real telecommunication or photonic systems. HF technology offers significant advantages in terms of reduced device length, reduced power requirements for a variety of nonlinear optical devices. Ultimately, HF technology should prove to be a powerful way to realise a wide range of practical nonlinear optical devices for fibre-optic communication systems.

PUBLICATIONS ARISING FROM MY PHD WORK

[1] J.H. Lee, L.K. Oxenløwe, M. Ibsen, K.S. Berg, A.T. Clausen, D.J. Richardson, and P. Jeppesen, "All-optical TDM data demultiplexing at 80 Gbit/s with significant timing jitter tolerance using a fiber Bragg grating based rectangular pulse switching technology," submitted to *J. Lightwave Technol.*, December 2002.

[2] J. H. Lee, W. Belardi, T. M. Monro, and D. J. Richardson, " Holey fiber based nonlinear optical devices for telecommunications," to be presented in *Conference on Laser and Electro-Optics (CLEO'2002),* Baltimore USA, June 2003 (Invited paper).

[3] J.H. Lee, L.K. Oxenløwe, M. Ibsen, K.S. Berg, A.T. Clausen, D.J. Richardson, and P. Jeppesen, "Timing jitter tolerant all-optical TDM data demultiplexing at 80 Gbit/s using fiber Bragg grating based rectangular pulse switching technology," to be presented in *Optical Fiber Communications Conference (OFC'2003),* TuH7, Atlanta USA, March 2003.

[4] F. Parmigiani, P. Petropoulos, P. J. Almeida, M. Ibsen, J. H. Lee, D.J.Richardson, "A direct assessment of the performance of pulse shaping superstructured fiber gratings using an optical sampling oscilloscope," to be presented in *Optical Fiber Communications Conference (OFC'2003),* MF36, Atlanta USA, March 2003.

[5] J. H. Lee, Z. Yusoff, W. Belardi, M. Ibsen, T. M. Monro, and D. J. Richardson, "A Tuneable WDM Wavelength Converter Based on Cross Phase Modulation effects in Holey Fiber," accepted for publication in *IEEE Photon. Technol. Lett.,* vol.15, March 2003.

[6] J. H. Lee, W. Belardi, K. Furusawa, P. Petropoulos, Z. Yusoff, T. M. Monro, and D. J. Richardson, "Four-Wave Mixing Based, 10Gbit/s Tuneable Wavelength Conversion Using a Holey Fiber with a High SBS Threshold," accepted for publication in *IEEE Photon. Technol. Lett.,* vol.15, March 2003.

[7] J. H. Lee, D. J. Richardson, Z. Yusoff, W. Belardi, and T. M. Monro, "System applications of holey fibers," *15th Annual meeting of the IEEE Lasers & electro-Optics Society (LEOS'2002)*, Glasgow Scotland, November 2002 (Invited paper).

[8] K. M. Kiang, K. Frampton, T. M. Monro, M. N. Petrovich, R. Moore, J. H. Lee, Z. Yusoff, J. Tucknott, D. W. Hewak, H. N. Rutt, and D. J. Richardson, "Extrusion of high nonlinearity single-mode holey optical fibers," *The American Ceramic Society, Glass & Optical Materials Division Fall Meeting,* Pittsburgh USA, October 2002.

[9] W. Belardi, J. H. Lee, K. Furusawa, Z.Yusoff, P. Petropoulos, M. Ibsen, T. M. Monro, and D. J. Richardson, "A 10 Gbit/s tuneable wavelength converter based on four-wave mixing in highly nonlinear holey fibre," *28th European Conference on Optical Communication (ECOC'2002),* PD1-2, Copenhagen Denmark, September 2002 (Postdeadline paper).

[10] J. H. Lee, Z. Yusoff, W. Belardi, T. M. Monro, B. Thomsen, and D. J. Richardson, "Holey fiber based tuneable WDM wavelength converter using cross-phase modulation and filtering," *28th European Conference on Optical Communication (ECOC'2002),* 3.4.3, Copenhagen Denmark, September 2002.

[11] B. C. Thomsen, P. C. Teh, M. Ibsen, J. H. Lee, and D. J. Richardson, "A multi-hop optical packet switching demonstration employing all-optical grating based header generation and recognition," *28th European Conference on Optical Communication (ECOC'2002),* 5.5.3, Copenhagen Denmark, September 2002.

[12] T. M. Monro, V. Finazzi, W. Belardi, K. M. Kiang, J. H. Lee, and D. J. Richardson, "Highly nonlinear holey optical fibres: design manufacture and device applications," *28th European Conference on Optical Communication (ECOC'2002),* SI.05, Copenhagen Denmark, September 2002 (Invited paper).

[13] D.J. Richardson, J.H. Lee, Z. Yusoff, W. Belardi, K. Furusawa, J. H.V. Price, M. Kiang, K. Frampton, D.Hewak, J.A. Tucknott, R.C. Moore, H.N. Rutt and T.M. Monro, "Holey fibers for nonlinear fiber devices," *Optical Amplifiers and Their Applications (OAA'2002)*, OMD1, Vancouver Canada, July 2002 (Invited paper).

[14] M. Ibsen, R. Feced, P. C. Teh, J. H. Lee, M. R. Mokhtar, P. Petropoulos, M. N. Zervas, D. J. Richardson, and D. N. Payne, "Advanced fibre Bragg gratings and where they are going," *AIP-ACOFT 2002,* Sydney Australia, 8-11 Jul 2002 (Invited paper).

[15] J. H. Lee, P. C. Teh, Z. Yusoff, M. Ibsen, W. Belardi, T. M. Monro, and D. J. Richardson, "A holey fiber based nonlinear thresholding device for optical CDMA

receiver performance enhancement," *IEEE Photon. Technol. Lett.,* vol.14, no.6, pp.876-878, June 2002.

[16] J. H. Lee, Z. Yusoff, W. Belardi, M. Ibsen , T. M. Monro, and D. J. Richardson, "Investigation of Brillouin effects in small core holey optical fiber: lasing and scattering," *Optics Lett.*, vol.27, no.11, pp.927-929, June 2002.

[17] J. H. Lee, Z. Yusoff, W. Belardi, T. M. Ibsen, M. Monro, B. Thomsen, amd D. J. Richardson, "Holey fiber based WDM wavelength converter incorporating an apodized fiber Bragg grating filter," *Conference on Laser and Electro-Optics (CLEO'2002),* Long beach USA, May 2002 (Postdeadline paper).

[18] Z. Yusoff, J.H. Lee, W. Belardi, M. Ibsen, T.M. Monro, and D.J. Richardson, "A holey fiber based Brillouin laser," *Conference on Laser and Electro-Optics (CLEO'2002),* CMJ7, Long beach USA, May 2002.

[19] Z. Yusoff, J.H. Lee, W. Belardi, T.M. Monro, P.C. Teh, and D.J. Richardson, "Raman effects in a highly nonlinear holey fiber: amplification and modulation," *Optics Lett.*, vol.27, no.6, pp.424-426, March 2002.

[20] T. M. Monro, K. M. Kiang, J. H. Lee, K. Frampton, Z. Yusoff, R. Moore, J. Tucknott, D. W. Hewak, H. N. Rutt, and D. J. Richardson, "High nonlinearity extruded single-mode holey optical fibers," *Optical Fiber Communications Conference (OFC 2002)* Anaheim, 19-21 March 2002 (Postdeadline paper).

[21] J. Nilsson, R. Selvas, W. Belardi, J. H. Lee, Z. Yusoff, T. M. Monro, D. J. Richardson, "Continuous-wave pumped holey fiber Raman laser," *Optical Fiber Communications Conference (OFC'2001),* CR6, Anaheim USA, March 2002.

[22] P. C. Teh, M. Ibsen, L.B. Fu, J. H. Lee, Z. Yusoff, and D. J. Richardson, "A 16-channel OCDMA system (4 OCDMA X 4WDM) based on 16-chip, 20 Gchip/s sperstructure fibre Bragg gratings and DFB laser transmitters," *Optical Fiber Communications Conference (OFC'2001)*, ThEE1, Anaheim USA, March 2002 (Invited paper).

[23] J. H. Lee, P. C. Teh, P. Petropoulos, M. Ibsen and D. J. Richardson, "All-optical modulation and demultiplexing systems with significant timing jitter tolerance through incorporation of pulse-shaping fiber Bragg gratings," *IEEE Photon. Technol. Lett.*, vol.14, no.2, pp.203-205, February 2002.

[24] P. C. The, M. Ibsen, J. H. Lee, P. Petropoulos, and D. J. Richardson, "Demonstration of a four-channel WDM/OCDMA system using 255-chip 320-Gchip/s quaternary phase coding gratings," *IEEE Photon. Technol. Lett.*, vol.14, no.2, pp.227-229, February 2002.

[25] J. H. Lee, P. C. Teh, P. Petropoulos, M. Ibsen and D. J. Richardson, "A grating based OCDMA coding:decoding system incorporating a nonlinear optical loop mirror for improved code recognition and noise reduction," *J. Lightwave Technol.*, vol.20, no.1, pp.36-46, January 2002.

[26] D. J. Richardson, P. C. Teh, M. Ibsen, P. Petropoulos, and J. H. Lee, "Superstructured gratings enable OCDMA/WDM compatibility," *WDM Solutions* October, 2001.

[27] J. H. Lee, Z. Yusoff, W. Belardi, T. M. Monro, P. C. Teh, and D. J. Richardson, "A holey fibre Raman amplifier and all-optical modulator," *27th European Conference on Optical Communication (ECOC'2001),* PD.A.1.1, Amsterdam the Netherlands, October 2001 (Postdeadline paper).

[28] J. H. Lee, P. C. Teh, Z. Yusoff, M. Ibsen, W. Belardi, T. M. Monro, and D. J. Richardson, "An OCDMA receiver incorporating a holey fibre nonlinear thresholder," *27th European Conference on Optical Communication (ECOC'2001),* PD.B.1.2, Amsterdam the Netherlands, October 2001 (Postdeadline paper).

[29] W. Belardi, T. M. Monro, J. H. V. Price, J. H. Lee, P. Petropoulos and D. J. Richardson, "Fabrication and applications of highly nonlinear silica holey fibres," *QEP-15*, Glasgow UK September 2001.

[30] P. Petropoulos, T. M. Monro, W. Belardi, K. Furusawa, J. H. Lee, and D. J. Richardson, "A 2R-regenerative all-optical switch based on a highly nonlinear fiber", *Optics Lett.*, vol. 26, no.16, pp.1233-1235, August 2001.

[31] J. H. Lee, P. C. Teh, P. Petropoulos, M. Ibsen and D. J. Richardson, "Reduction of interchannel interference noise in a two-channel, grating based OCDMA system using a nonlinear optical loop mirror," *IEEE Photon. Technol. Lett*, vol.13, no.5, pp.529-531, May 2001.

[32] J. H. Lee, P. C. Teh, P. Petropoulos, M. Ibsen and D. J. Richardson, " The use of nonlinear optical elements for signal recognition signature enhancement in a

grating based all-optical CDMA coding:decoding system," *Rank Prize Fund Mini symposium: Tera-bit Optical Networks*, Lake district UK, April 2001.

[33] J. H. Lee, P. C. Teh, P. Petropoulos, M. Ibsen and D. J. Richardson, "Timing jitter tolerant all-optical modulator and demultiplexing systems incorporating pulse-shaping friber Bragg gratings," *Optical Fiber Communications Conference (OFC'2001),* PD30, Anaheim USA, March 2001 (Postdeadline paper).

[34] P. C. Teh, M. Ibsen, J. H. Lee, P. Petropoulos, and D. J. Richardson, "A 4-channel WDM/OCDMA system incorporating 255-chip, 320 Gchip/s quaternary phase coding and decoding gratings," *Optical Fiber Communications Conference (OFC'2001),* PD37, Anaheim USA, March 2001 (Postdeadline paper).

[35] J. H. Lee, P. C. Teh, P. Petropoulos, M. Ibsen and D. J. Richardson, "High performance, 64-chip, 160Gchip/s fiber grating based OCDMA receiver incorporating a nonlinear optical loop mirror," *Optical Fiber Communications Conference (OFC'2001)*, ThH4, Anaheim USA, March 2001.

[36] P. C. Teh, J. H. Lee, M. Ibsen, P. Petropoulos, and D. J. Richardson, "A 10-Gbit/s all-optical code generation and recognition system based on a hybrid approach of a fiber delay line and superstructure fiber Bragg grating technologies," *Optical Fiber Communications Conference (OFC'2001)*, WDD91, Anaheim USA, March 2001.

[37] P. Petropoulos, T. M. Monro, W. Belardi, K. Furusawa, J. H. Lee, and D. J. Richardson, "A highly nonlinear holey fiber and its application in a regenerative optical switch," *Optical Fiber Communications Conference (OFC'2001)*, TuC3, Anaheim USA, March 2001.